ASME
SETTING THE STANDARD

Journal of Fluids Engineering

Published Monthly by ASME

VOLUME 131 • NUMBER 8 • AUGUST 2009

RESEARCH PAPERS

Flows in Complex Systems

081101 Aerodynamic Performance of Blade Tip End-Plates Designed for Low-Noise Operation in Axial Flow Fans
Alessandro Corsini, Franco Rispoli, and A. G. Sheard

081102 Experimental Evidence of Hydroacoustic Pressure Waves in a Francis Turbine Elbow Draft Tube for Low Discharge Conditions
Jorge Arpe, Christophe Nicolet, and François Avellan

081103 Impact of Orifice Length/Diameter Ratio on 90 deg Sharp-Edge Orifice Flow With Manifold Passage Cross Flow
W. H. Nurick, T. Ohanian, D. G. Talley, and P. A. Strakey

081104 An Experimental Investigation of the Flowfield and Dust Resuspension Due to Idealized Human Walking
Yoshihiro Kubota, Joseph W. Hall, and Hiroshi Higuchi

081105 An Efficient Quasi-2D Simulation of Waterhammer in Complex Pipe Systems
Huan-Feng Duan, Mohamed S. Ghidaoui, and Yeou-Koung Tung

Fundamental Issues and Canonical Flows

081201 Joint Computational/Experimental Aerodynamic Study of a Simplified Tractor/Trailer Geometry
Subrahmanya P. Veluri, Christopher J. Roy, Anwar Ahmed, Rifki Rifki, John C. Worley, and Bryan Recktenwald

081202 Spontaneous Break of Symmetry in Unconfined Laminar Annular Jets
Christian Del Taglia, Alfred Moser, and Lars Blum

Multiphase Flows

081301 Effect of Liquid Transparency on Laser-Induced Motion of Drops
R. Shukla and K. A. Sallam

Techniques and Procedures

081401 A Lattice Boltzmann Method Based Numerical Scheme for Microchannel Flows
S. C. Fu, W. W. F. Leung, and R. M. C. So

081402 Application of Fractional Scaling Analysis to Loss of Coolant Accidents, System Level Scaling for System Depressurization
Wolfgang Wulff, Novak Zuber, Upendra S. Rohatgi, and Ivan Catton

TECHNICAL BRIEFS

084501 Fluid Streaming in Micro/Minibifurcating Networks
Z. Zhang, A. Fadl, C. Liu, D. M. L. Meyer, and M. Krafczyk

(Contents continued on inside back cover)

Transactions of the ASME, Journal of Fluids Engineering (ISSN 0098-2202) is published monthly by The American Society of Mechanical Engineers, Three Park Avenue, New York, NY 10016. Periodicals postage paid at New York, NY and additional mailing offices.
POSTMASTER: Send address changes to Transactions of the ASME, Journal of Fluids Engineering, c/o THE AMERICAN SOCIETY OF MECHANICAL ENGINEERS, 22 Law Drive, Box 2300, Fairfield, NJ 07007-2300.
CHANGES OF ADDRESS must be received at Society headquarters seven weeks before they are to be effective. Please send old label and new address.

Canadian Goods & Services Tax Registration #126148048.

(**Contents continued**)

Journal of Fluids Engineering **Volume 131, Number 8** **AUGUST 2009**

DESIGN INNOVATION

085001 Modeling of Pumping Performance of Labyrinth Screw Pump (LSP) by 2D Reynolds Stress Equations
Runmei Ma and Kuisheng Wang

The ASME Journal of Fluids Engineering is abstracted and indexed in the following:

Applied Science & Technology Index, Chemical Abstracts, Chemical Engineering and Biotechnology Abstracts (Electronic equivalent of Process and Chemical Engineering), Civil Engineering Abstracts, Computer & Information Systems Abstracts, Corrosion Abstracts, Current Contents, Ei EncompassLit, Electronics & Communications Abstracts, Engineered Materials Abstracts, Engineering Index, Environmental Engineering Abstracts, Environmental Science and Pollution Management, Excerpta Medica, Fluidex, Index to Scientific Reviews, INSPEC, International Building Services Abstracts, Mechanical & Transportation Engineering Abstracts, Mechanical Engineering Abstracts, METADEX (The electronic equivalent of Metals Abstracts and Alloys Index), Petroleum Abstracts, Process and Chemical Engineering, Referativnyi Zhurnal, Science Citation Index, SciSearch (The electronic equivalent of Science Citation Index), Shock and Vibration Digest, Solid State and Superconductivity Abstracts, Theoretical Chemical Engineering

Aerodynamic Performance of Blade Tip End-Plates Designed for Low-Noise Operation in Axial Flow Fans

Alessandro Corsini
Franco Rispoli
Dipartimento di Meccanica e Aeronautica,
"Sapienza" University of Rome,
Via Eudossiana 18,
I00184 Rome, Italy

A. G. Sheard
Fläkt Woods Limited,
Axial Way,
Colchester CO4 5AR, UK

This study assesses the effectiveness of modified blade-tip configurations in achieving passive noise control in industrial fans. The concepts developed here, which are based on the addition of end-plates at the fan-blade tip, are shown to have a beneficial effect on the fan aeroacoustic signature as a result of the changes they induce in tip-leakage-flow behavior. The aerodynamic merits of the proposed blade-tip concepts are investigated by experimental and computational studies in a fully ducted configuration. The flow mechanisms in the blade-tip region are correlated with the specific end-plate design features, and their role in the creation of overall acoustic emissions is clarified. The tip-leakage flows of the fans are analyzed in terms of vortex structure, chordwise leakage flow, and loading distribution. Rotor losses are also investigated. The modifications to blade-tip geometry are found to have marked effects on the multiple vortex behaviors of leakage flow as a result of changes in the near-wall fluid flow paths on both blade surfaces. The improvements in rotor efficiency are assessed and correlated with the control of tip-leakage flows produced by the modified tip end-plates. [DOI: 10.1115/1.3026723]

1 Introduction

Aerodynamic efficiency and acoustic signature are the main factors to be considered in the design of axial flow fans in both low-speed ventilating equipment and high-bypass-ratio turbo-fan engines. Because the fan is recognized as the most significant source of noise in both subsonic and supersonic tip Mach number regimes [1], the objective of effective design must be to optimize fan-blade configurations in a manner that minimizes acoustic emissions, especially in terms of manipulating flow in the vicinity of the tip gap. In this regard, the tip-to-casing clearance is a design parameter that has a significant impact on stability and aerodynamic performance [2–4]. In addition, the tip-clearance flow is recognized as having an influence on rotor noise as a result of blade-tip-vortex interactions and high-frequency noise, which is generated as turbulent boundary-layer noise from the blade surfaces and the end-walls [5–7].

Apart from the acoustic radiation from steady rotor forces in the low-frequency range of high-speed machines, similar mechanisms determine broadband noise in subsonic fans, supersonic tip-speed fans, and compressors [8]. These mechanisms are a consequence of rotor noise originating from turbulent boundary layers on the blade surface and the annulus [9], and from vortex flow near the rotor tip. Techniques that help to reduce tip-clearance noise, without sacrificing aerodynamic efficiency, are therefore highly desirable. However, control (and reduction) of noise generated by the rotor-tip-flow field has not received the research attention that it deserves—primarily because of a lack of understanding of the complex flow-field involved.

Attempts to find solutions to the problem of noise control in fans and compressors have included active and passive noise-control techniques that aim to reduce the leakage-flow rate or to enhance the primary-to-secondary flow-momentum transfer. With respect to *passive* control techniques, the use of a swept blade-stacking line design [10] is known to improve stall-free operating margins [11]; however, the major gains in passive control techniques have been associated with modifications to machine geometry in the vicinity of the gap between the blade tip and the casing.

The use of casing treatments in the shroud portion over the blade tip has been reported to improve the stable flow range by weakening the tip-leakage vortex. Notable contributions have included the use of grooves and slots [12,13] or stepped-tip gaps [14]. In the specific instance of subsonic fans, recirculating vanes and annular rings have been proposed as antistall devices [15].

During the past decade, several researchers have proposed passive noise-control concepts based on modifications to the blade tip by means of antivortex appendages. End-plates have been proposed by Quinlan and Bent [7] and Corsini et al. [16], and various solutions have been proposed in patents for industrial fans [15,17–19].

The present study develops the theory of passive noise control by assessing the aerodynamic flow features associated with blade tips modified by the addition of aerodynamic appendages on a data blade. The original concept, developed by the Fläkt Woods Group (Colchester, England) [20], is compared with end-plate configurations that exploit a variable-thickness distribution [21,22]. In particular, the present study examines two new tip appendages in which constant and variable-thickness end-plates are implemented with sudden gap enlargement on the suction side in a stepwise fashion.

The study focuses on a family of commercially available fans and compares the aerodynamic and aeroacoustic performance of the data blade (which is typical of a class of low-noise industrial fans) with the proposed improvements in tip configurations. The single-rotor investigations are carried out in a ducted configuration under design conditions, adopting a large tip-pitch angle configuration of 28 deg (at which the fan provides the greatest static-pressure rise in its operational range).

The aerodynamic performance and noise experiments are conducted in the aerodynamic test rig and anechoic chamber of the research laboratories of the Fläkt Woods Group (Colchester, England). The tip-flow characteristics are analyzed at Rome University with an in-house 3D Reynolds-averaged Navier–Stokes (RANS) solver. The authors adopt a parallel multigrid (MG)

Contributed by the Fluids Engineering Division of ASME for publication in the Journal of Fluids Engineering. Manuscript received July 25, 2007; final manuscript received October 3, 2008; published online July 7, 2009. Assoc. Editor: Chunill Hah.

Table 1 List of nomenclature and abbreviations

	Latin letters
BPF	Blade-passing frequency
C_p	Static-pressure coefficient $((p-\bar{p}_{\mathrm{in}})/0.5\rho U_c^2)$
Δe_m	Nondimensional mechanical energy loss through the gap
H	Boundary-layer shape factor
He_n	Normalized helicity $(\xi_i w_i/\lvert\xi\rvert\lvert w\rvert)$
k	Turbulent kinetic energy
Ks	Specific noise level, $\mathrm{Ks}=\mathrm{SPL}-10\log_{10}(V\cdot\Delta p_{\mathrm{tot}}^2)$
ℓ	Blade chord
l.e.	Leading edge
P_s	Static-pressure rise
PS	Pressure side
p	Static pressure
r	Radius, radial distance from vortex axis
R	Nondimensional radius (r/r_c)
Ro	Rossby number $(W/r\Omega)$
SPL	Sound power level (dB)
SS	Suction side
TI	Turbulence intensity normalized by bulk velocity
t	Blade pitch
t.e.	Trailing edge
U_c	Casing relative peripheral velocity
V	Volume flow rate
W	Vortex axial velocity scale
v,w	Absolute and relative velocities
x,y,z	Cartesian coordinates
	Greek letters
ε	Turbulent dissipation rate
ζ	Total loss coefficient, $(\bar{p}_{0\mathrm{in}}-p_0/0.5\rho\bar{w}_{\mathrm{in}}^2)$
η	Efficiency
υ	Hub-to-casing diameter ratio
ξ_i	Vorticity vector
σ	Blade solidity
Φ	Global flow coefficient (annulus area-averaged axial velocity normalized by U_c)
χ	Rotor-tip clearance (% of the span)
Ψ	Pressure rise coefficient $(\Delta p/(\rho 0.5U_c^2))$
Ω	Tip-vortex rotation rate
ω	Rotor angular velocity
	Subscripts and superscripts
0	Total flow properties
c	Casing wall
h	Hub wall
I	Cartesian component index
in	Inlet section
$\bar{\ }$	Area-averaged value

scheme developed for the in-house finite-element method (FEM) [23]. The FEM formulation is based on an accurate, stabilized, Petrov–Galerkin (PG) scheme designed for turbomachinery computational fluid dynamics (CFD) [24]. The tip-leakage-flow structures of the fans are analyzed by detecting the multiple vortex structures and the chordwise evolution of leakage flow.

In assessing the technical merits of the modified tip configuration as a passive technique for controlling leakage flow and reducing rotor-tip noise, Powell's [25,26] sound-source distribution at the tip is measured to detect the predominant origins of noise. Finally, the loss behaviors are also studied in order to understand the influence of the modified tip configurations on efficiency gains. The nomenclature and abbreviations used in this study are listed in Table 1.

2 Test Fans

2.1 Fan Specifications. The study was performed on a family of commercially available cooling fans, named "AC90/6." This family of fans has been shown to provide state-of-the-art acoustic performance. The fans were equipped with a six-blade unswept rotor, with blade profiles of modified ARA-D geometry type originally designed for propeller applications. Table 2 provides the specifications for the data blades at the hub and the tip.

Table 2 AC90/6 fan family specifications

	AC90/6 fans	
Blade geometry	Hub	Tip
ℓ/t	1.32	0.31
Pitch angle (deg)	36	28
Camber angle (deg)	46	41
Fan rotor		
Blade number	6	
Blade tip-pitch angle (deg)	28	
Hub-to-casing diameter ratio υ	0.22	
Tip diameter (mm)	900.0	
Rotor tip clearance τ (% span)	1.0	
Rated rotational frequency (rpm)	900–935	

The studied blade configurations, for both data and modified rotors, featured a large tip-pitch angle of 28 deg (that is, 62 deg stagger angle). This angle setting was chosen to exploit operating points at which the vortex flow near the rotor tip dramatically affects the aerodynamic performance and noise characteristics of the fans under investigation.

2.2 End-Plate Geometry. The modified end-plate configurations developed for low-noise emission were designated as "TF" and "TFvte" [16]. Figure 1 provides a qualitative view (not to scale) of the thickness distributions of the modified tip configurations compared with the data blade.

The modified blade-tip configuration for the TF class of fans was originally inspired by techniques developed for control of tip vortex and reduction of induced drag in aircraft wings and catamaran hulls. The TF end-plate configuration represented the solution that offered the least noise and greatest efficiency after a systematic experimental evaluation of potential blade end-plate configurations [27]. The blade tip was modified by adding an end-plate along the blade pressure surface with constant thickness (three times larger than the data blade's maximum thickness at the tip) and a square-tail trailing edge. The end-plate was designed in accordance with the theory behind aircraft tip-vortex control, according to which the reference radial dimension of leakage vortex to be controlled should be 0.1–0.2 blade span fraction. A radial dimension of leakage vortex of 0.1–0.2 was in accordance with previous studies on the rotors of axial compressors [28] and fans [11].

Corsini et al. [20] previously assessed the improvements in aerodynamics and aeroacoustic performance of the TF rotor as compared with the data version. Their results indicated that a tip-leakage-vortex breakdown affected the TF rotor under design op-

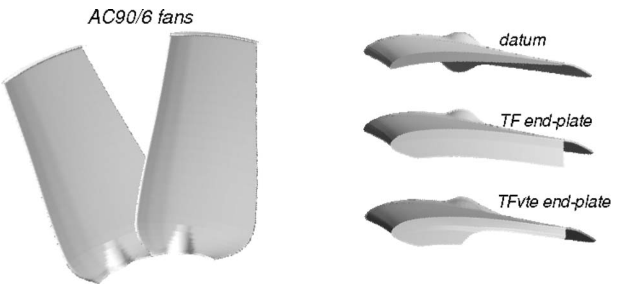

Fig. 1 Test fan rotor blades and tip end-plates (not to scale)

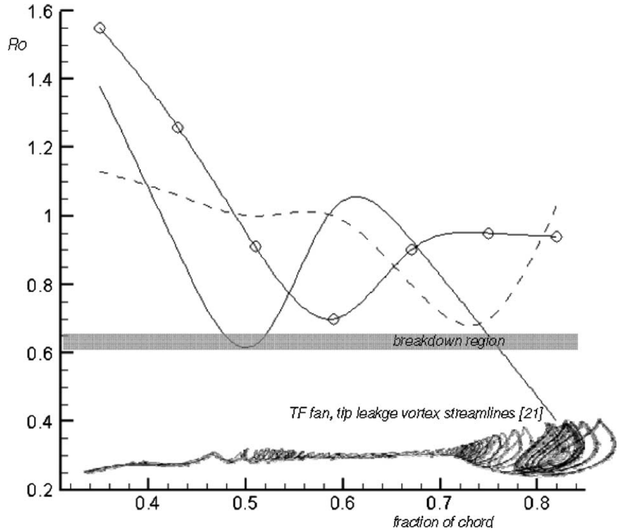

Fig. 2 Chordwise distributions of tip-leakage-vortex rotation number Ro under design operating conditions (dashed line: data fan; solid line: TF fan; solid-line-symbols: TFvte fan)

erating conditions, which resulted in an undesirable decrease in fan efficiency. To eliminate the tip-vortex breakdown, Corsini and Sheard [21] proposed a blade tip (designated TFvte in the present study) that exploits a variable-thickness distribution of the end-plate according to the concept of safe rotation number chordwise gradient. The configuration attempts to maintain the vortex rotation number above a threshold value in order to avoid vortex breakdown.

Corsini and Sheard [21] originally exploited a breakdown criterion based on the Rossby number (Ro) [29] in adopting velocity and swirl-scale definitions consistent with confined tip-leakage-vortex configurations. In Fig. 2, the chordwise distributions of the tip-leakage-vortex Rossby number (Ro) at design conditions are plotted against the critical Ro number for the data, TF, and TFvte rotors. The extant literature suggests that vortex breakdown occurs in a Rossby number (Ro) range from 0.64 (for a confined axisymmetric vortex breakdown) [30] to 0.6 (for wing-tip vortices class with bubble- or spiral-type vortex breakdown) [31].

The TF rotor, as shown by the numerical analysis in Ref. [21], attains the Ro critical value at midchord (Fig. 2), which is recognized as the onset of vortex breakdown, and then at the aft blade with the development of a large bubblelike bursting core featuring flow reversal. In this respect, the chordwise Ro distribution for the TFvte rotor confirms the effectiveness of the technique in controlling tip-leakage vortex.

The current study also reports on the performance of two additional end-plate concepts, which combine TF and TFvte with so-called "stepped-tip" sections. The addition of the stepped blade-tip feature is designed to provide an additional leakage-flow-weakening mechanism. The corresponding rotors are named "TF_step" and "TFvte_step."

2.3 Aerodynamic Performance. The aerodynamic tests were conducted in accordance with the international standard ISO 5801 for fully ducted fan configurations using installation type D. This installation features ducted inlets and outlets, and the fan is fitted with a bell-shaped inlet mouth.

Measurements of static and dynamic pressures were carried out with four taps, equally spaced on the casing wall, and a standard Pitot-probe. The probe was mounted on a traversing mechanism fixed to the outer wall of the test rig. A Furness Control digital multichannel micromanometer (Model FC012, Furness Controls Ltd., UK), with 2 kPa range and a resolution of 1 Pa, was used to read pressure data. The accuracy of pressure measurements was ±0.5% of read data. The efficiency was calculated as the ratio between the air power (computed on either static or dynamic pressure rise) and the electric power. The absorbed electric power was measured with an ac power analyzer that had an accuracy of 0.24% of read data.

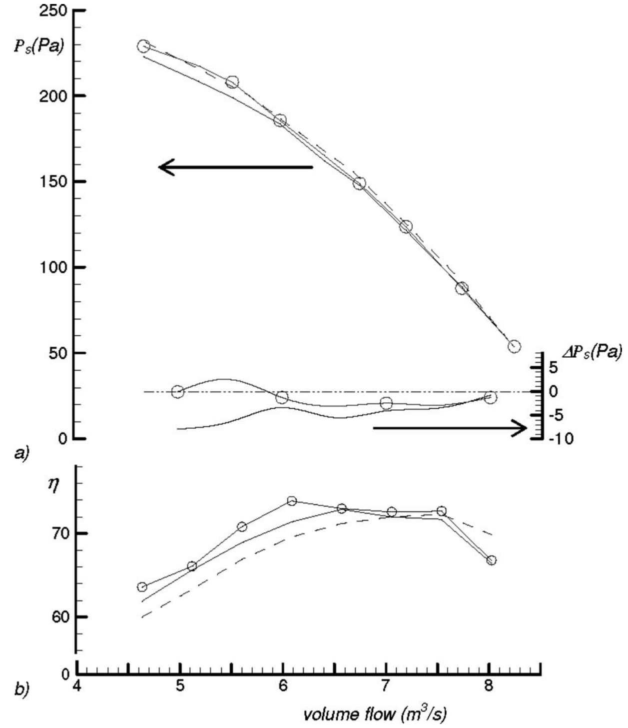

Fig. 3 Comparison of characteristic curves: (*a*) static-pressure rise and pressure rise difference; (*b*) efficiency curves (dashed lines: data fan; solid lines: TF fan; line-symbols: TFvte fan)

The characteristic curves of static pressure (Fig. 3(*a*)) and η_{tot} efficiency (Fig. 3(*b*)) for the data, TF, and TFvte rotors under design conditions were not markedly modified by the tip configuration. Figure 3 also includes curves of the pressure rises as compared with the database line. Comparison of the static-pressure curves, as shown in Fig. 3(*a*), revealed that a small reduction in performance in the TF rotor (of about 6 Pa, that is, 3% of data P_s at 6 m^3/s). This circumstance was associated with an interaction between the tip-clearance vortex and the suction-side surface fluid resulting in a 3D separated core. This interaction is in accordance with the findings of Gbadebo et al. [32] regarding tip-leakage-flow behavior for tight clearances. This diminished performance was partially recovered by the TFvte rotor, in which the static pressure increased specifically by throttling the rotor toward the peak pressure.

It is evident from the efficiency curves shown in Fig. 3 that both of the modified rotors (TF and TFvte) demonstrated an improvement in efficiency. This is indicated by extension of a high-efficiency plateau when using the tip end-plates, which shifted the peak η_{tot} volume flow rate toward the rotor stall margin. The predicted overall performance (under near-design conditions of 900 rpm rotational speed) is compared with the experimental data in Table 3, which shows that measured and predicted efficiencies, computed in terms of static-pressure rise (η_{stat}), were in general agreement.

To allow for mixing losses, the prediction of performance parameters referred to axial sections located at the inlet of the domain and 1.2 midspan chords downstream of the blade trailing edge. The comparison confirmed the validity of the predicted performance at the chosen angle setting (at which the blades have maximum loading and are more readily prone to flow separation).

Table 3 Predicted and measured fan overall performance under design conditions

	Measurements		Predictions	
AC90/6 fans	P_s(Pa)	η_{stat}	P_s(Pa)	η_{stat}
Data	134.8	0.49	133.3	0.510
TF	126.2	0.51	126.1	0.504
TFvte	129.0	0.52	128.2	0.516

3 Methodology

The single-rotor investigations were conducted for *five* configurations of the studied six-blade axial flow fan, namely, (i) the data fan (coded AC90/6), (ii) the fan modified by the adoption of the constant-thickness tip feature (coded TF), (iii) the fan modified by the adoption of the variable-thickness tip feature (coded TFvte), (iv) the TF fan with a stepped end-plate (coded TF_step), and (v) the TFvte fan with a stepped end-plate (coded TFvte_step). The Reynolds number, based on tip diameter and rotor-tip speed, was 8.3×10^5 (under normal air conditions).

The experimental and computational investigations focused primarily on the aerodynamic performance of the end-plate configurations and provided an overview of the far-field acoustics. The methodology that was adopted combined accurate computational modeling of the leakage-flow phenomena (under design conditions) with experimental assessment of the fan acoustic behaviors in terms of a range of operating points and angle settings.

3.1 Noise-Measurement Technique. The noise-performance tests were carried out in an anechoic chamber in accordance with BS848, equivalent to ISO 10302:1996, for type-A testing configuration [33]. Type-A testing places the fan downstream of a plenum chamber with a free outlet, in an arrangement similar to that used for compact cooling fans. The rotor was driven by a 2.5 kW, three-phase motor to a nominal rotational frequency of 935 rpm. The blade-tip speed was typically 44 m/s, with the exact value being dependent on the actual rotational speed and blade tip-to-casing clearance.

To isolate the aerodynamic noise, a preliminary test of the motor was conducted. This enabled information on its noise signature to be obtained and thus facilitated an appropriate correction of subsequent fan-motor noise measurements. An inlet bell-mouth was mounted on the fan inlet to ensure a uniform and unseparated inlet flow. The upstream plenum was acoustically treated to minimize external noise. Variation of the fan head and flow rate was achieved by controlling an airfoil damper in the top of the inlet section of the facility.

3.2 Far-Field Noise Test Setup. Far-field noise was measured at a distance of six fan diameters from the rotor outlet, as recommended in the literature for such far-field measurements [34]. Directing the fan noise into a semireverberant environment results in the maximum noise level coinciding with the axial direction [34], with a significant presence of dipole-type source phenomena at the fan inlet. The far-field microphone was therefore located 30 deg off center with respect to the fan. This approach minimizes direct interference from fluctuating air-flow on the microphone without losing the required strength and clarity of the noise signal. Despite its off-axis location, the microphone position allowed a direct line-of-sight to the entire rotor surface, thus facilitating fully representative far-field measurement of both overall sound level and spectra. The anechoic facility, Fig. 4, has a cutoff frequency of 50 Hz on far-field measurements.

3.3 Numerical Methods. The RANS equations were solved by an original parallel multigrid finite element (MGFE) flow solver [23]. Despite the steady-state conditions, RANS was adopted as an effective tool for this investigation because it is capable of capturing details of the vortex structures at the tip [35,36].

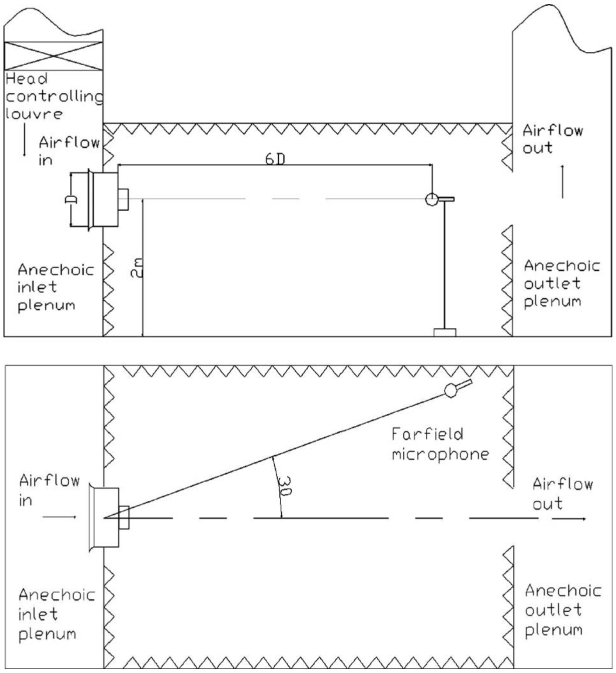

Fig. 4 Far-field setup of the test rig (not to scale) for outlet measurements

The fluid dynamics of incompressible 3D turbulent flows in a rotating frame of reference were modeled with a nonlinear k-ε model [37], utilizing its topology-free low-Reynolds variant. This turbulence-modeling strategy is considered to be a reasonable base line in turbomachinery simulation because it includes provisions that (i) account for curvature and nonequilibrium effects, and (ii) attenuate stagnation-point inconsistency. Moreover, the turbulence anisotropy (based on a cubic stress-strain relationship) has been shown to improve the simulation of confined swirling flows (such as tip vortex) in compressor cascade rotors and high-pressure industrial fan rotors [38].

Numerical integration of the partial differential equations (PDEs) was based on a consistent stabilized Petrov–Galerkin formulation developed and applied to control the instabilities that affect the advective-diffusive incompressible flow limits, and the reaction of momentum and turbulent scale-determining equations. The reactive features of the PDEs are related to (i) the Coriolis acceleration in the momentum equation and (ii) the dissipation/destruction terms in the turbulent scale-determining equations [24]. Equal-order linear interpolation spaces (Q1-Q1) were used for primary-turbulent and constrained variables, implicitly eliminating the undesirable pressure "checker-boarding" effects.

3.4 Rotor Modeling and Boundary Conditions. The mesh was constructed according to a nonorthogonal body-fitted coordinate system by merging two structured H-type grid systems: (i) the mesh in the vicinity of the main flow (surrounding the blade) and (ii) an embedded mesh in the vicinity of the tip gap. The mesh had $154 \times 68 \times 58$ nodes in the axial, pitch, and spanwise directions respectively. In the axial direction, the node distribution consisted of 20% of nodes upstream of the leading edge, 50% in the blade passage, and 30% downstream of it. Moreover, there were 14 grid nodes to model the tip clearance along the span. The resulting computational grid at the rotor hub and on blade surfaces is illustrated in Fig. 5.

The mesh was adequately clustered toward solid boundaries, with the ratio of minimum grid spacing on solid walls to midspan blade chord being set as 2×10^{-3} on the blade tip, casing wall, and

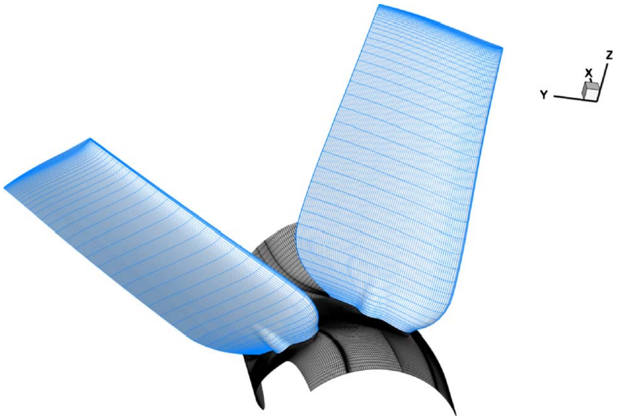

Fig. 5 Computational grid of fan rotor

blade surfaces. The adopted grid refinement toward the solid surfaces controlled the normalized wall distance (δ^+) value at about 1 on the first row of nodes.

Standard boundary condition settings were adopted, as previously used in studies on high-performance fans [11]. The Dirichlet conditions for the relative velocity components were imposed at the inflow section, half a midspan chord upstream from the leading edge, as obtained from flow simulation in an annular passage of an identical hub-to-casing diameter ratio that included an upstream spinner cone. The modeled incoming boundary layer at the tip had a shape factor $H_{\text{in,tip}}=2$, with a displacement thickness twice the tip clearance. The inlet distribution of the turbulent quantities was obtained from inflow turbulence measurements in ducted industrial fans [39]. Flow periodicity (upstream and downstream from the blading) and Neumann outflow conditions completed the set of boundary data.

4 Aeroacoustic Properties of the End-Plate

4.1 Narrowband Spectra Analysis. The sound-pressure measurements were made using Brüel & Kjær (Denmark) equipment connected to a 01 dB_Symphonie signal acquisition and sound analyzer with a frequency range of 0 Hz–20 kHz.

The results of the noise-performance tests, which are shown in Fig. 6, were used to compare narrowband sound-pressure level (SPL) spectra, measured under near-design operating conditions. For the sake of clarity, the frequency range has been subdivided into (i) the spectra up to 1 kHz (Fig. 6(*a*)) and (ii) the spectra from 1 kHz to 5 kHz (Fig. 6(*b*)). In the narrowband spectra up to 1 kHz, there was evidence of tones, not correlated with the blade-passing frequency (BPF), which matched the motor signatures. Furthermore, this signature (Fig. 6(*a*)) varied with different end-plate configurations (Fig. 3) as a consequence of variations in aerodynamic performance.

The effectiveness of the modified tips, with both constant-thickness and variable-thickness end-plates, was demonstrated by a reduction in tonal and broadband noise components, which related, respectively, to the convection of tip vortices and interaction with the static structures (producing mainly tonal noise). The tip-vortex instability could be linked to the broadband self-generated noise [40]. It could be also inferred, according to studies on jet noise [41], that the reduction in the broadband noise with the end-plate is a consequence of turbulence strength in the tip-flow region.

Specific consideration of the lower frequencies (Fig. 6(*a*)) revealed that the end-plates were able to influence the tonal noise up to four times BPF, with $\text{BPF}=90$ Hz. This coincides with the median frequency of Wright's [9] spectrum for turbulent self-generated noise.

Specific consideration of the higher frequencies (Fig. 6(*b*)) revealed that the noise-reduction potential of the modified tips was evident at about 2 kHz, when the SPL spectra began to differ significantly. This indicates that the beneficial effect of the stepped gap was more pronounced in the case of the constant-thickness (TF) end-plate than it was with respect to the variable-thickness (TFvte) end-plate.

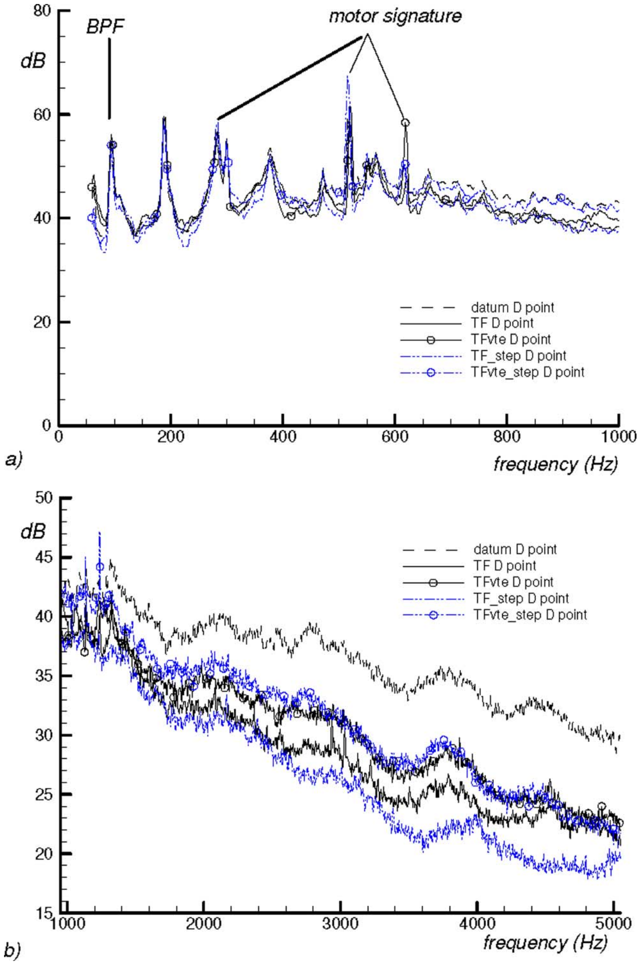

Fig. 6 SPL narrowband spectra: (*a*) up to 1 kHz; (*b*) 1–5 kHz (dashed lines: data fan; solid lines: TF fan; line-symbols: TFvte fan; dash-dotted line: TF_step fan; dashed-dotted line-symbols: TFvte_step fan)

To provide additional insight into tonal noise control in the narrowband, an analysis was made of the cross-spectra obtained by correcting the far-field noise signal with near-field spanwise measurements. Further details on the experimental technique could be found in Ref. [42]. The results are shown in Fig. 7.

At the *first* BPF, which is the most relevant BPF in terms of perceived fan tonal noise, both the TF configuration and the TFvte configuration were associated with a decrease in the tonal signature compared with the data blade; the reduction in tone associated with the TFvte configuration was especially significant (5 dB), whereas that associated with the TF configuration was slightly less (about 2 dB). The *second* BPF was found to be influenced by an ingested noise source distributed along the entire radius of the impeller, which was independent of the tip configuration [43].

In the *third* BPF, the TF configuration was associated with a slightly smaller increase in SPL compared with the data, whereas the TFvte configuration was associated with a reduction of 4 dB. The stepped configurations (TF_step and TFvte_step) were effective in reducing both tonal and broadband noise. In the narrowband domain, it was apparent that the tonal noise was reduced as

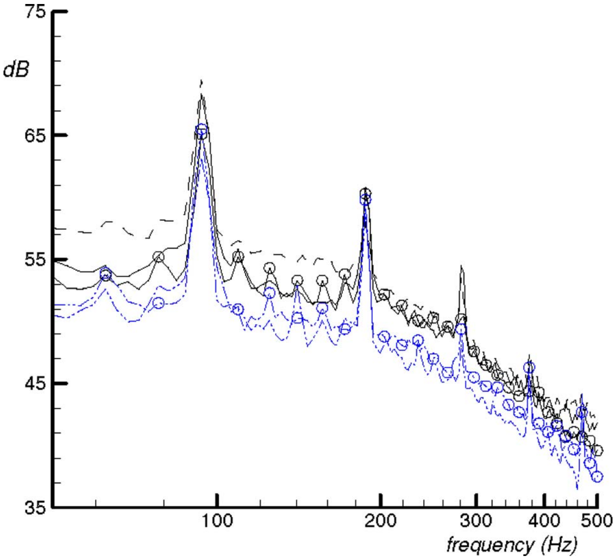

Fig. 7 Comparison of SPL far-field cross spectra (dashed lines: data fan; solid lines: TF fan; line-symbols: TFvte fan; dashed-dotted line: TF_step fan; dashed-dotted line-symbols: TFvte_step fan)

a result of the end-plates controlling turbulent mixing. The TF_step configuration outperformed the other fans in providing a reduction of 3 dB in total Lp (integrated from 50 kHz to 1 kHz) compared with the data fan.

The tonal reduction due to the stepped configurations, which is shown in Fig. 7, indicates that, for the first three BPFs, the TF_step configuration outperformed the TFvte_step fan, with the greatest benefit being associated with the odd tones.

4.2 Overall Sound Level Analysis. The aeroacoustic behavior was also assessed in terms of operating conditions (static-pressure rise ranging from 155 Pa to 190 Pa) and angle settings (tip-pitch angle ranging from 24 deg to 28 deg). The influence of the operating point on rotor acoustic signature was assessed by maintaining constancy in the impeller load (which is considered to be a determining factor in tip-leakage flows) while making slight variations in the flow rate. The influence of rotor-pressure rise on acoustic signatures was assessed by comparing the rotor-specific noise level (Ks) with the static-pressure rise at a 28 deg pitch angle [2]. The results, which are shown in Fig. 8, indicate that the use of a stepped configuration (TF_step or TFvte_step) influenced the part-load operation by contributing to the attenuation of Ks toward stall. The attenuation of Ks as the stall condition was approached was not anticipated because axial fan rotors usually exhibit discrete noise-frequency amplification [2].

Outlet far-field overall pressure level (OPL) data with respect to the tested angle settings and operating points, which are shown in Table 4, indicate that the OPL values for the data fan increased with an increasing pitch angle. The OPL values were computed by double integrating within the narrowband frequency range. The exception to the general observation that OPL values increased with pitch angle was the peak-pressure condition (190 Pa), under which the OPL flattened at a pitch angle of greater than 24 deg.

Table 4 shows that the OPL pay-off (of about 2 dB) was gained irrespective of the angle settings and the operating points. Moreover, with a rotor-tip-pitch angle of 24 deg, the data fan stalled (indicated by the peak OPL). In contrast, the behavior of the fans with modified tips agreed with the hypothesis that the end-plates were able to reduce the near-surface outward migration of fluid and as a consequence the extent of hub-corner separations leading to stall.

A comparison of the data for the step concepts revealed that the TF_step configuration was associated with slightly improved performance only at the greatest angle setting (28 deg) and a near-design pressure rise. It is significant that the combined use of the TF end-plate and the stepped tip eliminated the influence of blade-pitch angle on aeroacoustic performance, irrespective of the tip-angle settings.

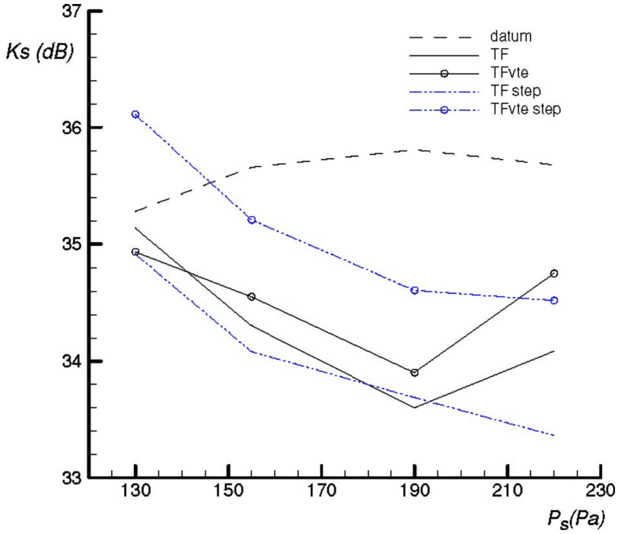

Fig. 8 Comparison of experimental specific noise level Ks in the operating range (dashed lines: data fan; solid lines: TF fan; line-symbols: TFvte fan; dashed-dotted line: TF_step fan; dashed-dotted line-symbols: TFvte_step fan)

5 Aerodynamic Behaviors of the End-Plate

It is apparent from the above discussion that the modified blade tips, with constant-thickness and variable-thickness end-plates, were able to control the aeroacoustic signature of the family of fans under investigation. Moreover, these benefits apparently correlated with an improvement in efficiency in the peak-pressure operating range.

These experimental results prompted a numerical investigation of the inner workings of the passive control devices; in particular, the investigation attempted to ascertain how they actually influenced the tip-leakage vortex and the systems of secondary vortices. This was analyzed by surveying the multiple vortex structures and the chordwise evolution of leakage flow. The Powell [25,26] sound-source distributions at the tip were compared, which identify the predominant origins of noise. Finally, the loss behaviors were studied to obtain a better understanding of the influence of

Table 4 Overall sound-pressure levels

AC90/6 fans	Unweighted SPL (dB)	
155 Pa	24 deg	28 deg
Data	70.5	72.4
TF	68.1	70.2
TFvte	68.9	70.5
TF_step	69.6	69.9
TFvte_step	70.2	71.1
190 Pa	24 deg	28 deg
Data	73.9	72.8
TF	70.6	69.7
TFvte	69.4	70.0
TF_step	69.7	69.7
TFvte_step	70.4	71.8

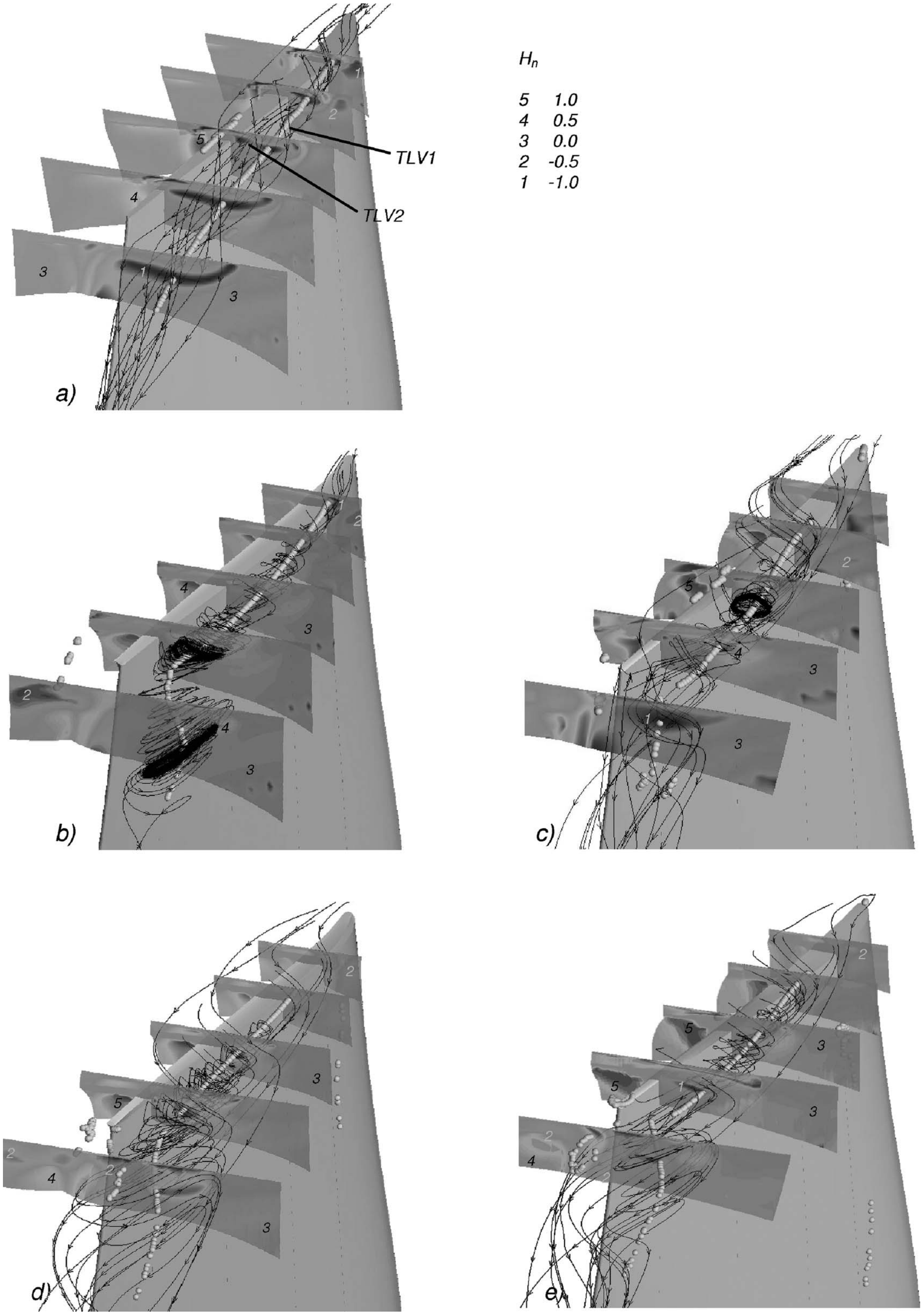

Fig. 9 Normalized helicity contours and leakage-vortex streamlines: (*a*) data fan, (*b*) TF fan, (*c*) TFvte fan, (*d*) TF_step fan, and (*e*) TFvte_step fan

improved tips on loss distributions within the blade passage. The investigations compared the fan rotors operated with a tip-pitch angle of 28 deg, and a volume flow rate of 7 m^3/s under near-design operating condition.

5.1 Tip-Leakage Flow Survey. The tip-leakage-vortex structures were primarily investigated in terms of normalized helicity (He_n) [4,36]. The normalized helicity distribution in the vicinity of the blade tip was established by comparing the contours of cross-flow planes under near-design operating conditions for fan rotors equipped with the various modified tip configurations. The behavior of streamlines delimiting the main tip-leakage-vortex structures was also determined. The results are shown in Fig. 9.

The multiple vortex behavior of the data fan rotor resulted in a helicity field with an essentially clockwise vortex structure (TLV1), Fig. 9(*a*). This helicity field developed a large skewing angle through the blade passage with respect to the blade surface, spreading from the first quarter of the tip chord. About midchord, a negative helicity core on the suction side of the blade indicated a weak secondary vortex corotating with the tip-leakage vortex (TLV2). In the aft-blade area, the leakage flow was mainly characterized by the merging of the tip-separation vortex (TLV2) and the leading-edge vortex (TLV1). This merged (clockwise) vortex structure at the trailing edge was capable of affecting a large proportion of the blade pitch on the casing annulus.

The helicity distribution for the TF rotor (Fig. 9(*b*)) revealed that a vortex-limiting mass leakage existed along the blade in the form of a pressure-side leg of a horseshoe-shaped structure. This vortex was responsible for the modifications in the leakage vortex that developed close to the suction side. A smaller in-passage extension was also coupled with a reduced helicity magnitude (when compared with the data rotor field). Moving downstream, the tip-leakage vortex at about midchord featured a gradual reduction in He_n, which was due to a weakening of the flow vortex and to deflection of the vortex core. This is in accordance with the proposition that mass-leaking reduction occurs along the chord, and that this gives rise to leakage-flow structures adjacent to the blade's suction surface. In the aft-portion of the blade, the tip-leakage vortex collapsed, which produced a "bubble-type" separation that indicates vortex breakdown [21]. The separated flow turned into a counterclockwise vortex under the influence of trailing-edge leakage-flow streams. The counterclockwise vortex rapidly washed out behind the rotor, where no coherent vortex structure was evident.

The helicity maps for the TFvte rotor (Fig. 9(*c*)), when compared with the data and TF blades, indicated that the origin of the main leakage-vortex structure moved downstream (about 0.3ℓ) and developed closer to the blade's suction surface. At about midchord, the weakened TLV1 interacted with an anticlockwise rotating cell. This cell, driven by a highly energetic leakage jet, merged with TLV provoking inversion of the vortex rotation. In the aft-chord portion of the blade, the tip vortex developed under the influence of the near-vortex axis swirl supply, which was related to the end-plate thickness reduction. The tip vortex finally merged with a rotating cell and exited the blade passage. It then appeared as a coherent clockwise vortex structure. For the TF end-plate configuration, the He_n field thus confirmed that a key role is played by the pressure-side vortex structures as indicated by the horseshoe-shaped vortex limb and by the corner vortex developing under the end-plate.

With respect to the two stepped configurations (TF_step and TFvte_step), there was evidence that, in general, the inclusion of steps in the tip configuration produced an overall reduction of mass leaking and momentum transfer within the clearance (Figs. 9(*d*) and 9(*e*)).

In the helicity maps of the TF_step configuration (Fig. 9(*d*)), the deceleration of the flow induced by the step on the tip suction side forced TLV1 to move downstream with respect to the TF end-plate. In addition, TLV1 developed with a reduced rotational momentum content—as indicated by the weakening in the helicity norm and by the contraction of the He_n peak core. Moreover, because although it featured a constant-thickness distribution (and therefore had regular chordwise leakage-flow reduction), the TF_step end-plate aerodynamics were not affected by the occurrence of a tip-leakage-vortex breakdown. The smaller TLV1 moved into the vicinity of the blade's suction surface, where it gradually evolved into a counterclockwise rotating core approaching the aft-portion of the blade under the competing effect of passage secondary flows.

In contrast, the inclusion of the step into the variable-thickness end-plate (TFvte_step) gave rise to modifications in leakage flow that appear to have been a consequence of a significant reduction in momentum transfer within the gap (from the pressure side to the suction side of the blade) (see Fig. 9(*e*)). The main tip-leakage-vortex structure (TLV1) therefore developed along the passage up to the trailing edge with a small skewing angle (compared with the TFvte configuration). Furthermore, as a second effect, the helicity chordwise evolution did not proceed to a rotation reversal. As a final observation on the TFvte_step rotor, the main tip-leakage vortex behind the rotor was observed to have a clockwise rotating core with a smaller crosswise dimension.

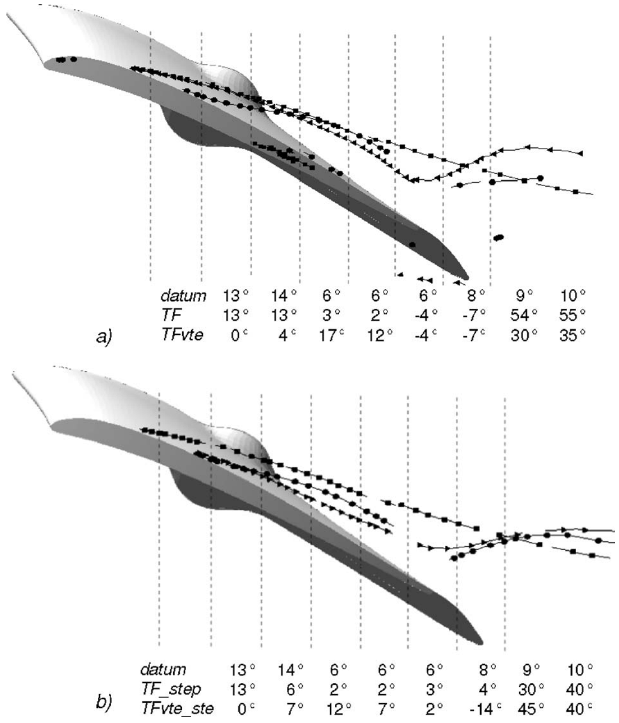

Fig. 10 Tip leakage-vortex TLV1 trajectories: (*a*) line-squares: data; line-circles: TF; line-triangles: TFvte, (*b*) line-squares: data, line-circles: TF_step; line-triangles: TFvte_step

To gain further insight into the aerodynamic flow fields associated with the proposed end-plates, the trajectories of the TLV1 vortex cores within the blade passage were derived by comparing the vortex paths for the improved tips against the data fan (Fig. 10). The vortex cores were calculated by postprocessing the 3D discretized velocity vector fields by means of an algorithm based on critical point theory, as developed by Sujudi and Haimes [44].

Apart from the location of the vortex origins, both the constant-thickness and variable-thickness end-plates featured TLV1 core trajectories developing along paths that were less skewed than the blade-tip section (Fig. 10(*a*)). Moreover, due to the antivortex action exerted by the end-plates, both of the modified tip rotors featured a sudden deviation in TLV1 core, which was due to an interaction between the low-energy leakage vortices and the passage flow exiting from the rotor.

As a corollary to the above analysis, it was observed that the vortex-core paths of the stepped configurations were modified in two ways (Fig. 10(*b*)). First, the leakage vortices moved downstream with respect to the data tip configuration, in accordance with a significant reduction in the leaked mass and momentum transfer. Second, as provided by the leakage-vortex angle distributions, the vortex-core paths were pushed closer to the blade's suction surface (as a result of the effect of the step).

The tip-leakage flow was surveyed in terms of the chordwise distribution of the leakage velocity (w_{LV}), normalized by the inflow bulk velocity (Fig. 11(*a*)). Leakage-flow skewing angle (β_{LV}) was computed between the leakage-flow direction and the

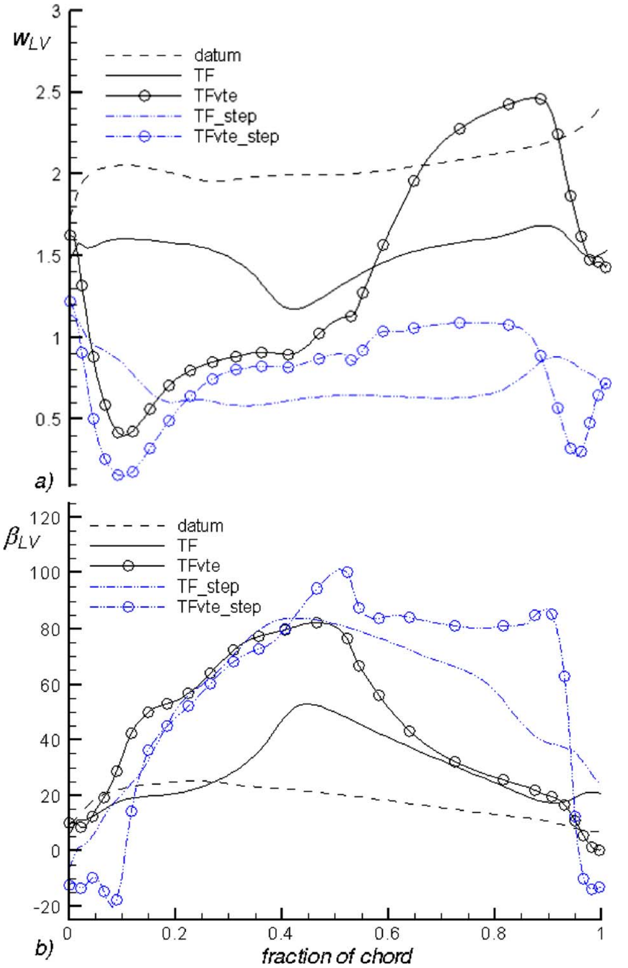

Fig. 11 Tip leakage flow: (*a*) velocity distribution; (*b*) skewing angle distribution

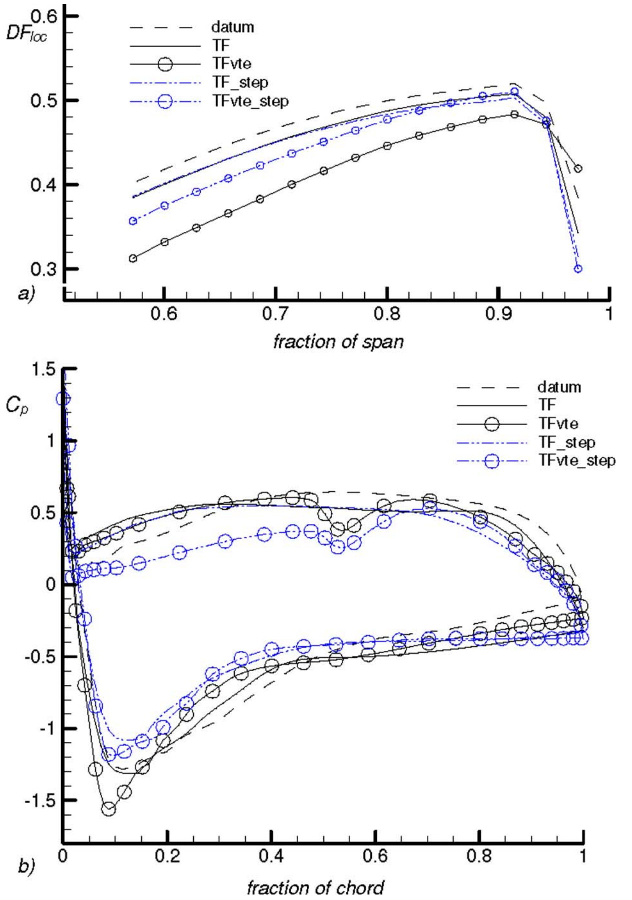

Fig. 12 Spanwise blade load analysis: (*a*) local diffusion factor (DF_{loc}) profiles and (*b*) static-pressure coefficients (C_p) at the blade tip (dashed lines: data fan; solid lines: TF fan; line-symbols: TFvte fan; dashed-dotted line: TF_step fan; dashed-dotted line-symbols: TFvte_step fan)

tip chord (Fig. 11(*b*)). Both of these quantities were averaged through the tip gap height.

The mass leaking through the tip gap was essentially governed by a constant velocity along the chord of the data fan blade due to the local loading condition (Fig. 11(*a*)). In this respect, the constant-thickness end-plate (TF fan) has been shown to work by reducing the leakage-flow velocity scale without affecting its distribution (which remained nearly uniform). The stepped-tip configuration (TF_step) was more capable of reducing the leakage-flow velocity than configurations without the step. For the stepped configuration, leakage-flow velocity remained less than the reference value without affecting the chordwise distribution.

In contrast, the use of the variable-thickness end-plate concepts (TFvte and TFvte_step) unloaded the front portion of the blade. Up to the midchord position, the working of the step was such that only minor changes in the velocity distribution were evident. It is significant that the stepped configurations worked effectively in the rear portion of the gap, where they contributed to attenuation of the rise in leakage velocity (balancing the end-plate thickness variation).

A comparative analysis of leakage-flow angles (Fig. 11(*b*)) provided additional information on the aerodynamic flow field associated with tip end-plates. In comparison with the data distribution, which featured a constant skewing angle, all of the modified end-plates increased the deflection of the leakage flow. At about midchord, the leaking direction was almost orthogonal to the blade chord. It is noteworthy that, in the front portion of the blade, the stepped configurations (TF_step and TFvte_step) produced a deviation in leakage flow that was comparable to the TFvte end-plate. Moreover, they both outperformed the tip configuration with constant gap in the rear fraction of the chord (providing higher skewing angles).

5.2 Blade-Tip Loading Analysis. To assess numerically the aerodynamic origin of the noise signatures associated with the experiments, a comparative analysis of the blade loading of the various fans was conducted. Studies on the role of the tip vortex in rotor noise, as reviewed by Cumpsty [8], had previously identified unloading of the blade tip as one of the elements responsible for noise generation and a number of design concepts to control the load distribution on blade-tip sections have appeared to date.

The spanwise distributions of the local diffusion factor (DF_{loc}) was recognized as a significant parameter for correlating blade loading and noise. The diffusion factor profiles under near-design conditions (Fig. 12(*a*)) indicated that the end-plates featured less local diffusion. Nonetheless, an order-of-magnitude analysis revealed that the reduction of DF_{loc} in the range 0.01–0.02 for TF and TFvte (as in the instance of 0.75 span) was well below the values identified in the literature as being necessary to obtain noise attenuation similar to the acoustic pay-off actually achieved (see Table 4) [45]. These findings suggested that the aerodynamic flow field associated with the end-plates (governing the rotor aeroacoustic performance) provided a mechanism for controlling tip-leakage flow without significantly unloading the blade-section at the higher radii.

Moreover, as demonstrated by comparing the distributions of the C_p coefficients (Fig. 12(*b*)), the adoption of the end-plates did

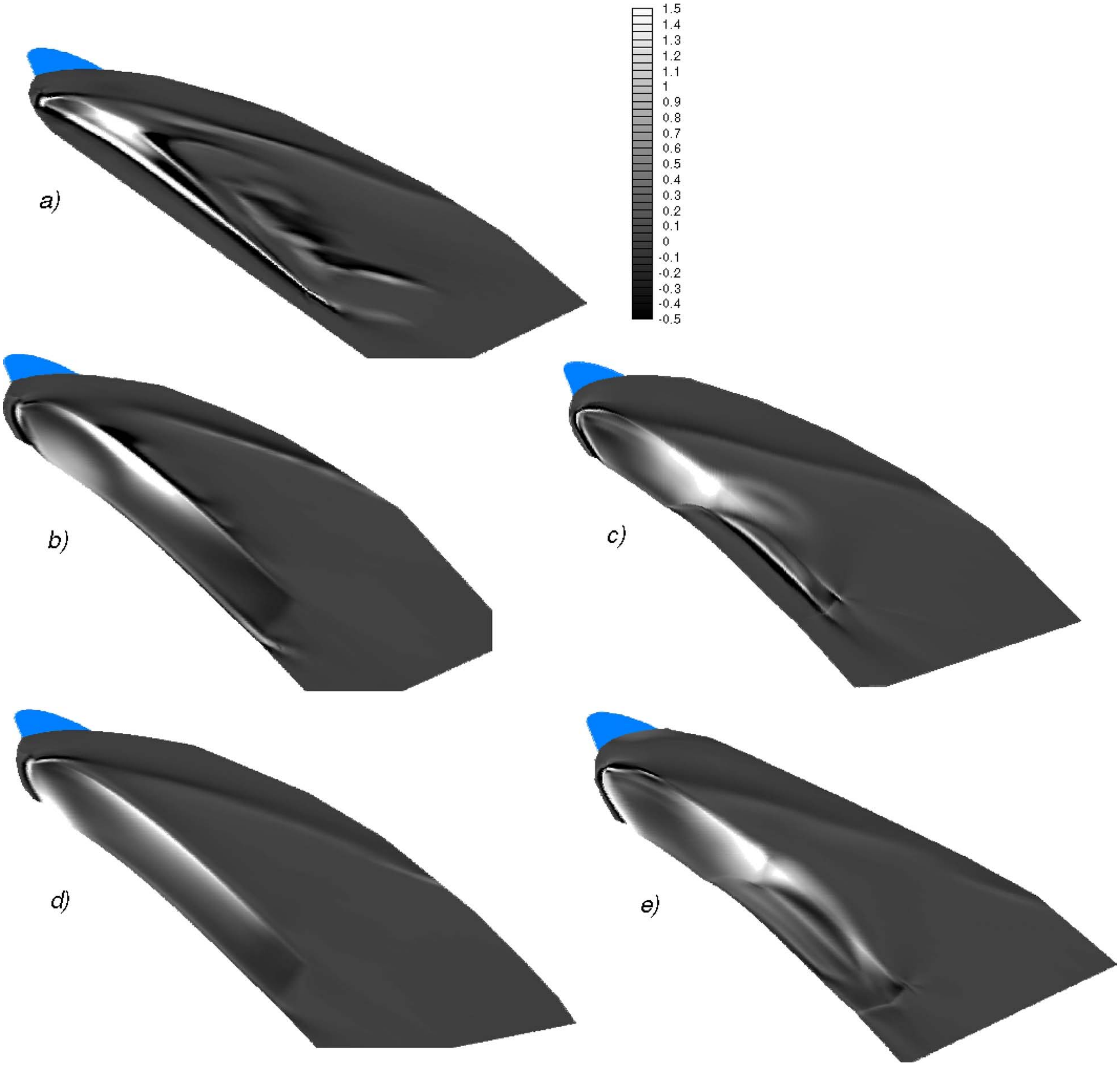

Fig. 13 Powell's [26] sound-source distributions in the tip gap at $R=0.998$: (*a*) data fan, (*b*) TF fan, (*c*) TFvte fan, (*d*) TF_step fan, and (*e*) TFvte_step fan

not have a significant effect on the static-pressure distribution about the blade tip. The larger variations that did occur were associated with the base-line distribution and appear to have been a consequence of the implementation of the variable-thickness end-plates (TFvte and TFvte_step). These end-plates led to abrupt acceleration-deceleration on the pressure side according to the growth of the leakage-flow velocity.

5.3 Powell's Sound-Source Survey. Powell [26] identified the characteristics of turbulent flow or eddy motion that are responsible for sound generation and found that the formation (and motion) of vortices is the fundamental noise-producing mechanism.

For a relatively high Reynolds number flow with no heat release, the entropy and viscous-stress terms in Lighthill's [46,47] acoustic tensor can be neglected, and the Reynolds-stress factor becomes the dominant contributor to sound generation. This provides the following sound-source term:

$$\nabla \cdot (\boldsymbol{\omega} \times \boldsymbol{v})$$

where, as in Ref. [25], the source terms depend on $\boldsymbol{\omega}$ (the vortex vector of the leakage flow) and $\boldsymbol{v}$ (its convection velocity).

Powell's [26] survey identified the most relevant sound sources of vortex-generated aerodynamic sound for low-speed flow. Sound-source intensity maps, as recently proposed by Arakawa et al. [48], can be used to detect dominant noise origins. The Powell [26] sound-source fields (steady-state computed) for the tested fan-tip configurations and the tip-vortex structures were correlated with the mechanism of noise generation, Fig. 13. With respect to the data tip configuration (Fig. 13(*a*)), a concentration of high values of Powell's [26] sound source was identified at the onset of the multiple tip vortex streamed by the highly skewed leading-edge vortex and the TLV1. It is noteworthy that peak absolute values of the sound source were also located in the rear fraction of the blade chord, where TLV1 reached the greatest momentum and crosswise dimension due to the completion of flow leaking.

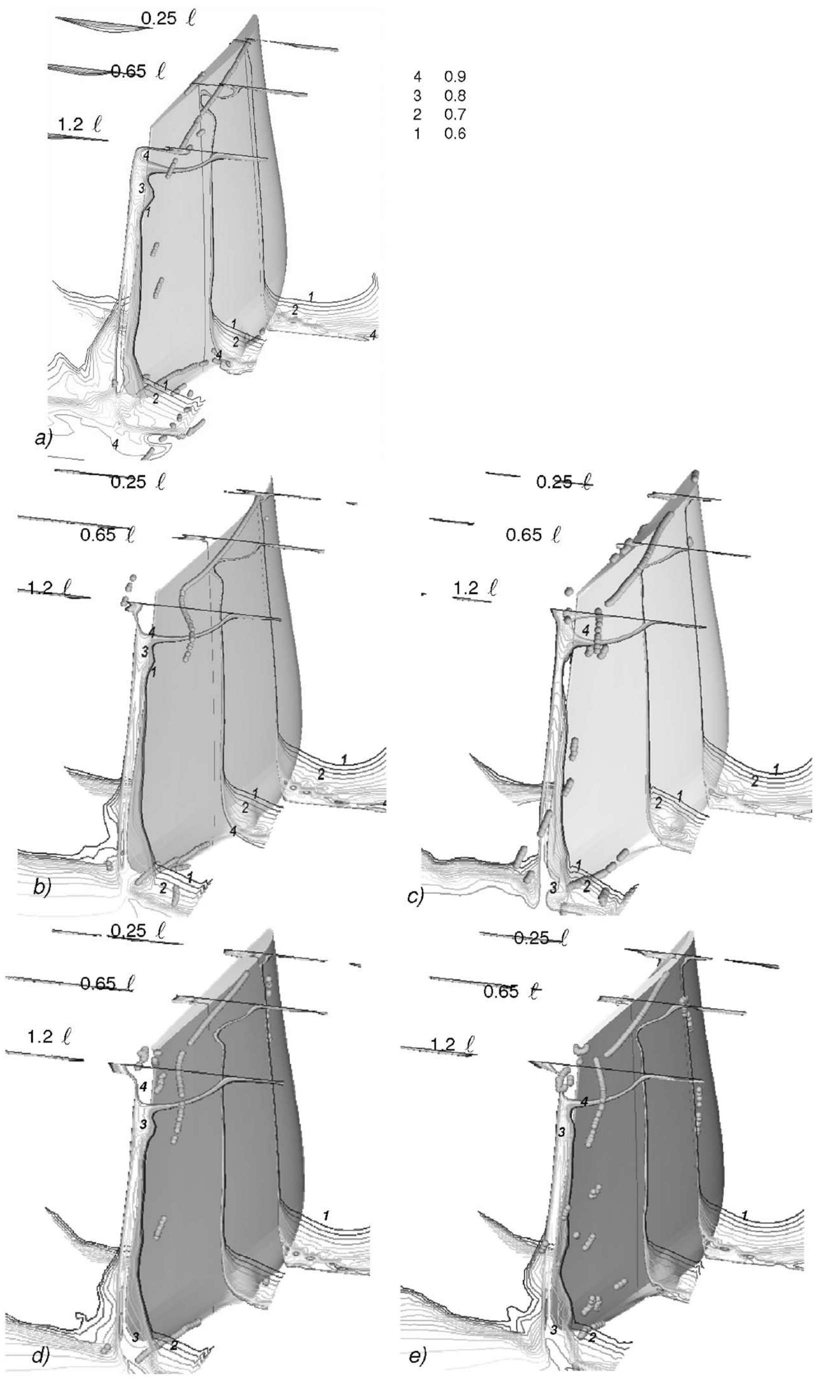

Fig. 14 Evolution of total pressure loss coefficient (ζ) inside the blade passage under design conditions: (*a*) data fan, (*b*) TF fan, (*c*) TFvte fan, (*d*) TF_step fan, and (*e*) TFvte_step fan

With respect to the modified end-plates (Figs. 13(*b*)–13(*e*)), all of the proposed tip configurations outperformed the data tip by reducing the sound-source level in the blade passage close to the suction surface of the blade. Furthermore, the stepped end-plate configurations (Figs. 13(*d*) and 13(*e*)) indicated that stretching of the peak source cores in the chordwise direction coincided with the step location.

5.4 Rotor Loss Behavior. Loss behavior was investigated with reference to the local total loss coefficient, which was defined as

$$\xi = \bar{p}_{0\mathrm{in}} - p_0/0.5\rho\bar{w}_{\mathrm{in}}^2$$

in which p_0 is the local total pressure and $\bar{p}_{0\mathrm{in}}$ and $0.5\rho\bar{w}_{\mathrm{in}}^2$ are, respectively, the reference pitch-averaged relative total and dynamic pressures computed at the inlet midspan plane.

The total loss coefficient distribution within the blade passage under near-design operating conditions, Figs. 14(*a*)–14(*e*), is probing the flow fields in the vicinity of the blade leading edge, about midchord and in the region behind the blade (respectively, approximately 0.25ℓ and 0.65ℓ and 1.2ℓ chord from the leading

Table 5 Loss of mechanical energy due to leakage under near-design operation

AC90/6 fans	Normalized leakage-flow rate	Δe_m
Data	8.9×10^{-3}	1.89×10^{-2}
TF	6.8×10^{-3}	7.9×10^{-3}
TFvte	6.6×10^{-3}	7.91×10^{-3}
TF_step	5.4×10^{-3}	1.36×10^{-3}
TFvte_step	5.6×10^{-3}	1.94×10^{-3}

edge). The predicted loss evolutions were in accordance with findings reported in the literature for low-speed rotors [11]. At the rotor inlet, all rotor distributions featured core losses (mainly concentrated on the hub annulus walls). Moving toward the vicinity of the aft-blade, the loss maps were characterized by a core loss directly related to the development of primary tip vortices crossing the blade passage.

Adoption of the TF tip end-plate produced a larger peak-loss core as a result of the occurrence of vortex breakdown (Fig. 14(*b*)). Nonetheless, a comparison of the loss map on the 1.2ℓ plane of the data rotor clearly indicated that the TF tip configuration produced a beneficial spanwise loss distribution. In this respect, the TF tip configuration outperformed the data fan within the wake and on the hub end-wall on the pressure-side and suction-side corners.

With respect to the TFvte fan rotor (Fig. 14(*c*)), the loss evolution within the blade passage indicated that the proposed end-plate design was able to reduce the high core loss at the tip as a result of control of the tip-leakage-vortex breakdown. It is also evident that this control produced a favorable loss distribution behind the rotor and along the suction side of the blade within the interaction region between leakage and near surface flows. This behavior, which is in accordance with the aerodynamic test results, can be considered a consequence of the reduced 3D flow rearrangement, which was itself a consequence of the reduction in mass leaking through the tip gap. The limited radial migration of near-wall surface fluid induced smaller hub core loss and contraction of suction/corner stall (illustrated by a hub-corner stall core in Figs. 14(*b*) and Fig. 14(*c*)).

With respect to the influence of the steps, TF_step and TFvte_step, it was apparent that the aerodynamic loss maps were affected by a larger core loss, which extended into the wake regions (Figs. 14(*d*) and 14(*e*)). Nevertheless, this behavior did not influence the loss reduction in the wake and hub-corner stall regions of any of the modified end-plate configurations.

Finally, Table 5 provides a comparison of the loss of mechanical energy (Δe_m) due to leakage flow per unit tip chord length in the form suggested by Senoo [49]. Despite the fact that the end-plate induced a significant deflection in the leakage flow (Fig. 10(*b*)) and that this should produce an increased level of loss, the data in Table 5 suggest that the improved tips controlled the mechanical loss through the gap by reducing the leakage-flow rate and its kinetic energy content.

6 Conclusions

The present study has assessed tip-leakage flow and its influence on fluid dynamics in a family of axial flow fans. In particular, the study has investigated the aerodynamic behavior of blade tips modified by the addition of aerodynamic appendages to a data blade. Four end-plate configurations were proposed and tested:

- constant thickness (TF)
- variable thickness (TFvte)
- constant thickness with a stepped gap on the tip (TF_step)
- variable thickness with a stepped gap on the tip (TFvte_step)

The aerodynamic tests demonstrated that the proposed tips were associated with a small reduction in performance; however, efficiency curves indicated an improvement in terms of increased peak performance and a wider high-efficiency plateau, which resulted in improved stall margin. In addition, the noise tests demonstrated a reduction in the rotor acoustic signature in terms of both tonal noise and broadband noise.

An assessment of the evolution of leakage-vortex structures showed that the data rotor produced multiple vortices characterized by (i) a dominant leading-edge vortex structure, which was highly skewed with respect to the local relative flow direction, and (ii) a weak secondary vortex in the vicinity of the suction surface of the tip. The modified configurations influenced the leakage flows at the leading edge by changing their orientation with respect to the local relative streamlines that govern the secondary flow advection in the rotor frame. The modified tip configurations were characterized by two vortex structures at the tip: (i) on the pressure side, the leg of an incoming horseshoe-shaped vortex; and (ii) on the suction side, the main leakage-flow vortex. The existence of this pressure-side vortex in association with the modified tip rotor was one of the factors that contributed to control of the leakage phenomenon and the promotion of a vena contracta effect. As a consequence of the vena contractor, the mass leaking was throttled close to the leading edge and the control of leakage flow thus obtained had the potential to improve aeroacoustic performance. In general, an assessment of the aerodynamics resulting from the introduction of a step into the tip configuration provided evidence of an overall reduction of mass leaking and momentum transfer within the clearance.

The Powell [26] sound-source fields (steady-state computed) of the fan-tip configurations were also assessed, and the tip-vortex structures were correlated with the mechanism of noise generation. All of the modified tip configurations outperformed the data configuration in attenuating the sound-source level in the blade passage from the suction surface of the blade.

The loss coefficient distributions confirmed that the highest loss regions were always observed to coincide with the leakage-vortex core (with a nearly constant peak-loss value). The comparative analysis of mechanical energy loss within the gap showed that the presence of the antivortex device at the tip led to a reduction in mechanical energy loss within the gap, suggesting that the loss level within the tip gap is mainly controlled by the mass leaking.

Acknowledgment

This research was conducted in accordance with contract FW-DMA06-09 between Fläkt Woods Ltd. and the Dipartimento di Meccanica e Aeronautica, Sapienza University of Rome. The authors acknowledge the assistance of the Italian Ministry for Academic Research under the auspices of projects Ateneo 2005 and Facoltà 2006. Stefano Bianchi is also gratefully acknowledged for his contribution to the experimental work.

References

[1] Ganz, U. W., Joppa, P. D., and Scharpf, D. F., 1998, “Boeing 18-inch Fan Rig Broadband Noise Test,” NASA Report No. CR-1998–208704.

[2] Fukano, T., Takamatsu, Y., and Kodama, Y., 1986, “The Effects of Tip Clearance on the Noise of Low-Pressure Axial and Mixed Flow Fans,” J. Sound Vib., **105**, pp. 291–308.

[3] Storer, J. A., and Cumpsty, N. A., 1991, “Tip Leakage Flow in Axial Compressors,” ASME J. Turbomach., **113**, pp. 252–259.

[4] Furukawa, M., Inoue, M., Kuroumaru, M., Saiki, K., and Yamada, K., 1999, “The Role of Tip Leakage Vortex Breakdown in Compressor Rotor Aerodynamics,” ASME J. Turbomach., **121**, pp. 469–480.

[5] Fukano, T., and Jang, C., 2004, “Tip Clearance Noise of Axial Flow Fans Operating at Design and Off-Design Condition,” J. Sound Vib., **275**, pp. 1027–1050.

[6] Jang, C., Fukano, T., and Furukawa, M., 2003, “Effects of the Tip Clearance on Vortical Flow and Its Relation to Noise in an Axial Flow Fan,” JSME Int. J., Ser. B, **46**, pp. 356–365.

[7] Quinlan, D. A., and Bent, P. H., 1998, “High Frequency Noise Generation in Small Axial Flow Fans,” J. Sound Vib., **218**, pp. 177–204.

[8] Cumpsty, N. A., 1977, “A Critical Review of Turbomachinery Noise,” ASME

J. Fluids Eng., **99**, pp. 278–293.
[9] Wright, S. E., 1976, "The Acoustic Spectrum of Axial Flow Machines," J. Sound Vib., **45**(2), pp. 165–223.
[10] Wadia, A. R., Szucs, P. N., and Crall, D. W., 1998, "Inner Workings of Aerodynamic Sweep," ASME J. Turbomach., **120**, pp. 671–682.
[11] Corsini, A., and Rispoli, F., 2004, "Using Sweep to Extend Stall-Free Operational Range in Sub-Sonic Axial Fan Rotors," Proc. Inst. Mech. Eng., Part A, **218**, pp. 129–139.
[12] Takata, H., and Tsukuda, Y., 1977, "Stall Margin Improvement by Casing Treatment—Its Mechanism and Effectiveness," ASME J. Eng. Power, **99**, pp. 121–133.
[13] Smith, G. D. J., and Cumpsty, N. A., 1984, "Flow Phenomena in Compressor Casing Treatment," ASME J. Eng. Gas Turbines Power, **106**, pp. 532–541.
[14] Thompson, D. W., King, P. I., and Rabe, D. C., 1998, "Experimental and Computational Investigation on Stepped Tip Gap Effects on the Flowfield of a Transonic Axial-Flow Compressor Rotor," ASME J. Turbomach., **120**, pp. 477–486.
[15] Jensen, C. E., 1986, "Axial-Flow Fan," U.S. Patent No. 4,630,993.
[16] Corsini, A., Rispoli, F., and Sheard, A. G., 2008, "A Meridional Fan," Patent Application No. GB 0800582.9.
[17] Longet, C. M. L., 2003, "Axial Flow Fan With Noise Reducing Means," U.S. Patent 2003/0123987 A1.
[18] Mimura, M., 2003, "Axial Flow Fan," U.S. Patent No. 6,648,598 B2.
[19] Uselton, R. B., Cook, L. J., and Wright, T., 2005, "Fan With Reduced Noise Generation," U.S. Patent No. 2005/0147496 A1.
[20] Corsini, A., Perugini, B., Rispoli, F., Kinghorn I., and Sheard A. G., 2006, "Investigation on Improved Blade Tip Concept," ASME Paper No. GT2006–90592.
[21] Corsini, A., and Sheard, A. G., 2007, "Tip End-Plate Concept Based on Leakage Vortex Rotation Number Control," J. Comput. Appl. Mech., **8**(1), pp. 21–37.
[22] Corsini, A., Rispoli, F., and Sheard, A. G., 2007, "Development of Improved Blade Tip Endplate Concepts for Low-Noise Operation in Industrial Fans," Proc. Inst. Mech. Eng., Part A, **221**, pp. 669–681.
[23] Borello, D., Corsini, A., and Rispoli, F., 2003, "A Finite Element Overlapping Scheme for Turbomachinery Flows on Parallel Platforms," Comput. Fluids, **32**(7), pp. 1017–1047.
[24] Corsini, A., Rispoli, F., and Santoriello, A., 2005, ""A Variational Multi-Scale High-Order Finite Element Formulation for Turbomachinery Flow Computations," Comput. Methods Appl. Mech. Eng., **194**(45–47), pp. 4797–4823.
[25] Powell, A., 1963, "Mechanisms of Aerodynamic Sound Production," AGARD Report No. 466.
[26] Powell, A., 1964, "The Theory of Vortex Sound," J. Acoust. Soc. Am., **36**, pp. 177–195.
[27] Kinghorn, I. R., and Millar, S., 2005, FW-RDLab Report No. r9124.
[28] Inoue, M., Kuroumaru, M., and Furukawa, M., 1986, "Behavior of Tip Leakage Flow Behind an Axial Compressor Rotor," ASME J. Eng. Gas Turbines Power, **108**, pp. 7–14.
[29] Spall, R. E., Gatski, T. B., and Grosch, C. E., 1987, "A Criterion for Vortex Breakdown," Phys. Fluids, **30**(11), pp. 3434–3440.
[30] Uchida, S., Nakamura, Y., and Ohsawa, M., 1985, "Experiments on the Axisymmetric Vortex Breakdown in a Swirling Air Flow," Trans. Jpn. Soc. Aeronaut. Space Sci., **27**(78), pp. 206–216.
[31] Garg, A. K., and Leibovich, S., 1979, "Spectral Characteristics of Vortex Breakdown Flowfields," Phys. Fluids, **22**(11), pp. 2053–2064.
[32] Gbadebo, S. A., Cumpsty, N. A., and Hynes, T. P., 2006, "Interaction of Tip Clearance Flow and Three-Dimensional Separations in Axial Compressors," ASME Paper No. GT2006–90071.
[33] 2000, BS 848-2.6:2000, ISO 10302:1996, Fans for General Purposes: Methods of Noise Testing.
[34] Leggat, L. J., and Siddon, T. E., 1978, "Experimental Study of Aeroacoustic Mechanism of Rotor-Vortex Interactions," J. Acoust. Soc. Am., **64**, pp. 1070–1077.
[35] Escudier, M. P., and Zehnder, N., 1982, "Vortex-Flow Regimes," J. Fluid Mech., **115**, pp. 105–121.
[36] Inoue, M., and Furukawa, M., 2002, "Physics of Tip Clearance Flow in Turbomachinery," ASME Paper No. FEDSM2002–31184.
[37] Craft, T. J., Launder, B. E., and Suga, K., 1996, "Development and Application of a Cubic Eddy-Viscosity Model of Turbulence," Int. J. Heat Fluid Flow, **17**, pp. 108–155.
[38] Corsini, A., and Rispoli, F., 2005, "Flow Analyses in a High-Pressure Axial Ventilation Fan With a Non-Linear Eddy-Viscosity Closure," Int. J. Heat Fluid Flow, **26**, pp. 349–361.
[39] Vad, J., and Bencze, F., 1998, "Three-Dimensional Flow in Axial Flow Fans of Non-Free Vortex Design," Int. J. Heat Fluid Flow, **19**(6), pp. 601–607.
[40] Khourrami, M. R., and Choudari, M., 2001, "A Novel Approach for Reducing Rotor Tip-Clearance Induced Noise in Turbofan Engines," AIAA Paper No. 2001-2148.
[41] Tam, C. K. W., 1994, "Jet Noise Generated by Large-Scale Coherent Motion," *Aeroacoustics of Flight Vehicles: Theory and Practice* (Noise Sources), H. H. Hubbard, ed., NASA Langley Research Center, Springer-Verlag, Berlin, Vol. I, pp. 311–390.
[42] Bianchi, S., Sheard, A. G., Kinghorn, I. R., Corsini, A., and Rispoli, F., 2009, "Experimental Development of a Measurement Technique to Resolve the Radial Distribution of Fan Aero-Acoustic Emissions," Noise Control Eng. J., July–August.
[43] Bianchi, S., Corsini, A., Rispoli, F., and Sheard, A. G., 2008, "Experimental Aeroacoustic Studies on Improved Tip Geometries for Passive Noise Signature Control in Low-Speed Axial Fan," ASME Paper GT2008–51057.
[44] Sujudi, D., and Haimes, R., 1995, "Identification of Swirling Flow in 3-D Vector Field," AIAA Paper No. AIAA95-1715.
[45] Burdsall, E. A., and Urban, R. H., 1973, "Fan-Compressor Noise: Prediction, Research and Reduction Studies," Paper No. FAA-RD-71-73.
[46] Lighthill, M. J., 1952, "On Sound Generated Aerodynamically. I: General Theory," Proc. R. Soc. London, Ser. A, **221**, pp. 564–587.
[47] Lighthill, M. J., 1954, "On Sound Generated Aerodynamically. II: Turbulence as a Source of Sound," Proc. R. Soc. London, Ser. A, **222**, pp. 1–32.
[48] Arakawa, C., Fleig, O., Makoto, I., and Masakazu, S., 2005, "Numerical Approach for Noise Reduction of Wind Turbine Blade Tip With Earth Simulator," Journal of the Earth Simulator, **2**, pp. 11–33.
[49] Senoo, Y., 1991, "Mechanics on the Tip Clearance Loss of Impeller Blades," ASME J. Turbomach., **113**, pp. 680–685.

Experimental Evidence of Hydroacoustic Pressure Waves in a Francis Turbine Elbow Draft Tube for Low Discharge Conditions

Jorge Arpe

Christophe Nicolet[1]
e-mail: christophe.nicolet@epfl.ch

François Avellan

Laboratory for Hydraulic Machines,
EPFL, Ecole Polytechnique Fédérale de Lausanne,
33 bis, Avenue de Cour,
CH-1007 Lausanne, Switzerland

The complex three-dimensional unsteady flow developing in the draft tube of a Francis turbine is responsible for pressure fluctuations, which could prevent the whole hydropower plant from operating safely. Indeed, the Francis draft tube is subjected to inlet swirling flow, divergent cross section, and the change of flow direction. As a result, in low discharge off-design operating conditions, a cavitation helical vortex, so-called the vortex rope develops in the draft tube and induces pressure fluctuations in the range of 0.2–0.4 times the runner frequency. This paper presents the extensive unsteady wall pressure measurements performed in the elbow draft tube of a high specific speed Francis turbine scale model at low discharge and at usual plant value of the Thoma cavitation number. The investigation is undertaken for operating conditions corresponding to low discharge, i.e., 0.65–0.85 times the design discharge, which exhibits pressure fluctuations at surprisingly high frequency value, between 2 and 4 times the runner rotation frequency. The pressure fluctuation measurements performed with 104 pressure transducers distributed on the draft tube wall, make apparent in the whole draft tube a fundamental frequency value at 2.5 times the runner frequency. Moreover, the modulations between this frequency with the vortex rope precession frequency are pointed out. The phase shift analysis performed for 2.5 times the runner frequency enables the identification of a pressure wave propagation phenomenon and indicates the location of the corresponding pressure fluctuation excitation source in the elbow; hydroacoustic waves propagate from this source both upstream and downstream the draft tube. [DOI: 10.1115/1.3155944]

1 Introduction

At part load operation, Francis turbines are subjected to the development of a swirling flow in the draft tube that may produce, under given conditions, unacceptable pressure, discharge, torque and power oscillations, see Refs. [1–4]. Indeed, the swirling flow injected by the constant pitch turbine runner in the draft tube yields to the development of a helical vortex core rotating in the draft tube and induces pressure fluctuations in the range of $0.2-0.4f_n$, see Refs. [5–7].

Swirling flows are characterized by simultaneous axial and rotation motion. The change in the flow pattern, from steady state axisymmetric flow to unsteady helical flow, when angular momentum is increased, is defined as the vortex breakdown phenomenon and has already been studied extensively; see Refs. [8–10]. The onset of helical vortices was first witnessed by Harvey [11] in air controlled swirling flow entering a straight diffusing pipe. Benjamin [12,13] performed small perturbation analysis, showing that, after the vortex breakdown the swirling flow is capable of sustaining standing waves. Cassidy and Falvey [14] introduced relevant similitude numbers to characterize the vortex breakdown phenomenon using similar experimental arrangement to Harvey [11]. Particularly, they introduced the momentum parameter defined as the ratio between the angular momentum and the axial momentum. They pointed out the proportionality of the reduced frequency of the vortex precession, i.e., the Strouhal number, to the momentum parameter, and the insensitivity of the frequency for a wide range of Reynolds number values. Later, Susan-Resiga et al. [15] studied the stability of the flow developing in the draft tube of a Francis turbine scale model. Based on experimental identification, the mean flow in the draft tube cone was modeled by the combination of three elementary vortices: a rigid body motion vortex and two Batchelor vortices. Eigenvalues analysis of the resulting analytical model of the flow for different discharge values points out the onset of the flow unsteadiness at part load operation. This coincides with experimental observations and measurements.

Dorfler [16] and Angelico et al. [17] demonstrated that the pressure fluctuations in the Francis draft tubes can be decomposed into a rotating component and a synchronous component. The rotating component is related to the unsteady three-dimensional convective pressure field associated to the vortex core precession, whereas the synchronous component is related to the hydroacoustic pressure pulsations. These synchronous pressure fluctuations may be considered as excitation, generating pressure waves, which propagate in the entire hydraulic system and which may induce hydraulic system resonance under given conditions [16].

The influence of the Thoma cavitation number σ, was investigated experimentally with a laboratory swirling flow generator by Nishi [18,19], pointing out the apparition of the so-called draft tube surge. The influence of the Thoma cavitation number on the swirling flow and the pressure fluctuations were thoroughly studied in the case of elbow draft tubes of Francis turbine scale model by Jacob [7] and, then, by Arpe [20]. To emphasize the influence of the Thoma cavitation number σ, the visualization of the cavi-

---

[1] Corresponding author.

Contributed by the Fluids Engineering Division of ASME for publication in the JOURNAL OF FLUIDS ENGINEERING. Manuscript received May 13, 2008; final manuscript received April 15, 2009; published online July 8, 2009. Assoc. Editor: Juergen Kompenhans.

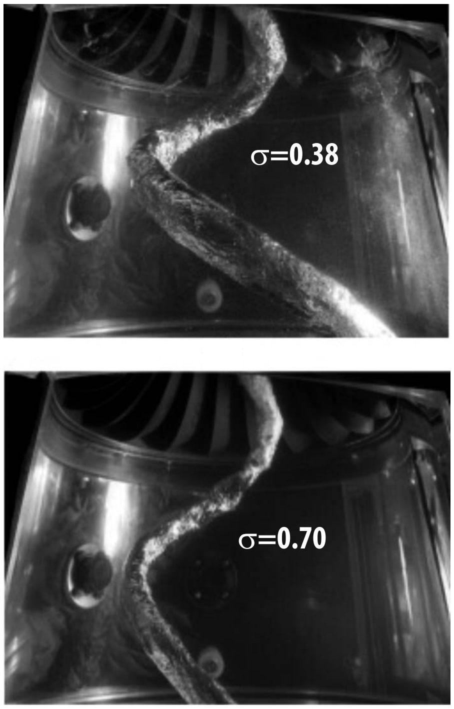

Fig. 1 Gaseous vortex core development for two different values of the Thoma cavitation number for the same low discharge operating condition

tation vortex core development is reported Fig. 1 for two different values of σ for the same operating conditions. Obviously, the gaseous volume of the cavitation vortex core decreases when σ increases.

Moreover, for the operating range corresponding to $Q/Q_{\mathrm{BEP}} = 0.65-0.85$, the pressure fluctuation's fundamental frequency has been reported on the scale model at higher values, ranging from 2 to $4f_n$ by Fischer et al. [21] and by Dörfler [22] and, more recently, by Koutnik et al. [23]. Usually, those pressure fluctuations, featuring significant amplitudes, are found on the Francis turbine scale model of high specific speed, $\nu > 0.45$, and for low σ values, see Ref. [22]. However, until now, the origin of those "high frequencies" pressure fluctuations has not been well understood.

The present paper presents a thorough experimental survey of the unsteady pressure field developing at low discharge operating conditions in the elbow draft tube of a high specific speed Francis turbine experiencing cavitation at usual plant value of Thoma number. The results corresponding to the cavitation free flow conditions have already been presented in a previous paper, see Ref. [24]. The present investigation focuses on the analysis of the unsteady pressure field at the same operating point, for a lower Thoma cavitation number, where high frequency pressure fluctuations are evidenced through the analysis of 104 wall pressure signals. The analysis of both the amplitude and the phase of the pressure fluctuations is performed over the whole draft tube at the fundamental frequency value of 2.5 times the runner rotational frequency. This analysis localizes the source of this corresponding pressure fluctuation at the elbow of the draft tube, from where the pressure waves propagate upward and downward, evidencing the hydroacoustic property of the phenomenon. Finally, the phase shift analysis of the pressure fluctuation measured signals allows the determination of the distribution of the wave speed in the draft tube.

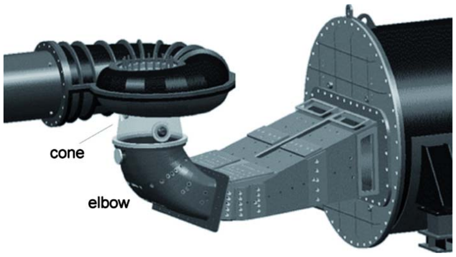

Fig. 2 CAD model of the Francis turbine scale model

2 Experimental Setup

The investigations are performed on the scale model of a high specific speed Francis turbine, $\upsilon = 0.56$, described by Ref. [25], installed on the EPFL experimental facility, see Fig. 2. The experimental investigations are carried out by following the IEC 60913 standards [26]. Thirteen cross sections of the elbow draft tube are instrumented with 292 pressure taps, see Fig. 3 left, to record the pressure time history by means of a set of 104 embedded miniature piezoresistive absolute pressure transducers, 2MI 0–0.3 MPa Keller sensor series, see Fig. 3 right. The static and dynamic calibration of the pressure transducers is performed in place with, respectively, Huber and Kistler reference pressure transducers. The acquisition system enables a high data transfer rate and simultaneous acquisition on 104 channels. To capture the phenomena of interest at low discharge operating conditions, series of 3 records of 430 vortex passages of 2^{14} samples each are acquired with a 200 Hz sampling frequency. The averaged power cross-spectra of the wall pressure fluctuations are estimated by using five sliding windows of 2^{13} samples width, leading to a 0.0244 Hz frequency resolution.

3 Pressure Fluctuations

The investigated low discharge operating point is defined by the following set of parameters: $\psi^* = 1.06$, $\varphi^* = 0.703$, $N = 750\ \mathrm{min}^{-1}$, and 16 deg guide vane opening, see Fig. 4.

The experimental procedure to investigate the cavitation influence on the pressure fluctuations amplitude spectrum in the draft tube cone consists of increasing σ stepwise until reaching the cavitation free condition. During this procedure, the pressure field in the cone is recorded for different values of σ. The resulting pressure amplitude spectra are given in Fig. 5. Two types of pressure fluctuations are pointed out: (i) pressure fluctuations related

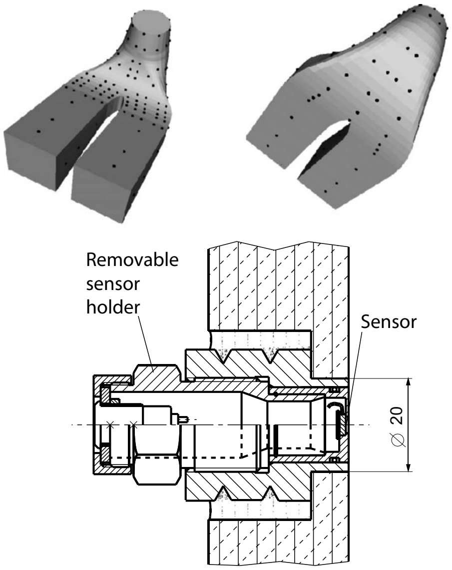

Fig. 3 Locations of the 292 pressure taps along the walls of the elbow draft tube (left), and mounting of the pressure transducer at the draft tube wall (right)

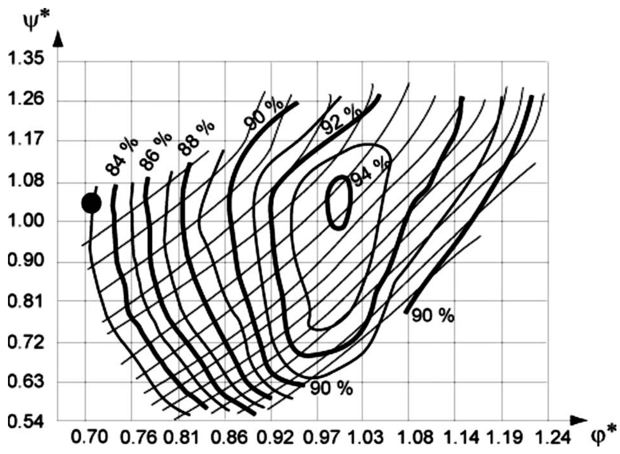

Fig. 4 The investigated low discharge operating point marked in the scale model efficiency hill chart

to the vortex rope precession, in the range of $0.3-0.4f_n$ slightly influenced by σ, and (ii) pressure fluctuations in the range $2-4f_n$ strongly influenced by σ.

Figure 6 presents the evolution of the amplitude and frequency for both types of pressure fluctuations. It can be noticed, that the frequency of the vortex precession slightly decreases from 0.4 to $0.31f_n$ when σ is increased and the related amplitude is rather constant, except for $\sigma < 0.45$, where amplitudes are reduced by a factor of 2. This is similar to the observations already made by Jacob [7]. More interesting is the influence of σ on the frequency and amplitude of the pressure fluctuations in the range of $2-4f_n$. The fundamental frequency value of these pressure fluctuations is quasiproportional to the Thoma cavitation number, while the amplitudes strongly increase when σ is below 0.45. Moreover, these pressure fluctuations are apparently modulated by the vortex precession, as it is pointed out by the shifts between the pressure peaks made apparent in Fig. 5. It can also be noticed that strong vibration and noise are reported for the low cavitation operating point.

An operating point featuring high amplitude of pressure fluctuations is selected for more detailed investigations, see Fig. 6. This operating point corresponds to a low Thoma cavitation number $\sigma=0.38$. Figure 7 shows the time history of the pressure fluctuations for five sections of the draft tube at the selected operating point. It can be noticed that all the signals feature modulations and, moreover, the maxima and minima are in phase.

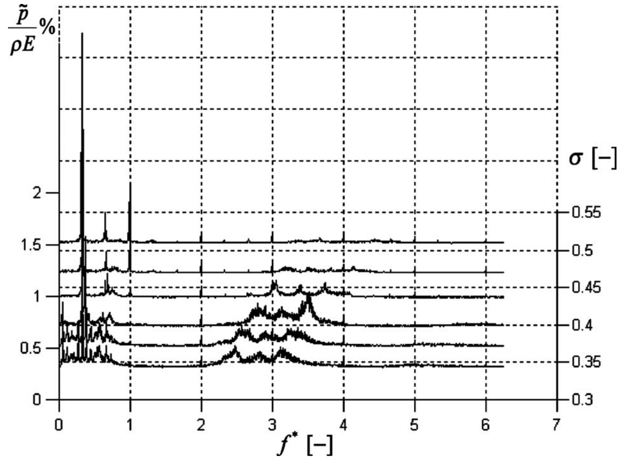

Fig. 5 Influence of σ on the pressure fluctuations amplitude spectrum; each curve is offset by the corresponding σ value

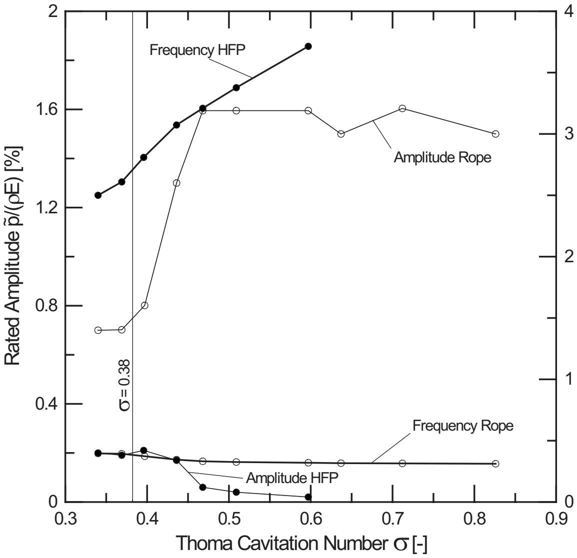

Fig. 6 Influence of σ on the frequency and the amplitude of pressure fluctuations related to the vortex rope precession and the high frequency phenomenon, HFP

The pressure fluctuations amplitude spectra are computed for four paths along the draft tube, and are presented as waterfall diagrams in Fig. 8. The waterfall diagrams evidence that the whole draft tube exhibits $2-4f_n$ high frequency pressure fluctuations, with a maximum amplitude located in the elbow. Meanwhile the pressure fluctuations caused by the vortex precession, in the range $0.2-0.4f_n$, are encountered only in the cone, sensors 1–3, and then vanish in the draft tube diffuser.

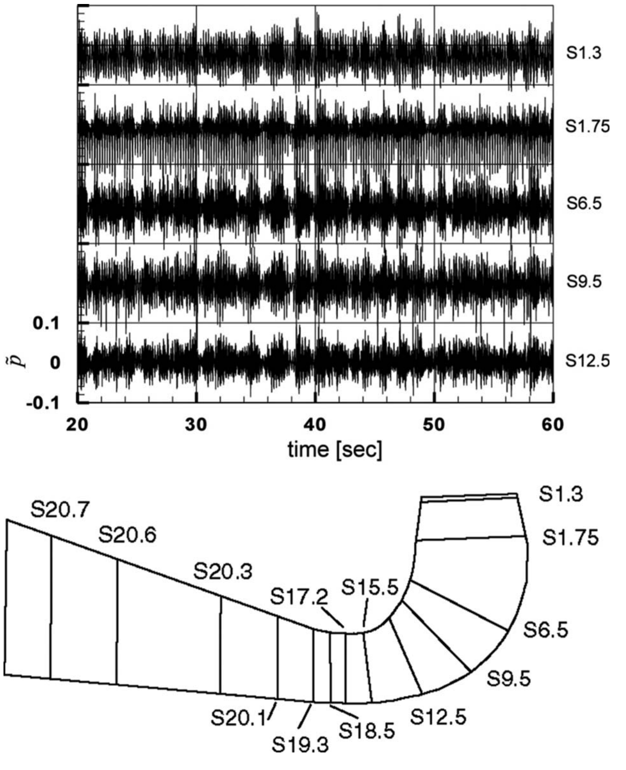

Fig. 7 Time history records of pressure fluctuations for the first five sections in the draft tube

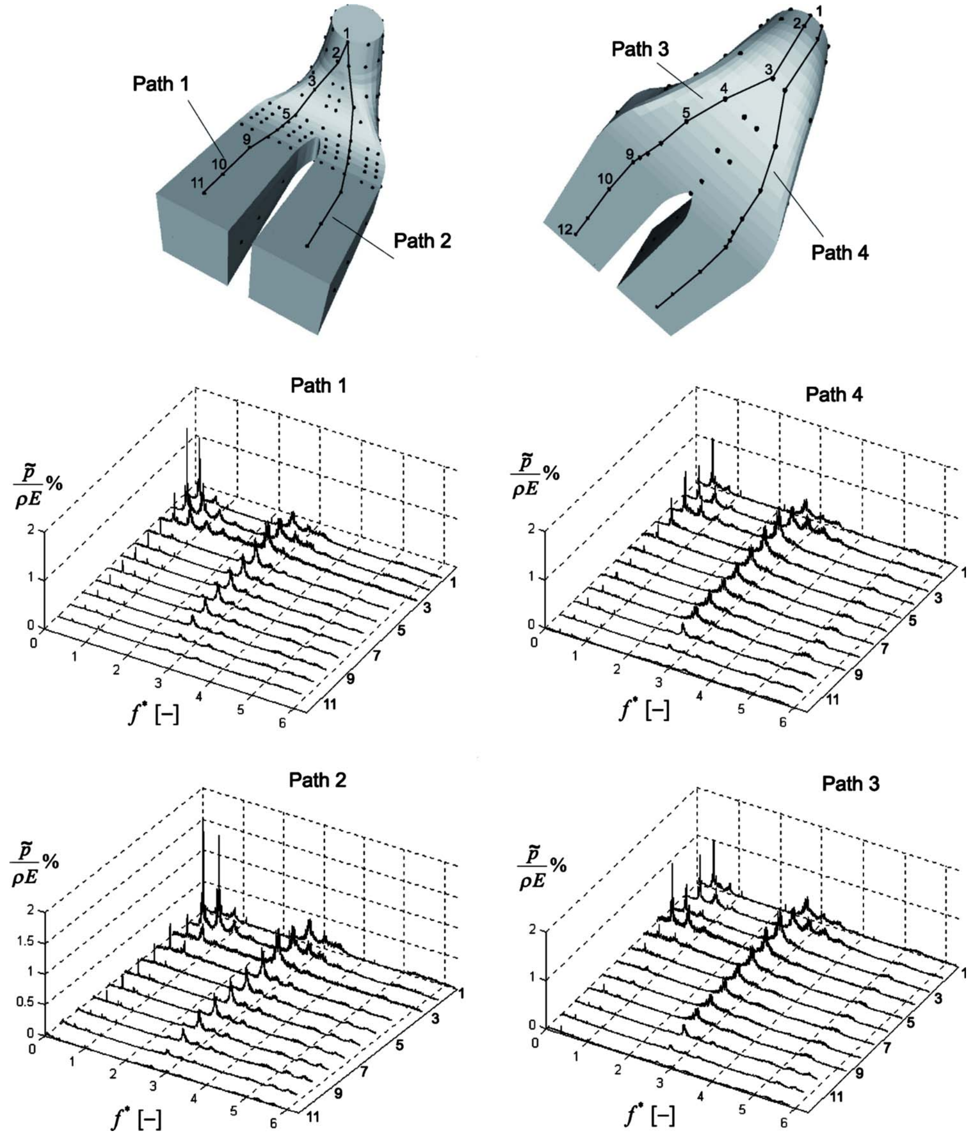

Fig. 8 Evolution of pressure fluctuations amplitude spectra for four paths along the draft tube

4 Modulation of Pressure Fluctuations

The amplitude spectrum of the pressure fluctuations measured in the cone, section S1.75, presented in Fig. 9, evidences the amplitude modulation between the vortex rotation (the modulating wave at fundamental f_v) and a phenomenon that occurs at the fundamental frequency f_c or $2.5f_n$ (the carrier wave). Therefore, the resulting modulations frequencies are $f_c - f_v, f_c + f_v, f_c + 2f_v$ and $2f_c$. Two periodic and time dependent signals with the fundamental frequencies f_c and f_v, can be expressed by the two following truncated Fourier series:

$$F_c(t) = \sum_{i=1}^{n} (A_i \cos(2\pi \cdot i \cdot f_c \cdot t) + B_i \sin(2\pi \cdot i \cdot f_c \cdot t)) \qquad (1)$$

$$F_v(t) = \sum_{i=1}^{n} (C_i \cos(2\pi \cdot i \cdot f_v \cdot t) + D_i \sin(2\pi \cdot i \cdot f_v \cdot t)) \qquad (2)$$

Therefore, the two series product, i.e., the modulated signal, yields

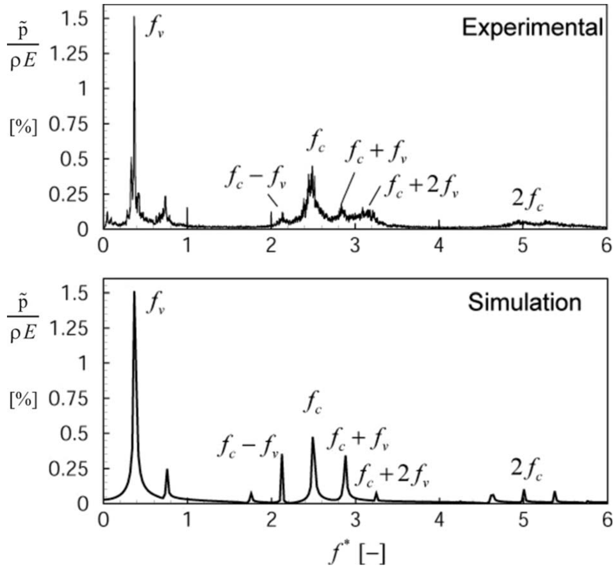

Fig. 9 Amplitude spectra of experimental pressure fluctuations measured at S1.75, and the corresponding amplitude spectra of the two signals modulation derived from Eq. (3))

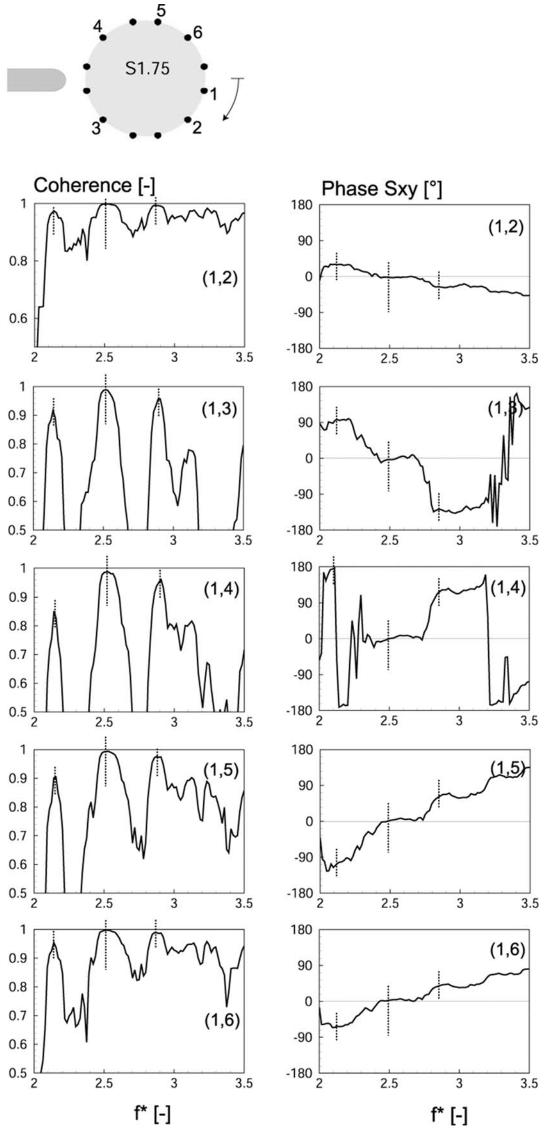

Fig. 10 Analysis at $2.5f_n$ frequency in the section S1.75 at the cone

$$
\begin{aligned}
F_c(t)\cdot F_v(t) = {} & E_1\cos(2\pi(f_c+f_v)t) + E_2\cos(2\pi(f_c-f_v)t) \\
& + E_3\cos(2\pi(f_c+2f_v)t) + E_4\cos(2\pi(f_c-2f_v)t) \\
& + E_5\cos(2\pi(2f_c+f_v)t) + E_6\cos(2\pi(2f_c-f_v)t) + \ldots
\end{aligned}
\tag{3}
$$

The corresponding spectrum of this product of elementary signals brings out all the characteristic frequencies observed experimentally, as reported in Fig. 9.

5 Analysis of the Experimental Wall Pressure Fluctuations Survey at $2.5f_n$

In the following, the high frequency phenomenon at $2.5f_n$ is investigated through the space and time analysis of the experimental survey of the pressure fluctuations performed on the wall of the elbow draft tube. Therefore the cross-spectrum density function S_{xy} and the coherence function Γ_{xy} between two signals are introduced. The cross-spectrum is expressed in terms of magnitude and associated phase angle as follows:

$$S_{xy}(f) = |S_{xy}(f)|e^{j\theta_{xy}(f)} \tag{4}$$

where

$$|S_{xy}(f)| = \sqrt{C_{xy}^2(f) + Q_{xy}^2(f)} \tag{5}$$

and

$$\theta_{xy}(f) = -\tan^{-1}\left[\frac{Q_{xy}(f)}{C_{xy}(f)}\right] \tag{6}$$

$C_{xy}(f)$ and $Q_{xy}(f)$ being the real and imaginary part of $S_{xy}(f)$, respectively.

The signs of the cross-spectrum terms $C_{xy}(f)$ and $Q_{xy}(f)$ determine for each frequency f whether $y(t)$ follows $x(t)$, as $y(t)$ is given by $y(t)=x(t-\tau_o)$, where $\tau_o>0$ represents a positive time. A negative value of $\theta_{xy}(f)$ means that $y(t)$ follows $x(t)$ for frequency f, whereas a positive value of $\theta_{xy}(f)$ means that $x(t)$ follows $y(t)$ at frequency f.

The results of the cross-spectrum analysis performed in the cone of the draft tube at the section S1.75 are presented in Fig. 10. The cross-spectrum density function S_{xy} clearly reveals the characteristic frequencies due to the modulation with high amplitudes for $2.5f_n$ frequency and $2.5f_n+f_v$ and lower amplitudes for $2.5f_n-f_v$. Moreover, the coherence function Γ_{xy} values close to 1 evidences high energy transfer at the related frequencies. Regarding the phase shift, one can notice that there is no phase shift between

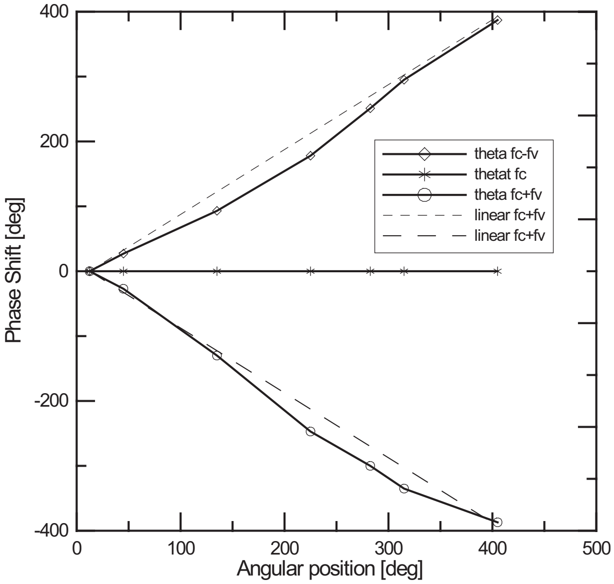

Fig. 11 Phase shift angular distribution in the section S1.75 for the frequencies f_c, f_c-f_v, and f_c+f_v

the signals for $2.5f_n$ frequency, evidencing synchronous pressure pulsation related to a 1D propagation wave phenomenon. It can be also noticed that the phase shift for the frequencies $2.5f_n+f_v$ and $2.5f_n-f_v$, respectively, decreases and increases according to the relative motion of the vortex rope into the cross section, as it is reported in Fig. 11. The deviation of the phase shift distribution for the frequencies $2.5f_n+f_v$ and $2.5f_n-f_v$ with respect to the linear distribution of the phase, corresponding to a constant angular speed of the vortex rope, points out the nonuniformity of the vortex rope angular speed induced by the draft tube elbow. The same results are obtained for the phase distribution at the vortex rope frequency f_v in the section S1.75, see Fig. 12. Following the same approach for all the sections according to the path defined in Fig. 13, the wave propagation can be derived for the $2.5f_n$ frequency. The cross-spectrum density and the coherence functions show that the draft tube experiences pressure fluctuation at this characteristic frequency from the inlet up to the outlet. The distribution of the phase shift between every pair of sensors along the path, from the inlet to the outlet, shows that the sign of the phase shift changes from the positive to the negative values passing by a null phase measured at the elbow.

To have an overview of the phenomena, the phase shift is presented on an unfolded draft tube, as a map of all phase shifts referred to a signal located in the cone, see Fig. 14 top. One may notice that the phase is constant in the whole section S1.3, as well as in section S1.75. This evidences 1D propagation in the cone. While between sections S1.75 and S12.5 the phase evolution appears to be more 3D with phase origin in section S6.5 at position angle 180 deg. The unfolded representation shows that pressure waves start from the elbow center and propagate both upward the draft tube inlet and downward the draft tube outlet. Based on these results, the location of the source of pressure waves is identified in the inner part of the elbow, as shown in the 3D representation, Fig. 14 bottom.

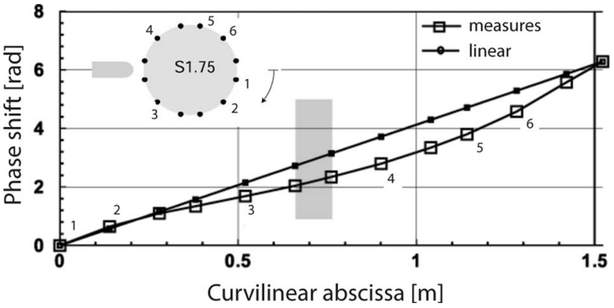

Fig. 12 Phase shift angular distribution in the section S1.75 for the frequency f_v

6 Phase Speed Derivation

With the help of the pressure fluctuations phase shift values, which can be expressed in terms of time for a given frequency $dt=\Delta\theta/(2\cdot\pi\cdot 2.5\cdot f_n)$, and the distance between the sensors dx, the corresponding phase speed is derived $a=dx/dt$, see Ref. [27]. The phase speed is calculated through all the sections and represented in Fig. 15 following the four paths defined in Fig. 8. The speed distribution obtained along the four paths points out the differences of phase speeds along the draft tube. The values of these speeds may be interpreted as pressure wave speeds corresponding to the sound velocity of pressure waves propagating in the draft tube at frequency $2.5f_n$. According to this interpretation, this velocity depends on the section diameter, the pipe wall thickness, the pipe material but also strongly on the free gas content [28]. It can be noticed that (i) the pressure wave speed is low in the cone, about 20 m/s, due to the presence of the vortex rope with a large diameter; (ii) the wave speed increases in the elbow to a mean value of 400 m/s because of the increase in the section stiffness, thick walls, and short pipe and mainly due to the decrease in the cavitation vortex rope cross section; (iii) the wave speed decreases in the draft tube channels because of the relative low stiffness of the rectangular sections of the channels, while there is no cavitation vortex rope in this part of the draft tube. It is also pointed out that the wave speed value is higher in the external part of the elbow than in the inner part of the elbow. It is due to the fact that the wave travel distance is longer in the external part than in the inner part when considering plane wave propagating in the elbow.

7 Analysis

The above analysis emphasizes pressure fluctuations with significant amplitudes at a higher frequency than the vortex rope frequency. The frequency and amplitudes of the pressure fluctuations are strongly influenced by the Thoma cavitation number. The consequences of these fluctuations are a high level of noise and vibrations of the draft tube and the experimental facility, the test rig.

From the draft tube space distribution of the pressure fluctuations amplitudes at $2.5f_n$, see Fig. 8, it can be noticed that the pressure fluctuations feature a 1D pressure mode shape pattern, which is suspected to result from a hydroacoustic resonance of the hydraulic circuit. Indeed, one can identify a node of pressure fluctuations at the tank and an antinode in the elbow, whereas the other pressure node probably takes place in the high pressure part of the turbine. Moreover, the resonance hypothesis is supported by the fact that the pressure fluctuations at $2.5f_n$ are synchronous in the same cross section, as shown in Fig. 14. It is also noticeable that the value of pressure fluctuations fundamental frequency increases when the vortex gaseous volume decreases, see Fig. 5. This increase follows the same trend as the eigenfrequencies of a hydraulic system whose vortex gaseous volume changes. So the $2.5f_n$ value is more likely to be the eigenfrequency of the investigated hydraulic system. The excitation of the system would result from a strong interaction between the vortex rope and the elbow leading to the pressure source located in the inner part of the elbow, as pointed out in Fig. 14.

If the phase speed distribution obtained experimentally is asso-

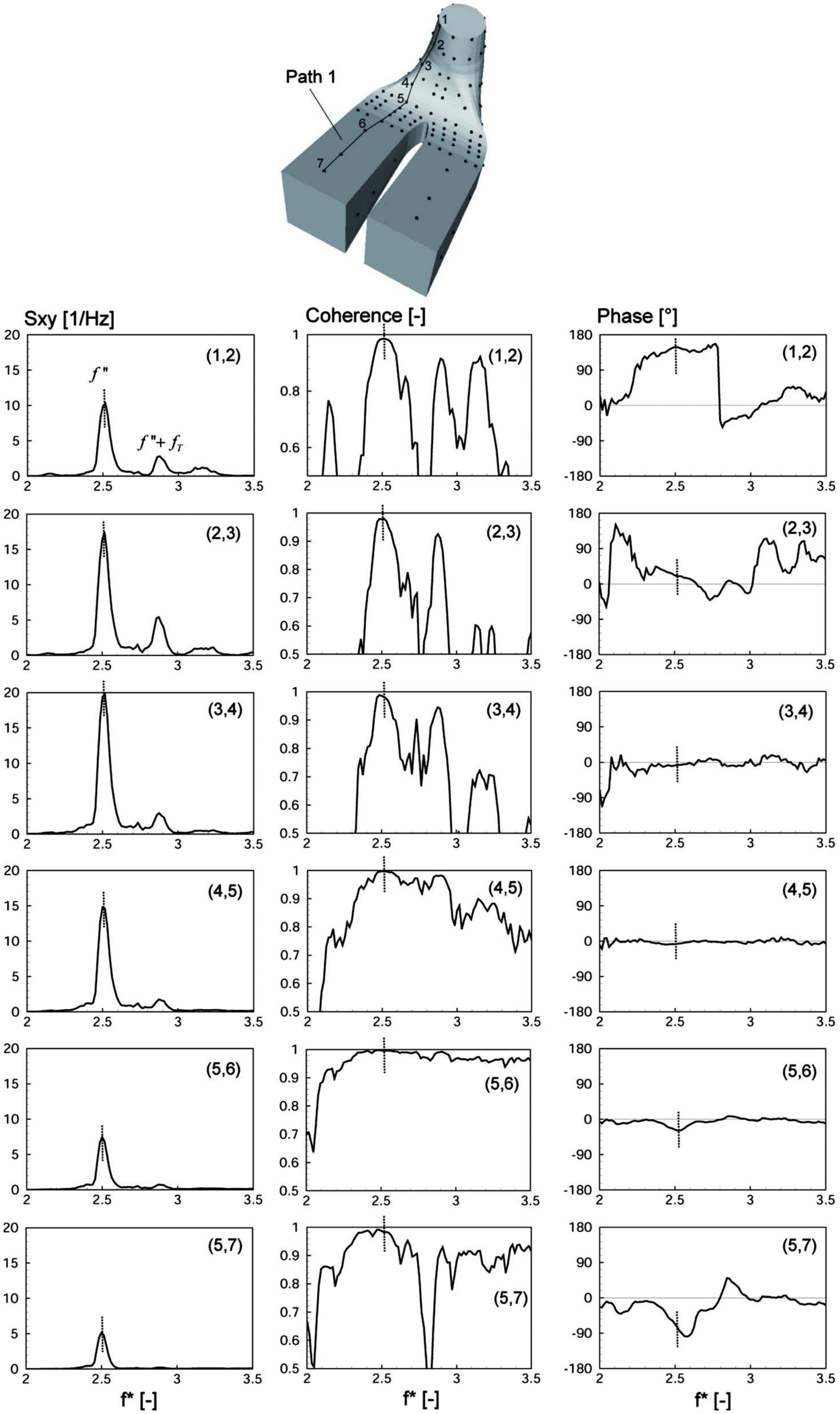

Fig. 13 Amplitude, coherence, and phase spectra of the pressure fluctuations evidencing the $2.5f_n$ pressure wave propagation along path 1

ciated to the pressure wave speed, it enables one to perform a hydroacoustic numerical simulation of the entire hydraulic system, including the draft tube and the test rig, by using either impedances or matrix methods [29]. For such numerical simulations the pressure wave speed is a key parameter enabling one to derive the natural frequencies of the test rig and to compare them with the experimental results. Moreover, this wave speed distribution will allow the use of enhanced draft tube modeling valid for higher frequency ranging up to 40 Hz [30,31], where the space variation in the wave speed have be taken into account.

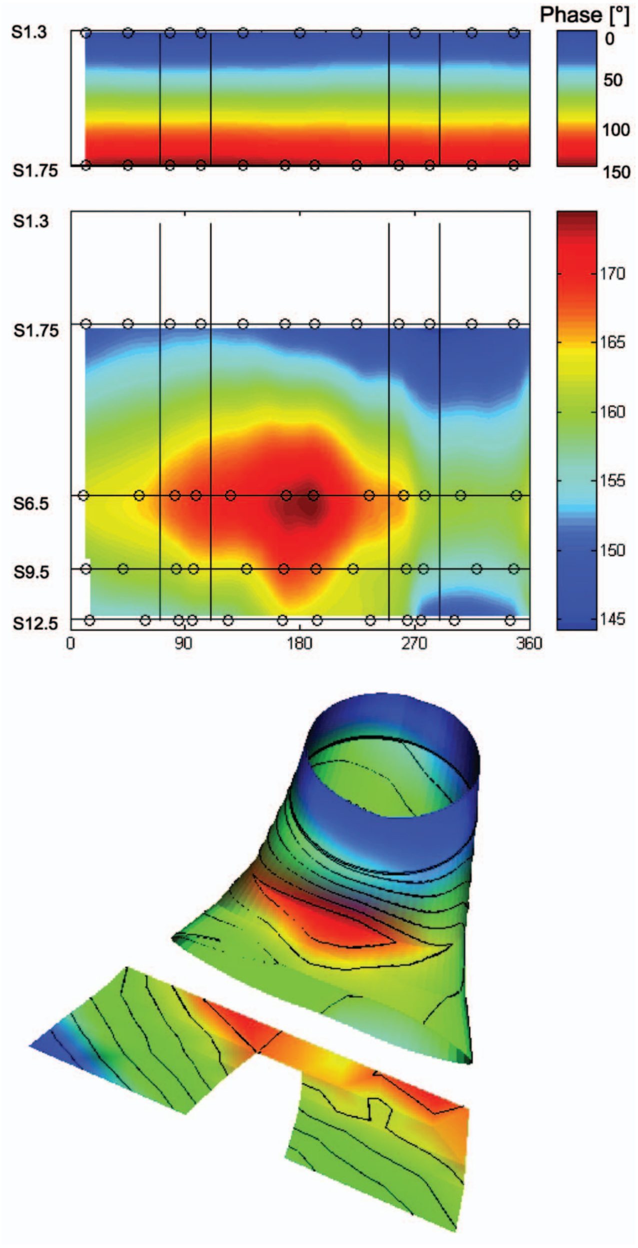

Fig. 14 Unfolded representation in 2D of the phase shift in the cone and the elbow of the draft tube (top) and 3D corresponding representation (bottom) at 2.5f_n frequency

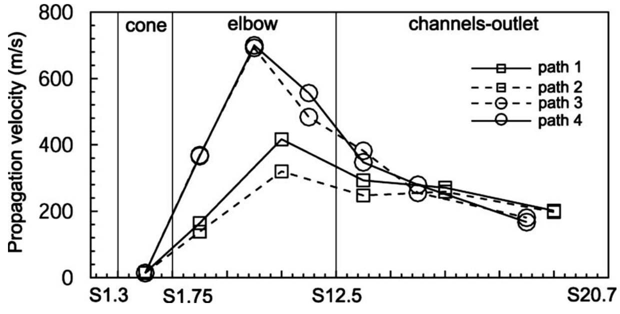

Fig. 15 Space distribution of the phase speed along the four paths defined in Fig. 8

8 Conclusion and Perspectives

Extensive wall pressure survey has been performed in the elbow draft tube of a Francis turbine scale model for $Q/Q_{\mathrm{BEP}}=0.703$ operating conditions. Strong pressure fluctuations have been identified along the draft tube for a frequency value of 2.5f_n. Phase shift analysis pointed out pressure wave propagations from the inner part of the elbow of the draft tube, identified as the source location of these pressure waves propagating upstream and downstream from the source. Also important is the modulation phenomenon between the vortex rope precession at the frequency f_v and the pressure fluctuations at 2.5f_n evidenced by the phase shift analysis.

The synchronous nature of the pressure fluctuations at the frequency 2.5f_n and the pressure distribution along the draft tube with pressure nodes and antinodes would indicate a hydroacoustic resonance of the entire hydraulic system including the test rig and the scale model as well.

The origin of the modulation process between the vortex rope and the pressure fluctuations at the frequency 2.5f_n is not well understood so far. Therefore, it would be of high interest to investigate the influence of the rotational speed effect of this phenomenon, i.e., changing the Froude number. High speed camera visualization of the vortex rope synchronized with pressure fluctuations measurements could also provide better understanding of the interaction between the gaseous vortex rope and the likely test rig resonance. Moreover, as the wave speed distribution is known from the phase shift analysis, it would be possible to develop a hydroacoustic model of the hydraulic system to investigate these resonance conditions further.

Acknowledgment

The authors would like to thank particularly the partners of the FLINDT II Eureka Project No. 1625, i.e., ALSTOM Hydro, EDF-CIH, GE Hydro, VA TECH Hydro, and VOITH-SIEMENS Hydro Power Generation for their financial support and assistance. The FLINDT II project is funded by PSEL, Funds for Projects and Studies of the Swiss Electric Utilities, Contract award No. 126, and CTI, Swiss Federal Commission for Technology and Innovation, Contract award No. 5190.2 EUS. The authors would like also to thank the staff members of the EPFL-LMH workshop for their technical support.

Nomenclature

E = turbine specific hydraulic energy, J/kg
Q = turbine discharge, m^3/s
Q_{BEP} = discharge value at the best efficiency operating point, m^3/s
N = runner speed, min^{-1}
f = frequency, Hz
f_n = runner rotation frequency, Hz
$f*$ = nondimensional frequency $f*=f/f_n$
f_T = vortex rope precession frequency, Hz
ψ = specific energy coefficient $\psi=2E/(\omega D/2)^2$
$\psi*$ = specific energy coefficient divided by the ψ BEP value
φ = discharge coefficient $\varphi=Q/\pi\omega(D/2)^3$
$\varphi*$ = specific energy coefficient divided by the φ BEP value
$\tilde{p}$ = fluctuating static pressure, Pa
$NPSE$ = Net specific positive energy of the turbine, J/kg
σ = Thoma cavitation number $\sigma=NPSE/E$
ν = turbine specific speed

References

[1] Rheingans, W. J., 1940, "Power Swing in Hydroelectric Power Plants," Trans. ASME, **62**, pp. 171–184.
[2] Campmas, P., 1960, "Stability of Operating Conditions for Francis Turbines,"

Proceedings of the 1st IAHR Symposium on Hydraulic Machinery and Systems, Nice, pp. 1–14, Paper No. B4.

[3] Vatcher, T. R., Hunter, M., Perreault, G., and Coulson, D. M., 1984, "Hydraulic Resonance in a 78 MW Francis Turbine - Field Test Results," *Proceedings of the 12th IAHR Symposium on Hydraulic Machinery and Systems*, Stirling, pp. 371–391.

[4] Jacob, T., Prénat, J.-E., Buffet, G., and Winkler, S., 1995, "Improving the Stability of Operation of a 90 MW Francis Turbine," *Proceedings of the International Conference on Hydropower Into the Next Century*, Barcelona.

[5] Dériaz, P., 1960, "A contribution to the Understanding of Flow in Draft Tubes of Francis Turbines," *Proceedings of the 1st IAHR Symposium on Hydraulic Machinery and Systems*, Nice, pp. 1–13, Paper No. B1.

[6] Ulith, P., Jaeger, E.-U., and Strscheletzky, M., 1974, "Contribution to Clarifying the Inception of Nonstationary Flow Phenomena in the Draft Tube of High Specific Speed Francis Turbines Operating at Part Load," *Proceedings of the 7th IAHR Symposium on Hydraulic Machinery and Systems*, Vienna, pp. 1–18, Paper No. III-4.

[7] Jacob, T., 1993, "Evaluation sur Modèle Réduit et Prédiction de la Stabilité de Fonctionnement des Turbines Francis," Ph.D. thesis, EPFL-Ecole Polytechnique Fédérale de Lausanne, Lausanne.

[8] Hall, M. G., 1972, "Vortex Breakdown," Annu. Rev. Fluid Mech., **4**, pp. 195–218.

[9] Leibovich, S., 1978, "Structure of Vortex Breakdown," Annu. Rev. Fluid Mech., **10**, pp. 221–246.

[10] Escudier, M., 1987, "Confined Vortices in Flow Machinery," Annu. Rev. Fluid Mech., **19**, pp. 27–52.

[11] Harvey, J. K., 1962, "Some Observations of the Vortex Breakdown Phenomenon," J. Fluid Mech., **14**, pp. 585–592.

[12] Benjamin, T. B., 1962, "Theory of Vortex Breakdown Phenomenon," J. Fluid Mech., **14**, pp. 593–629.

[13] Benjamin, T. B., 1967, "Some Developments in the Theory of Vortex Breakdown," J. Fluid Mech., **28**, pp. 65–84.

[14] Cassidy, J. J., and Falvey, H. T., 1970, "Observation of Unsteady Flow Arising After Vortex Breakdown," J. Fluid Mech., **41**, pp. 727–736.

[15] Susan-Resiga, R., Ciocan, G. D., Anton, I., and Avellan, F., 2006, "Analysis of the Swirling Flow Downstream a Francis Turbine Runner," ASME J. Fluids Eng., **128**(1), pp. 177–189.

[16] Dörfler, P., 1982, "System Dynamics of the Francis Turbine Half Load Surge," *Proceedings of the 11th IAHR Symposium on Hydraulic Machinery and Systems*, Amsterdam, Paper No. 39.

[17] Angelico, F. M. G., Muciaccia, F., and Rossi, G., 1986, "Part Load Behavior of a Turbine: a Study on a Complete Model of a Hydraulic Power Plant," *Proceedings of the 17th IAHR Symposium on Hydraulic Machinery and Systems*, Montreal, Paper No. 17.

[18] Nishi, M., 1984, "Surging Characteristics of Conical and Elbow Type Draft Tubes," *Proceedings of the 12th IAHR Symposium on Hydraulic Machinery and Systems*, Stirling, pp. 272–283.

[19] Nishi, M., 1986, "Effect of Draft Tube Shape on the Characteristics of Pressure Surge and Swirl Flow," *Proceedings of the IAHR Symposium on Hydraulic Machinery and Systems*, Montréal, Paper No. 7.

[20] Arpe, J., 2003, "Analyse du Champ de Pression Pariétale d'un Diffuseur coudé de Turbine Francis," Ph.D. thesis, EPFL-Ecole Polytechnique Fédérale de Lausanne, Lausanne.

[21] Fischer, R. K., Palde, U., and Ulith, P., 1980, "Comparison of Draft Tube Surging of Homologous Scale Models and Prototype Francis Turbines," *Proceedings of the 10th IAHR Symposium on Hydraulic Machinery and Systems*, Tokyo, pp. 541–556.

[22] Dörfler, P., 1994 "Observation of Pressure Pulsations on a Francis Model Turbine With High Specific Speed," Int. J. Hydropow. Dams, **1**, pp. 21–26.

[23] Koutnik, J., Krüger, K., Pochyly, F., Rudolf, P., and Haban, V., 2006, "On Cavitating Vortex Rope Form Stability During Francis Turbine Part Load Operation," *Proceedings of the 1st Meeting of the IAHR International Working Group on Cavitation and Dynamic Problems in Hydraulic Machinery and Systems*, Barcelona.

[24] Ciocan, G., Iliescu, M. S., Vu, T. C., Nennemann, B., and François Avellan, F., 2007, "Experimental Study and Numerical Simulation of the FLINDT Draft Tube Rotating Vortex," ASME J. Fluids Eng., **129**, pp. 146–158.

[25] Avellan, F., 2000, "Flow Investigation in a Francis Draft Tube: The FLINDT Project," *Proceedings of 20th IAHR Symposium on Hydraulic Machinery and Systems*, Charlotte, NC.

[26] International Electrotechnique Commission, 1999, "IEC 60913 Standard Hydraulic Turbines, Storage Pumps and Pump-Turbines-Model Acceptance Tests," International Electrotechnical Commission, Geneva.

[27] Whitham, G. B., 1974, *Linear and Nonlinear Waves*, Wiley, New York.

[28] Wallis, G. B., 1969, *One-Dimensional Two-Phase Flow*, McGraw-Hill, New York.

[29] Streeter, V. L., and Wylie, E. B., 1993, *Fluid Transients in Systems*, Prentice Hall, Englewood Cliffs, NJ.

[30] Couston, M., and Philibert, R., 1998, "Partial Load Modelling of Gaseous Francis Turbine Rope," *Proceedings of the III Conference on Modelling, Testing and Monitoring for Hydro Power Plants*, Aix en Provence, Oct. 5–7, pp. 525–533.

[31] Nicolet, C., and Arpe, J., and Avellan, F., 2004, "Identification and Modeling of Pressure Fluctuations of a Francis Turbine Scale Model at Part Load Operation," *Proceedings of the 22nd IAHR Symposium on Hydraulic Machinery and Systems*, Stockholm, Sweden, Jun. 29–Jul. 2.

Impact of Orifice Length/Diameter Ratio on 90 deg Sharp-Edge Orifice Flow With Manifold Passage Cross Flow

W. H. Nurick
e-mail: wnurick@verizon.net

T. Ohanian

Science and Technology Applications LLC (STA),
Moorpark, CA 93021

D. G. Talley
Air Force Research Laboratory,
Edwards Air Force Base,
AFRL/PRSA,
10 East Saturn Boulevard,
Edwards AFB, CA 93524-7660

P. A. Strakey
Energy Systems Dynamics Division,
National Energy Technology Laboratory,
Morgantown, WV 26505

The available information describing the various stages of flow conditions that occur as the flow transitions from noncavitation to cavitation (turbulent flow), supercavitation, and finally separation in sharp-edge 90 deg orifices is extensive. However, although sharp-edge orifices in cross flow represent a significant number of injection schemes inherent in many applications, data for this configuration are sparse or nonexistent. This study is intended to increase the database and understanding of the driving variables affecting the flow in all of these conditions. Tests were carried out in a unique test facility capable of achieving large variations in back pressure, flowrate, and operating upstream pressure. The configuration and test ranges of this study includes orifice length/diameter ratios from 2 to 10, upstream pressures from 7.03 kg/cm^2 to 105.1 kg/cm^2, orifice/manifold area ratio of 0.028 to 0.082, and manifold cross flow velocity of from 410 cm/s to 1830 cm/s. The results for these small area ratio configurations support two different first order models, one for cavitation and the other noncavitation both in turbulent flow. Under cavitation conditions the discharge coefficient is related to the contraction coefficient and the cavitation parameter to the 1/2 power. In the noncavitation flow regime the head loss is related to the loss coefficient and the dynamic pressure at the orifice exit. Both the head loss and contraction coefficient were found to be a strong function of the ratio of manifold/orifice exit velocity. Equations are provided defining the relationships that allow determination of the contraction coefficient, discharge coefficient, and head loss between the contraction coefficient, as well as the loss coefficient and operating conditions. Cavitation parameter values for cavitation inception, cavitation, and supercavitation are also provided. The potential flow theory was shown to predict the contraction coefficient when upstream (manifold to vena-contracta) losses are minimal.

[DOI: 10.1115/1.3155959]

1 Introduction

The discharge of a fluid from a circular orifice is a fundamental problem in fluid mechanics. In the classical treatment [1] the upstream manifold is in-line with the orifice such that, in the one-dimensional approximation, the flow is unidirectional. In addition, the cross-sectional area of the upstream reservoir is typically assumed to be much larger than the area of the orifice so that velocities in the reservoir are ignored. However, in many applications, such as in diesel injectors [2], commercial process pipe configurations [3], and rocket engines [4], the upstream manifold or sac may be required to supply more than one orifice and/or have fluid turning to enter an injection orifice or flow splitting pipe configuration. In these types of applications the flow can no longer be considered unidirectional or one-dimensional. In addition, with the introduction of cross flow velocities in the manifolds relative to the redirected flow, the upstream velocity can no longer be ignored and the flow can no longer be considered axisymmetric. Under these conditions the impact on the vena-contracta must be taken into consideration in defining the overall energy balance of the system, as well as where in the system the losses occur.

Previous studies have shown that the effect of the cross flow on the discharge characteristics can be significant [3,5–8]. Most recently Strakey and Talley [9] studied the effects of orifice length-to-diameter (L/D) and cross flow upstream of 90 deg sharp-edge orifices and also found the effects of the cross flow to be large. They suggested a model for the effects of L/D and cross flow on the discharge coefficient of the orifice, which showed some success in being able to represent the data. However, they also reported an apparent underprediction of orifice losses as L/D became shorter. In addition, only discharge coefficients were reported in that paper, whereas other quantities of interest, such as vena-contracta contraction ratios, were not reported. The objective of this paper is to introduce additional important details not previously reported and to present a more accurate and complete analysis. In a companion paper [10] the additional effects of orifice angle from 60 deg to 120 deg are introduced and analyzed.

2 Background

Depending on the configuration design and operating conditions flow through a sharp-edge orifice can be in the cavitation or noncavitation regime. Typically, at high downstream pressure an orifice will experience noncavitation (single phase) flow and as the back pressure is lowered eventually it will transition to cavitation (two-phase) at the orifice inlet. During this process there are various flow characteristics that are encountered. Sequentially, starting at the highest back pressure these are

1. noncavitation (single phase)
2. cavitation inception (bubble formation at orifice inlet)
3. cavitation (choked two-phase flow)

Contributed by the Fluids Engineering Division of ASME for publication in the Journal of Fluids Engineering. Manuscript received June 4, 2008; final manuscript received April 17, 2009; published online July 15, 2009. Assoc. Editor: Theodore Heindel.

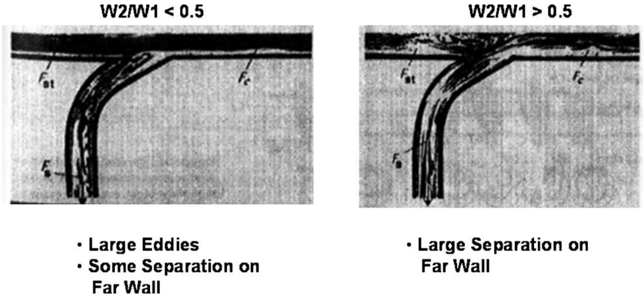

W2/W1 < 0.5

- Large Eddies
- Some Separation on Far Wall

W2/W1 > 0.5

- Large Separation on Far Wall

Fig. 1 Photograph documenting eddy formation and separation [3]

4. supercavitation (two-phase flow with attachment at orifice exit)

In addition separation and/or hydraulic flip can occur in both the cavitation or noncavitation regimes depending on the orifice L/D and operating conditions. These various flow characteristics have been extensively studied. The studies have included both; (1) nonvisual studies, where only the flow and pressure drop conditions are measured in addition to visual pictures of the exiting jet, and (2) visual (transparent material design) studies, where the processes occurring from the manifold/orifice entrance to the orifice exit are photographically documented.

In the noncavitation regime the acceleration forces are insufficient to reach vapor pressure in the entry region of the sharp-edge orifice. Nevertheless the accelerating fluid in the core separates from the sharp-edge entrance producing a fluid recirculation region between the separation and the reattachment point. The minimum static pressure occurs at the vena-contracta. As the acceleration forces decrease, the core flow area increases and, if sufficient orifice length is available, reattachment occurs. After reattachment the orifice pressure then decreases at a rate defined primarily by turbulent and friction losses such that the exit pressure matches that of the back pressure.

The numbers of studies relating to orifice discharge coefficient from orifices without cross flow are of course extensive (e.g., Refs. [11–13]). However, the number of studies related to orifices in cross flow is extremely limited. The most applicable is that of Idelchik [3] that covers a wide range of configurations with cross flow and provides loss coefficient correlations over the range of 15–90 deg orifice angles for the identical configurations of this study. The Idelchik correlations show that the loss coefficient is a function of both the turning angle and velocity ratio. Of particular interest is the photographic evidence; Fig. 1 shows the impact of the cross flow at the entrance to the formation of orifice eddies. Idelchik states for orifice/manifold flowrate ratio $(W_2/W_1) < 0.5$, large eddies are formed that are much greater than the turning flow, and large positive pressure gradients result in partial separation from the wall. He also stated that these conditions result in large total pressure losses. For $W_2/W_1 > 0.5$ the flow separates more vigorously from the outer wall resulting in an increase in losses in the manifold exit. This suggests that the eddy formation is related to the stagnation streamlines impacting the downstream wall. While Idelchik includes a factor to account for the manifold/orifice dimension ratio (i.e., diameter or width), there is no term to account for the impact of L/D.

Nurick and McHale [5] studied both circular and noncircular orifices with a cross flow of a 90 deg orifice and L/D from 2 to 6. Although the study was limited in objectives pertinent to this study, their results did show the quantitative impact of velocity ratio on loss coefficient, as well as the qualitative impact on the exiting jet characteristics. Specifically they found that the jet quality significantly deteriorates as the flowrate ratio decreases, and that as the L/D increases the jet becomes less bushy (although still unacceptably incoherent for the application of that study).

It is well understood that as the back pressure of a fluid entering a sharp-edge contraction is lowered, eventually the acceleration forces at the orifice entrance will lower the static pressure to the point where the onset of cavitation (two-phase flow) occurs. This is designated as cavitation inception. At this condition vapor bubbles are observed forming in the boundary layer [14,15], which quickly collapse as they are transported downstream. Koivula [15] noted that at the inception of cavitation the formation and collapse of the bubbles result in both a pressure oscillation frequency and overpressure. He found frequencies of 8 kHz at inception of cavitation but low overpressure fluctuations. The low overpressure is thought to be due to the limited number and size of vapor bubbles. In addition, the flowrate varies in the inception of cavitation zone and the discharge coefficient (C_d) starts to decrease from the single phase noncavitation regime value.

Continuing to lower the back pressure results in increased bubble formation and bubble coalescence that eventually forms a complete vapor cavity. At this point the flowrate becomes insensitive to downstream pressure [16,17]. This condition is defined as cavitation (i.e., constant contraction coefficient and choked flow). Once the cavitation condition is reached, the orifice cavity remains at the vapor pressure until, as the flow continues to move downstream, the acceleration forces diminish sufficiently for reattachment and full orifice flow. As the back pressure is lowered further the vapor cavity starts to lengthen [16,17], until it quickly increases to encompass the entire orifice length. When the cavity encompasses the entire orifice this condition is termed supercavitation. According to Chaves et al. [14] this occurs when the cavity extends past the exit of the nozzle, but the orifice does not experience separation and the spreading jet is surrounded by a vapor cloud. Chaves also noted that supercavitation is accompanied by a dramatic increase in the spray angle produced by the nozzle. Visual observations [14,18,19] of cavitation flows in nozzles have, in addition, shown a transient behavior caused by quasiperiodical re-entrant jet motion in the vena-contracta region, and random collapse of the cavitating bubbles at the nozzle exit. Koivula's results [15] in this regime suggest that, due to the implosion of vapor in the cavity, which produces shock waves, the frequency of oscillations decrease from 8 kHz at inception of cavitation to ~900 Hz at supercavitation, and the overpressure increases significantly. Since the flowrate is constant in this regime the increased energy loss is likely due to changes in the recovery process rather than manifold/orifice entrance impacts. Further lowering the back pressure results in the C_d experiencing either a dramatic step decrease followed by more gradual lowering (as the back pressure is further lowered) until the minimum is reached or complete separation occurs allowing the back pressure to surround the jet from the orifice exit to the vena-contracta.

The most significant efforts in the last 5–8 years in cavitation flow have been in diesel fuel injectors [14,20–25] and macro- [15,19] and micro-orifice [16,26–28] in-line and cross flow orifice configurations. These studies have shown that the flow characteristics are strongly dependent on the fluid feeder/orifice design and operating condition, which can significantly impact the resulting jet characteristics.

One objective of our study is concerned with the impact of flow conditions on the above described cavitation processes from manifold/orifice configurations with manifold cross flow that must turn to enter a 90 deg sharp-edge orifice. A search of the available literature related to this type of configuration where cavitation was studied reveals only a limited number of relevant publications. The most relevant is that of Ganippa et al. [20], who noted that for an orifice design, where the total manifold flow turns 90 deg to enter an orifice, it experiences nonaxisymmetric behavior in the generation of vapor bubbles at the inception of cavitation that occurs on the downstream side (see Fig. 2) of the entry at the corner of the orifice entrance. Typical separation and vapor formation on the upstream side of the orifice entrance are similar to that of in-line orifices. Furthermore, as the flow progresses to

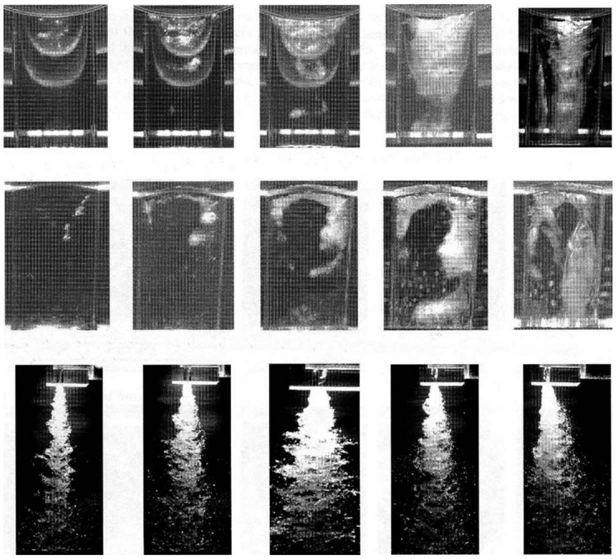

Fig. 2 Photographic documentation of bubble formation and jet behavior [20]

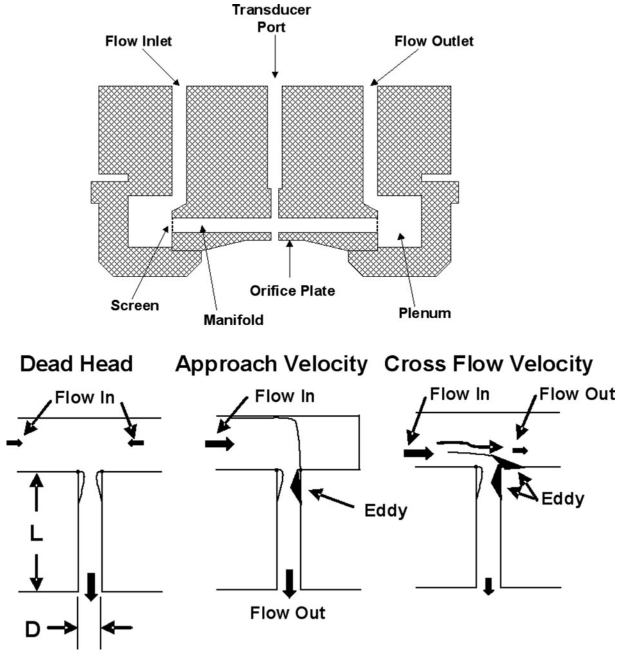

Fig. 3 Manifold/orifice design and flow configurations evaluated

cavitation (i.e., choked flow), the bubble size grows more significantly on the downstream side of the orifice entrance until a vapor cavity is formed, which is continuous to the orifice exit, and the cavitation process remains nonaxisymmetric. In addition, as cavitation proceeds through the various stages, the exiting jet becomes bushy and breaks up at the exit. This breakup continues downstream with increasing spray spreading angle, as the cavitation process proceeds through its various stages. Unfortunately, Ganippa et al. did not provide specific flow condition measurements so that a relationship can be developed between orifice flow conditions and jet quality. The significance of the study of Ganippa et al. is that the cavitation characteristics at the manifold/orifice entrance are nonaxisymmetric, unlike that from in-line feeder/orifice configurations, and significantly impact the resulting jet characteristics. Furthermore note that the vapor cavity does not appear to be continuous around the entire diameter even at cavitation (upper photo set—front view, middle photo set—side view).

Strakey and Talley [9] provided some insight into the relationship between the flow conditions and discharge coefficient over a range of orifice length to diameter ratios for 90 deg sharp-edge orifices in cross flow. This study covered both the cavitation and noncavitation regime. They compared the discharge coefficient defined by a two-dimensional potential flow theory based model [29] with that determined from experimental data. They found that this model does provide excellent comparison with long orifice L/D; however, the comparison significantly deteriorates as orifice L/D decreases. The authors hypothesize that this disparity is likely due to the declining reattachment and recovery efficiency at the shorter orifice lengths, although no proof is provided.

We have extended the work of Strakey and Talley by examining model predictions of the contraction coefficient at cavitation and noncavitation flow conditions, as compared with the experimental data to determine the efficacy of the assumptions inherent in the potential flow model and conditions where it may apply. In addition, in order to cover the entire range of operation, the results are applied to the development of an independent relationship between both the contraction coefficient and loss coefficient with velocity ratio allowing direct prediction of system discharge coefficient under cavitating and noncavitating flow conditions.

3 Experimental Setup

The test facility has been documented in several published papers [9,10] and therefore the description will be limited only to that which is directly related to the present study. The reader is referred to the referenced papers for a more inclusive description.

3.1 Hardware Dimensional and Data Measurement Accuracy. The orifices are either pilot drilled and reamed or made by electrical discharge machining with a diameter tolerance of $+/-13$ μm and an inlet edge radius to orifice diameter ratio of less than 0.003, ensuring a sharp-edged inlet. Chamber pressure, orifice pressure drop, and inlet and outlet flowrates are recorded by a 12 bit analog to digital conversion board, and data are stored on a personal computer. Experiments are typically conducted by setting the fluid pressure and flowrates to a predetermined value, with the back (i.e., chamber) pressure being gradually increased, while the data acquisition system records flowrates and pressures. This allows for a large amount of data to be collected in a relatively short period of time. Orifice pressure drop and chamber gas pressure are measured within an accuracy of $+/-0.25\%$. Manifold velocities are held constant to within $+/-1.5\%$ during the experiment. Because of the difficulty associated with directly measuring the orifice flowrate inside the pressurized vessel, the orifice flowrate is measured by subtracting the manifold outlet flowrate from the manifold inlet flowrate.

The experimental error associated with the discharge coefficient measurement is limited by the accuracy of the flow meters, which is $+/-0.5\%$. This translates to an error on the discharge coefficient data of about $+/-0.5\%$ at the lowest manifold flowrates and highest orifice flowrates, to $+/-10\%$ at the lowest orifice flowrates and highest manifold flows. A typical error for the intermediate flowrates is on the order of $+/-4\%$.

3.2 Manifold/Orifice Design and Configurations Evaluated. Tests were conducted to distinguish between flow that (1) entered a manifold from both ends and then contracted to enter a 90 deg sharp-edge orifice (dead head), (2) entered the manifold from one end and all of the flow contracted to enter a 90 deg sharp-edge orifice (approach velocity), and (3) entered the manifold from one end and only part of the flow contracted to enter a 90 deg sharp-edge orifice and the remainder exited through the manifold exit (cross flow velocity). A sketch of the manifold/orifice design and configurations evaluated are shown in Fig. 3.

The manifold inlet static pressure is measured using the transducer port directly above the orifice inlet, the back pressure is measured in the chamber, and manifold flowrates-in-and-out were measured using cavitating venturi. For the cross flow configuration, the orifice flowrate was determined by the difference between the measured manifold inlet and outlet flowrate.

The manifold is square with a dimension of 6.25 mm, and the orifice L/D studied was from 1 to 10. Since at L/D of 1 only separation occurred, it is not included in this paper. Two orifice diameters were evaluated; 1.19 mm and 1.99 mm.

3.2.1 Dead Head Configuration. In the dead head (DH) configuration the manifold flow is routed through both the manifold flow inlet and flow outlet (depicted in Fig. 3), so that the flow entering the orifice is the sum of the two flowrates. For this configuration it is important that the flows are balanced to ensure symmetry at the orifice entrance. In practice this is difficult as only a slight variation in flowrate or orifice entrance irregularities can cause nonaxisymmetric conditions at the orifice inlet. Care was taken to ensure balanced flow, but the ability to achieve this is of course is governed by facility measurement/control limitations. Due to this sensitivity the dead head configuration is not a recommended configuration.

At balanced input conditions the two flows meet, turn 90 deg, and contract to enter the orifice. The contraction results in acceleration of the fluid at the orifice entrance producing either a vapor pocket or a recirculation eddy depending on the upstream and downstream pressure conditions. This leads to the formation of a minimum flow area at the vena-contracta, which then quickly expands downstream. For all configurations the downstream flow characteristics depend not only on the upstream and downstream pressure conditions but on the orifice L/D ratio.

In all tests test chamber back pressure was initially set at a minimum values of $\sim 3.5\ \text{kg/cm}^2$ and the upstream pressure set at the desired value ($7.03\ \text{kg/cm}^2$, $35.2\ \text{kg/cm}^2$, $70.2\ \text{kg/cm}^2$, or $105.5\ \text{kg/cm}^2$). Then while the upstream pressure was maintained constant, the back pressure was systematically increased to a value near the upstream pressure. This resulted in the manifold inlet flowrate decreasing to meet the overall pressure drop requirements. For these tests since all flow exited only through the orifice the manifold/orifice velocity ratio was constant.

3.2.2 Approach Velocity Configuration. In this configuration the manifold inlet flow is routed through the manifold flow inlet, and the manifold flow outlet is closed so that all the flow can only exit through the orifice. All of the manifold flow then turns 90 deg from one direction and contracts to enter the orifice. For this configuration the turning is not axisymmetric. The entering flow separates from the near wall (left side) while the flow stagnates at the far wall (right side). This produces an eddy flow at the far wall; Fig. 1. Again depending on the upstream and downstream pressures, the eddy can be either vapor or liquid. In this configuration, where no physical wall exists, the flow turning should be smooth and well controlled. The test sequence for the approach velocity (AV) was identical to the dead head configuration, and the velocity ratio was also constant.

3.2.3 Cross Flow Velocity Configuration. The inlet manifold flowrate for the cross flow velocity (CFV) configuration is identical to the approach velocity configuration. However, in the cross flow velocity configuration, the flow entering the manifold exits through both the manifold outlet and the orifice. After the manifold inlet flowrate is set, the orifice flowrate is determined by the orifice exit pressure in the chamber. In this configuration the orifice inlet contraction and eddy formation processes are dependent on the ratio of manifold inlet to orifice outlet flow, and the turning may not be smooth at all flowrate ratios. As with the other configurations, depending on the upstream and downstream pressures, the eddy can be either vapor or liquid.

The test sequence for the cross flow velocity configuration differed from the other configurations in that the manifold inlet flowrate was held at a constant value for a test sequence and then changed for subsequent test sequences. Therefore, for all test sequences the ratio of the manifold/orifice flowrate ratio varied while the manifold inlet velocity was constant.

4 Analysis Approach

It is instructive to first establish the basic flow equations describing the various configurations studied. These relationships are the basis for reduction in data and understanding of the influencing variables.

4.1 Cavitation Turbulent Flow. The definition of cavitation number utilized by Knapp et al. [17] in 1970 did not include any losses incurred between the entrance and the orifice exit. In 1976 Nurick [16] introduced a different cavitation parameter defined in Eq. (1) that takes into account all the dynamic variables that impact the processes from the manifold to the orifice exit. This definition of the cavitation parameter is utilized in this study

$$K_{\text{cav}} = \frac{P_1 - P_v}{P_1 - P_2} \tag{1}$$

For all three configurations considered in the present study the manifold velocity (V_1) cannot be assumed to be negligible and therefore it is included in the determination of C_d. The resulting expression for the discharge coefficient is

$$C_d = \frac{V_2}{[(2g/\rho)(P_1 - P_2) + V_1^2]^{1/2}} \tag{2}$$

And finally, the contraction coefficient is defined as

$$C_c \equiv \frac{A_c}{A_2} \tag{3}$$

Using the continuity equation, the contraction coefficient is also

$$C_c = \frac{V_2}{V_c} \tag{4}$$

These equations are valid for all configurations.

4.1.1 Dead Head Configuration. For this configuration since all manifold flow from both inlets enter the orifice, the relationship between the manifold and the orifice velocity is

$$\frac{V_1}{V_2} = \frac{A_2}{2A_1} \tag{5}$$

Assuming that the head losses are small between the manifold and the vena-contracta the Bernoulli equation can be written as:

$$P_1 - P_v = \frac{\rho}{2g}(V_c^2 - V_1^2) \tag{6}$$

Then using Eqs. (1), (3), (4), and (6), Eq. (2) becomes

$$C_d = \frac{C_c K_{\text{cav}}^{1/2}}{\left[1 + \left(\frac{A_2}{2A_1}\right)^2 C_c^2 (K_{\text{cav}} - 1)\right]^{1/2}} \tag{7}$$

If the area ratio term in the denominator is small in relation to 1 then Eq. (5) can be reduced to

$$C_d = C_c \sqrt{K_{\text{cav}}} \tag{8}$$

Finally, Eq. (7) is rearranged such that once the discharge coefficient is determined using Eq. (2), the contraction coefficient can then be calculated

$$C_c = \frac{1}{\left[\left(\frac{K_{\text{cav}}}{C_d^2}\right) - \left(\frac{A_2}{2A_1}\right)^2 (K_{\text{cav}} - 1)\right]^{1/2}} \tag{9}$$

In the analysis of the test data Eq. (2) is used to define C_d and Eq. (9) for C_c.

4.1.2 Approach Velocity Configuration. In this configuration all the flow turns 90 deg from one direction. These turning losses can be significant if the flow stagnates against a wall before turning into the orifice (i.e., for 90 deg bends up to 0.75 times the kinetic head [30]). In approach velocity configuration, where no wall exists, the flow does not stagnate but smoothly turns and flows into the orifice. This results in a significant reduction in the turning losses (i.e., similar to a smooth bend [31]). Since all flow entering the orifice is fed from a single manifold inlet, the relationship between the manifold inlet/orifice velocity ratio and area ratio is

$$\frac{V_1}{V_2} = \frac{A_2}{A_1} \tag{10}$$

In the same manner as for the dead head configuration, the resulting relationship for discharge coefficient is

$$C_d = \frac{C_c K_{\text{cav}}^{1/2}}{\left[1 + \left(\frac{A_2}{A_1}\right)^2 C_c^2 (K_{\text{cav}} - 1)\right]^{1/2}} \tag{11}$$

Note that if the second term in the denominator is small relative to 1, then Eq. (11) reverts to Eq. (8).

Equation (11) can also be rearranged in order to calculate the contraction coefficient once the discharge coefficient, using the experimental data, is determined from Eq. (2). The resulting relationship is

$$C_c = \frac{1}{\left[\left(\frac{K_{\text{cav}}}{C_d^2}\right) - \left(\frac{A_2}{A_1}\right)^2 (K_{\text{cav}} - 1)\right]^{1/2}} \tag{12}$$

4.1.3 Cross Flow Velocity Configuration. For conditions where the flow entering the manifold exits by two paths, (i.e., the manifold exit and the orifice) and the total pressure in the manifold is constant, the discharge coefficient can still be defined by Eq. (2). For this configuration the V_1/V_2 relationship is

$$\frac{V_1}{V_2} = \left(\frac{W_1}{W_2}\right)\left(\frac{A_2}{A_1}\right) \tag{13}$$

The resulting discharge coefficient and contraction coefficient are defined as

$$C_d = \frac{C_c K_{\text{cav}}^{1/2}}{\left[1 + \left(\frac{V_1}{V_2}\right)^2 C_c^2 (K_{\text{cav}} - 1)\right]^{1/2}} \tag{14}$$

As for the other two configurations, if the second term in the denominator is small relative to 1, Eq. (14) reduces to Eq. (8).

Equation (14) is then converted to

$$C_c = \frac{1}{\left[\frac{K_{\text{cav}}}{C_d^2} - \left(\frac{V_1}{V_2}\right)^2 (K_{\text{cav}} - 1)\right]^{1/2}} \tag{15}$$

Originally, consideration was given to the head loss term in the Bernoulli equation, since the cavity formation and turning could be much more turbulent than for the DH and AV configurations. However, as discussed later, plots of C_c versus K_{cav} indicate that the head loss term is small and does not materially impact the value of C_c. This would not be the case for the noncavitation flow regime.

4.2 Noncavitation Turbulent Flow. The orifice discharge coefficient in turbulent noncavitation flow from sharp-edge orifices has traditionally been correlated in terms of C_d versus the Reynolds number. These correlations have been developed for flow entering the orifice with no cross flow and very low entrance velocity. For configurations where the flow must bend to enter the orifice or to contract, researchers have typically chosen to correlate head loss (rather than C_d) with either the manifold or orifice dynamic pressure. The correlating constant is termed the loss coefficient (K_L). The pressure head loss in terms of the orifice kinetic energy is defined by

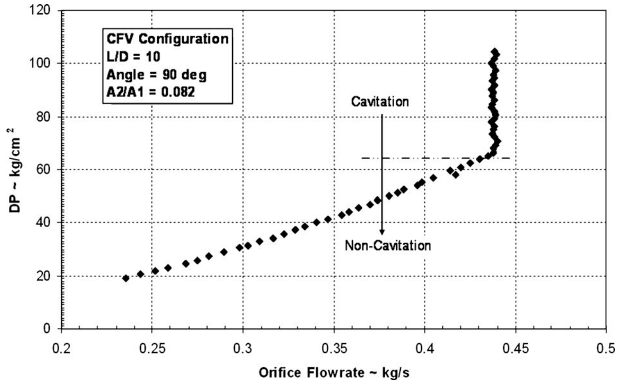

Fig. 4 Illustration of constant flowrate in the cavitation zone

$$H_L = K_L \frac{\rho}{2g} V_2^2 \tag{16}$$

The head loss can independently be determined using the Bernoulli equation:

$$H_L = (P_1 - P_2) + \frac{\rho}{2g}(V_1^2 - V_2^2) \tag{17}$$

Equation (17) is used to calculate the total head loss using the experimental measurements, and the loss coefficient is determined by the rearrangement of Eq. (16). Inserting the head loss from Eq. (16) into Eq. (17) and rearranging results in

$$K_L = \frac{\Delta P}{KE_2} + \left(\frac{V_1}{V_2}\right)^2 - 1 \tag{18}$$

where

$$KE_2 = \frac{\rho V_2^2}{2g} \tag{19}$$

The last two terms in Eq. (18) represent the change in kinetic energy and are recoverable energy terms, while the static pressure term represents all total pressure losses.

It is interesting to compare this with Idelchik [3] for the same configuration, where his expression is anchored to the manifold kinetic energy

$$K_{L1} = 1 + \left(\frac{V_2}{V_1}\right)^2 \tag{20}$$

For these two expressions to be similar, there must be a relationship between the pressure drop/kinetic energy and velocity ratio. This requirement is investigated in Sec. 5.

In all configurations the relationship between the discharge coefficient and the loss coefficient is

$$C_d = \frac{1}{\sqrt{K_L + 1}} \tag{21}$$

5 Results and Discussion

5.1 Cavitation Regime

5.1.1 Flow Characteristics. Cavitation is defined as the value of the cavitation parameter, where the flowrate becomes a constant value. This is commonly termed choked flow. Choked flow is defined by analysis of the flowrate versus pressure drop. A typical flowrate curve is shown in Fig. 4 to illustrate the analysis process.

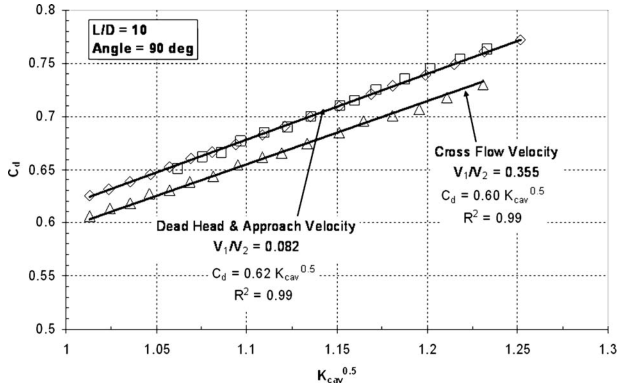

Fig. 5 Illustration of linear relationship between C_c and $K_{cav}^{0.5}$

The test data were first analyzed to determine the relationship between the discharge coefficient (C_d) and the cavitation parameter (K_{cav}). The discharge coefficient was calculated from the test data using Eq. (2) and the cavitation parameter, Eq. (1). In Fig. 5 all three configurations operating in cavitation are represented, and for each configuration the tests were fit with a straight line going through the origin. The resulting R^2 values were 0.99+, which is an excellent fit and supports a first order relationship for small area ratios (Eq. (8)). This relationship was also found for small area ratio in-line orifices [16]. The slopes of the curves in Fig. 5 are related to the velocity ratio, as indicated by the identical data for the DH and AV that have the same velocity ratios, while it is a different value for the CFV configuration.

The results of the analysis for all configurations and orifice L/Ds are summarized in Table 1. As noted in Table 1, orifice L/D did impact the cavitation parameter where cavitation (i.e., choked flow) occurred.

The findings of the analysis show that both L/D and orifice diameter impacts the initiation of choked flow. Increasing L/D from 5 to 10 lowered the cavitation parameter between 12% and 17% depending on orifice diameter. Sato and Saito [19] for in-line orifices of 22 mm diameter found that cavitation occurred at a cavitation parameter of 1.8 for L/D between 2.2 and 4.4. This would be compared with the approximate 1.76, L/D of 5, in this study. Mishra and Peles published a value of 1.28 for micro-orifices, which suggests that at least below an area ratio of 0.082, the orifice diameter impacts the onset of choked flow. It should be noted that cavitation inception (i.e., defined by the initial deviation from classical flow to choked flow; Fig. 4), was found to occur at $K_{\text{cav}} \sim 1.8$ for all configurations evaluated.

The data were also analyzed to determine the orifice discharge coefficient characteristics in choked flow cavitation with cross flow. For each flow configuration Eq. (2) was utilized to determine the discharge coefficient using the experimental data. When the data were plotted as suggested by the appropriate discharge coefficient equation (i.e., Equation (14) for CFV), it was clear that a linear relationship existed between C_d and $K_{\text{cav}}^{0.5}$, where the slope of the relationship is C_c. In addition it was also determined that the contraction coefficient, C_c, varied with velocity ratio. A correlation was then sought that related the contraction coefficient to the cross flow velocity/orifice flow velocity. This relationship is then used to define C_c for any flow condition in the cavitation regime and then substituted into the appropriate expression for C_d. For the other two flow configurations the velocity ratio is fixed for a given area ratio and therefore C_c is only a function of the area ratio, as defined for each configuration. The results for the DH and AV configurations are provided in Table 2.

Table 1 Impact of L/D and orifice diameter on cavitation parameter

Flow characteristic	L/D	A_2/A_1	K_{cav}
Cavitation	5	0.082	1.74
		0.028	1.77
	10	0.082	1.52
		0.028	1.59

Table 2 Contraction coefficient for DH and AV configurations

		C_c	
L/D	A_2/A_1	DH	AV
2	0.082	-	0.55
	0.028	-	-
5	0.082	0.59	0.59
	0.028	0.58	0.59
10	0.082	0.61	0.62
	0.028	0.60	0.60

While there are slight differences in the values of contraction coefficient for a given L/D, the differences are within experimental error. The mean value for the contraction coefficient in both the DH and AV configuration is 0.59. For in-line contractions the predicted values for the two area ratios tested would be near identical so it is expected that no difference would be measured. In-line contraction coefficient for this area ratio is 0.61.

As indicated in Fig. 5, the relationship between C_d and C_c is still linear even with cross flow velocity; however, it was found that the slope varied with velocity ratio. For the CFV configuration Eq. (15) was utilized to calculate C_c from the experimental data, and the results are plotted in Fig. 6 for the L/D of 5 and Fig. 7 for the L/D of 10. For both L/Ds the variation in C_c for each area ratio is within the experimental error, so a best-fit was made including all the data for each L/D. The resulting correlations are shown in each figure and did not vary within the area ratio range of this study.

5.1.2 Potential Flow Model. The complete derivation of the potential flow model can be found in Ref. [30]. The potential flow model relies on the flow characteristics adhering to the requirement that all the losses must be downstream of the vena-contracta. Meeting this requirement can only be achieved if the turning, orifice entrance (eddy), and contraction losses are zero or for practical purposes minimal. To assess this requirement the experimental data for the CFV configuration, in the cavitation regime, were utilized to define the fraction of the total loss that occurred between the manifold and the vena-contracta. Application of the Bernoulli equation between the manifold and the orifice exit defines the overall head loss and application between the vena-

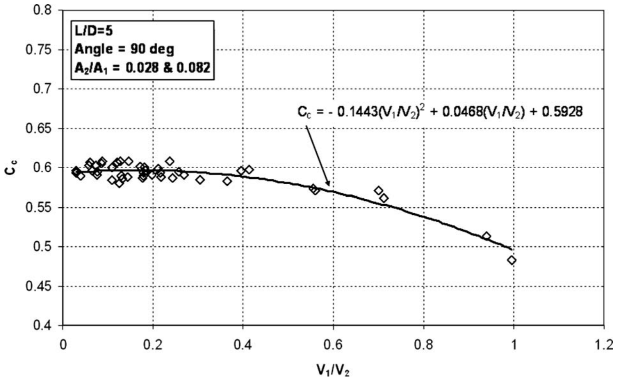

Fig. 6 Impact of velocity ratio on contraction coefficient; L/D=5

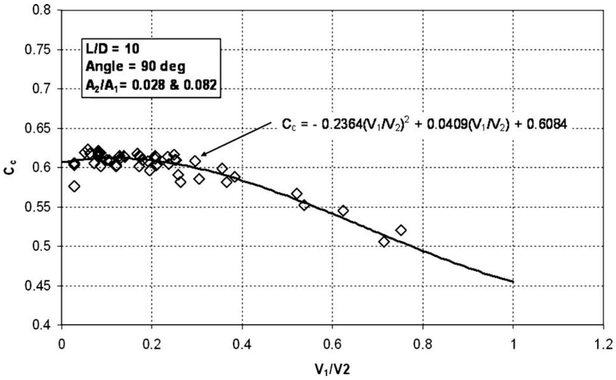

Fig. 7 Impact of velocity ratio on contraction coefficient; *L*/*D*=10

contracta, and the orifice exit defines the losses downstream of the vena-contracta. The ratio of these two loss calculations defines the fraction of overall loss downstream of the vena-contracta. One minus this fraction defines the upstream loss fraction. These losses are defined in Eq. (22)–(24). Note that the pressure at the vena-contracta is equal to the fluid vapor. All independent variables are defined from the experimental data

$$HL_{1-2} = P_1 - P_2 + \frac{\rho}{2g}(V_1^2 - V_2^2) \tag{22}$$

$$HL_{c-2} = P_c - P_2 + \frac{\rho}{2g}(V_c^2 - V_2^2) \tag{23}$$

$$\frac{HL_{1-c}}{HL_{1-2}} = 1 - \frac{HL_{c-2}}{HL_{1-2}} \tag{24}$$

The results for the L/D of 10, plotted in terms of the upstream loss (i.e., Equation (24)) are presented in Fig. 8 and shows that all of the loss is downstream of the vena-contracta (i.e., ~99% of the total loss). The variation within each test (~constant V_1/V_2) is small, suggesting that the flow is extremely well behaved.

This is contrasted with the shorter L/D of 5, where our data show that as the upstream pressure increases the upstream loss decreases. The exact reason for this is unknown at this time; however, it is most probably the result of the both the eddy generation at the orifice entrance and the expansion-reattachment process. The expansion-reattachment process impact on C_d is defined in Eq. (8) and, as noted in Fig. 9, is indicated by the spread in the loss at constant velocity ratio. Note that as the velocity ratio decreases, the spread decreases indicating that the reattachment process is becoming more efficient. When the reattachment is well behaved, the energy loss is identical to the L/D of 10 results (i.e., 105.5 kg/cm^2, Fig. 10).

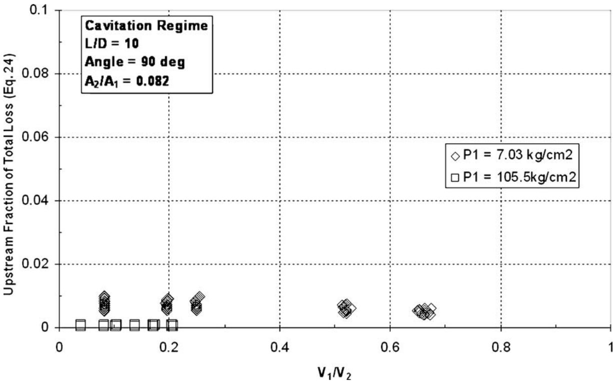

Fig. 8 Impact of velocity ratio on the fraction of total energy loss–*L*/*D*=10

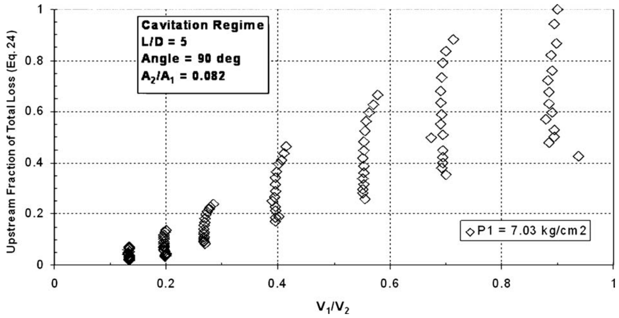

Fig. 9 Impact of velocity ratio on the fraction of total energy loss–*L*/*D*=5

Based on the above results the potential flow theory model was applied to the L/D of ten results and for the L/D of 5, only to the upstream pressure of 35.2 kg/cm^2 and 105.5 kg/cm^2 data, where upstream losses were minimal. The results are shown in Figs. 11 and 12 for L/D of 10 and 5 and both orifice diameters. The model predictions are considered excellent, and the spread is certainly within measurement error.

These comparisons are a verification of the potential flow theory for nonaxisymmetric flows in the cavitation regime when the upstream losses are minimal. The potential flow theory is not applied to the noncavitation results since the vena-contracta pressure varies [16] with orifice velocity, and no physical measurements were attempted in the cavity region.

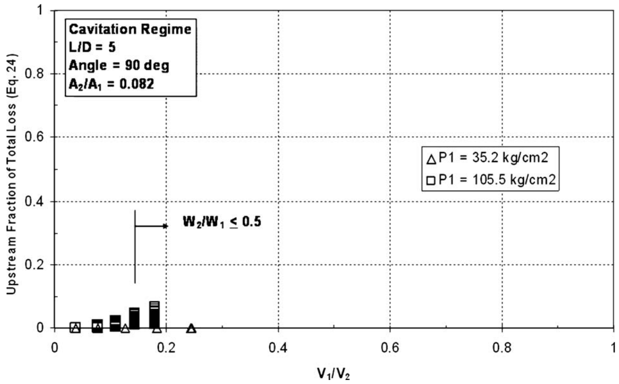

Fig. 10 Impact of velocity ratio on the fraction of total energy loss–*L*/*D*=5

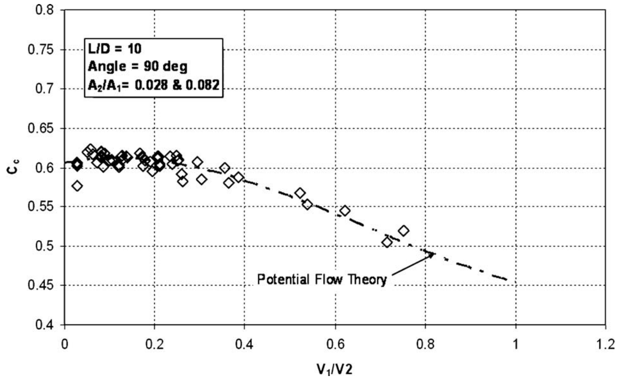

Fig. 11 Potential flow model C_c prediction versus experimental C_c–*L*/*D*=10

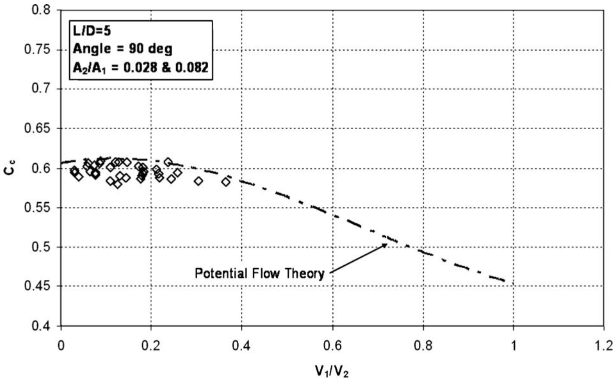

Fig. 12 Potential flow model C_c prediction versus experimental C_c–L/D=5

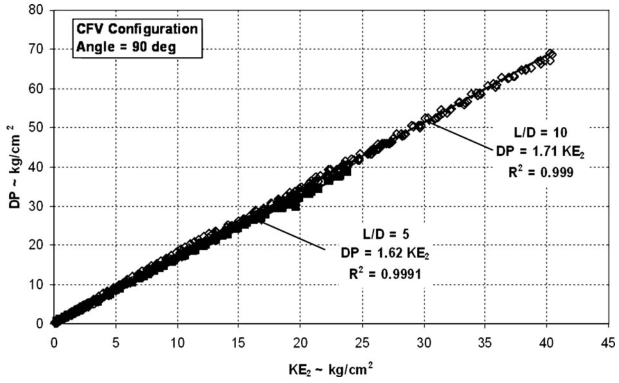

Fig. 14 Pressure drop versus orifice kinetic energy (all three configurations)

5.2 Noncavitation Regime Results

5.2.1 Flow Characteristics. The noncavitation data for the CFV configuration was first assessed to determine the validity of the linear relationship defined in Eq. (16). Typical test results are shown in Fig. 13 that illustrates the first order relationship between the head loss and the orifice exit kinetic energy. For this configuration, while the relationship is linear, the intercept is not zero and depends on the manifold cross velocity. The best-fit line is given simply to illustrate the linearity of the data. However, for the DH and AV configurations (not shown), all the flow enters the orifice, and therefore the velocity ratio is constant, and the intercept is at the origin.

The experimental data was analyzed to determine the relationship between the pressure drop and the orifice exit kinetic energy, which represents the loss term in Eq. (18). The results for the L/D of 10 and 5 are shown in Fig. 14, and for L/D of 2 in Fig. 15. The linearity of the data and the zero intercept confirms the validity of Eq. (16) for the CFV configuration. In addition, only the data where attachment occurred and where the data were not erratic were used in the correlations. Therefore application of the correlations assumes these conditions apply for any specific design and operating condition.

Substitution of the linear relationships shown in Fig. 14 into Eq. (18), for both L/Ds, results in the expressions

$$K_L = 0.71 + \left(\frac{V_1}{V_2}\right)^2, \quad L/D = 10 \tag{25}$$

$$K_L = 0.62 + \left(\frac{V_1}{V_2}\right)^2, \quad L/D = 5 \tag{26}$$

$$K_L = 0.57 + \left(\frac{V_1}{V_2}\right)^2, \quad L/D = 2 \tag{27}$$

A comparison of loss coefficient determined from the above equation and that defined from the experimental data is provided in Fig. 16. The predictive ability is well within the overall experimental measurement error.

5.2.2 Comparison With Ref. [3]. To be constant with Idelchik our data was converted to upstream conditions, and the resulting comparison is shown in Fig. 17. As expected the characteristic curve for both expressions are similar, however, Idelchik's expression results in a higher loss coefficient. Idelchik does not define the L/D for his correlation; however, it appears to be developed for industrial applications where L/D can be 20 or greater. This could account for the difference in loss coefficient.

6 Conclusions

The potential flow theory model provides excellent prediction of contraction coefficient for the 90 deg turning angle at L/D of 10, where the recovery process is completed before the orifice exit and the losses are downstream of the vena-contracta. In fact, at L/D of 10, ~99.5% of the total losses occur downstream of the vena-contracta. For L/D of 5 the model predictions are unsatisfactory except for a limited operating range, and use of the corre-

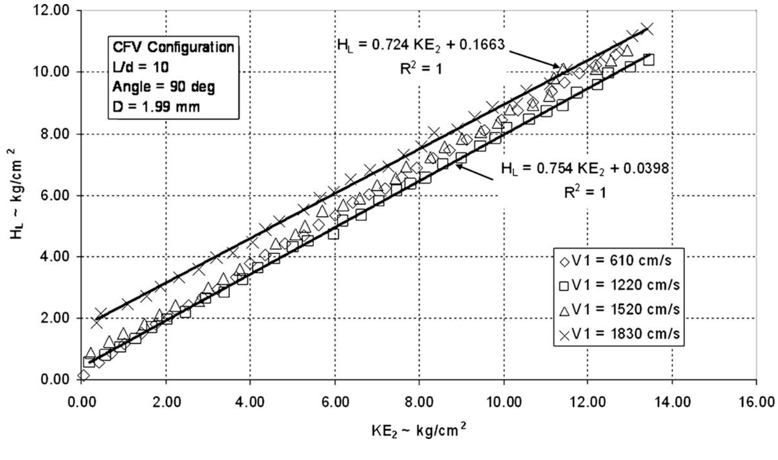

Fig. 13 Illustration of linear relationship between H_L and KE_2 at various manifold cross velocities

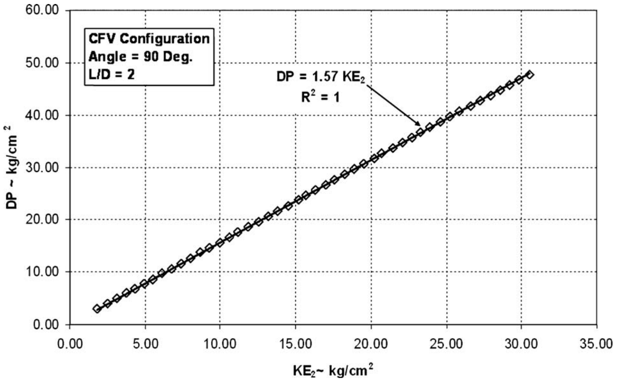

Fig. 15 Correlation of H_L coefficient for 90 deg sharp-edge orifice

lation developed to predict C_c is recommended. At L/D between 2 and 5 the upstream losses between the manifold and the vena-contracta can range from near 100% to 0% depending on the operating conditions.

The process characteristics as inferred from the various measurements provide some confirmation, as well as further insight into the interaction of flowrate and contraction coefficient in the cavitation regime and flowrate ratio on the loss coefficient in the noncavitation regime.

In the cavitation regime,

- Cavitation inception occurs at $K_{\text{cav}} \sim 1.8$.
- When cavitation is reached (i.e., choked flow), the measured flowrate and calculated C_c are found to be constant.
- Choked flow cavitation occurs at K_{cav} of between $\sim 1.75-1.8$.
- For the geometries evaluated the relationship between the discharge and contraction coefficients can be reduced to $C_d = C_c K_{\text{cav}}^{0.5}$.
- Within the cavitation regime, the slope defining C_c was found to depend only on the manifold/orifice velocity ratio.
- Orifice L/D impacts C_c, since it, in turn, impacts the recovery efficiency and friction, which is related to C_d.

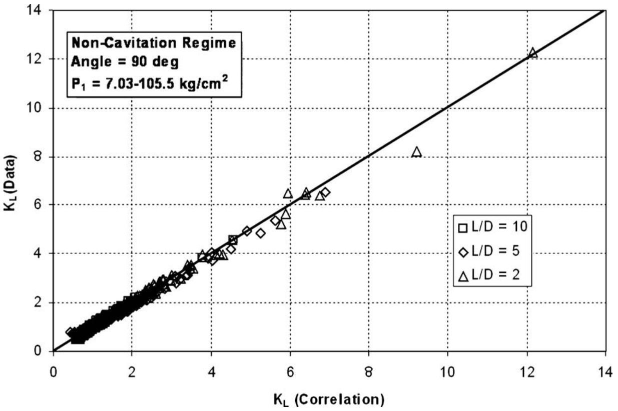

Fig. 16 Comparison of predicted versus data defined loss coefficient

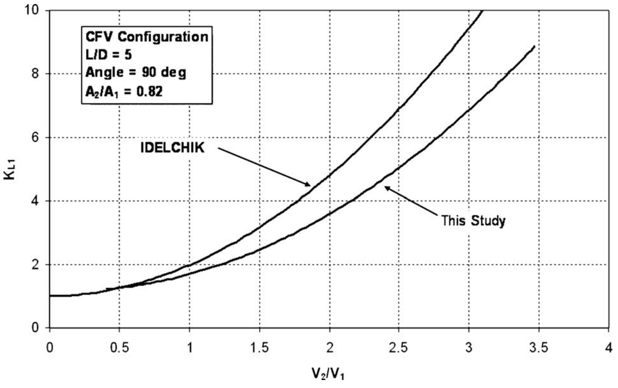

Fig. 17 Comparison of the results of this study with Idelchik correlation [3]

In the noncavitation regime,

- For the geometries evaluated the relationship between the head loss and loss coefficient was found to be consistent with other studies for in-line orifices, and turning flow; $H_L = K_L \times KE_2$.
- The value of K_L was found to be related to the manifold/orifice velocity ratio similar to that published by Idelchik.

Overall, the correlation relationships provide design engineers with the ability to more knowledgably predict flow regimes, as well as flow variables for determination of C_c, C_d, and K_L. The correlations presented for C_c and K_L should provide prediction of C_d within $\sim 10\%$.

Nomenclature

Symbols

A_1, A_2 = manifold and orifice area, mm^2
C_c = contraction coefficient at vena-contracta
C_d = discharge coefficient
D = orifice diameter, mm
DP, ΔP = pressure drop $(P_1 - P_2)$, g/cm^2
H_L = overall head loss using KE_2, g/cm^2
H_{Lc2} = head loss between vena-contracta and orifice exit, g/cm^2
K_L = loss coefficient based on KE_2
K_{L1} = loss coefficient based on KE_1
K_{cav} = cavitation parameter
KE_1 = manifold inlet kinetic energy, g/cm^2
KE_2 = orifice kinetic energy g/cm^2
L = orifice length, mm
P_1, P_2 = manifold and orifice pressure, g/cm^2
P_v = fluid vapor pressure, g/cm^2
V_1, V_2 = manifold and orifice velocity, cm/s
V_c = velocity at vena-contracta, cm/s
W_1, W_2 = manifold inlet and orifice flowrate, kg/s

Greek

ρ = liquid density, g/cm^3

Subscripts

1 = manifold
2 = orifice exit
c = at the vena-contracta

References

[1] White, F. M., 1986, *Fluid Mechanics*, 2nd ed., McGraw-Hill, New York, pp. 361–369.
[2] Arcoumanis, C., Gavaises, J. M., Nouri, J. M., Abdul-Wahab, E., and Horrocks, R. W., 1998, "Analysis of the Flow in the Nozzle of a Vertical Multi Hole Diesel Engine Injector," SAE Paper No. 980811.
[3] Idelchik, I. E., 2003, *Handbook of Hydraulic Resistance*, 3rd ed., Jaico.
[4] Gill, G. S., and Nurick, W. H., 1976, "Liquid Rocket Engine Injectors," NASA Report No. SP 8089.
[5] Nurick, W. H., and McHale, R. M., 1970, "Noncircular Orifice Holes and Advanced Fabrication Techniques for Liquid Rocket Injectors," Rocketdyne, Canoga Park, CA, Final Report No. NASA CR-108570.

[6] Northrup, R. P., 1951, "Flow Stability in Small Orifices," *Proceedings of the American Rocket Society*, ASME, New York, Nov. 30.

[7] Andrews, K. A., and Sabersky, R. H., 1990, "Flow Through an Orifice From a Transverse Stream," ASME J. Fluids Eng., **112**, pp. 524–526.

[8] Rohde, J. E., Richards, H. T., and Metger, G. W., 1969, "Discharge Coefficient for Thick Plate Orifices With Approach Flow Perpendicular and Inclined to the Orifice Axis," NASA Report No. TN D-5467, pp. 1–28.

[9] Strakey, P. A. and Talley, D. G., 1999, "The Effect of Manifold Cross-Flow on the Discharge Coefficient of Sharp-Edged Orifices," Atomization Sprays, **9**(1), pp. 51–68.

[10] Nurick, W. H., Ohanian, T., Talley, D. G., and Strakey, P. A., 2008, "The Impact of Manifold-to-Orifice Turning Angle on Sharp-Edge Orifice Flow Characteristics in Both Cavitation and Noncavitation Turbulent Flow Regimes," ASME J. Fluids Eng., **130**, p. 121102.

[11] Weisbach, J., 1855, *Die Experimental Hydraulik*, Englehardt, Frieburg.

[12] Lichtarowicz, A., Duggins, R., and Markland, E., 1965, "Discharge Coefficients for Incompressible Non-Cavitating Flow Through Long Orifices," J. Mech. Eng. Sci., **7**(7), pp. 210–219.

[13] 1976, *Flow of Fluids Through Valves, Fittings, and Pipe*, Crane Co., Stamford, CT.

[14] Chaves, H., Knapp, M., Kubitzek, A., Obermeier, F., and Schneider, T., 1955, "Experimental Study of Cavitation in the Nozzle Hole of Diesel Injectors Using Transparent Nozzles," SAE Paper No. 950290.

[15] Koivula, T., 2000, "On Cavitation in Fluid Power," *Proceedings of the First FPNI-PhD Symposium*, Hamburg, Germany, pp. 371–382.

[16] Nurick, W. H., 1976, "Orifice Cavitation and Its Effects on Spray Mixing," ASME J. Fluids Eng., **98**, pp. 681–687.

[17] Knapp, R., Daily, J. W., and Hammitt, F. G., 1970, *Cavitation*, McGraw-Hill, New York.

[18] Bergwerk, W., 1959, "Flow Pattern in Diesel Nozzle Spray Holes," Proc. Inst. Mech. Eng., **173**(21), pp. 655–660.

[19] Sato, K., and Saito, Y., 2002, "Unstable Cavitation Behavior in a Circular-Cylindrical Orifice Flow," JSME Int. J., Ser. B, **45**(3), pp. 638–645.

[20] Ganippa, L. C., Bark, G., Andersson, S., and Chomiak, J., 2004, "Cavitation: A Contributory Factor in the Transition From Symmetric to Asymmetric Jets in Cross-Flow Nozzles," Exp. Fluids, **36**, pp. 627–634.

[21] Martynov, S., Mason, D., and Heikal, M., 2005, "Hydrodynamic Similarity of Cavitation Flows in Nozzles," *Proceedings of the 5th International Symposium on Multiphase Flow, Heat Mass Transfer and Energy Conversion*, Xi'an, China, July 3–6.

[22] Schmidt, D. P., Rutland, C. J., and Corradini, M. L., 1997, "A Numerical Study of Cavitating Flow Through Various Nozzle Shapes," SAE Paper No. 971597.

[23] Schmidt, D. P., Rutland, C. J., and Corradini, M. L., 1999, "Cavitation in Two Dimensional Asymmetric Nozzles," SAE Paper No. 1999-01-0518.

[24] Soteriou, C., Andrews, R., and Smith, M., 1995, "Direct Injection Diesel Sprays and the Effect of Cavitation and Hydraulic Flip on Atomization," SAE Paper No. 950080.

[25] Nishimura, A., and Assanis, D. N., 2000, "A Model for Primary Fuel Atomization Based on Cavitation Bubble Collapse Energy," Eighth International Conference on Liquid Atomization and Sprays (ICLASS 2000), Pasadena, CA, Jul. 16–20.

[26] Mishra, C., and Peles, Y., 2005, "Cavitation in Flow Through a Micro-Orifice Inside a Silicon Microchannel," Phys. Fluids, **17**, pp. 013601.

[27] Zhang, L., Koo, J., Goodson, K., Santiago, J., and Kenny, T., 2002, "Measurements and Modeling of Two-Phase Flow in Microchannels With Nearly Constant Heat Flux Boundary Conditions," J. Microelectromech. Syst., **11**(1), pp. 12–19.

[28] Cubaud, T., and Ho, C.-H., 2004, "Transport of Bubbles in Square Microchannels," Phys. Fluids, **16**(12), pp. 4575–4585.

[29] McNown, J. S., and Hsu, E.-Y., 1950, "Application of Conformal Mapping to Divided Flow," First Midwestern Conference on Fluid Dynamics, pp. 143–155.

[30] Perry, C. H., and Chilton, R. H., 1973, *Chemical Engineers' Handbook*, 5th ed., McGraw-Hill, New York.

[31] Vernard, J. K., 1963, *Elementary Fluid Dynamics*, 5th ed., Wiley, New York.

An Experimental Investigation of the Flowfield and Dust Resuspension Due to Idealized Human Walking

Yoshihiro Kubota
Department of Mechanical and Aerospace Engineering,
Syracuse University,
Syracuse, NY 13244

Joseph W. Hall
Department of Mechanical Engineering,
University of New Brunswick,
Fredericton, NB, E3B 5A3, Canada

Hiroshi Higuchi
Department of Mechanical and Aerospace Engineering,
Syracuse University,
Syracuse, NY 13244

*In order to address how human foot movement causes particles to be resuspended from the floor, particle flow visualization and particle image velocimetry (PIV) measurements were performed on a simplified model of the human walking motion; a disk moving normal to the floor. Flow visualization of particles, seeded initially on the ground, indicates that particles are resuspended by both the downward and upward motions of the walking process. On both the upstep and the downstep, particle resuspension occurs due to a high velocity wall jet, forming between the wall and the disk in general accord with the mechanism for particle resuspension put forth by Khalifa and Elhadidi (2007, "Particle Levitation Due to a Uniformly Descending Flat Object," Aerosol Sci. Technol., **41**, pp. 33–42). Large-scale ring vortex structures were formed on both the downstep and the upstep, and did not cause particle resuspension, but were extremely effective at quickly moving the already resuspended particles away from the wall. By varying the seeding of the particles, it was determined that only particles underneath and toward the outer edge of the disk are resuspended.* [DOI: 10.1115/1.3176962]

1 Introduction

Contaminant free air is vital for the health of human beings. The overall air quality is affected by the type and amount of particulate matter (PM) suspended in the air [1]. All particles will naturally settle to the ground in the absence of an external flow and with sufficient time. These particles will remain strongly attracted to the wall via various forces (adhesion, electrostatic, Van der Waals forces [2]) until disturbed by a sufficient velocity to dislodge them from the wall. Once dislodged, the particles become airborne where they can ultimately be inhaled. Previous analysis has indicated that the velocities required to resuspend particles are much higher than typically encountered in the indoor environment [2–4]. Several studies have shown that a walking human has a significant impact on the airborne concentration of particles [5–8]; however, the details of the resuspension process are not yet clear. The present investigation will examine how the fluid motions caused by human walking can resuspend particles.

Particle resuspension can occur via either a ballistic mechanism or an aerodynamic mechanism. The ballistic mechanism occurs when particles collide and kinetic energy is exchanged between the particles. This mechanism, however, is not expected to be as relevant to the human walking problem due to the relatively low concentrations of particles expected in the indoor environment, and thus, the low probability of particle to particle contact. The aerodynamic mechanism, which is more relevant here, occurs when the particles are resuspended solely by flow disturbances. Since these flow disturbances have a more global effect on a larger area, and thus, a larger number of particles, it is a more effective means of particle resuspension than the ballistic mechanism. The aerodynamic mechanism of particle resuspension has received research interest as of late. In particular, particle resuspension due to a sphere impacting a wall was investigated by Eames and Dalziel [9], and Leweke et al. [10]. Together, these results highlight the importance of coherent vortices on the particle resuspension mechanism.

The human walking motion and the associated foot kinetics are quite complicated, and consist of both a vertical and a rotational component [11]. In order to simplify the fluid dynamics associated with walking, the walking process is often modeled as a disk moving normal to a wall [3,12]. For example, Khalifa and Elhadidi [3], studied analytically and numerically the resuspension mechanism of particles attached to the wall beneath a falling disk. They determined that high velocity wall jets were responsible for particle detachment and resuspension. However, until now, there have been no experimental investigations of this problem. The present experimental investigation will examine the aerodynamics associated with a disk moving normal to the wall, and in particular, will focus on the global flow field and associated particle resuspension around the disk. Both the downstep and the upstep are investigated.

2 Experimental Procedure

All measurements were performed in the Indoor-Air Flowfield Laboratory (IFL) at Syracuse University. A sketch of the experimental configuration is given in Fig. 1. A 15.24 mm (6 inch) in diameter acrylic circular disk was used as the idealized foot model to match a U.S. size 8 shoe. The foot was positioned using a computer controlled linear actuator that allowed the velocity, acceleration, stroke, and deceleration to be varied. The foot motion in these experiments is stopped just before touching the wall, thereby ensuring no vibration and no particles adhere to the disk surface. Both particle flow visualizations and flow-field velocity measurements were conducted in a 1.2×1.2 m^2 sealed acrylic enclosure, to ensure that no cross-flow drafts were present. The floor was also transparent to allow observation from below.

An experiment on human foot stomping motion was first conducted to provide inputs for the laboratory experiment. Stomping was examined because it was thought to be the extreme case of human walking, and should provide the upper bounds of the velocities encountered during the walking process. The velocity time history for stomping was obtained from the motion analysis. A

Contributed by the Fluids Engineering Division of ASME for publication in the Journal of Fluids Engineering. Manuscript received July 8, 2008; final manuscript received May 28, 2009; published online July 24, 2009. Assoc. Editor: Theodore Heindel.

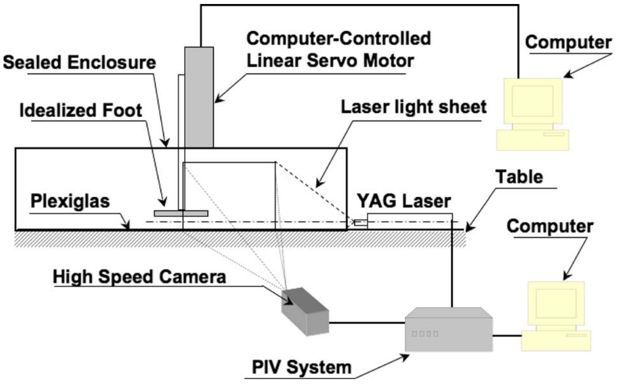

Fig. 1 Experimental setup

Table 1 Parameters used for walking and stomping

Case	Downstroke stomping	Upstroke stomping	Downstroke vertical walking
U_c (m/s)	1.875	1.725	0.5
Z_i (mm)	300	0.1	300
Z_f (mm)	0.1	300	0.1
Acc $(\mathrm{m/s^2})$	10.60	13.86	10.0
Dec $(\mathrm{m/s^2})$	−16.02	−9.55	−20.0
T_1	2.18	1.41	0.16
T_2	2.34	1.65	2.01
T_3	3.78	3.69	2.09
t_{dur} (s)	0.307	0.326	0.637
T_{final}	65	65	18.5
Re_{U_c}	18,500	17,500	5000

sample velocity time history of the downward idealized foot motion that was used in the experiment is shown in Fig. 2, which consists of three phases: acceleration from rest, constant velocity, and deceleration to rest. As shown, human foot stomping motion was approximated by a line fit. The details of both downward and upward motions are shown parametrically in Table 1, with a full list of symbols defined in the Nomenclature. Some pertinent symbols are U_c: the maximum velocity during the idealized motion, Z_i: the initial position of the foot in the motion, Z_f: the final position of the foot in the motion, Acc: the acceleration from rest until maximum velocity, Dec: the deceleration from the maximum velocity to the rest, T_1: the timing at the end of the acceleration phase, T_2: the timing at the end of the maximum velocity phase, T_3: the timing at the end of the foot motion, t_{dur}: the total duration of the foot motion, and Re_{U_c}: the Reynolds number based on the maximum velocity U_c and the disk diameter. The nondimensional time T is defined as $T=U_c t/D$, where t is the time. Parameters obtained for a walking human motion in the vertical direction from the literature were also used [11] in addition to the stomping parameters obtained here.

Particle resuspension from the wall was observed as follows: 3 M ceramic microspheres G-200 with a mean diameter of 8 μm were uniformly distributed on the floor underneath the foot model prior to the foot motion using a sifter [5]. The typical initial density of seeding was 5.6 $\mathrm{mg/cm^2}$. Originally, Arizona road dust was used as the test particle for flow visualization as this particle is used frequently in the indoor air community; however, Arizona road dust does not have a standard particle size distribution so ceramic particles of known density (2500 $\mathrm{kg/m^3}$) and known size distribution (1–12 μm) were used. This size range is inline with the size of particles that Long et al. [6] showed to be resuspended by a walking human. The results for both the Arizona road dust and the ceramic microspheres are qualitatively similar, and thus, the results are believed to be typical of particles in this size range. A Photron digital camera was operated at 125 frames per second to take time resolved images of the resuspended particles. The flow field was illuminated in its cross section with a thin light sheet from an argon ion laser, and a halogen light source was used to visualize the particles from below. A HDV Sony camcorder (HDR-HC3) operating at 30 frames per second was used to take the images during the upward motion for its wider view with a better sensitivity. The observation of the final particle distribution was made 5 s after the foot stopped ($T_{\mathrm{final}}=U_c(t_{\mathrm{dur}}+5)/D$).

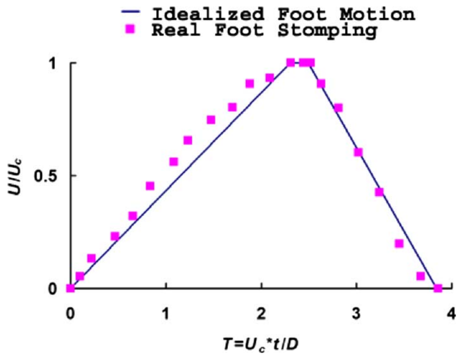

Fig. 2 Velocity time histories of an actual foot stomping and the idealized stomping motions

A Dantec two-component particle image velocimetry (PIV) system was used for quantitative velocity measurements. Seeding was provided by a Laskin-nozzle type seeder (TSI model 9307) with olive oil (nominal droplet size 1–5 μm in diameter). A cross section of the flow field was illuminated with a thin laser light sheet from a 120 mW Nd:YAG laser beam. The experiments were recorded with the 8-bit resolution, high speed CCD camera. The PIV measurements had an interrogation window size of 64×64 pixels with 75% overlap on each window. All vectors were computed using adaptive cross correlation. The resolution of the images was 1280×1024 pixels, yielding a spatial resolution for the global flow-field measurements of 0.45 mm/pixel and 0.17 mm/pixel for the near wall velocity measurements. The PIV image acquisition was triggered at various locations of the stepping cycle so that the results could be phase averaged. The results were averaged from 50 pairs of images at each foot position. The uncertainty in the phase-averaged velocity was computed directly using the standard deviation of the phase-averaged velocities at each instant, and determined to be no greater than 13% of the phase-averaged flow velocity at all measurement locations.

3 Experimental Results

3.1 Flow Visualization of Resuspended Particles During the Downward Motion. A sequence of flow visualization images during the downward stomping motion is shown in Fig. 3. This view shows a cross-sectional view illuminated along the centerline of the disk. In this case, the particles were initially seeded beneath the foot over the same diameter as the disk area to allow the initial particle resuspension process to be examined. The geometrical details of the foot model assembly are also given in the figure. The disk foot is attached to a flange, 101.6 mm (4 in.) in diameter, to connect the rod with the disk foot, and the thickness of the disk foot is 10 mm; the thickness of the flange is 12.7 mm (0.5 in.). The images are shown in sequence, referenced at the time before the foot has stopped. Thus, the negative value of time $t<0$ s, corresponds to the result during the foot motion, and the positive t corresponds to the events after the foot stopped. In $t=-0.016$ s and $Z=2.15$ mm, the particles were not yet expelled from the gap between the foot and the wall. Later at $t=-0.008$ s and $Z=0.61$ mm, the resuspended particles are visible ($t=0$ s). At $T=3.78$, the ejected particles were redistributed along

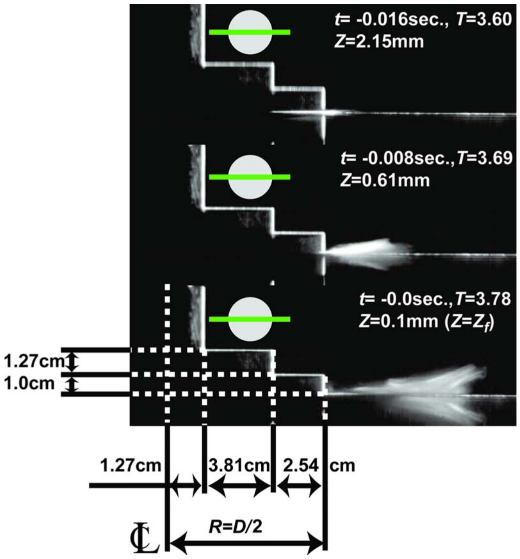

Fig. 3 Flow visualization of particles resuspended during the downward stomping motion. Particles are originally seeded beneath the disk only.

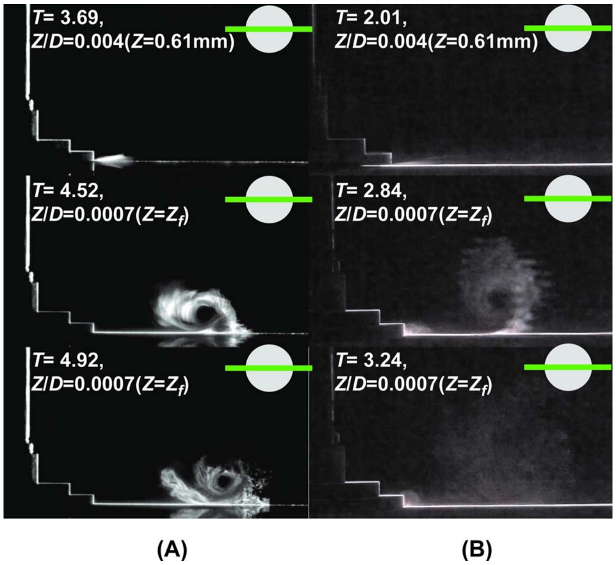

Fig. 4 Resuspended particles during (*a*) downward stomping and (*b*) walking motion

the floor. The particle resuspension occurred when the foot moved within the approximate height of $Z=0.5$ mm, consistent with the wall jet particle detachment model proposed by Khalifa and Elhadidi [3]. Since the foot does not touch the wall and the particle concentration is relatively low, the particles must have been resuspended by the aerodynamic mechanism.

A similar sequence of images is shown in Fig. 4, although they are zoomed out and are at later times. In this case, the left column corresponds to the downward stomping motion, and the right column corresponds to the downward walking motion. These images demonstrate the effectiveness of both the stomping and walking downward motion at resuspending particles, and then rapidly redistributing them away from the wall. For example, in the stomping motion at normalized time $T=3.69$ (immediately before the foot stops at $T=3.78$ and approximately coinciding with Fig. 3), particle ejection from the wall is clearly shown. Once resuspended, these particles are quickly ejected from the wall and appear to be entrained into a vortex structure. Later, there is no longer a discernible vortex structure, and a relatively homogenous distribution of particles is seen away from the foot and at a considerable distance from the wall. Similar behavior occurs for the walking motion, although here, fewer particles are resuspended from the wall and entrained into the vortex structure, as indicated by the brightness of the vortex.

A sequence of flow visualization images observed from below the foot and at the end of the stomping motion is shown in Fig. 5. Note that Figs. 5(*b*) and 5(*c*) are coincident with Fig. 4(*a*) at $T=4.52$ and at $T=4.92$. Evidence of an axisymmetric vortex ring is clearly observed, and as expected, the particle distribution along the wall spreads radially outward with increasing time. Also at $T=4.92$ (see Fig. 4(*a*) and 5(*c*)), the circular accumulation of particles roughly corresponds to the vortex core, likely caused by uplifting particles ahead of the vortex ring. Numerous radial streaks can be observed and are detectable even in the final particle distribution shown in Fig. 5(*d*), and can be attributed to an azimuthal vortex ring instability, as discussed, for example, by Widnall et al. [13]. Eames et al. [9] and Leweke et al. [10] also noted similar instability waves beneath an impacting sphere. The present streak pattern under the disk appears to have a much higher wave number than expected, and further study is needed to fully understand this behavior. Axisymmetric numerical simulations by Khalifa and Elhadidi [3] or DeGraw and Cimbala [12] could not capture this behavior.

Flow visualization was then conducted using different initial seeding patterns to fully understand the particle resuspension mechanism. In Fig. 6(*a*), the final particle distributions obtained in Fig. 5(*d*) are compared with the final particle distributions for four different types of initial seeding. These include the particles spread over half the diameter of disk (Fig. 6(*b*)), an annular pattern beneath the disk between half the diameter from the center to the edge of the disk (Fig. 6(*c*)), and an annular pattern immediately outside the disk seeded at 2.54 cm (1 in.) in width from the edge of the foot (Fig. 6(*d*)). As shown in these figures, the initial position of the particles clearly affects the particle redistribution. In particular, particles that are seeded at the middle of the disk do not spread significantly (Fig. 6(*b*)), whereas particles that are seeded closer to the outer edge of the disk (like in Fig. 6(*c*) and

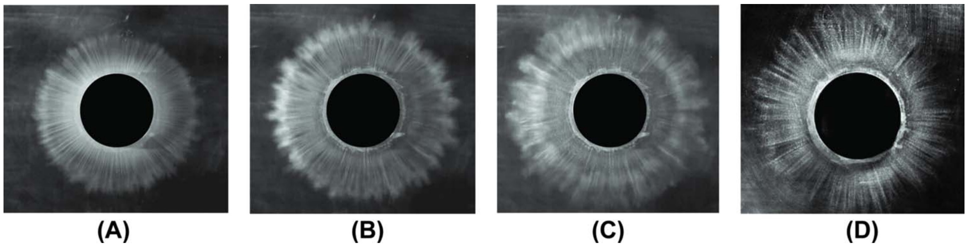

Fig. 5 Resuspended particle sequence taken during downward stomping motion. Foot motion is toward the reader and the view is from below: (*a*) $T=4.10$, $Z/D=0.0007$ ($Z=Z_f$), (*b*) $T=4.52$, $Z/D=0.0007$ ($Z=Z_f$), (*c*) $T=4.92$, $Z/D=0.0007$ ($Z=Z_f$), and (*d*) $T=T_{\text{final}}$, $Z/D=0.0007$ ($Z=Z_f$)

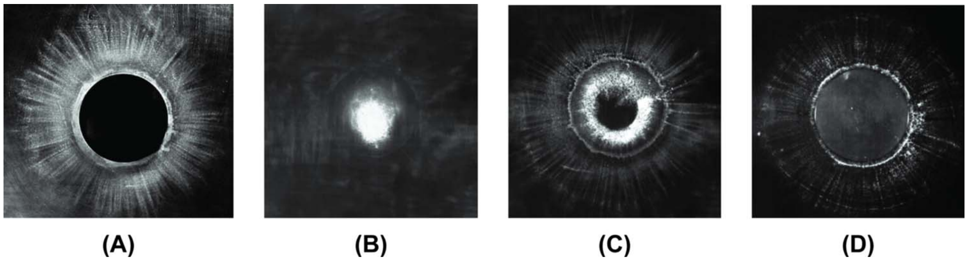

Fig. 6 Bottom view of particles trajectories for different seeding patterns at $T=T_{\mathrm{final}}$: (*a*) same diameter as a disk, (*b*) half diameter of disk beneath the disk, (*c*) ring shape beneath the disk, and (*d*) ring shape immediately outside the disk

Fig. 6(*d*)) escape from underneath the disk. Once these particles escape from underneath the disk, they are enveloped into the vortex ring structure, as indicated by the pattern on the wall that is consistent with a coherent vortex ring structure with some azimuthal instabilities. Flow visualization of particles that were initially seeded in a ring outside of the disk radius indicated that they were not significantly resuspended. These findings are consistent with those of Khalifa and Elhadidi [3], who analytically showed that it was mostly the particles within the outer half radius of the disk that would be resuspended and redistributed.

3.2 Velocity Field Measurement in Downward Motion. Phase-averaged velocity field measurements obtained during the downward stomping motion are shown in sequence in Figs. 7 and 8. The timing shown corresponds to the flow visualization images shown in Figs. 3 and 4. The formation of a coherent vortex is clearly seen in the wake of the foot on the downstep in Fig. 7(*a*), consistent with the flow visualization study. It is expected that the mechanism by which this vortex is formed is similar, as discussed by Higuchi et al. [14]. Balligand [15] showed that the maximum circulation in the vortex ring is achieved in the wake by $T\sim5$, and consistently, a strong rotational flow is consistently evident here at $T=4.92$. A vortex is clearly evident in the velocity field at $T=3.52$, however, a comparison to the flow visualization in Fig. 3 indicates that no particle resuspension has occurred at approximately this instant ($T=3.6$). From this, it can be inferred that the vortex formed above the foot does not induce the initial detachment or resuspension of particles. The velocity field shown at this instant, however, shows a gap flow formed between the foot and the floor. At this height (3.7 mm from the floor), the magnitude of the velocity is relatively low. The PIV data indicates that, in this case, the maximum velocity is less than 2.0 m/s at the disk edge. Later, at $T=4.31$, the velocity measurements indicate that a vortex ring has impacted the wall and is traveling radially outward. The flow visualization at approximately this instant (Fig. 4(*a*), $T=4.52$, and Fig. 5(*b*)) indicates that at this stage, the vortex ring is quite effective at redistributing the particles that have been resus-

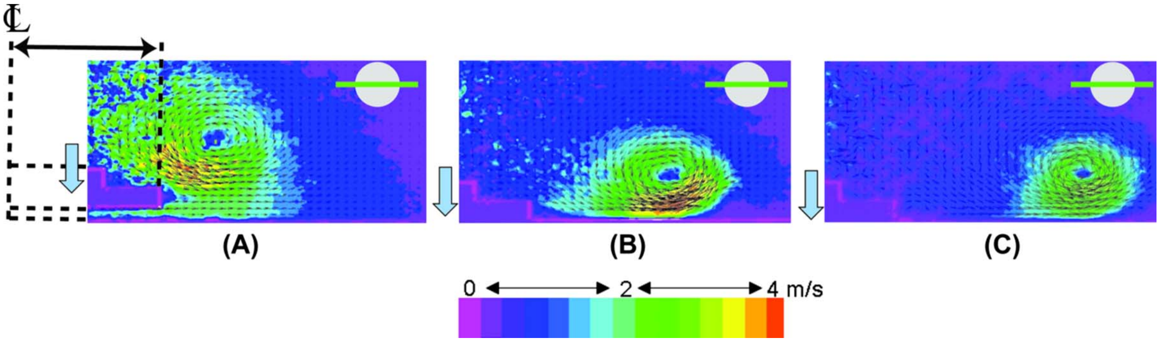

Fig. 7 A sequence of flow-field velocity measurements taken during the downward stomping motion: (*a*) $T=3.52$, $ZID=0.024$ ($Z=3.7$ mm) immediately before the foot stopped, (*b*) $T=4.31$, $ZID=0.0007$ ($Z=Z_f$), and (*c*) $T=4.92$, $ZID=0.0007$ ($Z=Z_f$)

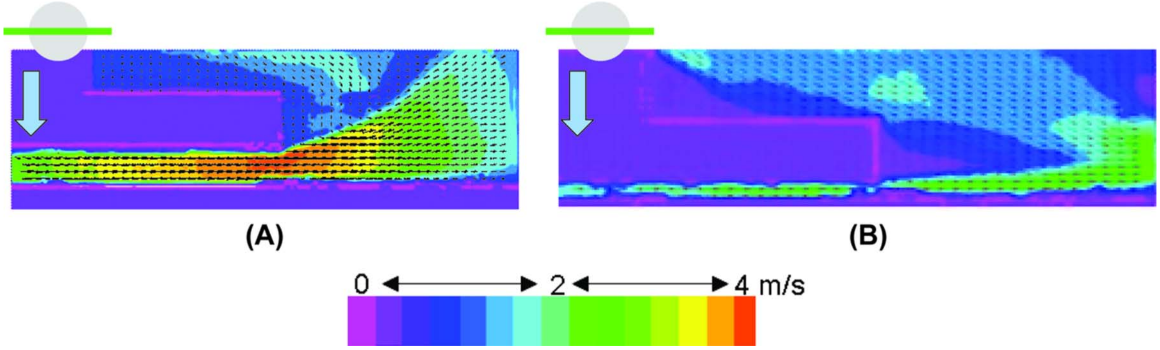

Fig. 8 Flow-field velocity measurements taken during the downward walking motion (*a*) $T=2.02$, $ZID=0.034$ and (*b*) $T=2.07$, $ZID=0.006$ ($Z=0.9$ mm)

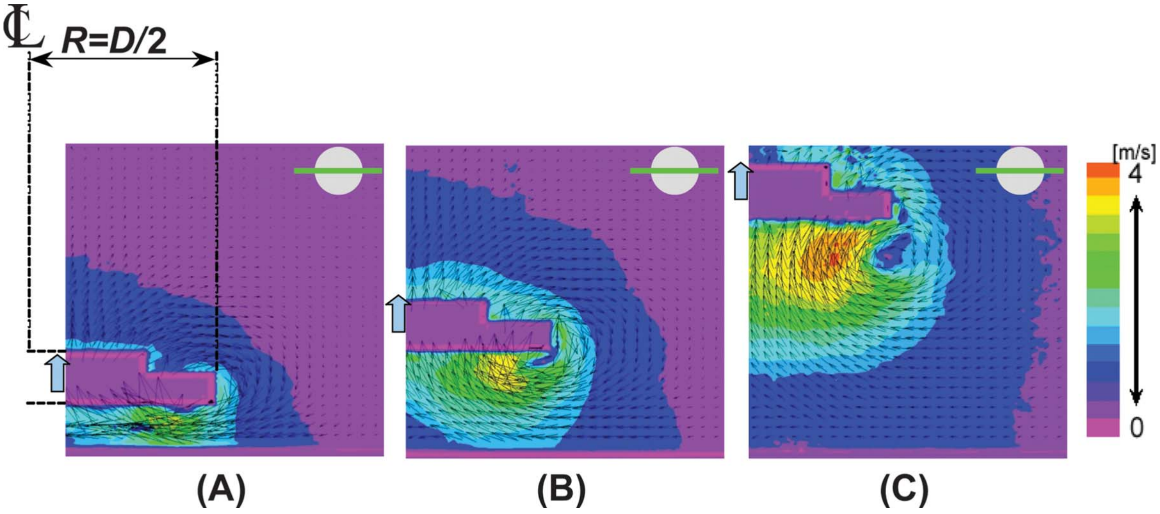

Fig. 9 A sequence of velocity flow-field measurements taken during the upward portion of the stomping motion: (*a*) $T=0.85$, $Z/D=0.256$, (*b*) $T=1.13$, $Z/D=0.455$, and (*c*) $T=1.70$, $Z/D=0.994$

pended by the wall jet mechanism. At $T=4.92$, the velocity measurements indicate that the vortex continues to travel radially outward along the wall and to further redistribute the bulk of the particles away from the disk. Thus, these results clearly demonstrate that the wall jet formed beneath the foot and the vortex dynamics associated with the disk wake are both crucial to the resuspension and subsequent redistribution of particles from the floor. In summary, the particle resuspension is caused by the wall jet formed beneath the foot, and the particle redistribution is attributed to the large-scale vortex dynamics. Similar findings were obtained for the walking motion and are not shown here.

3.3 Velocity Field Measurement and Flow Visualization During the Upward Idealized Foot Motion. The conditionally averaged velocity fields measured during the upward portion of the stomping motion are shown in Fig. 9. These images confirm the presence of large-scale vortices formed by the impulsively started disk. As the foot moves away from the wall, a strong inward gap flow is induced, causing circulation around the disk. The motion of the disk forces fluid away from the front of the disk and causes a strong rotational flow around the disk. A similar sequence of events has been observed during the formation of a vortex ring behind a rapidly accelerated disk [14,15].

The induced flow on the upward portion of the step can also cause particle resuspension, as shown for the stomping motion in Fig. 10. As the foot moves away from the wall, initially, a significant amount of particles are resuspended from the wall and entrained near the center of the disk foot. Interestingly, Leweke et al. [10] reported that the upward motion with the sphere did not affect the particle resuspension; however, this is certainly due to the differences in the inflow caused by the different geometries. Inspection of the velocity measurements at a similar time (Fig. 9(*a*)) reveals that the highest concentration of particles does not correspond to the highest flow velocities. Since the concentration is highest at the center of the disk where the pressure is expected to be the lowest, the particle resuspension is likely caused by an inwardly flowing wall jet, associated with the rapid inflow that

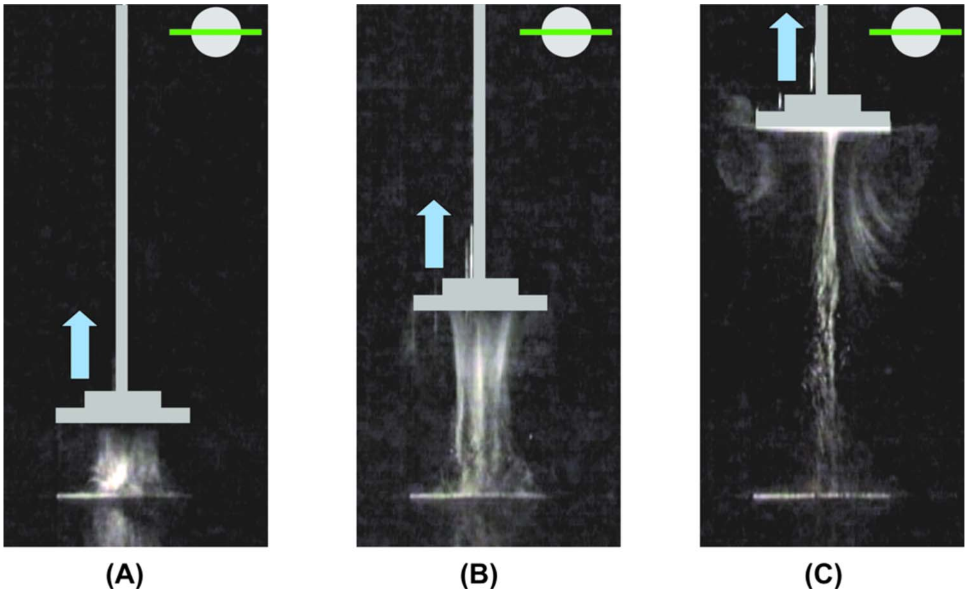

Fig. 10 Visualization of particles resuspended during the upward stomping motion: (*a*) $T=1.13$, $Z/D=0.455$, (*b*) $T=1.89$, $Z/D=1.17$, and (*c*) $T=3.02$, $Z/D=1.86$

occurs during startup. Later, as shown in Fig. 10(*b*), a vortex ring starts to form behind the disk. Similar to the down step, these large-scale structures are quite effective at redistributing the resuspended particles, up and away from the wall. Taken together, these findings demonstrate that the upward motion is just as important as the downward motion for resuspending particles and redistributing them away from the wall. Consistent with the downstep, the gap flow resuspends the particles, while the vortex dynamics are responsible for levitation and redistribution of the particles.

4 Discussion of Results and Concluding Remarks

Flow visualization and PIV flow-field measurements were carried out to understand the particle resuspension and redistribution associated with a disk, moving normal to the wall; this is the simplest model of a human walking motion. Overall, the results indicate that particles can be resuspended on both the downward and upward portion of the walking process by the aerodynamic mechanism. For both the upward and downward stepping motions, particle resuspension occurs due to high velocity flow in the gap between the wall and the disk, in general accordance with the mechanism for particle resuspension, as proposed by Khalifa and Elhadidi [3] and Soltani and Ahmadi [2]. The results indicate that the large-scale vortex structures are not responsible for particle resuspension, but are extremely effective at quickly moving the resuspended particles away from the disk and the wall. Fully understanding the particle resuspension mechanism requires information about the wall shear stress, but due to difficulties associated with phase averaged PIV, measurements near a wall could not be accurately determined here.

During the downward foot motion, the highest velocities measured here are approximately 2 m/s for either the walking or the stomping motions; these values are significantly less than the ones predicted by Khalifa and Elhadidi [3]. In this case, they simulated the flow around a disk, falling at a constant speed that impacts the wall. Naturally, in their simulation, the calculated gap flow increases to an unrealistically high velocity level, but at 0.5 mm, the gap flow velocity still reaches around 45 m/s. These discrepancies may be attributed to the lack of spatial resolution near the wall, with the present measurement configuration or the assumptions employed in their analytical modeling, but are more likely due to fundamental differences between the two flow conditions. In particular, the present experiment had to decelerate the disk to avoid ramming the foot through the wall, and thus, the disk did not impact the wall at constant velocity. As discussed by Higuchi et al. [14], the deceleration rate is an important parameter in the associated flow field around an impulsively started disk.

Since the large-scale flow structures play an important role in particle redistribution, it is likely that the geometries of the foot itself are important for the resuspension and the redistribution of particles. Currently, an investigation using more realistic foot geometries is underway and will be addressed in a forthcoming paper.

Acknowledgment

This work has been supported partially by the New York State STAR Center for Environmental Quality Systems and the U.S. Environmental Protection Agency (U.S. EPA grant/cooperative agreement Award No. CR-83199201-0). Although this research has been funded in part by the U.S. EPA, it has not been subjected to the agency's required peer and policy review, and therefore, does not necessarily reflect the views of the agency, and no official endorsement should be inferred. JWH would like to acknowledge the funding of the Natural Science and Engineering Research Council of Canada via a postdoctoral fellowship.

Nomenclature

D = diameter of circular plate
Z = gap in motion
Z_i = initial gap in motion
Z_f = final gap in motion
acc = acceleration in motion
dec = deceleration in motion
U = foot velocity
U_c = constant foot velocity
t = time, s
t_{dur} = total duration of foot motion
T = normalized time, $U_c t/D$
T_1 = timing at the end of acceleration phase
T_2 = timing at the end of constant velocity phase
T_3 = timing at the end of deceleration phase
T_{final} = 5 s after T_3
υ = kinematic viscosity
Re_{U_c} = Reynolds number based on disk diameter, $U_c D/\upsilon$
τ_0 = wall shear stress
u^* = friction velocity, $u^* = \sqrt{\tau_0/\rho}$

References

[1] Nazaroff, W., 2004, "Indoor Particle Dynamics," Indoor Air, **14**(s7), pp. 175–183.
[2] Soltani, M., and Ahmadi, G., 1994, "On Particle Adhesion and Removal Mechanisms in Turbulent Flows," J. Adhes. Sci. Technol., **8**, pp. 763–785.
[3] Ezzat Khalifa, H. E., and Elhadidi, B., 2007, "Particle Levitation Due to a Uniformly Descending Flat Object," Aerosol Sci. Technol., **41**, pp. 33–42.
[4] Bagnold, R., 1941, *Physics of Wind-Blown Sand and Desert Dunes*, Methuen, London.
[5] Ferro, A. R., Kopperud, R. J., and Hildmann, L. M., 2004, "Elevated Personal Exposure to Particulate Matter From Human Activities in a Residence," J. Expo Anal Environ. Epidemiol., **14**, pp. S34–S40.
[6] Long, C. M., Suh, H. H., and Koutrakis, P., 2000, "Characterization of Indoor Particle Source Using Continuous Mass and Size Monitors," J. Air Waste Manage. Assoc., **50**, pp. 1236–1250.
[7] Thatcher, T. L., and Layton, D. W., 1995, "Deposition, Resuspension, and Penetration of Particles Within a Residence," Atmos. Environ., **29**, pp. 1487–1497.
[8] Abt, E., Suh, H. H., Catalano, P., and Koutrakis, P., 2000, "Relative Contribution of Outdoor and Indoor Particle Sources to Indoor Concentrations," Environ. Sci. Technol., **34**, pp. 3579–3587.
[9] Eames, I., and Dalziel, S. B., 2000, "Dust Resuspension by the Flow Around an Impacting Sphere," J. Fluid Mech., **403**, pp. 305–328.
[10] Leweke, T., Thompson, M. C., and Hourigan, K., 2004, "Vortex Dynamics Associated With the Collision of a Sphere With a Wall," Phys. Fluids, **16**, pp. L74–L77.
[11] Winter, D. A., 2005, *Biomechanics and Motor Control of Human Movement*, Wiley, Hoboken, NJ.
[12] DeGraw, J., and Cimbala, J., 2007, "A Lightweight Particle Deposition System for Particle Resuspension Studies," Presentation at the American Physical Society's Annual Meeting of the Division of Fluid Dynamics, Salt Lake City, UT, Nov. 18–20.
[13] Widnall, S. E., Bliss, D. B., and Tsai, C. Y., 1974, "The Instability of Short Waves on a Vortex Ring," J. Fluid Mech., **66**(1), pp. 35–47.
[14] Higuchi, H., Balligand, H., and Strickland, J. H., 1996, "Numerical and Experimental Investigations of the Flow Over a Disk Undergoing Unsteady Motion," J. Fluids Struct., **10**, pp. 705–719.
[15] Balligand, H., 2000, "Wake Structure Behind a Solid Disk," Ph.D. thesis, Syracuse University, Syracuse, NY.

An Efficient Quasi-2D Simulation of Waterhammer in Complex Pipe Systems

Huan-Feng Duan
e-mail: ceduan@ust.hk

Mohamed S. Ghidaoui
e-mail: ghidaoui@ust.hk

Yeou-Koung Tung
e-mail: cetung@ust.hk

Department of Civil and Environmental Engineering,
The Hong Kong University of Science and Technology,
Hong Kong, SAR China

An efficient quasi-2D numerical waterhammer model for turbulent waterhammer flows has been previously developed for a single pipe system (reservoir-pipe-valve system). Basic boundary conditions, such as valves, reservoirs, and external flows, were also implemented. This paper extends this previously developed efficient scheme to a general model for a multipipe system. More specifically, an approach for matching the family of characteristic equations in each pipe at a junction of two or more pipes is proposed. In addition, the numerical stability conditions of the efficient scheme are investigated using the Von Neumann method. The resulting model is verified against experimental data and then applied to different complex systems involving pipes in series, branching, and network. Using this model, the effects of unsteady friction in complex pipe systems are examined and analyzed in this paper. From the case studies, it is found that the quasi-2D model is highly efficient, robust, and suitable for application to waterhammer problems in real complex pipe system. [DOI: 10.1115/1.3176978]

Keywords: complex pipe system, quasi-2D model, waterhammer, efficiency

1 Introduction

Recently, a range of turbulence models for waterhammer flows have been developed [1–10]. Such models are important for fundamental research and could potentially become a viable tool for solving practical waterhammer problems. For example, turbulence models can be used to (i) conduct numerical experiment in order to understand the interplay between waterhammer waves and turbulence, (ii) develop an understanding of energy dissipation relations in transient flows, and (iii) calibrate and validate one-dimensional models and derive the resistance coefficients of unsteady friction equations. In addition, turbulence models provide the needed detailed velocity field that is important for conducting the transport of contaminants during transients that could be due to biofilm sloughing or contaminant intrusion. Moreover, turbulence models serve to validate transient-based leakage identification methods, which are often derived from simplified, and in many cases, linearized version of the one-dimensional waterhammer equations.

The usage of turbulence models in waterhammer research and practice requires that such models are (i) efficient (i.e., solutions and scenarios do not require excessive computational resources and time) and (ii) applicable to realistic (complex) pipe systems. Pezzinga [2] developed a quasi-2D model for pipe network based on the model of Vardy and Huang [6] by integrating the continuity equation over the cross section. This model is solved by the finite difference (FD) scheme (explicit FD for continuity equation and implicit FD for momentum equation). However, through extensive different numerical simulations, it is found that the accuracy is affected sensitively by the integration steps of the cross-sectional flowrate, and the numerical stability must be guaranteed by enough number of radial sections or iterative steps. Therefore, its efficiency is greatly reduced for that.

On the other hand, the efficiency requirement has been largely resolved in the paper by Zhao and Ghidaoui [8] where they developed a highly efficient version of the quasi-2D model of Vardy and Hwang [6], and found that solutions that used to take tens of hours can be completed in a matter of seconds or minutes with enough high efficiency. This paper deals with the second requirement, namely, the extension of the model by Zhao and Ghidaoui [8] to complex pipe systems involving branching and network pipe systems.

The paper is organized as follows. Following the introduction, the quasi-2D-waterhammer is first provided. Second, the original solution of this model by Vardy and Hwang [2] and its highly efficient version by Zhao and Ghidaoui [8] are summarized. Third, the extension of this model to a more realistic pipe system is described. Fourth, the model stability is investigated and a criterion for its stability is established. Fifth, the model is verified against the experimental data and then applied to several numerical test cases including the single, series, and branching pipe systems. Furthermore, the results are inspected and discussed. Lastly, the main findings are summarized in Sec. 7.

2 Quasi-2D Model Equations

The quasi-2D-waterhammer model [6] is as follows:

$$\frac{g}{a^2}\frac{\partial H}{\partial t}+\frac{\partial u}{\partial x}+\frac{1}{r}\frac{\partial (rv)}{\partial r}=0 \tag{1}$$

$$\frac{\partial u}{\partial t}+g\frac{\partial H}{\partial x}=\frac{1}{r\rho}\frac{\partial (r\tau)}{\partial r} \tag{2}$$

where H is the piezometric head, u and v are the velocity components in the axial and radial directions, a is the wavespeed, g is the gravitational acceleration, ρ is the fluid density, τ is the shear stress, and x, r, and t are the longitudinal, radial, and temporal coordinates, respectively.

The characteristic form of Eqs. (1) and (2) is

Contributed by the Fluids Engineering Division of ASME for publication in the Journal of Fluids Engineering. Manuscript received September 24, 2008; final manuscript received June 19, 2009; published online July 24, 2009. Assoc. Editor: Dimitris Drikakis.

$$\frac{dH}{dt} \pm \frac{a}{g}\frac{du}{dt} = -\frac{a^2}{g}\frac{1}{r}\frac{\partial q}{\partial r} \pm \frac{a}{g}\frac{1}{r\rho}\frac{\partial (r\tau)}{\partial r} \quad \text{and along} \quad \frac{dx}{dt} = \pm a \tag{3}$$

where $q = rv$ = radial flowrate, and

$$\tau = \rho\upsilon\frac{\partial u}{\partial r} - \rho\overline{u'v'} = \rho(\upsilon + \upsilon_t)\frac{\partial u}{\partial r} = \rho\upsilon_T\frac{\partial u}{\partial r}$$

in which ν, ν_t, and ν_T are the kinematic, turbulent, and total viscosities, respectively, and u' and v' are the velocity fluctuations.

The two-layer turbulence model [2] and the five-region turbulence model [6] were mostly used in waterhammer simulations because they are efficient and easy to understand and implement. In addition, it is found that these models provide similar accuracy to more involved models such as the $\kappa - \varepsilon$ turbulence model [9]. In this research, the two-layer model and the five-region model have been implemented, applied, and found to produce similar achievements. Therefore, and for brevity, only the results of the five-region turbulence model are shown in this paper.

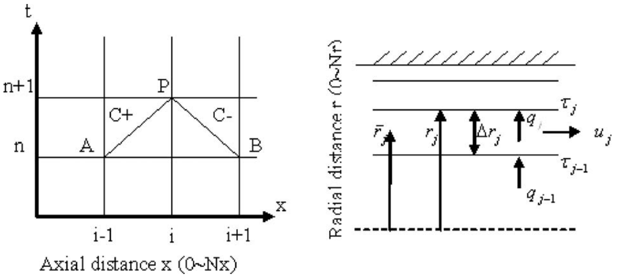

Fig. 1 Grid system for MOC solution

2.1 Original Vardy–Hwang Scheme. Method of Characteristics (MOC) scheme (Fig. 1), the solution can be written in matrix form as follows:

$$\mathbf{Az} = \mathbf{b} \tag{4}$$

where $\mathbf{z} = \{H_i^{n+1}, u_{i,1}^{n+1}, q_{i,1}^{n+1}, \ldots, u_{i,j}^{n+1}, q_{i,j}^{n+1}, \ldots, u_{i,\mathrm{N_r}-1}^{n+1}, q_{i,\mathrm{N_r}-1}^{n+1}, u_{i,\mathrm{N_r}}^{n+1}\}^T$, $\mathbf{b}$ is a known vector, which depends on the hydraulic parameters at time level n, and $\mathbf{A}$ is the following $2\mathrm{N_r} \times 2\mathrm{N_r}$ coefficient matrix:

$$\begin{pmatrix}
1 & \frac{a}{g} + C_{u2}(1) & C_q(1) & -C_{u3}(1) & & \cdots & \vdots & \cdots \\
1 & -\left[\frac{a}{g} + C_{u2}(1)\right] & C_q(1) & C_{u3}(1) & & \cdots & \vdots & \vdots \\
\vdots & \vdots & & \vdots & & \cdots & \vdots & \vdots \\
1 & \cdots & -C_{u1}(j) & -C_q(j) & \frac{a}{g} + C_{u2}(j) & C_q(j) & -C_{u3}(j) & \cdots \\
1 & \cdots & C_{u1}(j) & -C_q(j) & -\left[\frac{a}{g} + C_{u2}(j)\right] & C_q(j) & C_{u3}(j) & \cdots \\
\vdots & \vdots & & \vdots & & \vdots & & \vdots \\
1 & \cdots & & \cdots & & -C_{u1}(\mathrm{N_r}) & -C_q(\mathrm{N_r}) & \frac{a}{g} + C_{u2}(\mathrm{N_r}) \\
1 & \cdots & & \cdots & & C_{u1}(\mathrm{N_r}) & -C_q(\mathrm{N_r}) & -\left[\frac{a}{g} + C_{u2}(\mathrm{N_r})\right]
\end{pmatrix}$$

in which

$$C_{u1}(j) = \frac{a\Delta t\upsilon_{T(j-1)}}{g}\frac{1}{\bar{r}_j\Delta r_j}\frac{r_{j-1}}{(\bar{r}_j - \bar{r}_{j-1})}$$

$$C_{u3}(j) = \frac{a\Delta t\upsilon_{T(j)}}{g}\frac{1}{\bar{r}_j\Delta r_j}\frac{r_j}{(\bar{r}_{j+1} - \bar{r}_j)}$$

$$C_{u2}(j) = C_{u1}(j) + C_{u3}(j), \quad C_q(j) = \frac{a^2\Delta t}{g}\frac{1}{\bar{r}_j\Delta r_j}$$

It is noted that the $\mathrm{N_r}$ concentric cylinders are chosen, such that they all have the same cross-sectional area. This discretization strategy will be adopted in this paper.

2.2 Modified Scheme of Zhao and Ghidaoui. Since the Vardy–Hwang scheme that was just presented requires excessive CPU time, Zhao and Ghidaoui [8] proposed an efficient method to solve system (4). They showed that system (4) can be rewritten as follows:

$$\mathbf{BU} = \mathbf{b_u} \tag{5}$$

$$\mathbf{CV} = \mathbf{b_v} \tag{6}$$

in which $\mathbf{V} = \{H_i^{n+1}, q_{i,1}^{n+1}, \ldots, q_{i,j}^{n+1}, \ldots, q_{i,\mathrm{N_r}-1}^{n+1}\}^T$, $\mathbf{U} = \{u_{i,1}^{n+1}, \ldots, u_{i,j}^{n+1}, \ldots, u_{i,\mathrm{N_r}}^{n+1}\}^T$, $\mathbf{b_u}$ and $\mathbf{b_v}$ are the known vectors, which depend on the hydraulic parameters at time level n, and $\mathbf{B}$ and $\mathbf{C}$ are the tridiagonal $\mathrm{N_r} \times \mathrm{N_r}$ matrices as

$$\mathbf{B} = \begin{pmatrix} \dfrac{a}{g} + C_{u2}(1) & -C_{u3}(1) & & \cdots & \cdots \\ \vdots & & \vdots & & \vdots \\ \cdots & -C_{u1}(j) & \dfrac{a}{g} + C_{u2}(j) & -C_{u3}(j) & \cdots \\ \vdots & & \vdots & & \vdots \\ \cdots & & \cdots & -C_{u1}(\mathrm{N_r}) & \dfrac{a}{g} + C_{u2}(\mathrm{N_r}) \end{pmatrix}_{\mathrm{N_r} \times \mathrm{N_r}}$$

$$\mathbf{C} = \begin{pmatrix} 1 & C_q(1) & & \cdots & & \cdots \\ 0 & -[C_q(2) + C_q(1)] & & C_q(2) & \cdots & \\ \vdots & & & \vdots & & \vdots \\ \cdots & C_q(j-1) & -[C_q(j) + C_q(j-1)] & C_q(j) & & \\ \vdots & & & \vdots & & \vdots \\ \cdots & & & \cdots & C_q(\mathrm{N_r}-1) & -[C_q(\mathrm{N_r}) + C_q(\mathrm{N_r}-1)] \end{pmatrix}_{\mathrm{N_r} \times \mathrm{N_r}}$$

Under the same condition, the CPU time of the modified scheme and the original scheme are nearly of order $\mathrm{N_r}$ and $\mathrm{N_r^3}$, respectively [8,10], thus, the great gain in efficiency.

3 Implementation of Boundary Conditions

In the waterhammer literature, devices such as valves, reservoirs, dead ends, pump stations, surge tanks, air valves, etc., are represented by so-called boundary conditions, which provide mathematical relations between head H and flow Q. Using these relations in conjunction with two-dimensional models raises the difficulty of linking the $\mathrm{N_r}$ characteristic equations (describing the velocity profile) with the single equation at the boundary. Nixon [11] dealt with this problem for the case of valves and external flows by solving the velocity profile at boundary devices with iteration procedures. The problem of how to link the velocity profiles and their associated characteristics at junctions of pipes is addressed in the remainder of this section.

It is noted that the derivation could have been accomplished for a general junction with an arbitrary number of pipes. However, for clarity, the authors decided to illustrate such formulations for the junction with two and three pipes rather than in the general case.

3.1 Series Pipe System. For simplification in the 1D model, the head at the junction of two or more pipes is assumed unique (i.e., common/continuous) and the junction has no ability to store water (i.e., the inflows are equal to the outflows). These assumptions are commonly used in the quasi-2D model since the variables (head and flowrate) are functions generally only of longitudinal and temporal coordinate [2]. For convenience, they are also adopted in this paper. In addition, it is assumed that the number of radial sections in each pipe in the system is the same.

Mathematically, these assumptions lead to

$$\begin{gathered} H_m^{n+1,s} = H_0^{n+1,s+1} = H_p^{n+1} \\ q_{m,j}^{n+1,s} = q_{0,j}^{n+1,s+1} = q_{p,j}^{n+1} \\ Q_{m,j}^{n+1,s} = Q_{0,j}^{n+1,s+1} = Q_{p,j}^{n+1} \end{gathered} \tag{7}$$

where the subscript m refers to the location just upstream of the junction, and subscript "0" refers to the location just downstream of the junction.

Considering the mth section at pipe s and the first section at pipe $s+1$, as in Fig. 2, recalls that the flow equation that describes the wave moving downstream (toward the junction) in pipe s and the wave moving upstream (toward the junction) in pipe $s+1$ are, respectively, given by

$$\frac{dH}{dt} + \frac{a}{gA}\frac{dQ}{dt} = -\frac{a^2}{g}\frac{1}{r}\frac{\partial q}{\partial r} + \frac{a}{g}\frac{1}{r\rho}\frac{\partial(r\tau)}{\partial r} \quad \text{along} \quad \frac{dx}{dt} = a^s \tag{8}$$

$$\frac{dH}{dt} - \frac{a}{gA}\frac{dQ}{dt} = -\frac{a^2}{g}\frac{1}{r}\frac{\partial q}{\partial r} - \frac{a}{g}\frac{1}{r\rho}\frac{\partial(r\tau)}{\partial r} \quad \text{along} \quad \frac{dx}{dt} = a^{s+1} \tag{9}$$

where Q and q are the axial and radial flowrates in each section.

Applying the MOC method to the above ordinary differential equation gives

$$\begin{aligned} & B_q^s(j)H_m^{n+1,s} - \varepsilon B_{u1}^s(j)Q_{m,j-1}^{n+1,s} + [B_c^s + \varepsilon B_{u2}^s(j)]Q_{m,j}^{n+1,s} - \varepsilon B_{u3}^s(j)Q_{m,j+1}^{n+1,s} \\ & \quad - \theta[q_{m,j-1}^{n+1,s} - q_{m,j}^{n+1,s}] \\ & \quad = \{B_q^s(j)H_{m-1}^{n,s} + (1-\varepsilon)B_{u1}^s(j)Q_{m-1,j-1}^{n,s} \\ & \quad + [B_c^s - (1-\varepsilon)B_{u2}^s(j)]Q_{m-1,j}^{n,s} + (1-\varepsilon)B_{u3}^s(j)Q_{m-1,j+1}^{n,s} \\ & \quad + (1-\theta)[q_{m-1,j-1}^{n,s} - q_{m-1,j}^{n,s}]\} \end{aligned} \tag{10}$$

$$\begin{aligned} & B_q^{s+1}(j)H_0^{n+1,s+1} + \varepsilon B_{u1}^{s+1}(j)Q_{0,j-1}^{n+1,s+1} - [B_c^{s+1} + \varepsilon B_{u2}^{s+1}(j)]Q_{0,j}^{n+1,s+1} \\ & \quad + \varepsilon B_{u3}^{s+1}(j)Q_{0,j+1}^{n+1,s+1} - \theta[q_{0,j-1}^{n+1,s+1} - q_{0,j}^{n+1,s+1}] \\ & \quad = \{B_q^{s+1}(j)H_1^{n,s+1} - (1-\varepsilon)B_{u1}^{s+1}(j)Q_{1,j-1}^{n,s+1} \\ & \quad - [B_c^{s+1} - (1-\varepsilon)B_{u2}^{s+1}(j)]Q_{1,j}^{n,s+1} - (1-\varepsilon)B_{u3}^{s+1}(j)Q_{1,j+1}^{n,s+1} \\ & \quad + (1-\theta)[q_{1,j-1}^{n,s+1} - q_{1,j}^{n,s+1}]\} \end{aligned} \tag{11}$$

where ε and θ are the weighting coefficients; the superscripts s

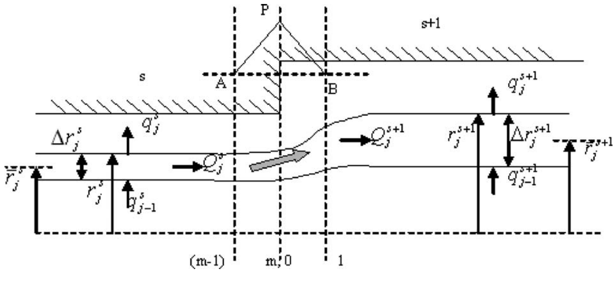

Fig. 2 Series junction system

and $s+1$ are the numbers of the up and down pipes; the subscripts 0 and m are the start point and end point of the pipes, respectively: and the subscripts j and n are the radial and temporal locations.

$$B_{u1}(j)=\frac{C_{u1}(j)}{A_{j-1}C_{q1}(j)}=\frac{\upsilon_{T(j-1)}}{2\pi a}\frac{1}{\bar{r}_{j-1}\Delta r_{j-1}}\frac{r_{j-1}}{(\bar{r}_j-\bar{r}_{j-1})}$$

$$B_{u3}(j)=\frac{C_{u3}(j)}{A_{j+1}C_{q1}(j)}=\frac{\upsilon_{T(j)}}{2\pi a}\frac{1}{\bar{r}_{j+1}\Delta r_{j+1}}\frac{r_j}{(\bar{r}_{j+1}-\bar{r}_j)}$$

$$\begin{aligned}B_{u2}(j)&=\frac{C_{u1}(j)+C_{u3}(j)}{A_jC_{q1}(j)}=\frac{1}{2\pi a\bar{r}_j\Delta r_j}\left[\frac{\upsilon_{T(j-1)}r_{j-1}}{(\bar{r}_j-\bar{r}_{j-1})}+\frac{\upsilon_{T(j)}r_j}{(\bar{r}_{j+1}-\bar{r}_j)}\right]\\&=B_{u1}(j+1)+B_{u3}(j-1)\end{aligned}$$

$$B_q(j)=\frac{1}{C_{q1}(j)}=\frac{g}{a^2\Delta t}\bar{r}_j\Delta r_j;\quad B_c=\frac{a}{gA_jC_{q1}(j)}=\frac{1}{2\pi a\Delta t}$$

Using the assumptions given in system (7), defining the total flow in pipe section (Q_{tot}) as

$$Q_{\text{tot}}=\sum_{j=1}^{\mathrm{N_r}}Q_j$$

adding Eqs. (10) and (11) from $j=1$ to $j=\mathrm{N_r}$ gives

$$H_p^{n+1}+\frac{a}{gA}(Q_{\text{tot}})_p^{n+1}=H_A^n+\frac{a}{gA}(Q_{\text{tot}})_A^n \tag{12}$$

$$H_p^{n+1}-\frac{a}{gA}(Q_{\text{tot}})_p^{n+1}=H_B^n-\frac{a}{gA}(Q_{\text{tot}})_B^n \tag{13}$$

Equations (12) and (13) are analogous in form to the 1D case and can easily solve H_p^{n+1} (and also the pipe flowrate $(Q_{\text{tot}})_p^{n+1}$)

$$\mathbf{RH}=\mathbf{B} \tag{14}$$

where $\mathbf{H}=\{H^{n+1},Q_{\text{tot}}^{n+1}\}^T$, $\mathbf{R}$, and $\mathbf{B}$ are the coefficient matrices from Eqs. (12) and (13).

Having Eq. (14), Eqs. (10) and (11) become

$$\begin{aligned}&-\varepsilon B_{u1}^s(j)Q_{p,j-1}^{n+1,s}+\lfloor B_c^s+\varepsilon B_{u2}^s(j)\rfloor Q_{p,j}^{n+1,s}-\varepsilon B_{u3}^s(j)Q_{p,j+1}^{n+1,s}\\&\quad-\theta\lfloor q_{p,j-1}^{n+1,s}-q_{p,j}^{n+1,s}]\\&\quad=\{B_q^s(j)H_{m-1}^{n,s}+(1-\varepsilon)B_{u1}^s(j)Q_{m-1,j-1}^{n,s}\\&\quad+[B_c^s-(1-\varepsilon)B_{u2}^s(j)]Q_{m-1,j}^{n,s}+(1-\varepsilon)B_{u3}^s(j)Q_{m-1,j+1}^{n,s}\\&\quad+(1-\theta)[q_{m-1,j-1}^{n,s}-q_{m-1,j}^{n,s}]-B_q^s(j)H_p^{n+1,s}\}\end{aligned} \tag{15}$$

$$\begin{aligned}&\varepsilon B_{u1}^{s+1}(j)Q_{p,j-1}^{n+1,s+1}-\lfloor B_c^{s+1}+\varepsilon B_{u2}^{s+1}(j)\rfloor Q_{p,j}^{n+1,s+1}+\varepsilon B_{u3}^{s+1}(j)Q_{p,j+1}^{n+1,s+1}\\&\quad-\theta\lfloor q_{p,j-1}^{n+1,s+1}-q_{p,j}^{n+1,s+1}]\\&\quad=\{B_q^{s+1}(j)H_1^{n,s+1}-(1-\varepsilon)B_{u1}^{s+1}(j)Q_{1,j-1}^{n,s+1}\\&\quad-[B_c^{s+1}-(1-\varepsilon)B_{u2}^{s+1}(j)]Q_{1,j}^{n,s+1}-(1-\varepsilon)B_{u3}^{s+1}(j)Q_{1,j+1}^{n,s+1}\\&\quad+(1-\theta)[q_{1,j-1}^{n,s+1}-q_{1,j}^{n,s+1}]-B_q^{s+1}(j)H_p^{n+1,s+1}\}\end{aligned} \tag{16}$$

Then, Eqs. (15) and (16) will get

$$E_{j1}Q_{p,j-1}^{n+1}+E_{j2}Q_{p,j}^{n+1}+E_{j3}Q_{p,j+1}^{n+1}=W_j \tag{17}$$

in which E_{ji} and W_j are the coefficients that depend on $B_{ui}(j)$, $B_q(j)$, ε, θ, and some known hydraulic state parameters, as stated above.

Rewriting Eq. (17) in matrix form gives

$$\mathbf{LQ}=\mathbf{W} \tag{18}$$

where $\mathbf{Q}=\{Q_{p,1}^{n+1},\ldots,Q_{p,j}^{n+1},\ldots,Q_{p,\mathrm{N_r}}^{n+1}\}^T$, $\mathbf{W}$ is the known vector, and $\mathbf{L}$ is the coefficient tridiagonal $\mathrm{N_r}\times\mathrm{N_r}$ matrix.

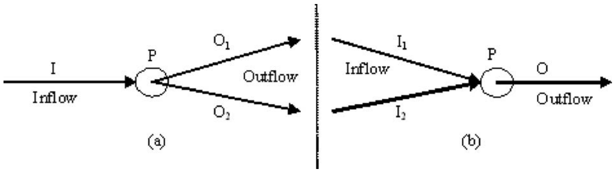

Fig. 3 Branch junction system

$$\mathbf{L}=\begin{pmatrix}E_{1,2} & E_{1,3} & & \cdots & & \cdots\\ & \vdots & & \vdots & & \vdots\\ \cdots & E_{j,1} & E_{j,2} & E_{j,3} & & \cdots\\ & \vdots & & \vdots & & \vdots\\ \cdots & & \cdots & & E_{\mathrm{N_r},1} & E_{\mathrm{N_r},2}\end{pmatrix}_{\mathrm{N_r}\times\mathrm{N_r}}$$

Once Q is known, Eq. (15) (or Eq. (16)) is used to calculate q. This is accomplished by subtracting the equation for the jth cylinder from that for the $(j+1)$ cylinder, which gives

$$\theta q_{p,j-1}^{n+1}-2\theta q_{p,j}^{n+1}+\theta q_{p,j+1}^{n+1}=J_j \tag{19}$$

The matrix form of Eq. (19) is as follows:

$$\mathbf{Kq}=\mathbf{J} \tag{20}$$

where $\mathbf{q}=\{q_{p,1}^{n+1},\ldots,q_{p,j}^{n+1},\ldots,q_{p,\mathrm{N_r}-1}^{n+1}\}^T$, $\mathbf{J}$ is the known vector, $\mathbf{K}$ is the coefficient tridiagonal $(\mathrm{N_r}-1)\times(\mathrm{N_r}-1)$ matrix as follows:

$$\mathbf{K}=\begin{pmatrix}-2\theta & \theta & \cdots & & \cdots\\ \theta & -2\theta & \theta & \cdots & \\ \vdots & & \vdots & & \vdots\\ \cdots & \theta & -2\theta & \theta & \\ \vdots & & \vdots & & \vdots\\ \cdots & & \cdots & \theta & -2\theta\end{pmatrix}_{(\mathrm{N_r}-1)\times(\mathrm{N_r}-1)}$$

Consequently, the series system could be solved by Eqs. (14), (18), and (20).

3.2 Branching Pipe Systems.

Since the cases in Figs. 3(a) and 3(b) are similar in principle; however, here, just the case in Fig. 3(a) is taken to demonstrate how the boundary condition is derived. The first two assumptions given in Eq. (7) remain valid here. The characteristic relation for the inflow and outflow are

$$\begin{aligned}&B_q^I(j)H_m^{n+1,I}-\varepsilon B_{u1}^I(j)Q_{m,j-1}^{n+1,I}+\lfloor B_c^I+\varepsilon B_{u2}^I(j)\rfloor Q_{m,j}^{n+1,I}-\varepsilon B_{u3}^s(j)Q_{m,j+1}^{n+1,I}\\&\quad-\theta\lfloor q_{m,j-1}^{n+1,I}-q_{m,j}^{n+1,I}]\\&\quad=\{B_q^I(j)H_{m-1}^{n,I}+(1-\varepsilon)B_{u1}^I(j)Q_{m-1,j-1}^{n,I}\\&\quad+[B_c^I-(1-\varepsilon)B_{u2}^I(j)]Q_{m-1,j}^{n,I}+(1-\varepsilon)B_{u3}^I(j)Q_{m-1,j+1}^{n,I}\\&\quad+(1-\theta)[q_{m-1,j-1}^{n,I}-q_{m-1,j}^{n,I}]\}\end{aligned} \tag{21}$$

$$\begin{aligned}&B_q^O(j)H_0^{n+1,O}+\varepsilon B_{u1}^O(j)Q_{0,j-1}^{n+1,O}-\lfloor B_c^O+\varepsilon B_{u2}^O(j)\rfloor Q_{0,j}^{n+1,O}\\&\quad+\varepsilon B_{u3}^O(j)Q_{0,j+1}^{n+1,O}-\theta\lfloor q_{0,j-1}^{n+1,O}-q_{0,j}^{n+1,O1}]\\&\quad=\{B_q^O(j)H_1^{n,O}-(1-\varepsilon)B_{u1}^O(j)Q_{1,j-1}^{n,O}-[B_c^O-(1-\varepsilon)B_{u2}^O(j)]Q_{1,j}^{n,O1}\\&\quad-(1-\varepsilon)B_{u3}^O(j)Q_{1,j+1}^{n,O}+(1-\theta)[q_{1,j-1}^{n,O}-q_{1,j}^{n,O}]\}\end{aligned} \tag{22}$$

Similar to Eqs. (12)–(14), it can easily get

$$\mathbf{RH}=\mathbf{S} \tag{23}$$

where $\mathbf{H}=\{H^{n+1},Q_{\text{tot}}^{n+1}\}^T$, $\mathbf{R}$, and $\mathbf{S}$ are the coefficient matrices, the superscript I and O are the inflow pipe and outflow pipe, and $O=1,2$.

According to continuity laws at the junction,

$$Q_{m,j-1}^{n+1,I} = Q_{0,j-1}^{n+1,O1} + Q_{0,j-1}^{n+1,O2} \tag{24}$$

Substituting Eqs. (23) and (24) into Eqs. (21) and (22), then applying the assumptions and canceling the $[q_{p,j-1}^{n+1} - q_{p,j}^{n+1}]$ term, will get

$$\begin{aligned}(2\alpha_{j1} - \beta_{j1})Q_{0,j-1}^{n+1,O1} + (2\alpha_{j1} - \gamma_{j1})Q_{0,j-1}^{n+1,O2} + (2\alpha_{j2} - \beta_{j2})Q_{0,j}^{n+1,O1} \\ + (2\alpha_{j2} - \gamma_{j2})Q_{0,j}^{n+1,O2} + (2\alpha_{j3} - \beta_{j3})Q_{0,j+1}^{n+1,O1} + (2\alpha_{j3} \\ - \gamma_{j3})Q_{0,j+1}^{n+1,O2} = 2A_j - C_{1j} - C_{2j}\end{aligned} \tag{25}$$

$$\begin{aligned}\beta_{j1}Q_{0,j-1}^{n+1,O1} - \gamma_{j1}Q_{0,j-1}^{n+1,O2} + \beta_{j2}Q_{0,j}^{n+1,O1} - \gamma_{j2}Q_{0,j}^{n+1,O2} + \beta_{j3}Q_{0,j+1}^{n+1,O1} \\ - \gamma_{j3}Q_{0,j+1}^{n+1,O2} = C_{1j} - C_{2j}\end{aligned} \tag{26}$$

in which α_{ji}, β_{ji}, γ_{ji}, A_j, and C_{kj} are the coefficients that depend on the former $B_{ui}(j)$, $B_q(j)$, ε, θ, and some known hydraulic state parameters.

Rewriting Eqs. (25) and (26) into matrix form will get

$$\mathbf{LQ} = \mathbf{W} \tag{27}$$

where $\mathbf{Q} = \{Q_{p,1}^{n+1,O1}, Q_{p,1}^{n+1,O2}, \ldots, Q_{p,j}^{n+1,O1}, Q_{p,j}^{n+1,O2}, \ldots, Q_{p,\mathrm{N_r}}^{n+1,O1}, Q_{p,\mathrm{N_r}}^{n+1,O2}\}^T$, $\mathbf{W}$ is the known vector, and $\mathbf{L}$ is a diagonal $2\mathrm{N_r} \times 2\mathrm{N_r}$ matrix as

$$\begin{pmatrix}
(2\alpha_{12} - \beta_{12}) & (2\alpha_{12} - \gamma_{12}) & (2\alpha_{13} - \beta_{13}) & (2\alpha_{13} - \gamma_{13}) & \cdots & & \cdots \\
\beta_{12} & -\gamma_{12} & \beta_{13} & -\gamma_{13} & & \cdots & \\
 & \vdots & & & \vdots & & \vdots \\
\cdots & (2\alpha_{j1} - \beta_{j1}) & (2\alpha_{j1} - \gamma_{j1}) & (2\alpha_{j2} - \beta_{j2}) & (2\alpha_{j2} - \gamma_{j2}) & (2\alpha_{j3} - \beta_{j2}) & (2\alpha_{j3} - \gamma_{j2})\cdots \\
 & \beta_{j1} & -\gamma_{j1} & \beta_{j2} & -\gamma_{j2} & \beta_{j2} & -\gamma_{j3}\cdots \\
\vdots & \vdots & & & \vdots & & \vdots \\
 & & & (2\alpha_{\mathrm{N_r}1} - \beta_{\mathrm{N_r}1}) & (2\alpha_{\mathrm{N_r}1} - \gamma_{\mathrm{N_r}1}) & (2\alpha_{\mathrm{N_r}2} - \beta_{\mathrm{N_r}2}) & (2\alpha_{\mathrm{N_r}2} - \gamma_{\mathrm{N_r}2}) \\
\cdots & \cdots & & \beta_{\mathrm{N_r}1} & -\gamma_{\mathrm{N_r}1} & \beta_{\mathrm{N_r}2} & -\gamma_{\mathrm{N_r}2}
\end{pmatrix}$$

Equation (27) can be easily solved by the Gauss elimination method or banded decomposition method. So far, the axial flowrates of all sections in each pipe have been obtained.

Similar to the former series pipe case, using Eq. (21) (or Eq. (22)) to calculate q gives

$$\theta q_{p,j-1}^{n+1} - 2\theta q_{p,j}^{n+1} + \theta q_{p,j+1}^{n+1} = J_j \tag{28}$$

the matrix form as

$$\mathbf{Kq} = \mathbf{J} \tag{29}$$

where $\mathbf{q} = \{q_{p,1}^{n+1}, \ldots, q_{p,j}^{n+1}, \ldots, q_{p,\mathrm{N_r}-1}^{n+1}\}^T$, $\mathbf{J}$ is the known matrix, and $\mathbf{K}$ is the same coefficient matrix as in Eq. (20).

As a result, the branching system could be solved by Eqs. (23), (27), and (29).

4 Numerical Stability Analysis

Zhao and Ghidaoui [8] derived the stability criteria for the efficient scheme for the particular case where the Courant number is 1 (i.e., $C_r = 1$). The condition $C_r = 1$ is almost never satisfied in multiple pipe systems when the fixed grid method of characteristics (FGMOCs) is used to solve the flow equations in such systems [12–14]. The following derivation provides the stability criterion for the efficient scheme as the function of C_r for the FGMOC with space line interpolation (see Fig. 4).

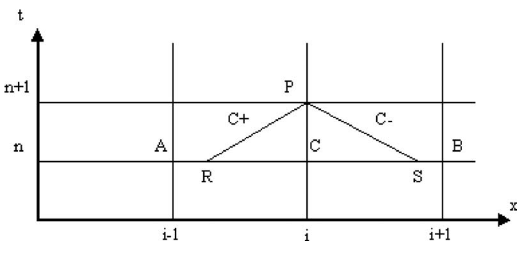

Fig. 4 Interpolation scheme of specified time interval

Using the space line interpolation, the values at point R and S can be obtained by [15]

$$Q_R \approx Q_C - \frac{\Delta t}{\Delta x}a(Q_C - Q_A), \quad q_R \approx q_C - \frac{\Delta t}{\Delta x}a(q_C - q_A)$$

$$H_R \approx H_C - \frac{\Delta t}{\Delta x}a(H_C - H_A)$$

$$Q_S \approx Q_C - \frac{\Delta t}{\Delta x}a(Q_C - Q_B), \quad q_S \approx q_C - \frac{\Delta t}{\Delta x}a(q_C - q_B)$$

$$H_S \approx H_C - \frac{\Delta t}{\Delta x}a(H_C - H_B)$$

in which Δt and Δx are the time step and the pipe reach.

The radial momentum in the quasi-2D model, which amounts to the pressure being invariant with the radius, can be written as follows:

$$\frac{\partial H}{\partial r} + \frac{1}{Gg}\frac{\partial v}{\partial t} = 0 \quad \text{with} \quad G \to \infty \tag{30}$$

By applying the Von Neumann's stability analysis [16], the head and velocities are given by the Fourier modes.

$$H_{i,j}^n = h^n e^{ik_x x} e^{ik_y y}; \quad u_{i,j}^n = u^n e^{ik_x x} e^{ik_y y}; \quad v_{i,j}^n = v^n e^{ik_x x} e^{ik_y (y + \Delta y/2)}$$

where $\boldsymbol{i}$ is the complex number with $\boldsymbol{i}^2 = -1$, and y is the Cartesian coordinate system $y = R - r$. Substituting these relations into the discrete forms of Eqs. (1), (2), and (30) gives

$$h^{n+1}+\left[\theta\frac{a^2\Delta t}{g\Delta y}i2\sin\frac{\beta}{2}\right]v^{n+1}$$
$$=\left[\left(1-a\frac{\Delta t}{\Delta x}\right)+a\frac{\Delta t}{\Delta x}\cos\alpha\right]h^n-\left[a\frac{\Delta t}{\Delta x}\frac{a^2\Delta t}{g\Delta x}i\sin\alpha\right]u^n$$
$$-\left[(1-\theta)\frac{a^2\Delta t}{g\Delta y}i2\sin\frac{\beta}{2}\right]\left[\left(1-a\frac{\Delta t}{\Delta x}\right)+a\frac{\Delta t}{\Delta x}\cos\alpha\right]v^n \tag{31}$$

$$\left[1-\varepsilon\frac{\upsilon_T\Delta t}{(\Delta y)^2}(2\cos\beta-2)\right]u^{n+1}$$
$$=-\left[a\frac{\Delta t}{\Delta x}\frac{g\Delta t}{\Delta x}i\sin\alpha\right]h^n-\left[1+(1-\varepsilon)\frac{\upsilon_T\Delta t}{(\Delta y)^2}(2\cos\beta-2)\right]$$
$$\times\left[\left(1-a\frac{\Delta t}{\Delta x}\right)+a\frac{\Delta t}{\Delta x}\cos\alpha\right]u^n \tag{32}$$

$$v^{n+1}=-\left[\frac{Gg\Delta t}{\Delta y}i2\sin\frac{\beta}{2}\right]\left[\left(1-a\frac{\Delta t}{\Delta x}\right)+a\frac{\Delta t}{\Delta x}\cos\alpha\right]h^n$$
$$+\left[\left(1-a\frac{\Delta t}{\Delta x}\right)+a\frac{\Delta t}{\Delta x}\cos\alpha\right]v^n \tag{33}$$

where θ and ε are the weighting coefficients, $\alpha=k_x\Delta x$, $\beta=k_y\Delta y$, and

$$\cos\alpha=1/2(e^{i\alpha}+e^{-i\alpha}),\quad \cos\beta=1/2(e^{i\beta}+e^{-i\beta}),$$

$$\sin\alpha=1/2i(e^{i\alpha}-e^{-i\alpha}),\quad \sin\beta=1/2i(e^{i\beta}-e^{-i\beta})$$

After some algebraic manipulations, one gets

$$\mathbf{z^{n+1}}=\mathbf{Fz^n} \tag{34}$$

where $z=\{h,u,v\}^T$, and $\mathbf{F}$ is the amplification factor matrix.

$$\mathbf{F}=\begin{pmatrix} \phi-\phi\dfrac{\theta G\left(a\Delta t2\sin\dfrac{\beta}{2}\right)^2}{(\Delta y)^2} & -a\dfrac{\Delta t}{\Delta x}\dfrac{a^2\Delta t}{g\Delta x}i\sin\alpha & -\phi\dfrac{a^2\Delta t}{g\Delta y}i2\sin\dfrac{\beta}{2} \\ \dfrac{-a\dfrac{\Delta t}{\Delta x}\dfrac{a^2\Delta t}{g\Delta x}i\sin\alpha}{1-\varepsilon\dfrac{\upsilon_T\Delta t}{(\Delta y)^2}(2\cos\beta-2)} & \dfrac{\phi\left[1+(1-\varepsilon)\dfrac{\upsilon_T\Delta t}{(\Delta y)^2}(2\cos\beta-2)\right]}{1-\varepsilon\dfrac{\upsilon_T\Delta t}{(\Delta y)^2}(2\cos\beta-2)} & 0 \\ -\phi\dfrac{Gg\Delta t}{\Delta y}i2\sin\dfrac{\beta}{2} & 0 & \phi \end{pmatrix}$$

in which

$$\phi=\left[\left(1-a\frac{\Delta t}{\Delta x}\right)+a\frac{\Delta t}{\Delta x}\cos\alpha\right]$$

The eigenvalues $\boldsymbol{\lambda}$ and $\mathbf{F}$ are given by

$$|\mathbf{F}-\boldsymbol{\lambda}\mathbf{I}|=0 \tag{35}$$

The limit of Eq. (35) as G tends to infinity gives

$$\lambda^2-\phi\left[\frac{1+(1-\varepsilon)\dfrac{\upsilon_T\Delta t}{(\Delta y)^2}(2\cos\beta-2)}{1-\varepsilon\dfrac{\upsilon_T\Delta t}{(\Delta y)^2}(2\cos\beta-2)}+\left(1-\frac{1}{\theta}\right)\right]\lambda$$
$$+\phi^2\frac{1+(1-\varepsilon)\dfrac{\upsilon_T\Delta t}{(\Delta y)^2}(2\cos\beta-2)}{1-\varepsilon\dfrac{\upsilon_T\Delta t}{(\Delta y)^2}(2\cos\beta-2)}\left(1-\frac{1}{\theta}\right)=0$$

which leads to

$$\lambda_1=\left[\left(1-a\frac{\Delta t}{\Delta x}\right)+a\frac{\Delta t}{\Delta x}\cos\alpha\right]\left[1-\frac{1}{\theta}\right]$$

$$\lambda_2=\left[\left(1-a\frac{\Delta t}{\Delta x}\right)+a\frac{\Delta t}{\Delta x}\cos\alpha\right]\frac{1+(1-\varepsilon)\dfrac{\upsilon_T\Delta t}{(\Delta y)^2}(2\cos\beta-2)}{1-\varepsilon\dfrac{\upsilon_T\Delta t}{(\Delta y)^2}(2\cos\beta-2)}$$

The numerical stability conditions for the above models are

$$|\lambda_1|\le 1,\quad |\lambda_2|\le 1$$

that is,

$$|(1-C_r+C_r\cos\alpha)|\cdot\left|\left(1-\frac{1}{\theta}\right)\right|\le 1$$

$$|(1-C_r+C_r\cos\alpha)|\cdot\left|\frac{1+(1-\varepsilon)\dfrac{\upsilon_T\Delta t}{(\Delta y)^2}(2\cos\beta-2)}{1-\varepsilon\dfrac{\upsilon_T\Delta t}{(\Delta y)^2}(2\cos\beta-2)}\right|\le 1 \tag{36}$$

in which $C_r=a\Delta t/\Delta x$ is the Courant number.

Therefore, the stability domain for the extended 2D model is controlled mutually by the parameters C_r, θ, and ε from the inequations in Eq. (36). The inequalities are satisfied if

$$|(1-C_r+C_r\cos\alpha)|\le 1,\qquad \left|\left(1-\frac{1}{\theta}\right)\right|\le 1\quad\text{and}$$

$$\left|\frac{1+(1-\varepsilon)\dfrac{\upsilon_T\Delta t}{(\Delta y)^2}(2\cos\beta-2)}{1-\varepsilon\dfrac{\upsilon_T\Delta t}{(\Delta y)^2}(2\cos\beta-2)}\right|\le 1$$

This leads to the following stability criteria for the efficient conditions when used in conjunction with the FGMOC with space line interpolation:

$$C_r\le 1 \tag{37}$$

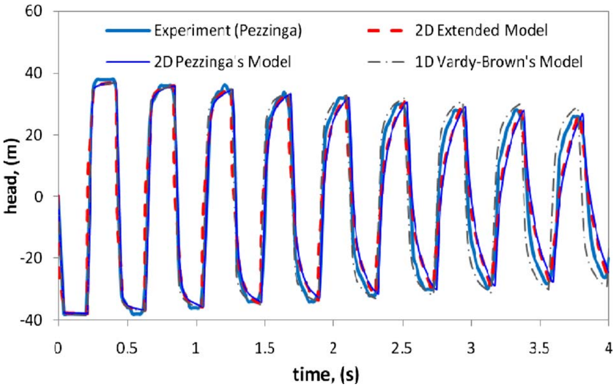

Fig. 5 Piezometric head for case A1

$$0.5 \leq \theta \leq 1 \tag{38}$$

$$0.5 \leq \varepsilon \leq 1 \quad \text{or} \quad 0 \leq \varepsilon \leq 0.5, \quad \frac{\upsilon_T \Delta t}{(\Delta y)^2} \leq \frac{1}{2-4\varepsilon} \tag{39}$$

In the following simulations of this paper, to satisfy the numerical stability conditions, the parameters are set as $\varepsilon = \theta = 1$; C_r is large enough but $C_r \leq 1$ for all pipes (e.g., for single pipe system $C_r = 1$; for complex multipipe system, let $C_r \leq 1$ but get the largest time step Δt for all pipes for given N_x value).

5 Verification of Extended Model

The experimental cases here are extracted from Pezzinga's investigation [2] for the verification of the extended quasi-2D model. Meanwhile, the accuracy and efficiency could be compared for the proposed model and Pezzinga's model. The cases A1 and G4 from the total of 14 experimental cases are taken for the investigation of a single and branching pipe system, respectively.

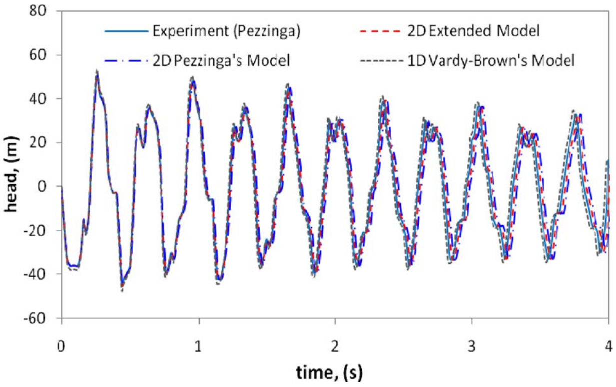

Fig. 6 Piezometric head for case G4

Table 1 CPU time consumption for different models

	Extended model (min)	Pezzinga's model (min)	Original 2D Vardy–Hwang model (h)	1D Vardy–Brown model (h)
Single pipe	11	21	5.2	>50
Series pipe	13	28	7.1	
Network	21	45	9.4	

The results are shown in Figs. 5 and 6. Under the same initial and boundary conditions (as in Ref. [2]) and computation environment (e.g., on the same personal computer), the efficiency evaluation by the CPU time consumption for the different models is shown in Table 1.

From the results in Figs. 5 and 6, it is found that these three models have the similar accuracy (the result curves are nearly on top of each other). Combining with the result of Table 1, it can be concluded that: First, the extended efficient quasi-2D model is improved greatly in simulation efficiency compared with the original 2D Vardy–Hwang model. Second, compared with Pezzinga's model, the extended model has the same accuracy but its efficiency is higher (i.e., more than two times faster than latter). Furthermore, both of these two quasi-2D models are much faster than the weighting-function based model (e.g., 1D Vardy–Brown unsteady friction model [7]).

6 Application of Extended Model

6.1 Simulation and Results

6.1.1 Case T1. Test case T1 is a single pipe system (see Fig. 7), and it is listed here just for the comparison with the following two complex pipe systems. Relevant geometric and hydraulic parameters for both pipes are shown in Table 2. The initial flow rate at the valve is 0.114 l/s, and the viscosity is $1.0 \times 10^{-06}\ \text{m}^2/\text{s}$. The

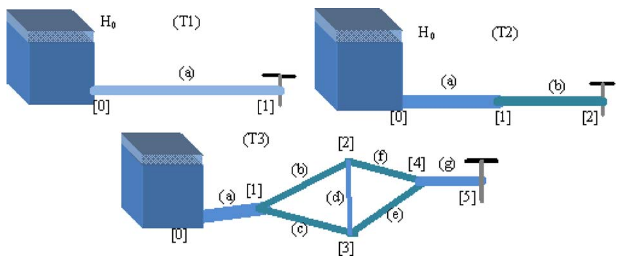

Fig. 7 Systems for the three test cases

Table 2 System information for three cases

Case No.	Pipe No.	Diameter (mm)	Length (m)	Wavespeed (m/s)	Initial velocity (m/s)	Reservoir head (m)	N_x/N_r (min)	Cause of transient
T1	(a)	22	37.2	1276	0.30	32.0	50/50	Sudden full closure of valve
T2	(a)	30	30	1200	0.16	32.0	50/50	
	(b)	22	37.2	1276	0.30			
T3	(a)	30	30	1200	0.16	32.0	50/50	
	(b)	16	20	1000	0.29			
	(c)	16	30	1500	0.28			
	(d)	12	20	1000	0.11			
	(e)	18	30	1200	0.27			
	(f)	15	30	1000	0.26			
	(g)	22	37.2	1276	0.3			

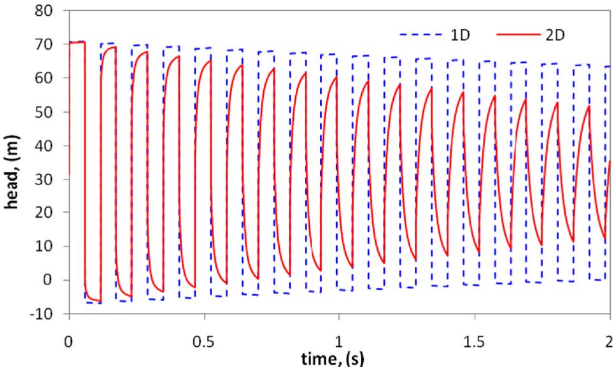

Fig. 8 Pressure head traces at the node [1] for case T1

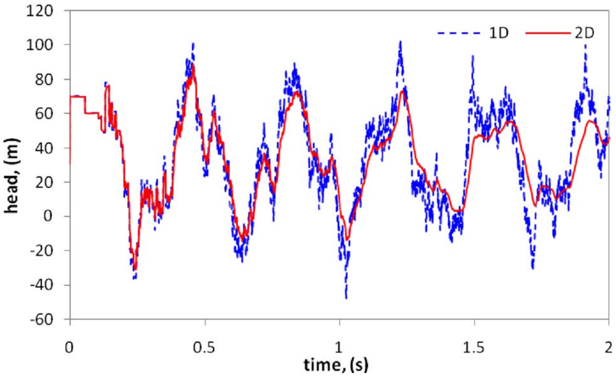

Fig. 10 Pressure head traces at the node [5] for case T3

simulation time interval is $t=2$ s; the precision of convergence is defined by the relative difference between two continuous calculation steps: eps=0.001.

The transient is generated by a sudden full closure of the valve at the node [1]. The pressure head traces at the node [1], obtained by the classical 1D model with the quasisteady friction model and the proposed efficient 2D model, are plotted in Fig. 8. The total CPU execution time of the 2D model is about 4.3 s on a P4 2.0 GHz personal computer.

6.1.2 Case T2. Test case T2 involves two pipes in the series, as sketched in Fig. 7. Relevant geometric and hydraulic parameters for both pipes are also shown in Table 2. Some other parameters of hydraulics and simulation are similar to the above case in T1.

The transient is generated by a sudden full closure of the valve at the node [2]. The pressure head traces at the node [2], obtained by classical 1D model and the proposed 2D model, are plotted in Fig. 9. The total execution time of the 2D model is about 10.3 s on a P4 2.0 GHz personal computer.

6.1.3 Case T3. Test case T3 (Fig. 7 and Table 2) is used here to illustrate the applicability as well as the efficiency of the scheme for networks. The other parameters are the same to be set as cases T1 and T2. Similar to cases T1 and T2, the transient is generated by a sudden full closure of the valve at the node [5]. The pressure head traces at the node [5], obtained by the two models, are plotted in Fig. 10. The total execution time is about 63.7 s on the above same personal computer.

6.2 Observations. As expected, the results of the 1D and 2D models for both cases are very similar for the first few (about one or two) wave cycles, and began to depart from one another as the simulation time increases beyond the third and fourth wave cycles. Such departure is due to the fact that the 1D model does not incorporate the unsteady friction effects. In addition, it is important to note that the 2D simulation takes a very short time. For example, on a P4 2.0 GHz personal computer, the execution time of the 2D model for cases T2 and T3 are about 10 s and 64 s, respectively. The short computational time means that the 2D efficient model is a viable tool for research and practice in the waterhammer field.

It is worthwhile to look into the difference between the 1D and 2D results in more details. Let this difference be defined by

$$D(t)=\frac{|(H_{1\mathrm{D}})_t^p-(H_{2\mathrm{D}})_t^p|}{|(H_{1\mathrm{D}})_t^p|}\times 100\% \qquad (40)$$

in which $(H)_t^p$ is the pressure head peak at or nearby the time t, subscripts 1D and 2D are the value from the 1D and 2D models, respectively, and $D(t)$ is the percentage of difference.

The changing percentages of difference between these two models for these three cases are plotted in Fig. 11. This implies that unsteady friction effects are more pronounced for the network case. To explain, it is noted that the wave frequency for the network case is larger than the series pipe or single pipe cases (see Fig. 12) due to the many reflections that occur from the junctions of the network. As a result, for a given time interval, the network case exhibits more excitations, which changes the velocity more frequently, and thus produces more wall unsteady shear pulses. In addition, the time interval between consecutive excitations is shorter for the network problem, and thus, less time for the unsteady friction component to relax and become small.

Extensive numerical testing indicates that in addition to stability conditions in Eqs. (37)–(39), the following empirical but not required condition $0.1N_x \leq \mathrm{N}_r \leq 10N_x$ is suggested to ensure the stability of program code for the cases of interest here.

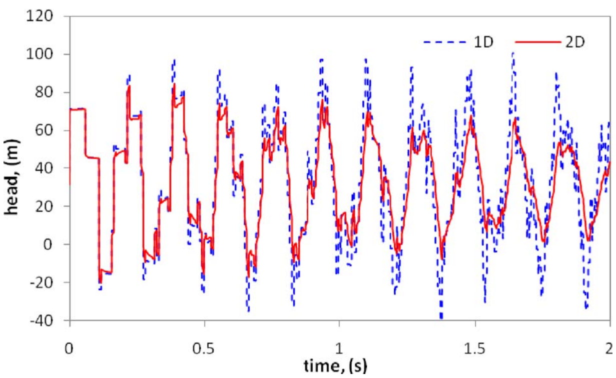

Fig. 9 Pressure head traces at the node [2] caseT2

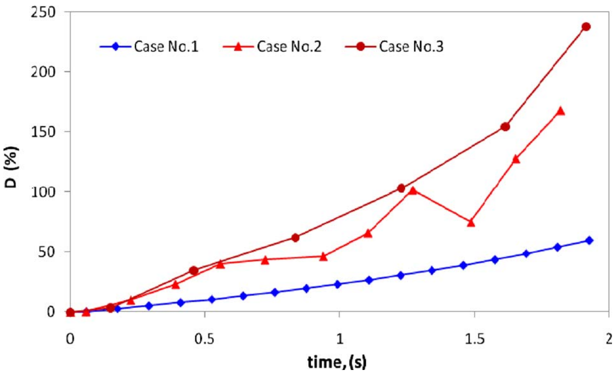

Fig. 11 Difference of pressure head peak at valve by 1D and 2D models

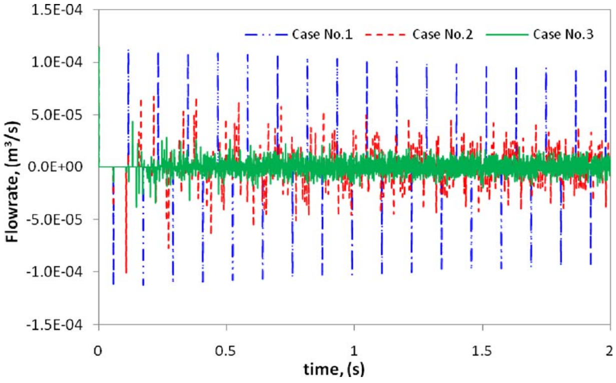

Fig. 12 Flowrate versus time nearby the valve for the three cases

7 Conclusions

An efficient quasi-2D numerical waterhammer model for turbulent waterhammer flows has previously been developed for a single pipe system (reservoir-pipe-valve system). Basic boundary conditions, such as valves, reservoirs, and external flows were also implemented. This paper extends this previously developed efficient scheme to a general model for a multipipe system. More precisely, an approach for matching the family of characteristic equations in each pipe at a junction of two or more pipes is proposed. In addition, the numerical stability conditions of the efficient scheme are investigated using the Von Neumann method. The resulting model is applied to two systems involving pipes in series, and another system involving a pipe network. From the case studies, it is found that the quasi-2D model is highly efficient, robust, and suitable for application to waterhammer problems in real complex pipe systems. For example, on a P4 2.0 GHz personal computer, the execution time of the 2D model for two pipes in series is about 10 s, and for a network with involving seven pipes is about 64 s under the presented setting conditions. This short computational time means that the 2D efficient model is a viable tool for research and practice in the waterhammer field. It is also noted that the effect of unsteady friction is found to be more pronounced for the network cases than that in the simplex system of interest in this paper. This is because of the high frequency of the flow excitations induced by the multitude of reflections from the junctions in the network.

Acknowledgment

The writers would like to thank the Research Council of Hong Kong for the financial support under Grant Nos. 620706 and 613306.

Nomenclature

$\boldsymbol{A},\boldsymbol{B},\boldsymbol{C}$ = coefficient matrix
C_{u1},C_{u2},C_{u3},C_q = coefficient matrix for original model
$B_{u1},\ B_{u2},\ B_{u3},\ B_q$ = coefficient matrix for extended model
C_r = Courant number
D_2 = percentage of difference between 1D and 2D models
E_{ij} = coefficient
$\boldsymbol{F},\boldsymbol{J},\boldsymbol{K},\boldsymbol{L},\boldsymbol{R},\boldsymbol{S},\boldsymbol{W}$ = coefficient matrix
$\boldsymbol{H},\boldsymbol{Q},\boldsymbol{U},\boldsymbol{V}$ = unknown vectors
G = infinite constant
H = piezometric head
$\boldsymbol{I}$ = unit matrix
Nr = number of radial sections
Q = flowrate variable
a = wavespeed
$\boldsymbol{b},\boldsymbol{b_u},\boldsymbol{b_v}$ = coefficient vector
g = gravitational acceleration
$\boldsymbol{i}$ = complex number
q = radial flowrate
$\boldsymbol{q},\boldsymbol{z}$ = unknown vectors
u,v = axial, radial velocity components
u',v' = axial, radial velocity fluctuations
x,r,t = axial, longitudinal coordinates
α,β,γ = constant coefficient
$\Delta x,\Delta r,\Delta t$ = step length in axial, radial, and temporal directions
$\boldsymbol{\lambda}$ = matrix eigenvalues
ε,θ = weight coefficient
ν,ν_t,ν_T = kinematic, eddy, and total viscosities
ρ = water density
τ = shear stress

Superscripts

O, I = out and in for pipe direction
^{n} = time step
$^{s,s+1}$ = time step

Subscripts

1D, 2D = 1D, 2D model
$_P$ = present axial position
$_{i,j,0,m}$ = axial position index

References

[1] Eichenger, P., and Lein, G., 1992, "The Influence of Friction on Unsteady Pipe Flow," *Unsteady Flow and Fluid Transients*, R. Bettes and, J. Watts, eds., Balkema, Rotterdam, The Netherlands, pp. 41–50.

[2] Pezzinga, G., 1999, "Quasi-2D Model for Unsteady Flow in Pipe Networks," J. Hydraul. Eng., **125**(7), pp. 676–685.

[3] Pezzinga, G., 2000, "Evaluation of Unsteady Flow Resistances by Quasi-2D or 1D Models," J. Hydraul. Eng., **126**(10), pp. 778–785.

[4] Rodi, W., 1993, "Turbulence Model and Their Application in Hydraulic Engineering: A State-of-the-Art Review," *IAHR, Delft*, 3rd ed., Balkema, Rotterdam, The Netherlands.

[5] Silva-Araya, W. F., and Chaudhry, M. H., 1997, "Computation of Energy Dissipation in Transient Flow," J. Hydraul. Eng., **123**(2), pp. 108–115.

[6] Vardy, A. E., and Hwang, K. L., 1991, "A Characteristics Model of Transient Friction in Pipes," J. Hydraul. Res., **29**(5), pp. 669–684.

[7] Vardy, A. E., Hwang, K. L., and Brown, J. M. B., 1993, "A Weighting Function Model of Transient Turbulent Pipe Friction," J. Hydraul. Res., **31**(4), pp. 533–548.

[8] Zhao, M., and Ghidaoui, M. S., 2003, "Efficient Quasi-Two-Dimensional Model for Water Hammer Problems," J. Hydraul. Eng., **129**(12), pp. 1007–1013.

[9] Zhao, M., and Ghidaoui, M. S., 2006, "Investigation of Turbulence Behavior in Pipe Transients Using a $\kappa-\varepsilon$ Model," J. Hydraul. Res., **44**(5), pp. 682–692.

[10] Ghidaoui, M. S., Zhao, M., McInnis, D. A., and Axworthy, D. H., 2005, "A Review of Water Hammer Theory and Practice," Appl. Mech. Rev., **58**(1), pp. 49–76.

[11] Nixon, W., 2005, "Unsteady Friction Under the Influence of External Flows, and the Implications to Transient-Based Leak Detection Methods," MS thesis, Hong Kong University of Science and Technology, Hong Kong, SAR China.

[12] Chaudhry, M. H., 1987, *Applied Hydraulic Transients*, Van Nostrand Reinhold, New York.

[13] Lister, M., 1960, "The Numerical Solution of Hyperbolic Partial Differential Equations by the Method of Characteristics," *Mathematical Methods of Digital Computers*, A. Ralston and H. S. Wilf, eds., Wiley, New York, pp. 165–179.

[14] Wiggert, D. C., and Sundquist, M. J., 1977, "Fixed-Grid Characteristics for Pipeline Transient," J. Hydr. Div., **103**(HY12), pp. 1403–1415.

[15] Streeter, V. L., and Wylie, E. B., 1967, *Hydraulic Transients*, McGraw-Hill, New York.

[16] Anderson, D. A., Tannehill, J. C., and Pletcher, R. H., 1984, *Computational Fluid Mechanics and Heat Transfer*, Hemisphere, New York.

Subrahmanya P. Veluri[1]
e-mail: veluris@vt.edu

Christopher J. Roy

Department of Aerospace and Ocean Engineering,
Virginia Tech,
215 Randolph Hall,
Blacksburg, VA 24061

Anwar Ahmed

Rifki Rifki

John C. Worley

Bryan Recktenwald

Department of Aerospace Engineering,
Auburn University,
211 Aerospace Engineering Building,
Auburn, AL 36849-5338

Joint Computational/Experimental Aerodynamic Study of a Simplified Tractor/Trailer Geometry

Steady-state Reynolds averaged Navier–Stokes (RANS) simulations are presented for the three-dimensional flow over a generic tractor trailer placed in the Auburn University 3 $\times 4$ ft^2 suction wind tunnel. The width of the truck geometry is 10 in., and the height and length of the trailer are 1.392 and 3.4 times the width, respectively. The computational model of the wind tunnel is validated by comparing the numerical results with the data from the empty wind tunnel experiments. The comparisons include the boundary layer properties at three different locations on the floor of the test section and the flow angularity at the beginning of the test section. Three grid levels are used for the simulation of the truck geometry placed in the test section of the wind tunnel. The coarse mesh consists of 3.4×10^6 cells, the medium mesh consists of 11.2×10^6 cells and the fine mesh consists of 25.8×10^6 cells. The turbulence models used for both the empty tunnel simulations and the truck geometry placed in the wind tunnel are the standard Wilcox 1998 k-ω model, the SST k-ω model, the standard k-ε model, and the Spalart–Allmaras model. The surface pressure distributions on the truck geometry and the overall drag are predicted from the simulations and compared with the experimental data. The computational predictions compared well with the experimental data. This study contributes a new validation data set and computations for high Reynolds number bluff-body flows. The validation data set can be used for initial assessment in evaluating RANS models, which will be used for studying the drag or drag trends predicted by the baseline truck geometries.

[DOI: 10.1115/1.3155995]

1 Introduction

The trucking industry is the backbone of the freight transportation system in the United States. According to 2003 data collected by the U.S. Department of Energy (DOE)[1], there are approximately 2.2×10^6 tractor-trailers operating on U.S. highways. These vehicles average 62,900 miles traveled per year at fuel consumption rate of 5.2 miles/gal, resulting in an estimated consumption of 2.6×10^{10} gal of diesel fuel per year. With current diesel fuel costs near \$3.00/gal, this translates into an annual cost of \$80 billion. In addition to the high costs associated with transporting goods, the U.S. produces only 40% of the oil supplied to refineries. The remaining 60% is imported from other countries, with nearly half of all imports coming from the Organization of the Petroleum Exporting Countries (OPEC).

At typical highway speeds, roughly 60% of the truck engine's energy output goes to overcoming aerodynamic drag [2]. This is due to the fact that aerodynamic drag increases to the square of the vehicle speed, while the rolling resistance between the tires and the road increase linearly with the speed. Because it is such a large portion of the engine energy output at highway speeds, reductions in aerodynamic drag can significantly reduce the vehicle's fuel consumption. For example, a 25% reduction in the aerodynamic drag translates into a roughly 10% decrease in fuel consumed. When applied across the entire trucking industry, a 10% increase in fuel efficiency would save 2.6×10^9 gal of diesel fuel per year, or approximately \$8 billion. To put these numbers in perspective, if we account for the fact that only approximately half of every barrel of crude oil is used to make diesel fuel, the U.S. imported the equivalent of 3.7×10^9 gal of diesel fuel from OPEC in 2003 (nearly half of all U.S. imports). In addition to the economic impact and the implications on oil imports, increases in fuel efficiency also translate directly into reductions in pollution emissions and are thus more environment friendly.

There have been a number of studies, which have examined the aerodynamic drag on tractor-trailers. In the 1970s and 1980s, the majority of this work was experimental in nature. A recent review of this work was presented by Cooper [3], who used both full-scale and subscale truck experiments to study the effects of various aerodynamic drag reduction devices for both the tractor and the trailer. More recently, researchers have also applied modern computational fluid dynamics (CFD) tools to study the aerodynamic drag of tractor-trailers. A recent DOE consortium has focused on both experimental methods and computational approaches to study the aerodynamic drag problem for trucks [2]. Their study resulted in high-quality experimental data at near full-scale Reynolds numbers on two different geometries: the simplified ground transportation system (GTS) model [4], and the more realistic generic conventional model (GCM) [5]. The simplified GTS model is an approximately 1/8 scale, class-8 tractor/trailer configuration, which do not have any truck features on it with a smooth combined surface of the tractor and trailer (Fig. 1). GCM is the representative of the class-8 tractor/trailer with the engine in front of the cab. The tractor geometry is the streamline-shaped representative of a modern tractor design, without most of the small scale surface details. For this model, the tractor-trailer gap is present, but no undercarriage of the tractor or trailer is present, which are replaced by a flat surface and also include the portion of the wheels below the tractor/trailer lower surface. The experiments were designed with the dual purpose of evaluating drag

---

[1] Corresponding author.

Contributed by the Fluids Engineering Division of ASME for publication in the JOURNAL OF FLUIDS ENGINEERING. Manuscript received December 16, 2008; final manuscript received May 13, 2009; published online July 7, 2009. Assoc. Editor: Rajat Mittal.

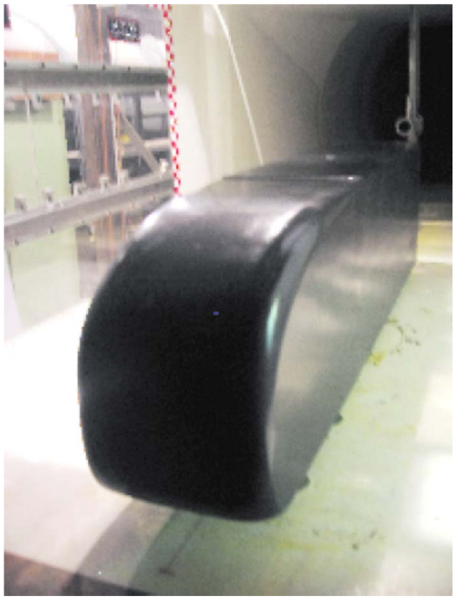

Fig. 1 Flow visualization/force model mounted in the wind tunnel test section

Table 1 List of CFD simulations performed

CFD simulations	Turbulence models	Grids used
Empty wind tunnel	k-ω	Coarse grid (1,569,182 cells)
	SST k-ω	Fine grid (4,643,435 cells)
Truck in wind tunnel	Spalart–Allmaras	Coarse grid (3,385,287 cells)
	k-ε	Medium grid (11,179,943 cells)
	k-ω	Fine grid (25,833,079 cells)
	SST k-ω	

reduction devices and also providing a high-quality experimental database for the validation of the CFD models. The primary modeling uncertainties are related to the choice for the turbulence model. The DOE consortium has examined the Reynolds averaged Navier–Stokes (RANS) approach, where all of the turbulent scales are modeled [6–8], and the large eddy simulation (LES), where the smaller turbulent scales are modeled but the larger scales resolved [9].

Much has been learned in the past 30 years of research on aerodynamic drag reduction for tractor-trailers. Reductions in aerodynamic drag are generally reported in terms of the drag coefficient

$$C_D \frac{D}{\frac{1}{2}\rho_\infty V_\infty^2 S}$$

or possibly the wind-averaged drag coefficient, which accounts for variations in wind velocity and direction [3]. In the expression for the drag coefficient, D is the total drag on the truck, V_∞ is the freestream velocity, ρ_∞ is the freestream density, and S is the frontal surface area of the truck. Drag reduction techniques such as cab side extenders and cab roof air deflectors are commonly found on today's tractor-trailers and have resulted in wind-averaged drag coefficient reductions of up to 0.25 from the baseline value, which is near unity. More advanced techniques such as tractor-trailer gap seals and trailer side skirts are less commonly seen on U.S. highways, but also can provide significant drag reduction. The remaining region where almost no drag reduction devices are found in use is the trailer base (immediately behind the trailer). This region is not aerodynamically efficient as compared with typical aerodynamic shapes (airfoils, tear drop shapes, etc.). Storms et al. [5] showed experimentally that adding boat-tail plates or base flaps can further reduce the wind-averaged drag coefficient by 0.06; however, these add-on devices for the base region are not optimized configurations.

One way to optimize the drag reduction devices is to use CFD within some type of optimization strategy. This approach requires that the CFD tool be able to accurately predict the drag, or at least accurately predict the trends in the drag as the device is changed. The turbulence modeling approach that has the potential to produce the rapid turn-around time for drag reduction predictions is RANS, probably with wall functions used to alleviate the extremely fine wall spacing associated with integration of the turbulence modeling equations to the wall. The RANS turbulence modeling approach has been shown to accurately predict the drag for baseline configurations (i.e., without add-on base drag reduction devices); however, the details of the time averaged vortical structures and base pressure are very different from those found in the experiment in Ref. [6]. Because the details of the time-averaged flow are not correct, it is unclear whether RANS methods will accurately predict drag or even drag trends when drag reduction devices are included. More sophisticated turbulence modeling approaches such as LES do appear to more accurately capture the details of the flow [10], but will be much too expensive to use as the primary aerodynamic prediction tool in a drag optimization strategy.

There are a number of open questions related to aerodynamic drag on tractor-trailers. For example, it is not clear what the theoretical minimum drag coefficient is for a tractor-trailer. Standard aerodynamics packages found on U.S. trucks have a wind-averaged drag coefficient of ~7, while Ref. [3] indicates that additional proven technologies can further reduce this drag coefficient to ~0.55. The most sophisticated modeling approach amenable to a design optimization process requiring a large number of solutions is the steady-state RANS approach. However, the ability of RANS methods to accurately predict drag and/or drag trends has not been proven. Furthermore, it is unclear if add-on drag reduction devices can be designed on simpler shapes than full-blown tractor-trailers. Finally, even if significant advances are made in aerodynamic drag reduction, how can we ensure that the resulting designs will be cost effective and see wide-spread use by the trucking industry?

2 Program Overview

Our research efforts on tractor-trailer aerodynamics are funded by the U.S. Department of Transportation and focus both on reducing fuel consumption (as discussed in detail above) and improving highway safety. Tractor-trailers can produce locally strong unsteady wind conditions that can be hazardous to smaller vehicles. The ultimate goal of this program is to use optimization methods to design add-on devices, which reduce aerodynamic drag while at the same time reducing the large-scale fluctuation intensity in the vehicle wake. With increases in computing power, it is now becoming possible to use CFD as the aerodynamic prediction tool in a design optimization process. Part of our current research program is to demonstrate this CFD-based optimization capability [11]. The other aspect of the current program is to examine the validity of RANS-based turbulence models for predicting drag (or drag trends) for tractor-trailers with add-on drag reduction devices. This aspect of the program includes both wind tunnel experiments and CFD analysis of simplified tractor-trailer geometry, and is the subject of the current paper. Various turbulence models run during the CFD analysis of the truck geometry in the wind tunnel are mentioned in Table 1.

3 Experimental Facilities

Tests were conducted in the Auburn University 3×4 ft^2 test section closed circuit wind tunnel capable of producing a maximum speed of 200 ft/s. Two types of wind tunnel truck models,

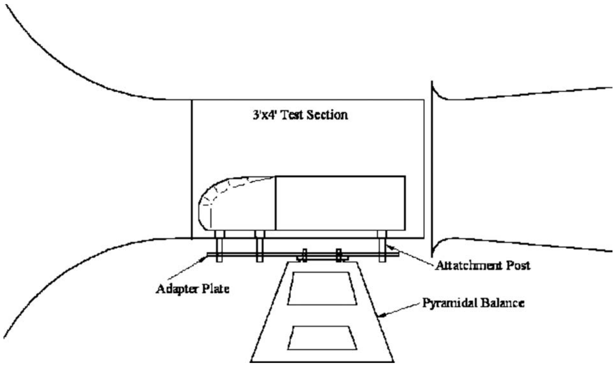

Fig. 2 Schematic of the simplified truck geometry in the wind tunnel

each model consisted of a tractor and a trailer, were made from balsawood, reinforced with hardwood. The first model was finished with several layers of flat black paint for flow visualization purposes, as shown in Fig. 1. The same model was later used for the drag measurement. The second model was built for surface pressure distribution measurement. This model is equipped with 219 pressure taps, with 84 taps located on the tractor. A sandpaper, which is 0.04 in. thick, was placed on the nose of the pressure model in order to obtain fully turbulent flow on the surface of the model. The schematic of the truck in the wind tunnel is shown in Fig. 2.

4 Simplified Tractor/Trailer Geometry

The simplified tractor/trailer geometry was based on the modified ground transportation system (MGTS) geometry developed by Hammache and Browand [12]. The simplified tractor/trailer geometry tested at Auburn University is a combination of a tractor with forward corners rounded to prevent flow separation and a rectangular trailer. The computational geometry of the simplified tractor/trailer placed in the wind tunnel test section is shown in Fig. 3. The width of the trailer is 10 in. and the height to width ratio is 1.392. The length to width ratio of the trailer is 3.4 (this is a shorter trailer when compared with the actual trailers on road). A shorter trailer had to be used for the simulations due to the limitation of the test section length in the experiments. The target conditions are at Reynolds numbers greater than 1×10^6 based on the trailer width since the drag and wake properties are independent of the Reynolds number in this range [5]. There are six streamlined posts with a height of 4 in. each on which the truck model stands. The height of the posts was chosen after conducting the empty tunnel simulations and predicting the boundary layer height on the floor of the test section. It is desirable to know the boundary layer height on the floor of the test section to determine the position of the truck relative to the test section floor. In the case of the truck on the road, there will be no boundary layer developed on the road. In the computational simulations and the experiments, a moving ground plane is not employed. Considering the boundary layer developed on the floor of the test section and the bottom of the truck, a certain distance needs to be maintained between the truck bottom surface and the floor of the test section such that the boundary layers will not merge. The merging of the boundary layers leads to a fully developed flow under the truck and will affect the wake structure behind the truck.

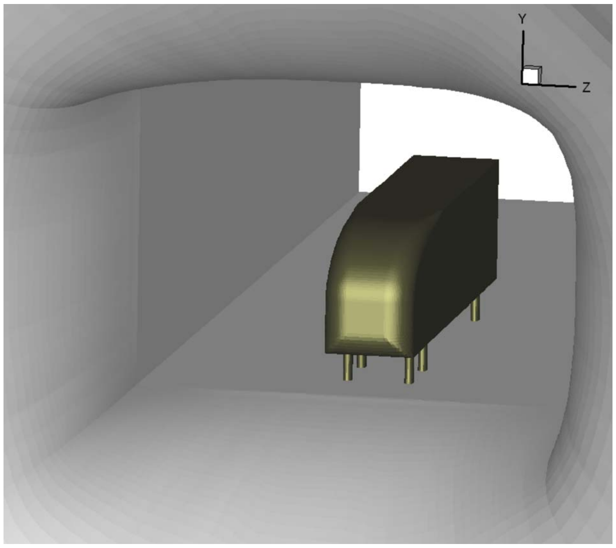

Fig. 3 Computational geometry of the simplified tractor/trailer placed in the wind tunnel

5 Computational Fluid Dynamics Code

5.1 Mesh Generation. The GRIDGEN [13] grid generation tool is used for meshing the simplified tractor/trailer geometry and the empty wind tunnel. The wind tunnel surface geometry is found by taking measurements of the Auburn University wind tunnel, and the surface definition is imported into GRIDGEN. Two different mesh levels are considered for the empty wind tunnel. The coarse mesh has approximately 1.5×10^6 cells and the fine mesh has approximately 4.6×10^6 cells. Initially a structured quadrilateral mesh is used on the surface of the wind tunnel. Before generating the volume mesh, the height of the first layer of cells from the wind tunnel surface is determined such that the Y^+ values are close to 1 for both meshes. Empty wind tunnel simulations are run to compare computed flow angularity and boundary layer properties with the experimental data.

In the simulations, which involved the truck geometry in the wind tunnel, three mesh levels termed as coarse, medium, and fine are used [14]. The coarse, medium, and fine meshes consist of approximately 3.4×10^6 cells, 11.2×10^6 cells, and 25.8×10^6 cells, respectively. Most of the meshing is done using a structured mesh except for some regions in the front of the truck (well outside the boundary layer), which are meshed using an unstructured grid. The reason for mostly using structured grid is that, it is easy to uniformly refine/coarsen the mesh, which is required for solution verification purposes [15]. Comparatively, it is difficult to uniformly refine an unstructured mesh with tetrahedral cells, and it cannot be achieved when meshing is done using commercial software. Also it is advisable to use structured hexahedral cells in the boundary layer flow as structured meshes do a better job in resolving the boundary layer flow when compared with the unstructured meshes.

5.2 Discretization. The steady-state RANS simulations are conducted on the empty wind tunnel geometry using the FLUENT [16] CFD code. A segregated solver is used for the computations, which employs a cell-centered finite volume method. A second-order accurate upwind discretization is used for the momentum, turbulent kinetic energy, and specific dissipation rate equations [16] for all the simulations except for the standard k-ε model on the fine mesh, where only a first-order accurate upwind discretization is used for the turbulent kinetic energy equation and turbulent dissipation rate equations, since convergence is not achieved with the second-order upwind discretization. The SIMPLE algorithm [16] is used to obtain a relationship between velocity and pressure corrections to enforce mass conservation and to obtain the pressure field.

5.3 Boundary Conditions. In the case of the empty wind tunnel, the velocities are close to 0.1 M, and as there is not much variation in the temperature, the flow is considered incompressible during the simulations. At the inlet, a stagnation pressure boundary condition is applied. A gauge pressure value of 0.248846 psi (1715.733 $\mathrm{N/m^2}$) measured from the experiments is used. The outlet boundary condition is set to atmospheric. The tunnel walls are defined as stationary no-slip walls with a surface roughness of 0.015748 in. (0.4 mm) to achieve a better agreement with the actual rough wall in the experiments. The boundary conditions during the simulations are applied such that the conditions match the empty wind tunnel experiments conducted at Auburn University.

The turbulence models used are the standard Wilcox 1998 k-ω model [17], the SST k-ω model, the standard k-ε model, and the Spalart–Allmaras model. The freestream turbulence parameters k, ω, and ε are calculated using the formulas from Ref. [18]. To determine these parameters, a turbulent intensity (T_u) of 1% and the ratio of turbulent to laminar viscosity equal to 10 are considered. The turbulent intensity used in the computations is measured for the wind tunnel. The values of k, ω, and ε calculated are 0.18816, 1288.119, and 17.801, respectively. The formulas for calculating the turbulent kinetic energy k and the specific dissipation rate ω are as follows:

$$k = \frac{1.2}{2}\left(\frac{T_u}{100}\right)^2 V_\infty^2, \quad \omega = \frac{(\rho k/\mu)}{(\mu_t/\mu)}$$

In the expression for the calculation of specific dissipation rate, ρ is the density, k is the turbulent kinetic energy, μ_t is the turbulent viscosity, and μ is the laminar viscosity

6 Results

Results include both the computational predictions and the experimental data of the flow properties in the empty wind tunnel and also with the truck model placed in the wind tunnel test section. The empty wind tunnel results consist of the measurements of flow angularity at the beginning of the test section and the boundary layer properties on the floor of the test section. The truck simulations include the surface pressure distribution on the truck geometry and the overall drag prediction and are compared with the experimental data.

7 Empty Wind Tunnel Simulations

The empty wind tunnel simulations are done to validate the computational model of the wind tunnel, by comparing the computational predictions with the data from the empty tunnel experiments. Another purpose of conducting the empty tunnel simulations is to find the boundary layer height on the floor of the test section to determine the position of the truck relative to the test section floor. The Auburn University wind tunnel consists of a $3 \times 4\ \mathrm{ft}^2$ test section, which has a length of 65 in. The upstream portion of the test section gradually changes from a circular cross section to a rectangular cross section as the flow enters the test section. Immediately downstream of the test section is a small gap, which is opened to the atmosphere. The turning vanes, which are used for diverting the flow in the axial direction upstream of the contracting section, are not considered in the computations, but are replaced by a flat surface, which is at a 45 deg angle with the axial flow direction. A top view of the wind tunnel showing the vanes, which turn the flow, is shown in Fig. 4.

7.1 Computational Predictions. The steady-state RANS simulations are conducted on the empty wind tunnel geometry using FLUENT [18]. The empty tunnel simulations are performed to validate the computational model of the wind tunnel. Empty wind tunnel simulations are carried out to find the boundary layer height from the test section floor. The boundary layer properties are predicted at three different locations on the floor of the test section. The boundary layer heights at 9 in., 20 in., and 39 in. from the beginning of the test section are predicted to be 0.772 in., 0.975 in., and 1.33 in., respectively. In the simulations, a surface roughness of 0.015748 in. (0.4 mm) is used to achieve a better agreement with the boundary layer properties from the experiments. After the comparisons it was decided to place the truck geometry at a height of 4 in. from the test section floor. Hence, the streamlined posts on which the truck geometry stands were set to a height of 4 in. This height of the posts is also matched in the computations.

The empty tunnel simulations are converged until the iterative error in the simulations is considered small. The convergence criterion for the continuity equation is 5×10^{-6} and it is set to 1×10^{-6} for the momentum, k and ω equations. These convergence criteria are found by monitoring the estimated numerical error in the drag. When the error in the drag becomes lower than 0.01%, then the required convergence levels are set.

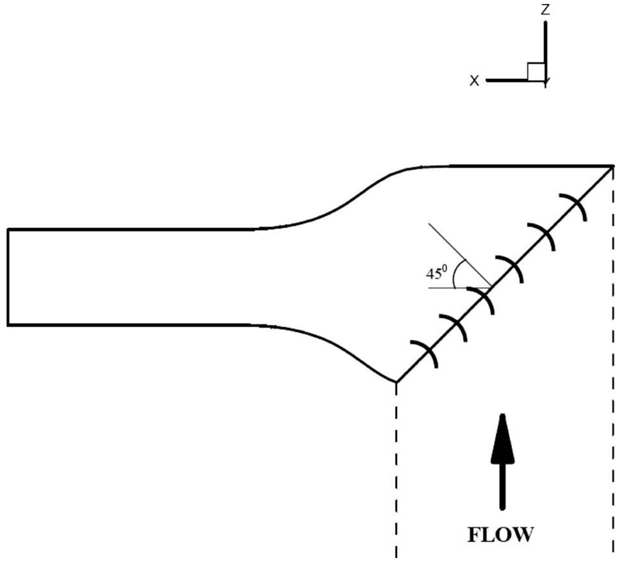

Fig. 4 Top view of the wind tunnel geometry

7.2 Model Validation. The numerical predictions are compared with the experimental results for the validation of the model. The validation of the computational model of the empty wind tunnel includes the comparison of the boundary layer properties at the three locations on the floor of the test section and the flow angularity at the beginning of the test section with the experimental data. The boundary layer thickness, the displacement thickness, and momentum thickness at 9 in., 20 in., and 39 in. from the beginning of the test section on the wind tunnel floor are compared with the experimental results. The boundary layer properties predicted from the computations are compared with the experimental data and are tabulated in Table 2. The boundary layer properties matched closely with the experimental data except for

Table 2 Comparison of numerical results of boundary layer properties with experimental results

Boundary layer properties (in.)		Numerical	Experimental	Percentage error
Beginning of the test section $X=9$	δ_{99}	0.772	0.76	−1.58
	δ^*	0.1426	0.13	−9.69
	θ	0.0985	0.11	10.45
End of the tractor $X=20$	δ_{99}	0.975	0.96	−1.56
	δ^*	0.1794	0.18	0.33
	θ	0.126	0.15	16
End of the trailer $X=39$	δ_{99}	1.33	1.56	14.74
	δ^*	0.2313	0.23	−0.56
	θ	0.1651	0.20	17.45

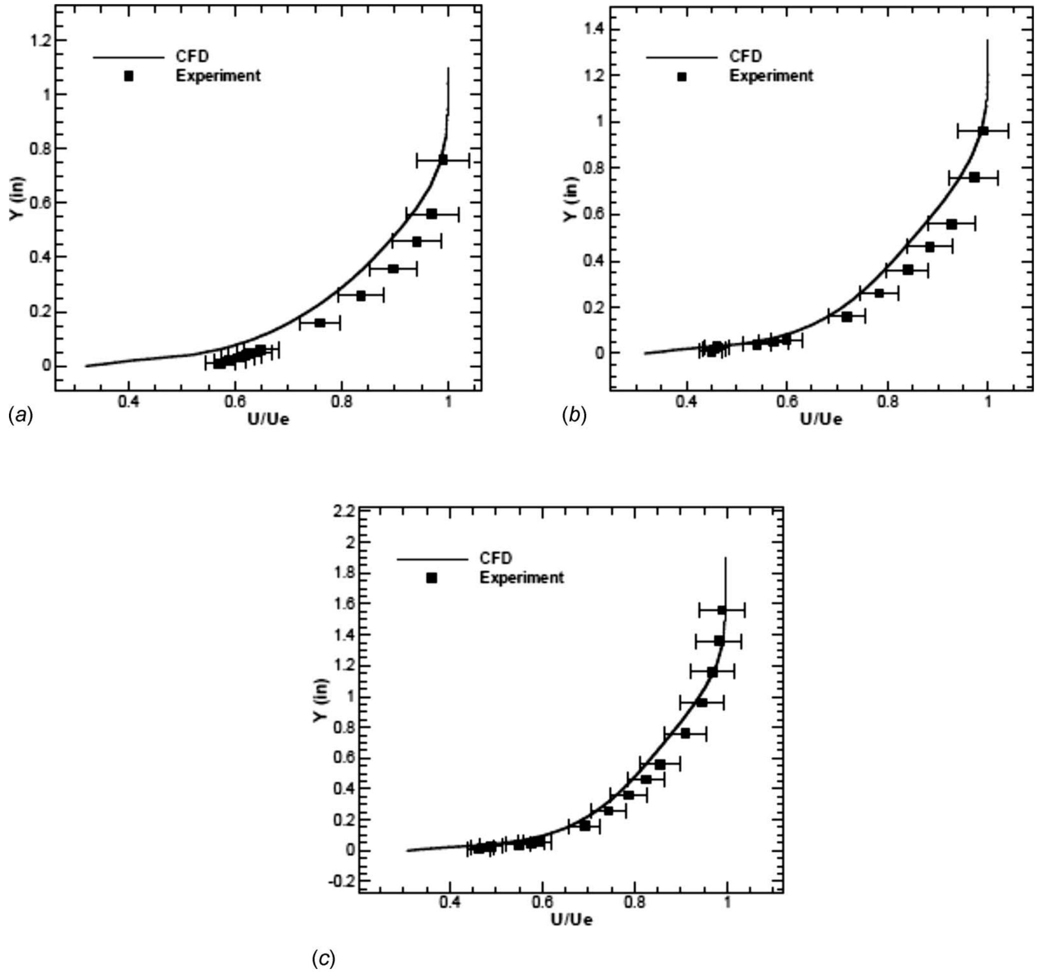

Fig. 5 Comparison of boundary layer profiles (*a*) at 9 in., (*b*) at 20 in., and (*c*) at 39 in. from the beginning of the test section

the boundary layer height at the farthest downstream section. A higher value of boundary layer thickness is observed in the experiments at the last station, i.e., 39 in. from the beginning of the test section, possibly due to the highly rough surface present on the test section floor at that location. The boundary layer profiles from the computations are compared with the experimental measurements at the three locations and are shown in Fig. 5.

The flow angularity data in the experiments at the beginning of the test section are matched with the flow angularity prediction from the computations by changing the flow angle at the inlet boundary condition in the computations, and it is observed that an inlet flow angle of 20 deg with the axial direction shows better agreement when compared with the other flow angles. Different flow angles at the inlet had to be tested to match the flow angularity at the beginning of the test section, since there is no information on the flow direction and behavior of the flow at the vanes in the experiments. The flow angularity comparison at 9 in. from the beginning of the test section at the vertical centerline location is shown in Fig. 6.

8 Truck Simulations

8.1 Computational Predictions. For the RANS simulations of the truck geometry in the wind tunnel, an extended test section is considered in order to move the outflow boundaries sufficiently far away from the truck wake [19]. The test section length is made twice the actual length in the experiments. The simulations are carried on three mesh levels. The coarse, medium, and fine meshes consists of approximately 3.4×10^6 cells, 11.2×10^6 cells, and 25.8×10^6 cells, respectively. The computational mesh (coarse grid) with the truck geometry placed in the wind tunnel test section is shown in Fig. 7.

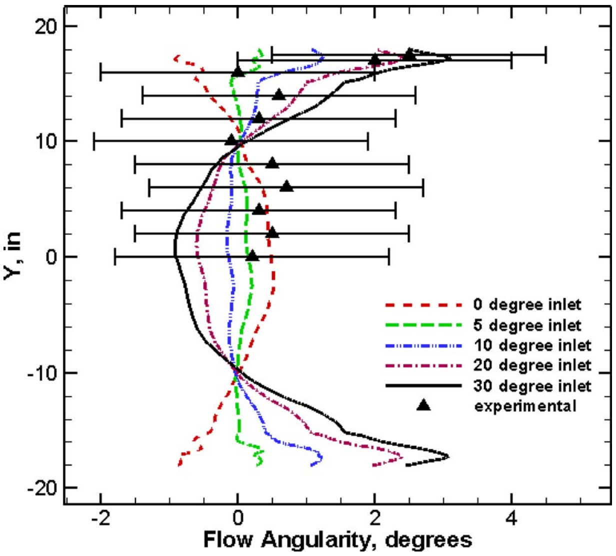

Fig. 6 Flow angularity at a vertical center at 9 in. from the beginning of the test section

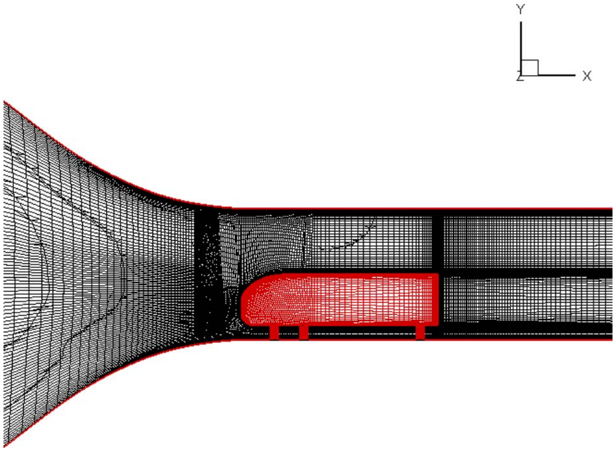

Fig. 7 Computational mesh (coarse grid) for the truck geometry placed in the wind tunnel

The simulations are conducted at a Reynolds number approximately equal to 1×10^6 based on the trailer width in order to match the value used in the experiment. The drag has been found to be independent of Reynolds number above this range [5]. All four turbulence models are tested on both the coarse and medium grids: the standard Wilcox 1998 k-ω model [16], the SST k-ω model [16], the standard k-ε model [16], and the Spalart–Allmaras [16]. Only two turbulence models, the SST k-ω model [16] and the standard k-ε model [16], are tested on the fine mesh. The stagnation pressure and temperature values are set at the 45 deg inlet plane to match the stagnation conditions in the wind tunnel, and the back pressure is varied at the outlet to match the reference pressures. The truck walls and the tunnel walls are defined as no-slip walls with a surface roughness of 0.015748 in. (0.4 mm) on the tunnel walls. With these boundary conditions, a static pressure very close to atmospheric is achieved at the cross section downstream of the test section, where there is a gap in the actual wind tunnel. Also, the back pressure is varied such that the pressure values at three locations in the upstream region of the test section are matched, which are initially considered as the reference pressures. Later, the pressure values are replaced by the pressure value on the top of the trailer surface as the reference pressure, and the reference pressure on the trailer surface is used for the calculation of the pressure coefficient and the drag coefficient. This change has to be made because the three reference pressure locations in the upstream region of the test section are too close to the truck geometry and are located at the beginning of the test section after the converging portion of the wind tunnel. Their use requires a highly accurate simulation of the pressure variations at that location because of the acceleration of the flow due to presence of the truck geometry.

Before comparing the results from the computations with the experiments, it is important to estimate the numerical errors. The turbulence cases are initially converged using a first-order spatial discretization, and then subsequently restarted with a second-order discretization. It is observed from the residuals that the convergence is rather slow when the second-order upwind discretization [16] is used as compared with the first-order discretization. The convergence of the residuals is faster for the first-order scheme due to additional dissipation, but for the second-order scheme, the residuals do not converge to steady-state due to the unsteady wake that was found to form behind the posts and the truck.

To find out whether the solution is converged, the drag variation with iterations is examined, and it can be seen that the drag values oscillate along a constant mean value. The behavior of drag on the truck with the iterations is shown in Fig. 8. The source of oscillations is the unsteady flow behind the truck base and the posts. Even behind the posts, there is a flat rear surface, which leads to separation and hence the oscillations in the drag convergence. When the drag is no longer converging, and only oscillating about a constant mean value, the pressure coefficient and the drag coefficient are calculated. The pressure values on the top, bottom, sides, front, and backside of the truck are extracted to calculate the pressure coefficient. The pressure coefficient is calculated using the formula

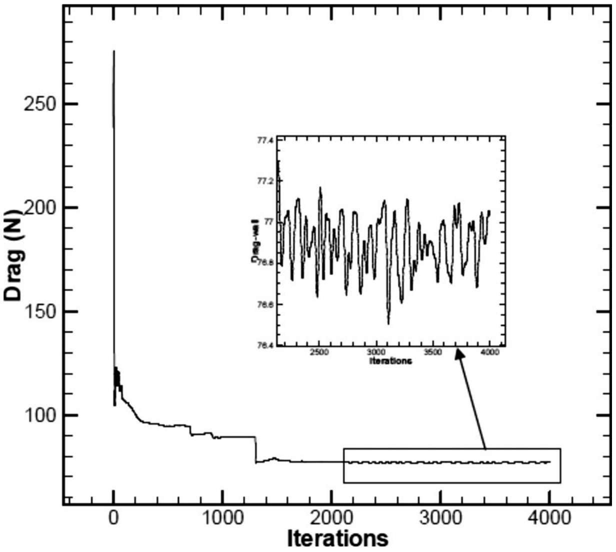

Fig. 8 Drag convergence on truck

$$C_P = \frac{p - p_{\text{ref}}}{\frac{1}{2}\rho_\infty V_\infty^2}$$

where p is the static pressure, and p_{ref} is the reference pressure.

The overall drag coefficient calculated using all four turbulence models for the different mesh levels is tabulated in Table 3. To get an error estimate on the numerical solution, grid convergence index (GCI) values are calculated for the medium and fine mesh solutions and the calculated values are tabulated in Table 3. A GCI value on a fine grid solution, as proposed by Roache [20], is defined as

$$\text{GCI} = \frac{F_s}{r^p - 1}\left|\frac{f_2 - f_1}{f_1}\right|$$

where F_s is the factor of safety, f_1 and f_2 are the finer grid solution and the coarser grid solutions, respectively, r is the refinement factor between the two grids considered, and p is the observed order of accuracy. The refinement factor is 1.5 between the coarse and medium meshes, and it is 1.33 between the medium and fine meshes. The observed order of accuracy cannot be calculated using two grids, and hence, in the case of the standard Wilcox 1998 k-ω and the Spalart–Allmaras turbulence models, the observed order of accuracy is assumed to be equal to formal order of two. For this case, Roache [21] recommends a conservative factor of

Table 3 Computational prediction of the overall drag coefficient using different turbulence models

	Drag coefficient C_D			GCI (%)
	Coarse mesh	Medium mesh	Fine mesh	
Spalart–Allmaras	0.4039	0.3975	-	6.28
k-ε	0.3124	0.3088	0.3072	1.14
k-ω	0.3139	0.3089	-	13.14
SST k-ω	0.3088	0.3024	0.3003	0.56

safety value of $F_s=3$. For the SST k-ω and the standard k-ε turbulence models, there are solutions from three grid levels, and hence an observed order of accuracy value can be calculated. In this case, the GCI can be calculated using the calculated observed order of accuracy. Assuming the observed order of accuracy matches the formal order, a less conservative factor of safety of 1.25 can be used for these cases. The GCI converts the estimate of the error in the numerical solution into an error of uncertainty band. The observed order of accuracy is 2.32 for the SST k-ω turbulence model and 1.166 for the k-ε turbulence model. In the case of k-ε turbulence model, the k- and ε-equations are run first-order as the residuals diverged when they are run second-order upwind scheme. The reduction in the order of accuracy may be due to first-order convergence of the k- and ε-equations. The formula used for the calculation of order of accuracy is given below

$$\frac{f_3-f_2}{r_{23}^p-1}=r_{12}^p\left(\frac{f_2-f_1}{r_{12}^p-1}\right)$$

where f_1 is the fine grid solution, f_2 is the medium grid solution, f_3 is the coarse grid solution, r_{12} is the refinement factor between the fine and medium grids, and r_{23} is the refinement factor between the medium and coarse grids. Observed order of accuracy p in the equation is obtained using a Newton–Raphson method.

8.2 Experimental Results. Due to limited data acquisition resources, the surface pressure measurements were done in two stages. The first stage measured the surface pressure distribution on the tractor through the 84 pressure taps located on the tractor, and the second measured the surface pressure distribution on the trailer. In both stages, pressure taps were connected to 48 port pressure scanners (Scanivalve Corp.) by plastic pressure tubes. All tubes were made to have an equal length, approximately 4 ft, in order to minimize differences in pressure reading due to the resonance effect. The pressure scanners were connected to a DSA-3217 (Scanivalve Corp.) that has 16 pressure transducers. Only five to six transducers were used for tractor or trailer pressure measurements, respectively, with three transducers dedicated to measure the reference pressures discussed earlier. The sampling frequency of the DSA-3217 was 0.5 Hz/channel. The maximum uncertainty of the pressure measurement was calculated to be 5%.

Force measurements were conducted using an external pyramidal force balance. Calibration of the balance was performed and verified within an accuracy of 2.0%. The model was attached to an adapter plate, which was connected securely to the top of the pyramidal balance. The struts were connected firmly to the wind tunnel floor, leaving a gap of 1/16 in. between the strut and model. This allowed for free movement of the model and balance during dynamic forces. A LABVIEW program was written to run these tests while data were collected through a D/A board.

Collecting the data from the experiments, the overall drag coefficient is calculated. The experiment is repeated several times to test the repeatability. The average drag measured from the experiments is 12.53 lbf. The atmospheric pressure and density measured during the experiments are 14.2866 psi and $0.002198\ \text{slug/ft}^3$, respectively. The average value of the overall drag coefficient calculated from the experimental data is 0.325. The experimental uncertainty is estimated to be 5%, and hence with the error bounds, the average drag coefficient from the experiments is reported as 0.325 ± 0.016.

8.3 Model Validation. The pressure distribution on the truck model from the simulations is compared with the experimental measurements from the ports located at various positions on the truck geometry. The location of the pressure taps on the truck geometry is shown schematically in Fig. 9. The pressure distributions include the C_p variations on the top, bottom, sides, front, and back of the truck geometry. The comparison of C_p of the two turbulence models (SST k-ω and standard k-ε) for the fine mesh to the experimental measurements on the top and bottom of the truck geometry is shown in Fig. 10. Similarly, the comparison of the C_p values of the two turbulence models to the experimental measurements on the two sides of the truck geometry is shown in Fig. 11. The C_p comparisons on the front side and back side are shown in Figs. 12 and 13, respectively. The deviation of the experimental data of the C_p values from the computations on the front of the truck is due to the difficulty in the measurement of the port location on the curvature. On the back of the trailer, the turbulence models did not accurately predict the behavior of the flow when compared with the experiments, and hence the difference in the C_p comparisons. The turbulence models predicted a symmetric pair of counter-rotating vortices on the back of the trailer, but from the pressure distribution in the experiments, it looked like the counter-rotating vortices have a different structure, which is not symmetric, and only one large vortex seems to be present exactly behind the trailer. The velocity contours along with the streamlines on the vertical symmetry plane at the back of the trailer for the SST k-ω turbulence model are shown in Fig. 14. The pressure contours on the back side of the trailer compared with the pressure data at the port location from the experiments are shown in Fig. 15. The contours in the circular spots show the

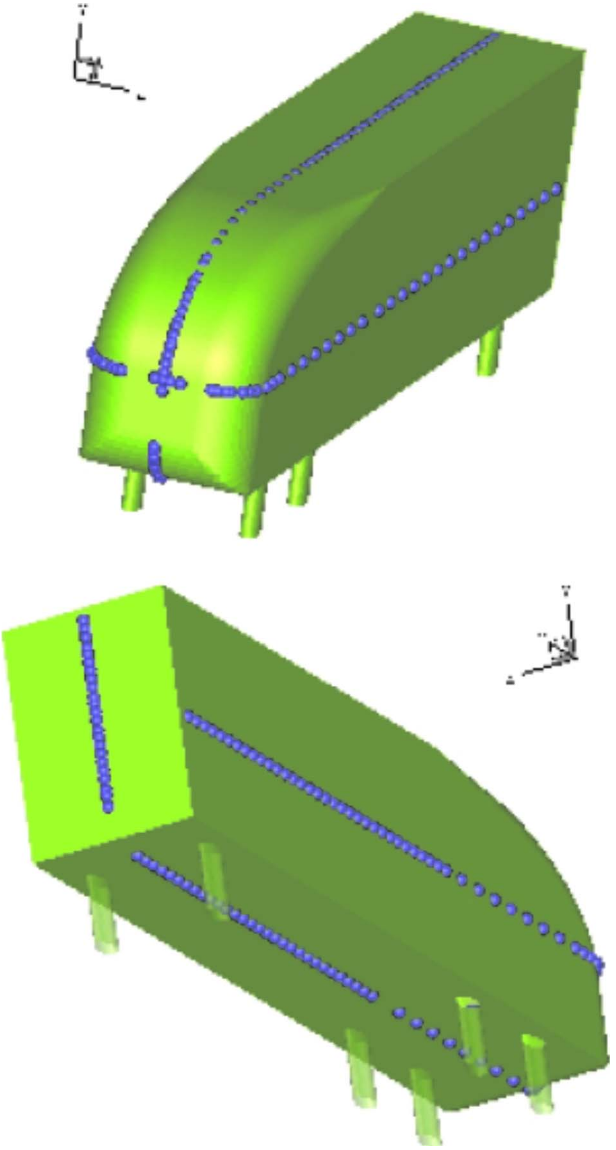

Fig. 9 Schematic of the location of the pressure ports on the truck geometry

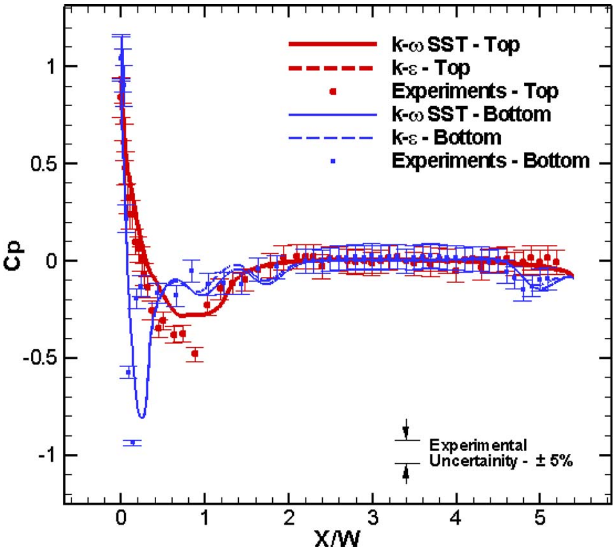

Fig. 10 Comparison of the C_p variation on the top and bottom of the truck geometry

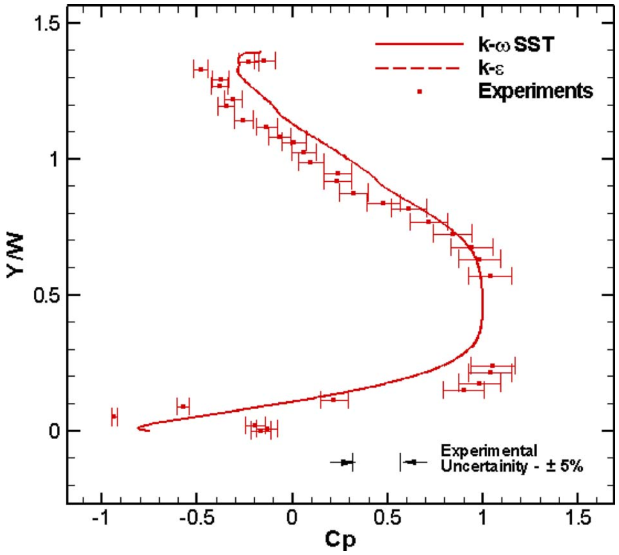

Fig. 12 Comparison of the C_p variation on front of the truck geometry

pressure values from the experimental data at the port locations. The comparison shows a higher negative pressure toward the top and bottom of the trailer back surface in the computations, but a higher negative pressure only toward the bottom of the trailer back surface, which represents an asymmetric flow behavior in the experiments behind the trailer.

Initially, the reference pressures at three different locations in the test section, one on the floor and the other two on the side walls of the test section, are obtained from the simulations and compared with the experimental data. Later the location of the reference pressure is changed to one of the ports on the top of the trailer. The reason for this change in the location of the reference pressure is that the three ports initially considered on the wind tunnel test section fall in the region of high pressure variations. They are located on the test section at the beginning of the truck where the flow is accelerated due to the presence of the truck geometry. Hence the reference pressure position is changed to the location on the top of the trailer.

Finally the drag coefficient predicted from the simulations, for Wilcox 1998 k-ω and the Spalart–Allmaras turbulence models on the medium mesh, and the SST k-ω model and the standard k-ε model on the fine mesh, is compared with the experimental result. The comparison of the drag coefficient along with the percentage error in their mean predictions relative to the experiment is shown in Table 4.

9 Conclusions

RANS simulations were performed on the empty wind tunnel geometry and the truck model placed in the wind tunnel. The boundary layer height in the wind tunnel test section was calculated to determine the position of the truck geometry relative to the test section floor. The boundary layer properties on the floor along the test section length and the flow angularity at the beginning of the test section were predicted and compared with the experiments carried out in the 3×4 ft^2 Auburn University wind tunnel for validation. After the calculation of the boundary layer

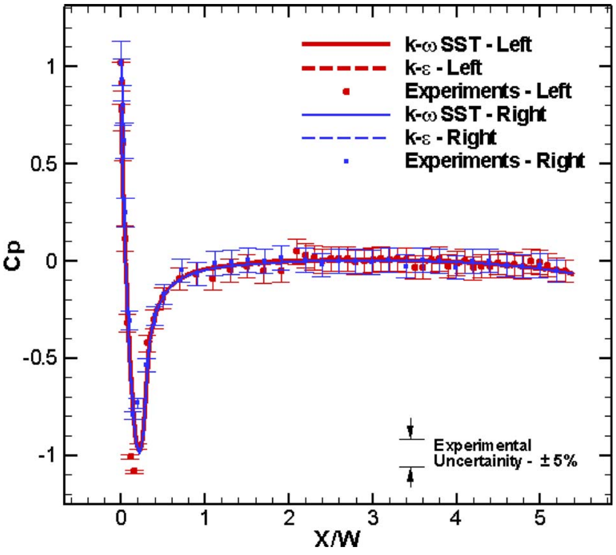

Fig. 11 Comparison of the C_p variation on the sides of the truck geometry

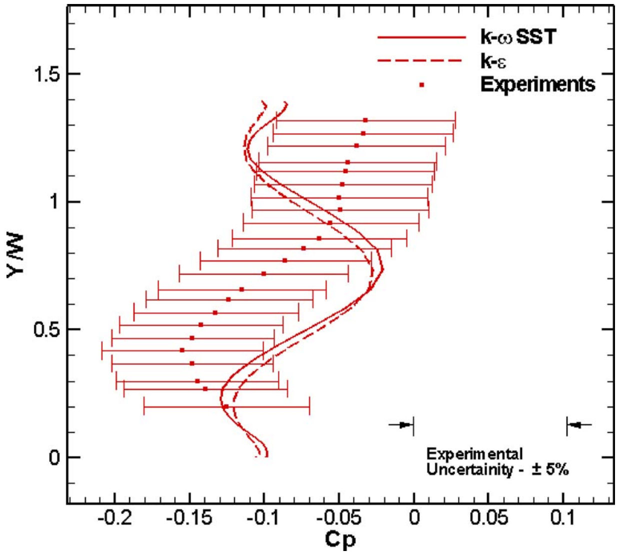

Fig. 13 Comparison of the C_p variation on the back of the truck geometry

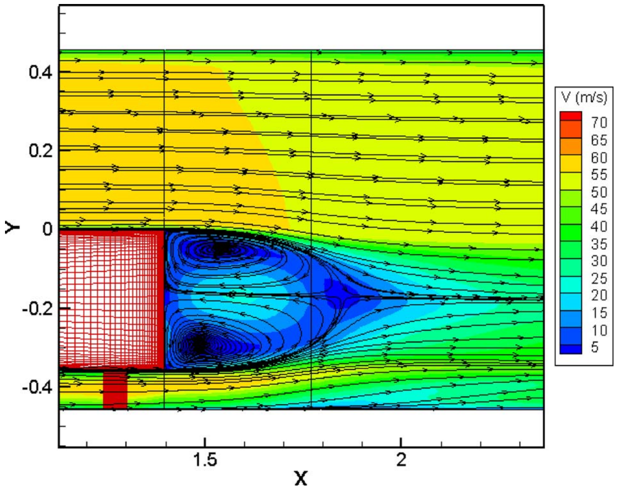

Fig. 14 The velocity contours along with the streamlines on the vertical symmetry plane for the SST *k*-*ω* turbulence model

height from the test section floor, the tractor/trailer geometry was placed at a height of 4 in. from the test section floor.

The steady-state RANS simulations over the modified ground transportation system placed in the 3×4 ft^2 Auburn University wind tunnel were conducted to predict the surface pressure distribution on the truck geometry and the overall drag. The computational predictions are compared with the experimental data for validation. The surface pressure distributions from the computations agreed reasonably well with the experimental data except in the base region. The RANS models predicted a symmetric pair of counter-rotating vortices behind the trailer, but from the pressure distribution in the experiments, it looked like there is only one large vortex in the trailer base region. The behavior in the computations is consistent with other RANS simulations of high Reynolds number bluff-body flows [6–9]. Also, the overall drag is predicted well by the RANS two equation models: The standard Wilcox 1998 *k*-*ω* model, the SST *k*-*ω* model, and the standard *k*-*ε* model. The Spalart–Allmaras model overpredicted the overall drag value, and the drag coefficient value is 22.3% higher than the experimental value.

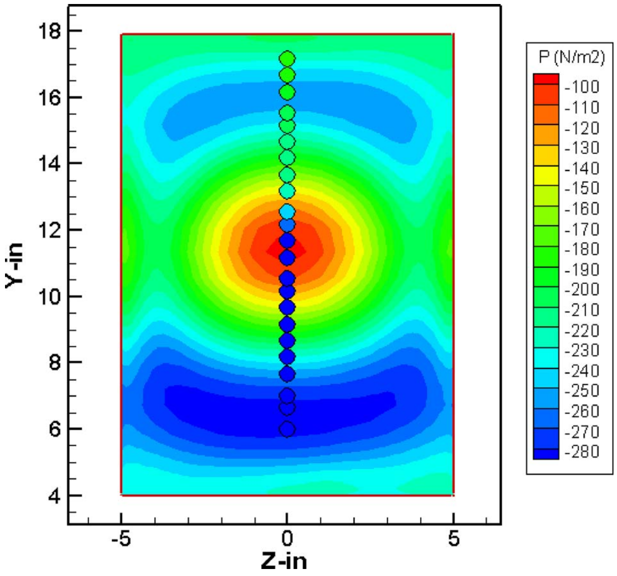

Fig. 15 Pressure data comparisons on the back of the trailer

Table 4 Drag coefficient comparison

	Drag coefficient C_D	Error (%)
Spalart–Allmaras	0.3975 ± 0.0249	−22.3
k-*ε*	0.3072 ± 0.0035	5.48
k-*ω*	0.3089 ± 0.0405	4.95
SST *k*-*ω*	0.3003 ± 0.0017	7.6
Experiments	0.325 ± 0.016	-

Acknowledgment

We would like to thank Andy Weldon of Auburn University for his invaluable help in building the truck model and his aid with the experimental set up. This work was supported by the U.S. Department of Transportation's Federal Motor Carrier Safety Administration (FMCSA) under Grant No. MH-05-01-1 with Mr. Chris Flanigan serving as the technical monitor.

References

[1] 2003, US DOE Transportation Energy Data Book: Edition z23, http://www-cta.ornl.gov/data/.

[2] McCallen, R. C., Salari, K., Ortega, J. M., DeChant, L. J., Hassan, B., Roy, C. J., Pointer, W. D., Browand, F., Hammache, M., Hsu, T.-Y., Leonard, A., Rubel, M., Chatalain, P., Englar, R., Ross, J., Satran, D., Heineck, J. T., Walker, S., Yaste, D., and Storms, B., 2004, "DOE's Effort to Reduce Truck Aerodynamic Drag—Joint Experiments and Computations Lead to Smart Design," AIAA Paper No. 2004-2249.

[3] Cooper, K. R., 2003, "Truck Aerodynamics Reborn—Lessons From the Past," SAE Paper 2003-01-3376.

[4] Storms, B. L., Ross, J. C., Heineck, J. T., Walker, S. M., Driver, D. M., and Zilliac, G. G., 2001, "An Experimental Study of the Ground Transportation System (GTS) Model in the NASA Ames 7- by 10-ft Wind Tunnel," NASA, Report No. TM-2001-209621.

[5] Storms, B., Satran, D., Heineck, J., and Walker, S., 2004, "A Study of Reynolds Number Effects and Drag-Reduction Concepts on a Generic Tractor-Trailer," AIAA Paper No. 2004-2251.

[6] Roy, C. J., Payne, J. L., and McWherter-Payne, M. A., 2006, "RANS Simulations of a Simplified Tractor/Trailer Geometry," ASME J. Fluids Eng., **128**, pp. 1083–1089.

[7] Salari, K., Ortega, J. M., and Castellucci, P. J., 2004, "Computational Prediction of Aerodynamic Forces for a Simplified Integrated Tractor-Trailer Geometry," AIAA Paper No. 2004-2253.

[8] Pointer, W., 2004, "Evaluation of Commercial CFD Code Capabilities for Prediction of Heavy Vehicle Drag Coefficients," AIAA Paper No. 2004-2254.

[9] Roy, C. J., Brown, J. C., DeChant, L. J., and Barone, M. A., 2004, "Unsteady Turbulent Flow Simulations of the Base of a Generic Tractor/Trailer," AIAA Paper No. 2004-2255.

[10] Unaune, S. V., Sovani, S. D., and Kim, S. E., 2005, "Aerodynamics of a Generic Ground Transportation System: Detached Eddy Simulation," SAE Paper No. 2005-01-0548.

[11] Doyle, J. B., Hartfield, R. J., and Roy, C. J., 2006, "Tractor Trailer Optimization by a Genetic Algorithm With CFD," AIAA Paper No. 2006-3863.

[12] Hammache, M., and Browand, F., 2004, "On the Aerodynamics of Tractor-Trailers," *The Aerodynamics of Heavy Vehicles: Trucks, Buses and Trains (Lecture Notes in Applied and Computational Mechanics)*, R. C. McCallen, F. Browand, and J. C. Ross, eds., Springer-Verlag, Heidelberg, Vol. 19.

[13] Pointwise Inc., GRIDGEN V.15, User Manual.

[14] Roy, C. J., 2005, "Review of Code and Solution Verification Procedures in Computational Simulation," J. Comput. Phys., **205**(1), pp. 131–156.

[15] Salas, M. D., 2006, "Some Observations on Grid Convergence," Comput. Fluids, **35**, pp. 688–692.

[16] Fluent Inc., 2003, FLUENT 6.1 User's Guide.

[17] Wilcox, D. C., 1998, *Turbulence Modeling for CFD*, 2nd ed., DCW Industries, Inc., La Canada, CA.

[18] Roy, C. J., and Blottner, F. G., 2003, "Methodology for Turbulence Model Validation: Application to Hypersonic Flows," J. Spacecr. Rockets, **40**(3), pp. 313–325.

[19] Veluri, S. P., Roy, C. J., Ahmed, A., and Rifki, R., 2006, "Preliminary RANS Simulations and Experimental Study of a Tractor/Trailer Geometry," AIAA Paper No. 2006-3857.

[20] Roache, P. J., 1994, "Perspective: A Method for Uniform Reporting of Grid Refinement Studies," ASME J. Fluids Eng., **116**, pp. 405–413.

[21] Roache, P. J., 1998, *Verification and Validation in Computational Science and Engineering*, Hermosa, New Mexico.

Spontaneous Break of Symmetry in Unconfined Laminar Annular Jets

Christian Del Taglia[1]
AFC Air Flow Consulting AG,
8006 Zurich, Switzerland
e-mail: christian.deltaglia@afc.ch

Alfred Moser
Science Services Alfred Moser,
8400 Winterhur, Switzerland

Lars Blum
Linde Kryotechnik AG,
8422 Pfungen, Switzerland

Numerical investigations show that the spontaneous break of symmetry in annular incompressible jets occurs in the laminar flow regime and is controlled by both the Reynolds number and the blockage ratio. In the blockage ratio range between 0.50 and 0.89 the transition critical Reynolds number decreases with increasing blockage ratio, according to a defined formula. Transition to asymmetry happens in the steady regime, before the transition to the unsteady flow. Asymmetry is characterized by a preferential flow direction from one side of the jet boundary layer to the diametrically opposite side. The plane of preferential direction passes through the geometry centerline and represents the single plane of flow symmetry. Experiments reported in literature have confirmed the existence of flow asymmetry in an annular jet flow. [DOI: 10.1115/1.3176960]

Keywords: annular jets, break of symmetry, laminar flow, CFD

1 Introduction

Asymmetric flows originating from symmetric geometries and boundary conditions have been quite often observed in the past. Flow asymmetry has been observed in sudden expansion flows with one jet [1–5] or two jets [6], in confined swirling flows [7–11] and after the constriction in a tube flow [12]. Asymmetric states are possible solutions of the nonlinear problem expressed by the Navier–Stokes equations [6]. Asymmetry resulting from symmetric boundary conditions is referred to spontaneous break of symmetry. On the other hand, asymmetric boundary conditions lead to forced break of symmetry.

The asymmetric flow studied in this work occurs in annular jets. Annular jet flows have been investigated in the past because of their intense recirculation flow [13–27]. When used in gas combustion recirculation flows yield stable flames [28,29]. The characteristic parameters of an annular jet are the Reynolds number Re and the blockage ratio BR.

Asymmetry has been observed in the time-averaged annular jet flows [13–15,18,30]. Pinho and Whitelaw [30] performed LDA measurements of a confined annular water jet flow and a water-carboxy methyl cellulose (CMC) mixture for analyzing the differences between Newtonian and non-Newtonian flows. The blockage ratio was 0.50. In the Reynolds number range between 400 and 6,000 the pure water flow exhibited an asymmetric flow field. In this range of Reynolds numbers they identified an oscillation frequency, which was associated with the propagation of instabilities shed from the disk edge. In contrast to the results obtained for the plane sudden expansion, where the asymmetry persists also at high Reynolds numbers [5], the confined annular jet shows a limited range of Reynolds numbers where the flow is asymmetric.

Del Taglia et al. [14] showed numerically and experimentally the existence of flow asymmetry in an annular jet flow with a blockage ratio of 0.89 and Re=4400. Asymmetry was observed with both symmetric and asymmetric boundary conditions. The forced asymmetry was more pronounced than the spontaneous asymmetry. The flow oscillation had a frequency of 10 Hz.

Recent experiments at the Swiss Federal Institute of Technology Zurich with LDA technique at Re=4400 and different blockage ratios [13] clearly showed asymmetry, especially for high blockage ratios.

The present contribution deals with the numerical investigations of the spontaneous symmetry break in steady incompressible annular jets in the laminar flow regime. The objectives are (1) to describe the features of the asymmetry, (2) to present a map on the BR-Re plane, which describes the different regimes (symmetric/asymmetric and steady/unsteady), and (3) to provide a formula for the determination of the symmetry breaking point.

After the description of the simulations in Sec. 2 the results are shown and discussed in Sec. 3.

2 Numerical Simulations

The two characteristic parameters of an unconfined annular jet flow are the Reynolds number and the blockage ratio. The Reynolds number is based on the bulk velocity U_o at the annular jet nozzle and on the hydraulic diameter [4×(passage area)/(wetted perimeter)] of the nozzle (Fig. 1). The nozzle hydraulic diameter is equal to $D_o - D$, D being the bluff-body diameter (or the nozzle inner diameter) and D_o the nozzle outer diameter.

$$\mathrm{Re} = \frac{U_o(D_o - D)}{\nu} \tag{1}$$

The blockage ratio is given by

$$\mathrm{BR} = \left(\frac{D}{D_o}\right)^2 \tag{2}$$

Figure 2 shows the 21 BR-Re combinations for which computations were performed to study the different flow features in the laminar regime. The computations were carried out for the three different high range blockage ratios, 0.50, 0.70, and 0.89. The Reynolds number range was between 10 and 345.

For the flow computations the solver CFX-5 (Version 5.6) was used. It is based on the finite volume method for the spatial discretization of the Navier–Stokes equations. The pressure-velocity coupling is implemented through grid collocation. Fully implicit discretization of the equations is performed at any given time step. For steady-state computations the time step behaves like a relaxation parameter. For each time-step the nonlinear equations are linearized and assembled into the solution matrix. Then the linear equations are solved using an Algebraic Multigrid accelerated In-

---

[1] Corresponding author.

Contributed by the Fluids Engineering Division of ASME for publication in the JOURNAL OF FLUIDS ENGINEERING. Manuscript received June 30, 2008; final manuscript received April 4, 2009; published online July 24, 2009. Assoc. Editor: Paul Durbin.

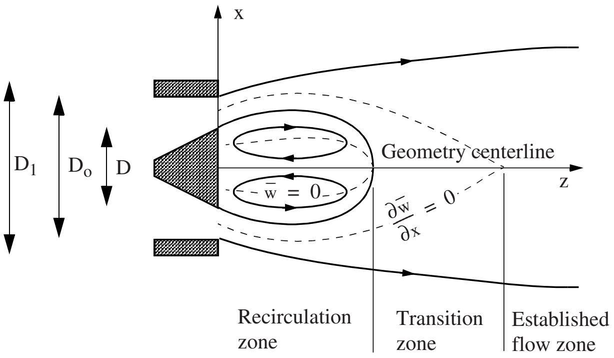

Fig. 1 Sketch of an annular jet. The three flow zones are described in Ref. [27].

complete Lower Upper (ILU) factorization technique. The time and space discretization is of second order.

Table 1 summarizes the 39 computations, which were carried out to study the 21 BR-Re combinations already mentioned. The computations were performed by solving the steady incompressible and isothermal Navier–Stokes equations. At BR=0.50, Re =200, at BR=0.89, Re=50, and at BR=0.89, Re=200, a detailed sensivity analysis was necessary to check for the results accuracy. These three combinations reflect specific transition regimes, as will be explained later. For the combination BR=0.89, Re=200 (indicated by a solid square in Fig. 2), unsteady computations were performed in addition to the steady computation.

For three BR-Re combinations in Table 1, at which the steady computations did not converge with the standard grid (grid L086, as described later), computations with a finer grid (grid L151) were carried out. These three combination, are at BR=0.50, Re =250, at BR=0.70, Re=100, and at BR=0.89, Re=60. The fine grid computations did not converge, neither (see Table 1).

For the combinations at BR=0.5, Re=200 and BR=0.89, Re =50, the solution sensitivity to changes in boundary conditions and numerical grid was studied. These computations are indicated by solid triangles in Fig. 2 and described in Table 2.

The computational domain had a shape of a cylinder (Fig. 3), with a specified diameter and height. The diameters and heights of the different numerical grids are described in Table 3. The axis of the cylinder in Fig. 3 was coincident with the centerline of the annular jet device. In the simulations the annular jet device was modeled by setting wall boundary conditions at the circular surface of the bluff-body and at the annular surface of the tube. These two surfaces were located at the bottom of the cylindrical computational domain ($z=0$). The origin of the Cartesian system of reference was set at the center of the circular bluff-body surface.

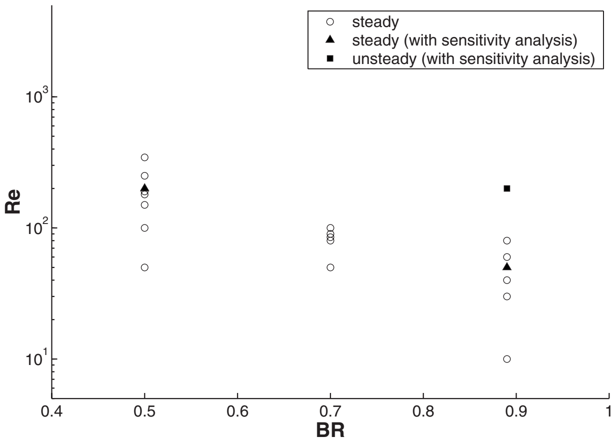

Fig. 2 Summary of performed computations in the BR-Re plane

Table 1 Type of computations for different BR-Re combinations

BR	Re	Computation type	Convergence	Computation label
0.50	50	Steady	Yes	V38
0.50	100	Steady	Yes	V22
0.50	150	Steady	Yes	V24
0.50	180	Steady	Yes	V25
0.50	190	Steady	Yes	V26
0.50	200	Steady	Yes	V27, V28
0.50	250	Steady	**No**	V34, V44
0.50	345	Steady	**No**	V35
0.70	50	Steady	Yes	V07
0.70	80	Steady	Yes	V18
0.70	85	Steady	Yes	V20
0.70	90	Steady	Yes	V21
0.70	100	Steady	**No**	V23, V43
0.89	10	Steady	Yes	V02
0.89	30	Steady	Yes	V04
0.89	40	Steady	Yes	V05
0.89	50	Steady	Yes	V06, V08, V09, V10, V11, V12, V13, V14, V15, V16, V45
0.89	60	Steady	**No**	V17, V42
0.89	80	Steady	**No**	V19
0.89	200	Steady	**No**	V40
0.89	200	**Unsteady**	Yes	V29, V30, V31, V32, V33

Table 2 shows the different sensitivity analysis computations in detail. The third column indicates the grid used, as described in Table 3. The fourth and fifth columns describe the type of boundary condition used for the far field surfaces. The far field surface at the bottom of the cylindrical computational domain is defined as entrainment surface. At this entrainment surface two different boundary condition approaches were used. One approach was to set a pressure-specified opening condition. The other approach was to set a velocity-specified inlet condition. Since the jet entrains air from the surrounding, the most realistic boundary condition is the pressure-specified opening. This condition allows only the strictly necessary amount of fluid to enter into the computational domain. However, the velocity-specified inlet is numerically more stable, and it was therefore preferred. The sensitivity analysis was carried out to quantify the differences obtained from different inflow velocities compared to the pressure-specified opening condition. The same discussion holds for the lateral surface boundary condition (fifth column in Table 2). In all computations a pressure-specified opening condition was set at the top surface of the cylindrical computational domain (Fig. 3).

For the boundary condition of the annular jet, a uniform velocity inlet was set at the annular slot (Fig. 4). The magnitude of the velocity was U_o, which appears in the Reynolds number according to Eq. (1).

It must be mentioned that the time behavior of the inflow may have an impact on the onset of asymmetry. In this work the inflow is steady. In the flow configuration of Mallinger and Drikakis [12], the inflow was pulsating and generated flow asymmetry. In contrast, the flow remained symmetric when a steady inflow was set.

The computational grids used in the computation had a five-block structured butterfly configuration, with only hexahedral elements. The central block contained the centerline and was surrounded by the other four blocks. Figures 5–7 show details of the grid labeled L086 (Table 3). Local grid refinement was employed in the vicinity of the annular jet nozzle and the bluff-body surface (Fig. 5). In all computations the bluff-body diameter D and the

Table 2 Summary of sensitivity analysis computations. These computations were steady.

BR	Re	grid	B.c. at entrainment surface	B.c. at lateral surface	Initial lateral velocity	Computation label
0.50	200	L086	Inflow, $0.02U_o$	Inflow, $0.02U_o$	$0.0U_o$	V27
0.50	200	**L151**	Inflow, $0.02U_o$	Inflow, $0.02U_o$	$0.0U_o$	V28
0.89	50	L086	Inflow, $0.02U_o$	Inflow, $0.02U_o$	$0.0U_o$	V08
0.89	50	L086	**Inflow, $\mathbf{0.05U_o}$**	Inflow, $0.02U_o$	$0.0U_o$	V09
0.89	50	L086	**Inflow, $\mathbf{0.10U_o}$**	Inflow, $0.02U_o$	$0.0U_o$	V10
0.89	50	L086	**Inflow, $\mathbf{0.90U_o}$**	Inflow, $0.02U_o$	$0.0U_o$	V11
0.89	50	L086	**Pressure opening**	**Pressure opening**	$0.0U_o$	V12
0.89	50	**L018**	Inflow, $0.02U_o$	Inflow, $0.02U_o$	$0.0U_o$	V15
0.89	50	**L103**	Inflow, $0.02U_o$	Inflow, $0.02U_o$	$0.0U_o$	V13
0.89	50	**L151**	Inflow, $0.02U_o$	Inflow, $0.02U_o$	$0.0U_o$	V14
0.89	50	**S087**	Inflow, $0.02U_o$	Inflow, $0.02U_o$	$0.0U_o$	V16
0.89	50	L086	Inflow, $0.02U_o$	Inflow, $0.02U_o$	**$\mathbf{0.5U_o}$**	V45

outer tube diameter $D_1=2D$ were the same. The different blockage ratios were varied by changing the inner tube diameter D_o.

All steady and unsteady simulations (except simulation V45) have the following initial conditions: zero velocity and constant pressure. The effects of initial conditions were analyzed in simulation V45, for which an initial lateral velocity of $0.50U_o$ (i.e., $u/U_o=0.5$, $v/U_o=0$, $w/U_o=0$, see also sixth column in Table 2) was assumed. These settings correspond to a relatively large asymmetry in the initial flow field. The results show that the steady computation with an asymmetric initial velocity flow field converge to the same solution as with the zero-velocity initial condition. See computations V08 and V45 in Tables 1 and 2 for details.

The details of the unsteady computations at BR=0.89 and Re =200 are given in Table 4. The effects of time and space discretization were investigated by using different grids and time steps.

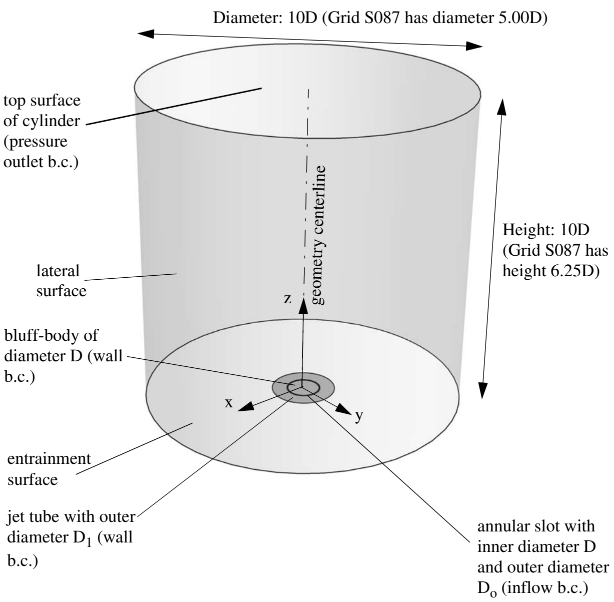

Fig. 3 The computational domain had a shape of a cylinder. The origin of the Cartesian system of reference was the bluff-body center. A pressure outlet boundary condition was set at the top surface of the cylindrical domain.

Table 3 Grid characteristics and sizes of computational domain

Grid label	Domain diameter	Domain height	Grid points	Computation label
L018	10*D*	10*D*	18,000	V15
L086	10*D*	10*D*	86,000	V02, V04, V05, V06, V07, V08, V09, V10, V11, V12, V17, V18, V19, V20, V21, V22, V23, V24, V25, V26, V27, V29, V30, V31, V32, V34, V35, V38, V40, V45
L103	10*D*	10*D*	103,000	V13, V33
L151	10*D*	10*D*	151,000	V14, V28, V42, V43, V44
S087	5*D*	6.25*D*	87,000	V16

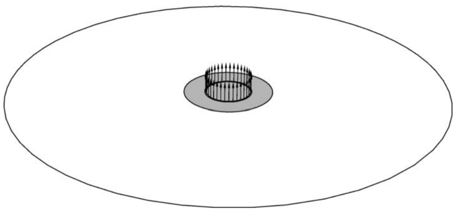

Fig. 4 Bottom part of the computational domain. A uniform velocity profile of magnitude U_o was set at the annular slot. This annular inlet boundary condition is shown as vectors in the picture.

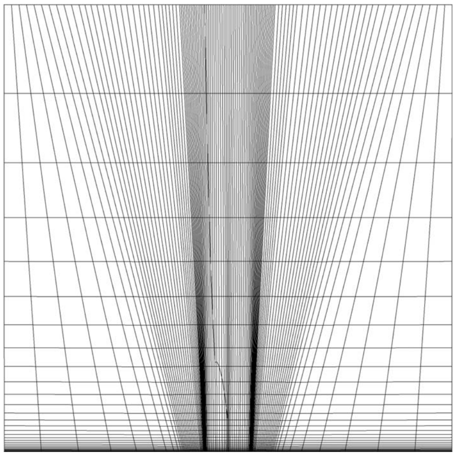

Fig. 5 Computational grid L086: Plane through the geometry centerline

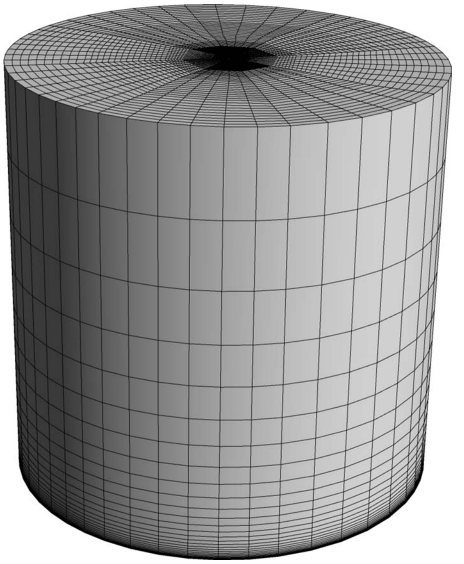

Fig. 6 Computational grid L086: Lateral and top surfaces of the cylindrical computational domain.

3 Results

The results of the computations are presented in Secs. 3.1–3.3. The numerical accuracy was checked by a sensitivity analysis based on series of systematic computations (Sec. 3.1). The features of the asymmetric flow are presented in Sec. 3.2. Finally, the condition for the break of symmetry is given (Sec. 3.3).

3.1 Sensitivity Analysis: Grids and Boundary Conditions. As described in Table 2, different boundary conditions at the entrainment surface were used to study the effect of the entrainment of surrounding air caused by the annular jet. The most realistic boundary condition is the pressure-opening condition, for which a value of pressure is set at the boundary, and the fluid is allowed to flow into or out of the computational domain. However, this boundary condition gives the same results as putting a low velocity inflow boundary condition, provided the velocity is below $0.10U_o$, see Figs. 8 and 9.

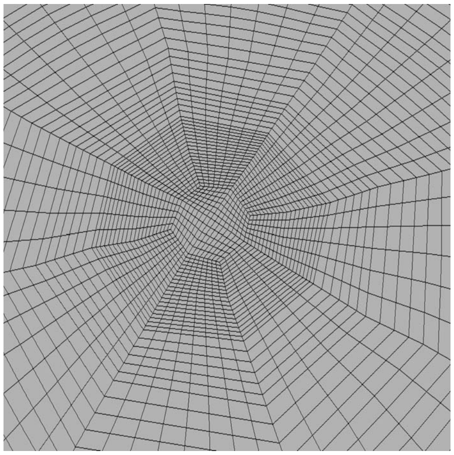

Fig. 7 Computational grid L086: Detailed view of the central region of the top surface, where a pressure-specified boundary condition was set

Table 4 Details of the usteady computations at BR=0.89 and Re=200

Grid label	Time step	Computation label
L086	$0.0646D/U_o$	V29
L086	$0.129D/U_o$	V30
L086	$0.323D/U_o$	V31
L086	$1.29D/U_o$	V32
L103	$0.129D/U_o$	V33

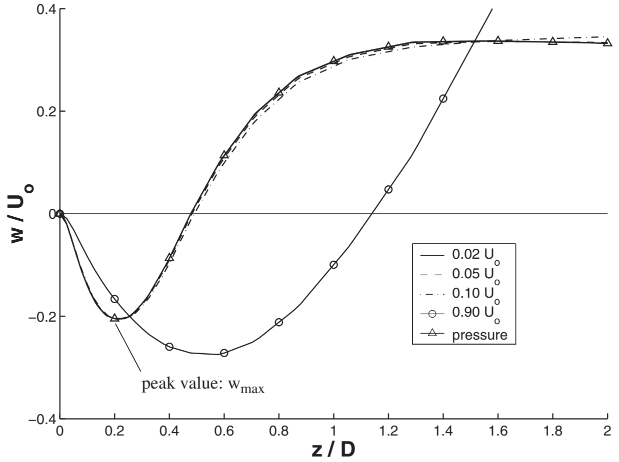

Fig. 8 BR=0.89, Re=50: Axial velocity component on the geometry centerline, using different boundary conditions at the entrainment surface

Figure 8 shows the axial velocity component on the geometry centerline (see Fig. 3 for the position of the geometry centerline) for the BR=0.89, Re=50 combination. At low values of z/D the axial velocity is negative, indicating that the flow has a backward orientation. This is due to the recirculation flow induced by the flow separation at the jet nozzle and the associated low pressure region.

Figure 9 represents the radial velocity component on the geometry centerline. The radial velocity component is given by

$$u_r = \sqrt{u^2 + v^2} \tag{3}$$

with u and v being the velocity components in x- and y-directions respectively.

Summarizing Figs. 8 and 9 it is stated that the boundary condition used at the entrainment surface and at lateral surface of the

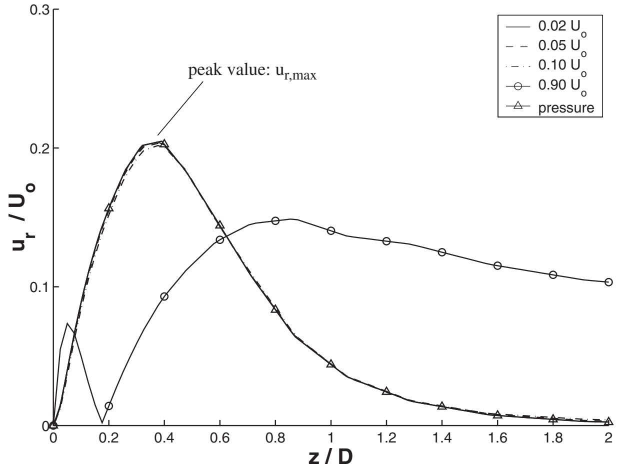

Fig. 9 BR=0.89, Re=50: Radial velocity component on the geometry centerline, using different boundary conditions at the entrainment surface

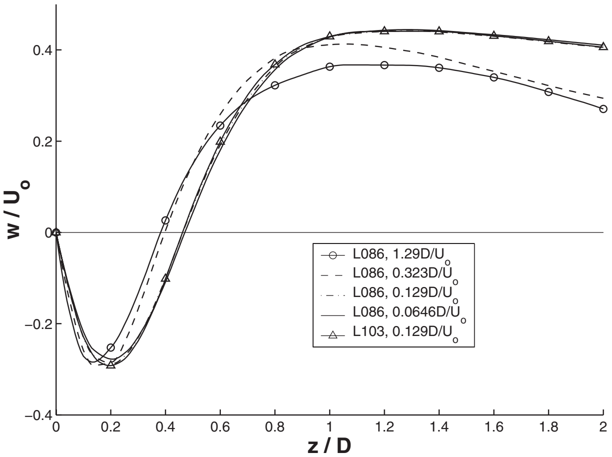

Fig. 10 BR=0.89, Re=200: Time-averaged axial velocity component on the geometry centerline for different time steps and different grids (Table 4)

computational domain can be a velocity-specified inlet, provided the velocity does not exceed $0.1U_o$. For all the following computations, a $0.02U_o$-inflow boundary condition is set at the entrainment and the lateral surfaces of the computational domain. The assumption of a velocity-specified boundary condition with velocity $0.02U_o$ is endorsed by the fact that the maximum velocity at the entrainment and the lateral surface obtained by the pressure-specified boundary condition (computation V12) is equal to $0.019U_o$.

Solution grid independence of the steady computations has been checked by performing the same computations on different grids. The grids differed both in resolution (i.e., same volume size but different number of points) and in volume size, as described in Table 3. The results show that grid independent results can be obtained with a cylindrical computational domain of diameter 10D and height 10D, having at least 86,000 points. This numerical grid is labeled as L086 in Table 3.

For three BR-Re combinations in Table 1, at which the steady simulations did not converge, a grid sensivity analysis was preformed. These three states are at BR=0.50, Re=250, at BR=0.70, Re=100, and at BR=0.89, Re=60.

The results of the unsteady computations at BR=0.89 and Re=200 show a significant spreading, Figs. 10 and 11. However, the results with a time step of $0.0646D/U_o$ have a discretization error of less than 10%. Figures 10 and 11 reflect the time-averaged flow field of the unsteady annular jet flow. It is evident that the shape of the velocity profiles are similar to the curves obtained for steady flows, which have been shown in the previous figures.

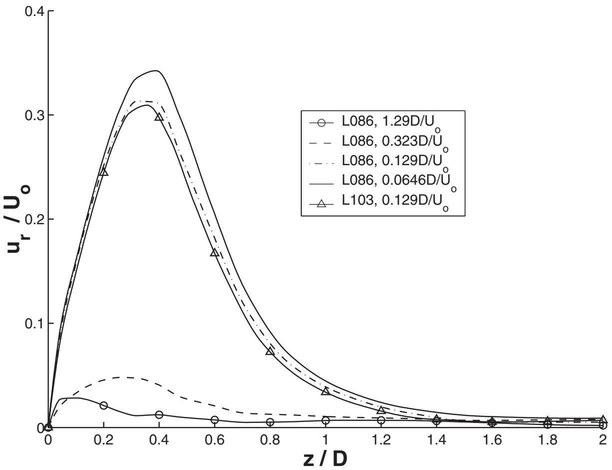

Fig. 11 BR=0.89, Re=200: Time-averaged radial velocity component on the geometry centerline for different time steps and different grids (Table 4).

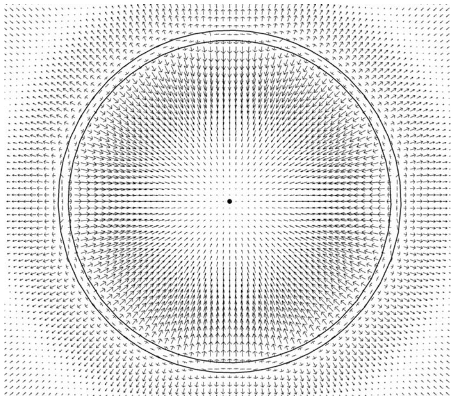

Fig. 12 BR=0.89, Re=10: (u,v)-velocity components on the plane z=0.25D. The point in the center indicates the position of the geometry centerline.

3.2 Description of Flow Asymmetry.

As the radial component of the velocity on the geometry centerline is nonzero (Figs. 9 and 11), the flow at the corresponding combinations of BR and Re is not axisymmetric. The features of this asymmetric flow are described in this section, using the results at the blockage ratio 0.89. However, qualitatively the same flow features are observed in the results at BR=0.5 and BR=0.7.

Figures 12–14 show the flow features at BR=0.89, Re=10 (symmetric flow), whereas the flow features at BR=0.89, Re=50 (asymmetric flow) are shown in the Figs. 15–17. Figure 12 is a representation of the (u,v)-velocity components on the plane z=0.25D. It is a plane located inside the recirculation zone (i.e., where $w/U_o<0$ on the centerline). The velocity vectors are all pointing towards the geometry centerline (shown by a point) and the azimuthal velocity component of all velocity vectors is negligible. From this picture it is evident, that the flow on the plane z=0.25D is axisymmetric. Figure 13 shows the velocity vectors on an arbitrary plane through the geometry centerline. The flow features are symmetrical with respect to the centerline. A three-

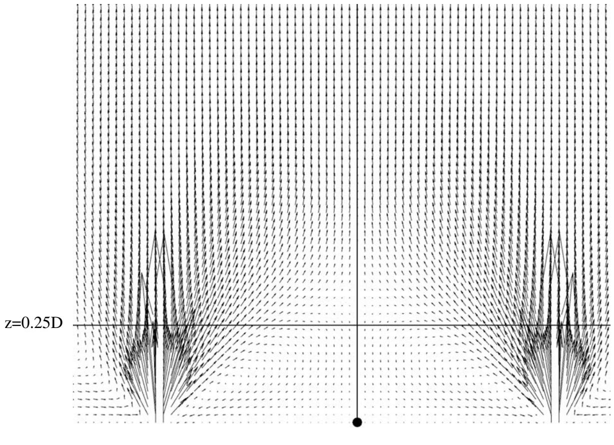

Fig. 13 BR=0.89, Re=10: Velocity vectors on an arbitrary plane through the geometry centerline (vertical line). The point at the bottom indicates the position of the bluff-body center. The section shown in Fig. 12 is indicated by the horizontal line at z=0.25D.

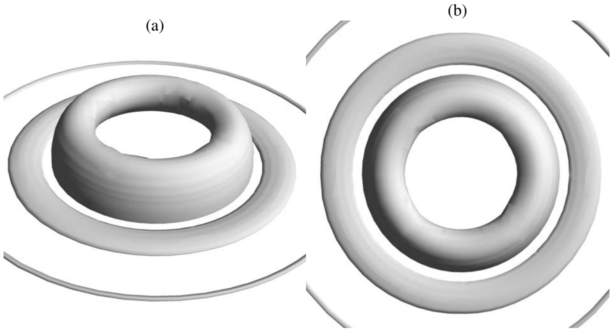

Fig. 14 BR=0.89, Re=10: Isosurface of azimuthal vorticity ω_θ at the value $\omega_\theta D/U_o=-0.516$. (*a*) Perspective view. (*b*) Top view.

dimensional representation of the flow symmetry is given by Fig. 14, where an isosurface of the azimuthal vorticity is shown. This isosurface is also axisymmetric.

Completely different flow characteristics are found at BR =0.89, Re=50. Figure 15 represents the (u,v)-vectors on a plane inside the recirculation zone. Here, the azimuthal velocity components are large. The fluid flows from one side to the diametrically opposite side of the annular jet, passing through the geometry centerline. A preferential direction can be clearly identified, which is shown by a line in Fig. 15. The line passes through the geometry centerline and divides the plane into two symmetrical flow regions.

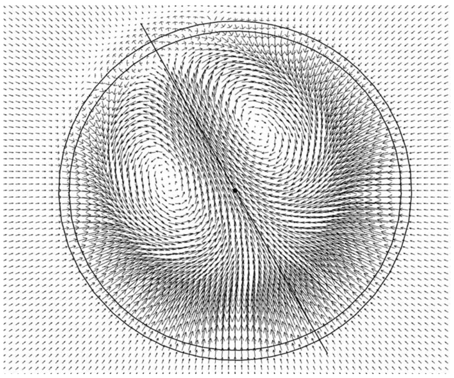

Fig. 15 BR=0.89, Re=50: (u,v)-velocity components on the plane $z=0.25D$. There is a net mass flow in the direction indicated by the line in the picture. The point in the center indicates the position of the geometry centerline.

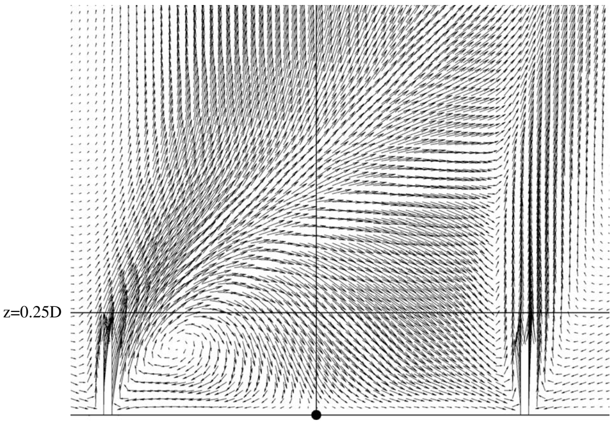

Fig. 16 BR=0.89, Re=50: Velocity vectors on the plane of preferential direction. The geometry centerline is represented by the line in the picture. The point indicates the position of the bluff-body center. The section shown in Fig. 15 is indicated by the horizontal line at $z=0.25D$.

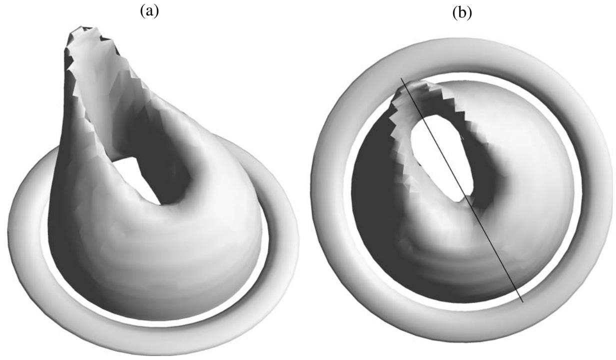

Fig. 17 BR=0.89, Re=50: Isosurface of azimuthal vorticity ω_θ at the value $\omega_\theta D/U_o=-1.03$. (*a*) Perspective view. (*b*) Top view. The line in (*b*) shows the plane of preferential direction.

A geometrical plane can be defined by the line of preferential direction shown in Fig. 15 and the geometry centerline. This plane is referred to as plane of preferential direction. It is observed that all the velocity vectors on this plane are coplanar to the plane itself. Figure 15 shows again that there is a net mass flow from one side to the diametrally opposite side of the annular jet.

The isosurface of the azimuthal vorticity confirms the flow asymmetry (Fig. 17). Moreover it illustrates that the preferential plane divides the space into two symmetrical regions.

Similar flow characteristics can be observed in the time-averaged turbulent flow fields at BR=0.89 and Re=4400 [14] and for other annular jet configurations [22,18,17].

3.3 Map of Flow States. In order to identify the conditions of the symmetry break, it is necessary to quantify asymmetry. This is achieved by introducing an asymmetry index that indicates to which extent an annular flow is asymmetric. The asymmetry index α is defined as

$$\alpha=\left|\frac{u_{r,\max}}{w_{\max}}\right| \tag{4}$$

where $u_{r,\max}$ and $w_{\max}$ are the centerline peak values of the radial and axial velocity components, respectively (see Figs. 8 and 9). In a symmetric or nearly symmetric flow $u_{r,\max}$ is negligible compared to $w_{\max}$, therefore giving $\alpha\approx 0$. In an asymmetric flow $u_{r,\max}$ is comparable to $w_{\max}$, and $\alpha \gg 0$.

Figure 18 presents the values of α for the 15 converged results of the steady computations described in Table 1. It is observed that for a constant blockage ratio the asymmetry index α grows rapidly at a specific Reynolds number. Assuming $\alpha_c=0.1$ as the limit between symmetry and asymmetry, it can be concluded that above a certain critical Reynolds number Re_c the flow becomes asymmetric. Moreover, the critical Reynolds number decreases with increasing blockage ratio.

The time-averaged flow field of the unsteady simulation at BR=0.89, Re=200 (computation V29) is asymmetric. The corresponding asymmetry index is shown in Fig. 18. It does not differ much from the value just after break of symmetry (Re=50).

Table 5 summarizes the different flow states, based on all computations of Table 1. It can be observed, that at $0.50 \leq \mathrm{BR} \leq 0.89$, the transition to asymmetry happens at smaller Reynolds numbers than the transition to unsteadiness. The not-converged computations of Table 1 do not allow to make definitive conclusions on the flow state. However, the converged unsteady computations at BR=0.89, Re=200 (computation V29) show an unsteady flow with an asymmetric time-averaged flow field. So, it is

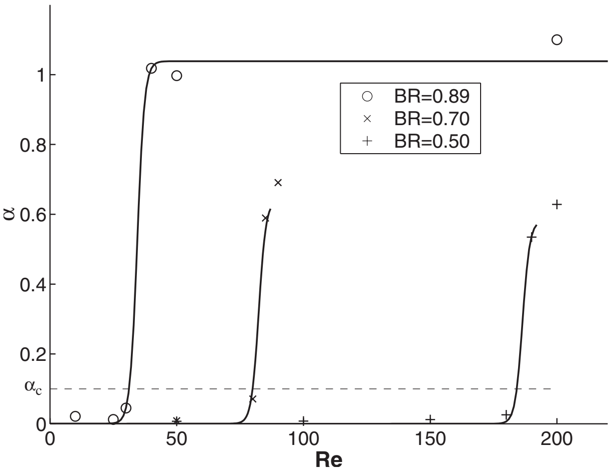

Fig. 18 Transition to asymmetry for different blockage ratios

reasonable to assume that all not-converged steady simulations of Table 1 reflect the same flow features, i.e., an unsteady regime with an asymmetric time-averaged flow field. Therefore, in Table 5 the flow states associated the not-converged computations are denoted by "probably" unsteady and asymmetric.

As mentioned at the beginning of Sec. 2, annular jet flows are characterized completely by a given BR-Re combination. Therefore, the transition point to asymmetry can be expressed in terms of a function of the variables BR and Re. Previous investigations on sudden expansion flows [4] associated the flow asymmetry to the propagation of instabilities. This observation is in agreement with the existence of a symmetry breaking critical Reynolds number [3,6], as flow instabilities grow with increasing Reynolds number. Moreover, it was shown for sudden expansion flows that the critical Reynolds number decreases with increasing expansion ratio [3]. An analogous conclusion can be made for annular jets, since Fig. 18 shows that the critical Reynolds number Re_c decreases with increasing blockage ratio.

The three bold typed Reynolds numbers in Table 5 are the smallest for which the computations result in a steady asymmetric flow state at a given blockage ratio. These BR-Re combinations are described in Table 6 and correspond with a certain degree of accuracy to the symmetry/asymmetry transitions.

These values can be fitted by the expression

$$\ln(\mathrm{Re}_c) = \lambda_c - B \cdot \mathrm{BR} \tag{5}$$

with $\lambda_c = 7.26$ and $B = 4.02$. The state parameter λ expressed by

$$\lambda = \ln(\mathrm{Re}) + B \cdot \mathrm{BR} \tag{6}$$

describes the state of the steady flow, as it is shown in Fig. 19. The heavy line in this figure is a plot of the function given by Eq. (5).

Table 5 Flow states for different BR-Re combinations

BR	Re	Flow state
0.50	50, 100, 150, 180	Steady symmetric
0.50	**190**, 200	*Steady asymmetric*
0.50	250, 345	Probably unsteady asymmetric
0.70	50, 80	Steady symmetric
0.70	**85**, 90	*Steady asymmetric*
0.70	100	Probably unsteady asymmetric
0.89	10, 30	Steady symmetric
0.89	**40**, 50	*Steady asymmetric*
0.89	60, 80	Probably unsteady asymmetric
0.89	200	Unsteady asymmetric

Table 6 BR-Re combinations of the steady symmetric/steady asymmetric transition

BR	Re_c
0.50	190
0.70	85
0.89	40

The points on this curve (solid triangles) express symmetry/asymmetry transitions of the steady flow (Table 6). All BR-Re pairs below this curve are in the steady symmetric state.

Figure 20 shows the computational results in terms of the asymmetry index α and the state parameter λ. The experimental results at different blockage ratios and Re=4400 [14,13] are also included. The computed data points can be fitted by a low-order monotonic curve of the type

$$\alpha = \frac{a_1}{2}(1 + \tanh(a_2(\lambda - \lambda_c))) \tag{7}$$

with $a_1 = 1.04$ and $a_2 = 14.74$. This curve expresses a universal correlation between α and λ. Values of λ below $\lambda_c = 7.26$ indicate

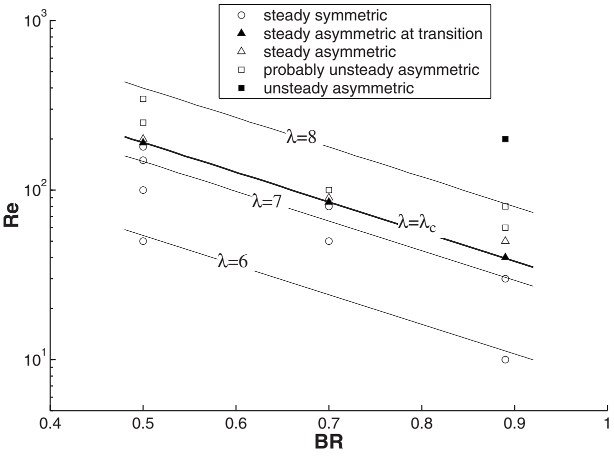

Fig. 19 Map of steady symmetric, steady asymmetric and unsteady states. All the computed points (circles) below the $\lambda = \lambda_c$-line reflect steady symmetric states. All the computed and converged points (white triangles, solid triangles, and the solid square) above the $\lambda = \lambda_c$-line reflect asymmetric states.

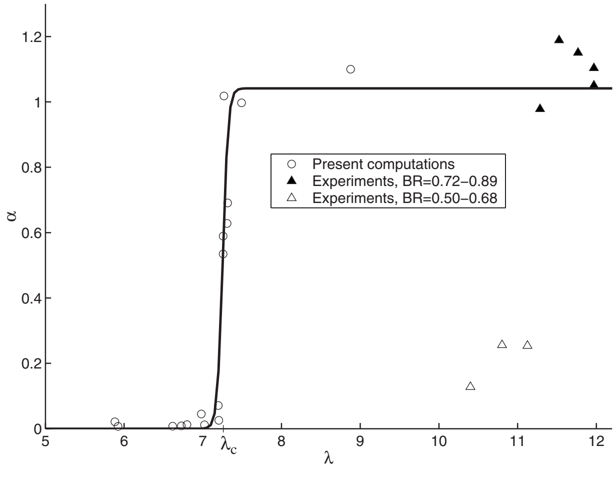

Fig. 20 Monotonic relationship between the asymmetry index α and the state parameter λ.

a steady symmetric flow.

As mentioned, the present results do not allow to draw clear conclusions about flow asymmetry in the region $\lambda > \lambda_c$. At BR $=0.89$ and Re$=4400$ (i.e., $\lambda=12$), however, asymmetry was observed in the time-averaged flow through LDA measurements and by unsteady computations [14]. Systematic LDA measurements at Re$=4400$ and different blockage ratios [13] show an asymmetric flow for BR>0.70. The experiments at BR>0.70 are in good agreement with the best-fit curve in Fig. 20. In contrast, the experiments at $0.50 \leqslant$ BR<0.70 show a less pronounced asymmetry. In experiments at BR$=0.50$, Pinho and Whitelaw [30] observed an asymmetric time-averaged flow field in a limited range of Reynolds numbers only. So, it is reasonable to assume that for unsteady flows at $0.50 \leqslant$ BR<0.70 the asymmetic time-averaged flow field seems to exist only in a limited range of Reynolds numbers.

4 Conclusions

This work deals with the numerical investigation of the spontaneous break of symmetry in steady laminar incompressible annular jets. Asymmetry is characterized by a preferential flow direction across the geometry centerline. The plane of preferential direction passes through the geometry centerline and represents the single plane of flow symmetry.

Transition to asymmetry occurs in the steady laminar regime, and it depends on both the blockage ratio and the Reynolds number. In the blockage ratio range between 0.50 and 0.89 the transition critical Reynolds number decreases with increasing blockage ratio, according to the formula $\ln(\mathrm{Re}_c)=\lambda_c - B\cdot\mathrm{BR}$, with $\lambda_c=7.26$ and $B=4.02$. With the state parameter $\lambda=\ln(\mathrm{Re})+B\cdot\mathrm{BR}$ steady symmetric states of an annular jet flow are identified by $\lambda<\lambda_c$.

Acknowledgment

The fruitful technical discussions and the encouragement by Professor Dimos Poulikakos of the Laboratory for Emerging Technologies (LTNT), ETH Zurich, are kindly acknowledged. We are also grateful to AFC Air Flow Consulting AG, Zurich, for providing its CFD facilities.

References

[1] Schreck, E., and Schäfer, M., 2000, "Numerical Study of Bifurcation in Three-Dimensional Sudden Channel Expansions," Comput. Fluids, **29**, pp. 583–593.
[2] De Zilwa, S. R. N., Khezzar, L., and Whitelaw, J. H., 2000, "Flows Through Plane Sudden Expansions," Int. J. Numer. Methods Fluids, **32**, pp. 313–329.
[3] Drikakis, D., 1996, "Bifurcation Phenomena in Incompressible Sudden Expansion Flows," Phys. Fluids, **9**(1), pp. 76–87.
[4] Cherdron, W., Durst, F., and Whitelaw, J. H., 1978, "Asymmetric Flows and Instabilities in Symmetric Ducts With Sudden Expansions," J. Fluid Mech., **84**, pp. 13–31.
[5] Restivo, A., and Whitelaw, J. H., 1978, "Turbulence Characteristics of the Flow Downstream of a Symmetric, Plane Sudden Expansion," ASME J. Fluids Eng., **100**, pp. 308–310.
[6] Goodwin, R. T., and Schowalter, W. R., 1996, "Interactions of Two Jets in a Channel: Solution Multiplicity and Linear Stability," J. Fluid Mech., **313**, pp. 55–82.
[7] Yu Gelfgat, A., Bar-Yoseph, P. Z., and Solan, A., 2001, "Three-Dimensional Instability of Axisymmetric Flow in a Rotating Lid—Cylinder Enclosure," J. Fluid Mech., **438**, pp. 363–377.
[8] Blackburn, H. M., and Lopez, J. M., 2002, "Modulated Rotating Waves in an Enclosed Swirling Flow," J. Fluid Mech., **465**, pp. 33–58.
[9] Marques, F., Lopez, J. M., and Shen, J., 2002, "Mode Interactions in an Enclosed Swirling Flow: A Double Hopf Bifurcation Between Azimuthal Wavenumbers 0 and 2," J. Fluid Mech., **455**, pp. 263–281.
[10] Marques, F., and Lopez, J. M., 2001, "Processing Vortex Breakdown Mode in an Enclosed Cylinder Flow," Phys. Fluids, **13**, pp. 1679–1682.
[11] Blackburn, H. M., and Lopez, J. M., 2000, "Symmetry Breaking of the Flow in a Cylinder Driven by a Rotating Endwall," Phys. Fluids, **12**, pp. 2698–2701.
[12] Mallinger, F., and Drikakis, D., 2002, "Instability in Three-Dimensional, Unsteady, Stenotic Flows," Int. J. Heat Fluid Flow, **23**, pp. 657–663.
[13] Blum, L., 2005, "Flow Field and Turbulence Measurements in Different Non-Reacting and Reacting Flow Configurations," Ph.D. Thesis, Swiss Federal Institute of Technology Zurich.
[14] Del Taglia, C., Blum, L., Gass, J., Ventikos, Y., and Poulikakos, D., 2004, "Numerical and Experimental Investigation of an Annular Jet Flow With Large Blockage," ASME J. Fluids Eng., **126**(3), pp. 375–384.
[15] Del Taglia, C., 2003, "Numerical Investigation of the Non-Reacting Unsteady Flow Behind a Disk Stabilized Burner With Large Blockage," Ph.D. Thesis, Swiss Federal Institute of Technology Zurich.
[16] Travnicek, Z., and Tesar, V., 2003, "Annular Synthetic Jet Used for Impinging Flow Mass-Transfer," Int. J. Heat Mass Transfer, **46**(17), pp. 3291–3297.
[17] Patte-Rouland, B., Lalizel, G., Moreau, J., and Rouland, E., 2001, "Flow Analysis of an Annular Jet by Particle Image Velocimetry and Proper Orthogonal Decomposition," Meas. Sci. Technol., **12**, pp. 1404–1412.
[18] Vucinic, D., and Hazarika, B. K., 2001, "Integrated Approach to Computational and Experimental Flow Visualization of a Double Annular Confined Jet," J. Visualization, **4**(3), pp. 245–256.
[19] Stroomer, P. P. J., 1995, "Turbulence and OH Structure in Flames," Ph.D. thesis, TU-Delft, Netherlands.
[20] Durão, D. F. G., Knittel, G., Pereira, J. C. F., and Rocha, J. M. P., 1991, "Measurements and Modelling of Turbulent Near Wake Flow of a Disk With a Central Jet," *Eighth International Symposium on Turbulent Shear Flows*.
[21] Aly, M. S., and Rashed, M. I. I., 1991, "Experimental Investigation of an Annular Jet," J. Wind. Eng. Ind. Aerodyn., **37**, pp. 155–166.
[22] Roquemore, W. M., Tankin, R. S., Chiu, H. H., and Lottes, S. A., 1986, "A Study of a Bluff-Body Combustor Using Laser Sheet Lighting," Exp. Fluids, **4**, pp. 205–213.
[23] Taylor, A. M. K. P., and Whitelaw, J. H., 1984, "Velocity Characteristics in the Turbulent Near Wakes of Confined Axisymmetric Bluff Bodies," J. Fluid Mech., **139**, pp. 391–416.
[24] McGuirk, J. J., Taylor, A. M. K. P., and Whitelaw, J. H., 1982, "The Assessment of Numerical Diffusion in Upwind Difference Calculations of Turbulent Recirculating Flows," *Turbulent Shear Flows 3*, Selected Papers from the Third International Symposium on Turbulent Shear Flows, L. J. S. Bradbury, F. Durst, B. E. Launder, F. W. Schmidt, and J. H. Whitelaw, eds., Springer-Verlag, Berlin.
[25] Ko, N. W. M., and Chan, W. T., 1978, "Similarity in the Initial Region of Annular Jets: Three Configurations," J. Fluid Mech., **84**, pp. 641–656.
[26] Durão, D. F. G., and Whitelaw, J. H., 1978, "Velocity Characteristics of the Flow in the Near Wake of a Disk," J. Fluid Mech., **85**, pp. 369–385.
[27] Davies, T. W., and Beér, J. M., 1971, "Flow in the Wake of Bluff-Body Flame Stabilizers," *13th Symposium International on Combustion*, The Combustion Institute, pp. 631–638.
[28] Turns, S. R., 1996, *An Introduction to Combustion*, McGraw-Hill, New York.
[29] Bowman, C. T., 1992, "Control of Combustion-Generated Nitrogen Oxide Emissions: Technology Driven by Regulation," *24th Symposium (International) on Combustion*, The Combustion Institute, pp. 859–878.
[30] Pinho, F. T., and Whitelaw, J. H., 1991, "Flow of Non-Newtonian Fluids Over a Confined Baffle," J. Fluid Mech., **226**, pp. 475–496.

Effect of Liquid Transparency on Laser-Induced Motion of Drops

R. Shukla

K. A. Sallam[1]
e-mail: khaled.sallam@okstate.edu

School of Mechanical and Aerospace Engineering,
Oklahoma State University,
Stillwater, OK 74078

An experimental investigation of the role of liquid transparency in controlling laser-induced motion of liquid drops is carried out. The study was motivated by application to manipulation of liquid drops over a solid substrate. Droplets with diameters of 1–4 mm were propelled on a hydrophobic substrate using a pulsed-laser beam (532 nm, 10 Hz, 3–12 mJ/pulse) with a 0.9 mm diameter fired parallel to the substrate. The test liquid was distilled water whose transparency was varied by adding different concentrations of Rhodamine 6G dye. Motion of the drops was observed using a video camera. Measurements include direction of motion and the distance traveled before the drops come to rest. The present results show that the direction of the motion depends on the drop transparency; opaque drops moved away from the laser beam, whereas transparent drops moved at small angles toward the laser beam. The motion of both transparent and opaque drops was dominated by thermal Marangoni effect; the motion of opaque drops was due to direct heating by the laser beam, whereas in the case of transparent drops, the laser beam was focused near the rear face of the transparent drops to form a spark that pushed the drops in the opposite direction. Energies lower than 3 mJ were incapable of moving the drops, and energies higher than 12 mJ shattered the drops instead of moving them. A phenomenological model was developed for the drop motion to explain the physics behind the phenomenon. [DOI: 10.1115/1.3156000]

1 Introduction

Manipulation of liquid drops over a substrate has a wide range of applications, especially in microfluidics. In channel-based microfluidics, whole bulk of fluid is moved around using mixing channels, micropumps, and valves. An alternative approach to conventional channel-based microfluidics is the use of discrete liquid drops to perform fluidic operations. Droplet-based techniques offer several other advantages over channel-based techniques, such as simple substrates, no moving parts, and better fault tolerance. Droplet microfluidics allows the use of very small quantities of samples and reagents for biochemical analysis [1,2] with the potential to replace an entire laboratory with a droplet-based lab-on-a-chip. Microdroplets can be formed in microchannels [3] and can be used as the digital equivalent of microelectronics for constructing basic microfluidic logic gates [4].

Droplet motion actuated by surface forces is an efficient method for fluid transport at the microscale since surface forces dominate at this scale. Several attempts have been made at droplet manipulation by creating a surface tension gradient. The drop moves in the direction where the surface tension is higher. The surface tension gradient can be created by oxidation-reduction reactions [5], electric field gradient [6], thermal gradients [7–11], and light forces using photoisomerization to change the surface energy by photoirradiation of a photoresponsive substrate, causing a surface energy gradient [12]. Droplet manipulation can also be achieved via excitation of surface plasmons [9–11]. On a substrate with a wettability gradient, drops move from a region of hydrophobic substrate to a region which is more hydrophilic [13,14]. The wettability of a surface can be controlled by surface morphology change [15] or by applying electric field as in electrowetting-on-dielectric (EWOD) [6,16].

Surface tension generally drops as the temperature is increased. If a thermal gradient is applied on a droplet, the droplet moves toward the colder region [7–11,17,18]. This effect, called the thermal Marangoni effect, has been used to manipulate drops on a liquid substrate for mixing applications [19]. Varying the temperature of a heated grid of thin metal lines can be used to move the drops. The drop moves toward the colder lines due to the thermal Marangoni effect [8]. The thermal gradient can also be created by a laser beam [9–11,18,20–24]. Zardecki and Pendleton [20] studied the internal motion of water drops irradiated by a pulsed laser. Recently, Kotz et al. [22] moved water drops immersed in decanol by introducing a laser beam from below the substrate to heat a part of the drop. The drop moved normal to the beam and away from the laser. Rybalko et al. [23] used a laser beam to control the direction of translation of a nitrobenzene drop in a water substrate by changing the optical path of the laser through the drop. The drop moved toward the laser beam when the laser beam was introduced at the oil-air interface and away from the laser when introduced at the bottom of the drop.

Motion of drops on a solid surface using acoustic radiation pressure was shown by Alzuaga et al. [25]. They migrated a drop on a vibrating beam toward the antinode of the vibration. Radiation pressure forces can be used as optical traps [26] and optical tweezers [27]. Transparent particles with a higher index of refraction than their surrounding medium are attracted toward the region of maximum laser intensity. Therefore, it is possible to grab and move objects by moving the focus of the beam around. This found application in an optically driven pump consisting of two optically trapped rotating particles, whose rotation causes a flow between them [28]. Other studies in this field include the spreading of microscale liquid films on solid substrates and liquid flow manipulation on a surface using optical perturbations [21], laser-induced motion in droplets of nanoparticle suspension spreading on a flat surface [24], and the motion of a phase separated fluid under the influence of laser light scattering of density fluctuations within the liquid [29]. The effect of laser radiation on drops is not new and was studied for applications of cloud-clearing using high-energy laser beams and wireless communication using laser beams. Previous studies include the propagation of laser radiation through water aerosol [30], heating of water droplets by laser [31,32], the explosion of drops under intense laser radiation [33–35], the effect of laser on opaque drops [36], and the hydrodynamics of a drop when exposed to pulsed laser [20,37].

---

[1] Corresponding author.

Contributed by the Fluids Engineering Division of ASME for publication in the JOURNAL OF FLUIDS ENGINEERING. Manuscript received July 20, 2008; final manuscript received April 22, 2009; published online July 7, 2009. Assoc. Editor: Theodore Heindel.

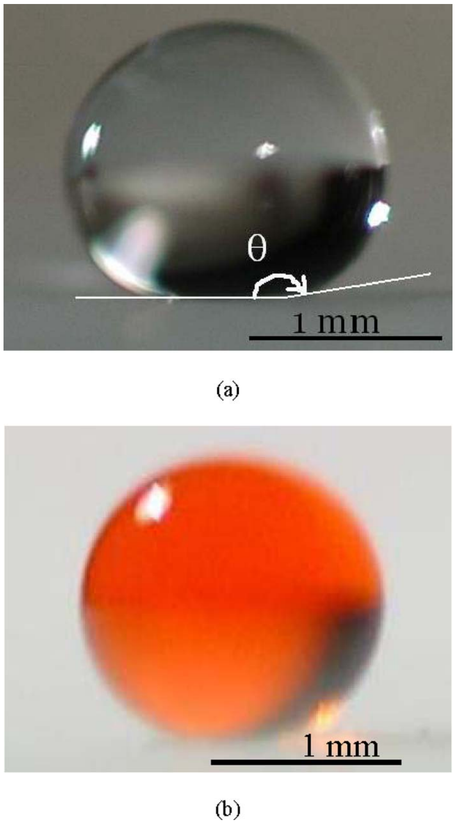

(a)

(b)

Fig. 1 (*a*) A transparent water drop on the Fluoropel® substrate with a contact angle of 169 deg and a drop diameter of 1.7 mm and (*b*) contact angle for a 0.2% Rhodamine 6G (by weight) water drop on Fluoropel® with a contact angle of 170 deg and a drop diameter of 1.6 mm

In continuation of the recent findings on laser-droplet interactions, the present work focuses on the manipulation of millimeter-sized liquid drops directly on a solid substrate using a pulsed laser beam. In the present experimental study a pulsed Nd:YAG laser beam (532 nm, 10 Hz) was used for moving water drops on a hydrophobic substrate. The effects of the drop transparency on the drop-laser interaction and subsequent drop kinematics are discussed. A phenomenological model is introduced to help interpret the experimental results.

2 Experimental Methods

2.1 Apparatus. The drops in the present study were produced by mechanically vibrating a 26-gauge syringe needle (inner diameter of 0.25 mm and outer diameter of 0.46 mm). The drops produced had diameters from 1 mm to 4 mm. A hydrophobic substrate on which the drops moved was produced by applying a thin layer of Fluoropel® PFC M1604V (manufactured by Cytonix, Beltsville, MD) on a standard glass slide. The slide was then heated at a temperature of 70–90°C for 5 min and then heated at 175–200°C for additional 15 min. This process resulted in a solid hydrophobic coating with good glass-adhering properties, good thermal resistance (which is required to resist laser radiation), and stationary water contact angles of up to 170 deg, as shown in Fig. 1. Frequency-doubled pulsed Nd:YAG laser (SpectraPhysics (Mountain View, CA): model Lab-150-10, 532 nm, 10 Hz) was used in the present study for moving the drops. The laser beam exit diameter was 9 mm and was reduced to 0.9 mm using two planoconvex lenses with focal lengths of 150 mm and 15 mm (Thorlab LA4372 and L4917), as shown in Fig. 2. This intense laser beam was aligned horizontally with the hydrophobic substrate. The position of the laser beam was manipulated by rotating a mirror, as shown in Fig. 2. An energy meter (Ophir (Logan, UT): model Nova II) was placed at the end of the optical path to record the beam energy within a measurement uncertainty of 0.5%. Laser beam energies in the range of 3–12 mJ/pulse were generated and used in the present study. Energies lower than 3 mJ/pulse were unable to move the drops, whereas at energies higher than 12 mJ/pulse, most drops shattered instead of being propelled.

2.2 Instrumentation. The droplet motion was observed from two views: the top view of the slide, which recorded the direction and velocity of the drop, and the side view of the droplet on the substrate to record the contact angles. A charge-coupled device (CCD) camera (Nikon D70, 6 megapixels) was used to record a side view of the droplet to measure the contact angle of the drops. The images shown in Fig. 1 were recorded from the side view. The lens used in the camera was 105 mm (Nikkor-Macro) and provided a magnification of 240 pixels/mm and a resolution of 14.3 cycle/mm, as found by standard USAF 1951 resolution pattern. The contact angle measurements had an error of ±5 deg (3%) due to the difficulty of focusing on the drop surface near the solid substrate and the imaging resolution. The motion direction was recorded from the top view using a digital camcorder (Panasonic DV, 15 fps, 320×240 pixels) with a resolution of 180 μm. The digital movie was then converted into individual frames. The droplet velocities were measured using a high speed camera (IDT model XS-4, 512×512 pixels, 5000 fps, on-board memory storage of 8000 frames) equipped with a 105 mm lens (Nikkor-Macro).

The frames were combined to form a single image by "adding" them together. They were then analyzed using SIGMA SCAN® 5.0 to measure the distance traveled by the drops and the angle at which the motion occurred. The uncertainties in measuring the distances on the individual frames were within 15%. Drop velocity was

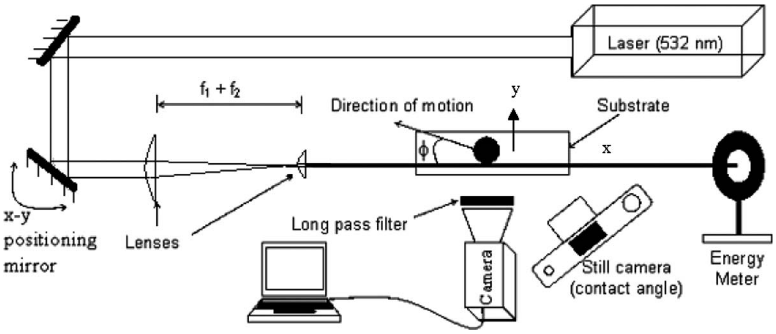

Fig. 2 Experimental setup. The video camera connected to the computer observes the top view of the substrate (to measure the direction of the motion), whereas the still camera observes the side view (to measure the contact angle).

calculated by dividing the distance traveled by the drop by the time it took to travel this distance. The uncertainties in the velocity measurements were dominated by sampling limitations and were estimated to be 18%.

A long pass filter (optical density (OD) of 5.5 at 532 nm) was used to protect the camera from overexposure, especially in the presence of laser-induced sparks. A graph paper was placed below the glass substrate for spatial calibration and for alignment. The centerline of the graph paper was aligned with the initial direction of the laser beam. The laser beam was moved to different locations using a mirror. This also resulted in the laser beam not always staying parallel to its initial position. The angle that the laser beam made with the drop motion was measured by recording a picture of the laser beam without the long pass filter. This picture clearly showed the angle of the beam with the *x*-direction, and direct measurement of the beam angle with the *x*-direction was carried out.

2.3 Test Conditions. Drops with varying transparency were produced by adding different concentrations of Rhodamine 6G dye to distilled water. The test liquids were as follows: distilled water for transparent drops, distilled water with 0.2% (by weight) Rhodamine 6G for translucent drops, and distilled water with 2% (by weight) of Rhodamine 6G for opaque drops. The uncertainty of the weight measurement was 0.1%. The values of the surface tension τ (N/m) and the dynamic viscosity μ (Pa s) of pure water as a function of temperatures were as follows [38,39]:

$$\mu_i = 2.414 \times 10^{-5} \times 10^{(247.8/(T-140))} \tag{1}$$

$$\tau = 6.3173 T^{-0.7865} \tag{2}$$

where T is the absolute temperature (K). The error from both equations is less than 1% in the range of 273–375 K. The addition of Rhodamine 6G to the water changed its properties. The surface tensions of the test liquids were measured using a platinum-iridium ring tensiometer (Fisher Scientific (Pittsburgh, PA) model 20), and the kinematic viscosity was measured using glass kinematic viscometer tubes (Cannon-Fenske type).

3 Results and Discussion

3.1 Experimental Results. Drops with contact angles of 160 ± 10 deg were used in this study. Drop velocities in the range of 11–240 mm/s were observed with a mean velocity of 130 mm/s. The motion of the drop did not take place normal to the beam, as observed by earlier researchers [22], who used a different setup where the beam was introduced from the bottom, such that it came through the substrate rather than beside it. When a drop is heated nonuniformly, it develops a surface tension gradient along its surface due to the thermal gradient (thermal Marangoni effects [7–11,17,18]). The highest surface tension occurs on the coldest part of the drop, and the lowest surface tension develops on the hottest part of the drop. This surface tension gradient induces a net force; the actuating force for the motion F_{act} pulls the drop in the direction of the cold part of the drop. The thermal and fluid processes occurring within a droplet with a thermal gradient were explained by Savino et al. [7] and Passian et al. [10]. Unlike the work of Grigoriev et al. [19] where the moving drop is suspended in some other liquid and moves in it, here the drop moves directly on a solid substrate, and the heating takes place directly by the laser beam for opaque liquids and indirectly by the laser beam for transparent drops.

As the laser beam passes through a transparent drop, the drop acts like a ball lens, focusing the laser beam near its focal point. The focal length f is given by

$$f = \mu d / 4(\mu - 1) \tag{3}$$

where d is the drop diameter and μ is the refractive index of the water drop. For a water drop with a diameter of 1 mm, f is 1 mm, and for a water drop with a diameter of 4 mm, f is 4 mm. As the laser beam converges at the focal point of this liquid ball lens, it results in the production of a spark behind the drop, distinctly visible at high laser beam energy (6 mJ) and even producing a loud clicking sound due to the ionization and breakdown of the air at the spark. The laser-induced spark behind a liquid drop, observed in the present study, had been reported much earlier [40]. The subsequent breakdown of air under the action of this spark was also studied [41]. This optical breakdown results in the formation of plasma [37] that absorbs much of the incident laser radiation. This laser-induced spark had found ignition applications in internal combustion engines [42,43] due to the several advantages it offers over the conventional spark plug. The motion of the drop took place nearly diametrically opposite to this hot spot (spark) for the transparent and the near transparent drops due to the thermal gradient that the hot spot generates. For a transparent drop this is schematically represented in Fig. 3(*a*). The first frame shows the location of the spark behind the drop.

When the drop was made less transparent and more toward being completely opaque by adding increasing amounts of the dye (Rhodamine 6G), the intensity and thus the heating effect of the spark steadily fell off. This resulted in larger angles between the drop motion and the beam direction. For a translucent drop, some of the laser is transmitted, some of it is reflected back, but most of it is absorbed inside the drop along the laser beam bath; thus the drop heats up along the laser path. This results in almost a perpendicular motion to the laser, as shown in Fig. 3(*b*). For an opaque drop, a negligible percentage of the laser beam energy is transmitted through the drop, and some is lost as emissive radiation, and most of the laser is absorbed by the drop at the first surface. This results in a motion at very large angles with the oncoming laser, as shown in Fig. 3(*c*).

The angles at which the various drops have moved are shown in Fig. 4 where 0 deg is the laser beam direction. The radius axis represents the distance traveled by each drop x normalized by drop diameter (d). The droplets that moved at smaller angles were the transparent ones, whereas those that moved at about 90 deg were translucent, and the ones that moved at larger angles were nearly opaque.

3.2 Model of the Drop Motion. Next we introduce a phenomenological model to predict the drop movement. The power flux incident on the drop E_i (W/m^2) and the flux absorbed by the drop E_a (W/m^2) are given as follows:

$$E_i = P/A_l \tag{4}$$

$$E_a = aE_i \tag{5}$$

where P is the power of the laser beam in W, A_l is the cross-sectional area of the laser beam in m^2, and a is the absorptance of the drop (0.002–1), which is given by

$$a = 1 - 10^{-\alpha} \tag{6}$$

where α is the absorbance and is given by

$$\alpha = c_a L \tag{7}$$

L is the path length of the laser beam, and c_a (m^{-1}) is the absorption coefficient of the laser radiation. For a wavelength of 532 nm, the absorption coefficient of pure water is 0.05 m^{-1} [44], and for the Rhodamine 6G solution are 150 m^{-1} and 600 m^{-1} for concentrations of 2.14×10^{-5} mol/l and 8.55×10^{-5} mol/l, respectively [45]. The absorption coefficient for Rhodamine 6G is approximated to have a nearly linear dependence on concentration for 532 nm laser radiation [45]. The maximum value of a can thus be equal to 1, in which case all of the incident flux is absorbed by the drop. The absorbed flux E_a was estimated between 9.8×10^{-6} W and 4.1×10^{-5} W for transparent drops, and 0.06 W and 0.12 W for dyed drops.

Radiation losses dominate at the start of the motion since the time interval is too small for convection and conduction losses to

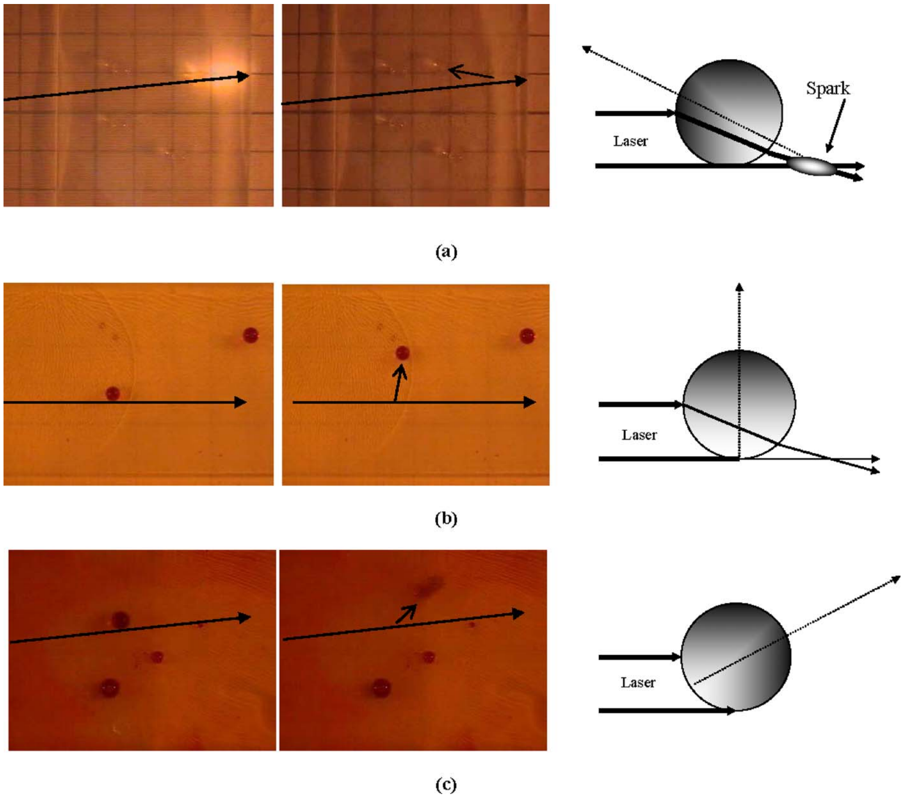

(a)

(b)

(c)

Fig. 3 Laser-induced motion for (*a*) a transparent drop, (*b*) a translucent drop, and (*c*) an opaque drop. The long arrow on the photo represents the laser beam direction. The small arrow on the photo (and the dotted arrow in the sketch) indicates the direction of the motion of the drop in each case. The squares in the background of (*a*) are 5 ×5 mm^2.

occur. However, it is convection and conduction heat transfers that eventually reduce the thermal gradient and stop the motion when the actuating force (F_{act}) falls below the threshold needed to propel the drop forward. The radiation loss (E_e) from the drop is given by

$$E_e = \varepsilon \sigma A_h T_2^{\ 4} \tag{8}$$

where T_2 is the temperature of the heated portion of the drop, ε is the emissivity of the drop liquid, which is the same as its absorptivity based on Kirchhoff's law, σ is the Stefan–Boltzmann constant, and A_h is the heated surface area of the drop. Calculations show E_e to be between 8.8×10^{-8} W and 1.4×10^{-7} W for transparent drops, 4×10^{-4} W and 5×10^{-5} W for translucent drops, and 5×10^{-4} W and 4×10^{-2} W for opaque drops, depending on the drop diameters. The temperature rise of the heated portion of the drop can then be estimated as

$$E_a - E_e = mcdT/dt \approx mc\Delta T/\Delta t \tag{9}$$

where m is the mass of the heated region in kg, and c is the specific heat capacity of water (4200 J/kg K). It is this rise in temperature (ΔT) that induces the surface tension imbalance ($\Delta \tau$), which in turn produces the force required to start the drop motion. To calculate ΔT from the heating rate $\Delta T/\Delta t$, the time interval ΔT is taken to be 0.8 s for transparent drops and 0.5 s for dyed drops based on experimental observations. The final temperatures reached by the heated portion of the drops based on direct laser heating are calculated to be between 315 K and 580 K. These high temperatures explain why some drops exploded when they were irradiated by pulsed laser instead of being propelled. Temperatures as high as 2400 K were reported by Carls and Brock [35], who studied droplet explosion by pulsed lasers. This rise in temperature is small for transparent drops because most of their heating comes from the spark and not directly from the laser beam. The temperature rise was large for opaque drops, which received most of their heating directly from the laser beam.

The angular direction of the drop motion depends on which area of the drop is heated. The cooler side of the drop has a higher surface tension (τ_{high}), and the heated side had a lower surface

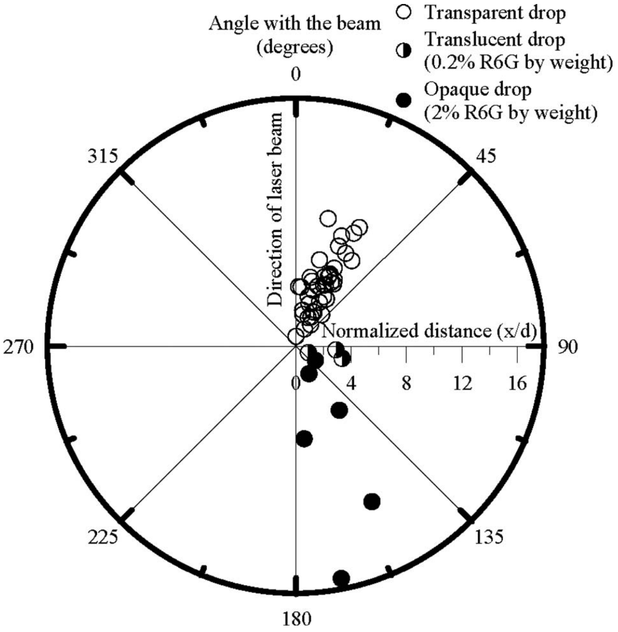

Fig. 4 Measurements of the direction of the movement and the distance traveled. The laser beam comes from the north.

tension (τ_{low}); thus there is a force (F_{act}) in the direction of the cooler region which pulls the drop toward the cooler region. The actuating force (F_{act}) being a surface force depends only on the surface tension gradient ($\Delta\tau$) and the effective circumference between the cooler and the heated sides of the drop. The actuating force (F_{act}) due to surface tension difference along the drop is given by

$$F_{\text{act}} = r(\tau_{\text{high}} - \tau_{\text{low}}) \tag{10}$$

where r is a characteristic length (m) of the heated region (the spherical cap). The values of F_{act} calculated from the present model were in the range of 1.5×10^{-5}–7.6×10^{-5} N. The force due to radiation pressure (F_{RP}), i.e., photoreactive force [36], depends on the laser beam power and the speed of light. This force, however, is much less than the F_{act} calculated in Eq. (10) for the present test conditions and can be neglected. The resisting force (F_{res}) of the motion comes from the aerodynamic drag (F_{aero}) and the surface resistive drag (F_{sres}), which is the surface drag for a drop traveling on a solid substrate as follows:

$$F_{\text{res}} = F_{\text{aero}} + F_{\text{sres}} \tag{11}$$

The aerodynamic drag for a creeping flow past a fluid sphere [46] is given by

$$F_{\text{aero}} = 6\pi R\mu_0 u(1 + 2\mu_0/3\mu_i)/(1 + \mu_0/\mu_i) \tag{12}$$

where u is the drop velocity, R is the radius of the drop, μ_0 is the dynamic viscosity of air, and μ_i is the dynamic viscosity of the liquid. An empirical constant based on flow characteristics needs to be added to the above expression to accommodate for the present higher Reynolds numbers and the wall effect [47–49]. Values of F_{aero} range from 6.2×10^{-9} N to 1.6×10^{-7} N. The surface resistive force is dominated by surface drag [13] and is given by

$$F_{\text{sres}} = \tau_{\text{high}} f_1 w(\cos\theta_R - \cos\theta_A) \tag{13}$$

where f_1 is the length fraction of drop that actually makes contact with the substrate [13], w is the contact diameter (m), θ_R is the receding contact angle, and θ_A is the advancing contact angle. Typical values of F_{sres} range between 6.5×10^{-8} N and 2.0×10^{-7} N. Applying a force balance on the drop yields

$$F_{\text{net}} = F_{\text{act}} - F_{\text{aero}} - F_{\text{sres}} \tag{14}$$

The acceleration of the drop can then be found at any instant of time. To find the acceleration at the start of the motion, however, F_{aero} and F_{sres} are set to zero. To estimate the total distance traveled by the drops before it comes to stop, an energy balance is conducted. All the energy gained by the drop SE is gained at the start of the motion when the drop is in contact with the laser beam. This energy is then dissipated in doing work against the movement resisting forces. The total traveling distance s is given by

$$s = SE/F_{\text{res}} \tag{15}$$

To determine the movement direction, the length of the heated region is divided into multiple cells, as shown in Fig. 5. For the opaque and nearly opaque drops, the absorbed flux in each cell depends on the liquid absorptance. Based on the number of cells penetrated and heated by the laser beam, the angle at which the drop moves can be calculated. The direction of the drop motion is normal to the z-direction, as shown in Fig. 5. The numbered arrows (3, 6, and 7) in Fig. 5 show the direction of the drop motion corresponding to the number of cells the laser beam penetrates and heats (3, 6, and 7) within the drop. The model predictions are generally in agreement with the experimental results for translucent and opaque drops.

For a transparent drop, however, almost all the laser energy exits the drop (E_t) to form a spark behind the drop. The heat emitted from the spark is not emitted uniformly in all directions; most of the heat is emitted in the direction of the oncoming laser [50]. There is a creation of plasma, and a shock wave is created traveling away from the spark toward the laser beam [51]. This explains the loud clicking sound observed in the present study during the creation of the spark. The high temperature of the shock wave and the plasma, which carries most of the spark energy, is what pushes the drop in the opposite direction of the spark since it would be hard for the drop to heat itself from the spark only through radiation since its absorbance is still the same, i.e., very low.

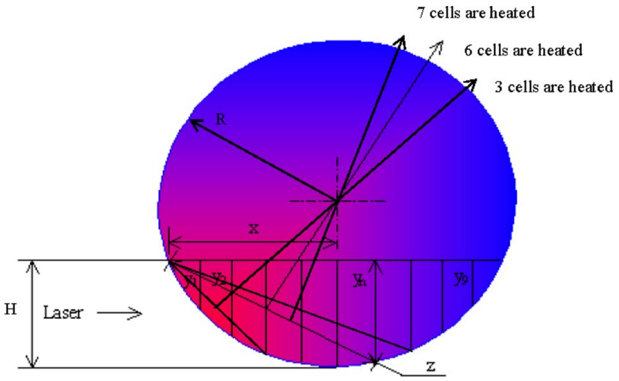

Fig. 5 **Schematic of the present model. The heated volume is divided into ten cells for the model.**

4 Conclusions

Drops of varying transparencies (absorption coefficient c_a ranging from 0.05 m^{-1} to 6000 m^{-1}) and diameters (1–4 mm) were manipulated on a hydrophobic substrate, produced from Fluoropel® PFC M1604V coated glass slide, using a Nd:YAG laser (532 nm) pulsing at 10 Hz, energy range of 3–12 mJ/pulse. The drop kinematics was found to depend on the drop transparency, the drop size, and the laser beam energy. A phenomenological model was developed to explain the physics behind the observations. The following conclusions can be drawn from the present study.

1. Transparent drops moved toward the laser beam since the energy required for the motion came primarily from the spark that was produced behind the drop due to the drop acting like a ball lens, whereas dyed drops (translucent and opaque) moved at large angles with the oncoming laser beam and the angle of motion depended on the drops' absorbance, resulting in higher angles for highly absorbent drops.
2. Higher laser-induced drop velocities were observed when the drops moved on a hydrophobic glass substrate, compared with suspending them on immiscible liquid substrate [19] or immersing them in another immiscible liquid on a glass substrate [22]. This could be useful for quick response applications.
3. A model was developed for translucent and opaque drop motions that could predict the drop motion based on beam energy, drop diameter, and absorption coefficient. The drops can be moved at any desired angle by varying the drops' absorbance and vice versa, i.e., the drops' absorbance can be determined based on the angle at which it moves upon interacting with a laser beam.

The present model, however, is simplified and does not account for plasma formation around the spark and the shock wave emanating from the spark in the case of transparent drops. These effects should be incorporated in future models. Also future studies should address whether the drops move with a rolling mode or a sliding mode in order to model accurately the forces acting on the drops during the motion. Finally, the sizes of the droplets investigated in this study were limited to the millimeter range. Thus, the feasibility of the present approach for controlling microdroplets in microfluidics devices merits further studies.

Nomenclature

a = absorptance
A_h = surface area of the heated region (m^2)
A_l = cross-sectional area of the laser (m^2)
c = specific heat capacity of water (4200 J/kg K)
c_a = absorption coefficient (m^{-1})
d = diameter of the drop (m)
E_a = flux absorbed ($\mathrm{W/m^2}$)
E_e = flux emitted ($\mathrm{W/m^2}$)
E_i = incident laser flux ($\mathrm{W/m^2}$)
f = focal length of the drop ball lens (m)
f_1 = fraction of the drop in physical contact with the substrate
F_{act} = actuating force on the drop (N)
F_{aero} = aerodynamic drag on the drop (N)
F_{sres} = surface resistive force on the drop (N)
F_{net} = net force acting on the drop (N)
F_{res} = total resisting force on the drop (N)
L = path length of the laser beam inside the drop (m)
m = mass of the drop (kg)
P = laser power (W)
r = characteristic length of the heated region of the drop (m)
R = radius of the drop (m)
s = distance traveled by the drop (m)
SE = energy gained by the drop before the start of the movement (J)
T = temperature (K)
t = time (s)
u = drop velocity (m/s)
w = surface contact diameter (m)
x = distance (m)
z = the normal to the movement direction

Greek

α = absorbance
ε = emissivity of the drop
ϕ = angle of drop motion (deg)
θ_A = advancing contact angle
θ_R = receding contact angle
μ = refractive index of the drop liquid
μ_0 = viscosity of air ($\mathrm{N\,s/m^2}$)
μ_i = viscosity of water ($\mathrm{N\,s/m^2}$)
σ = Stefan–Boltzman constant ($5.67\times10^{-8}\ \mathrm{W/m^2\,K^4}$)
τ = surface tension (N/m)
τ_{high} = higher surface tension at ambient temperature (N/m)
τ_{low} = lower surface tension at elevated temperature (N/m)

References

[1] Kotz, K. T., Gu, Y., and Faris, G. W., 2005, "Optically Addressed Droplet-Based Protein Assay," J. Am. Chem. Soc., **127**, pp. 5736–5737.
[2] Song, H., Chen, D. L., and Ismagilov, R. F., 2006, "Reactions in Droplets in Microfluidic Channels," Angew. Chem., Int. Ed., **45**(44), pp. 7336–7356.
[3] Ozen, O., Aubry, N., Papageorgiou, D. T., and Petropoulos, P. G., 2006, "Monodisperse Drop Formation in Square Microchannels," Phys. Rev. Lett., **96**, p. 144501.
[4] Cheow, L. F., Yobas, L., and Kwong, D.-L., 2007, "Digital Microfluidics: Droplet Based Logic Gates," Appl. Phys. Lett., **90**, p. 054107.
[5] Kitahata, H., 2006, "Spontaneous Motion of a Droplet Coupled With Chemical Reaction," Prog. Theor. Phys., **161**, pp. 220–223.
[6] Cho, S. K., Moon, H., and Kim, C.-J., 2003, "Creating, Transporting, Cutting, and Merging Liquid Droplets by Electrowetting-Based Actuation for Digital Microfluidic Circuits," J. Microelectromech. Syst., **12**(1), pp. 70–80.
[7] Savino, R., Monti, R., and Alterio, G., 2001, "Drops Pushing by Marangoni Forces," Phys. Fluids, **13**(5), pp. 1513–1516.
[8] Farahi, R. H., Passian, A., Ferrell, T. L., and Thundat, T., 2004, "Microfluidic Manipulation via Marangoni Forces," Appl. Phys. Lett., **85**(18), pp. 4237–4239.
[9] Farahi, R. H., Passian, A., Zahrai, S., Lereu, A. L., Ferrell, T. L., and Thundat, T., 2006, "Microscale Marangoni Actuation: All-Optical and All-Electrical Methods," Ultramicroscopy, **106**, pp. 815–821.
[10] Passian, A., Zahrai, S., Lereu, A. L., Farahi, R. H., Ferrell, T. L., and Thundat, T., 2006, "Nonradiative Surface Plasmon Assisted Microscale Marangoni Forces," Phys. Rev. E, **73**, p. 066311.
[11] Lereu, A. L., Passian, A., Farahi, R. H., Zahrai, S., and Thundat, T., 2006, "Plasmonic Marangoni Forces," J. Eur. Opt. Soc. Rapid Publ., **1**, p. 06030.
[12] Oh, S.-K., Nakagawa, M., and Ichimura, K., 2000, "Light-Guided Movement of a Liquid Droplet," Mol. Cryst. Liq. Crys. Sci. Technol., **345**, pp. 311–316.
[13] Yang, J.-T., Chen, J. C., Huang, K.-J., and Yeh, J. A., 2006, "Droplet Manipulation on a Hydrophobic Textured Surface With Roughened Patterns," J. Microelectromech. Syst., **15**(3), pp. 697–707.
[14] Moumen, N., Subramanian, R. S., and McLaughlin, J. B., 2006, "Experiments on the Motion of Drops on a Horizontal Solid Surface Due to a Wettability Gradient," Langmuir, **22**, pp. 2682–2690.
[15] Chen, T.-H., Chuang, Y.-J., Chieng, C.-C., and Tseng, F.-G., 2007, "A Wettability Switchable Surface by Microscale Surface Morphology Change," J. Micromech. Microeng., **17**, pp. 489–495.
[16] Fowler, J., Moon, H., and Kim, C.-J., 2002, "Enhancement of Mixing by Droplet-Based Microfluidics," 15th IEEE International Conference on Micro Electro Mechanical Systems, Las Vegas, NV, pp. 97–100.
[17] Ford, M. L., and Nadim, A., 1994, "Thermocapillary Migration of an Attached Drop on a Solid Surface," Phys. Fluids, **6**(9), pp. 3183–3185.
[18] Farahi, R. H., Passian, A., Ferrell, T. L., and Thundat, T., 2005, "Marangoni Forces Created by Surface Plasmon Decay," Opt. Lett., **30**(6), pp. 616–618.
[19] Grigoriev, R. O., Schatz, M. F., and Sharma, V., 2006, "Chaotic Mixing in Microdroplets," Lab Chip, **6**(10), pp. 1369–1372.
[20] Zardecki, A., and Pendleton, J. D., 1989, "Hydrodynamics of Water Droplets Irradiated by a Pulsed $\mathrm{CO_2}$ Laser," Appl. Opt., **28**(3), pp. 638–640.
[21] Garnier, N., Grigoriev, R. O., and Schatz, M. F., 2003, "Optical Manipulation of Microscale Fluid Flow," Phys. Rev. Lett., **91**(5), p. 054501.
[22] Kotz, K. T., Noble, K. A., and Faris, G. W., 2004, "Optical Microfluidics," Appl. Phys. Lett., **85**(13), pp. 2658–2660.
[23] Rybalko, S., Magome, N., and Yoshikawa, K., 2004, "Forward and Backward Laser-Guided Motion of an Oil Droplet," Phys. Rev. E, **70**(4), p. 046301.
[24] Dietzel, M., and Poulikakos, D., 2005, "Laser-Induced Motion in Nanoparticle Suspension Droplets on a Surface," Phys. Fluids, **17**(10), p. 102106.
[25] Alzuaga, S., Manceau, J. F., and Bastien, F., 2005, "Motion of Droplets on Solid Surface Using Acoustic Radiation Pressure," J. Sound Vib., **282**(1–2), pp. 151–162.
[26] Ashkin, A., 1987, "Optics: Laser Manipulation of Atoms," Nature (London), **330**, pp. 608–609.
[27] Dholakia, K., Spalding, G., and MacDonald, M., 2002, "Optical Tweezers: The Next Generation," Phys. World, **15**(10), pp. 31–35.
[28] Leach, J., Mushfique, H., di Leonardo, R., Padgett, M., and Cooper, J., 2006, "An Optically Driven Pump for Microfluidics," Lab Chip, **6**(6), pp. 735–739.
[29] Schroll, R. D., Wunenburger, R., Casner, A., Zhang, W. W., and Delville, J.-P., 2007, "Liquid Transport Due to Light Scattering," Phys. Rev. Lett., **98**(13), p. 133601.
[30] Bisyarin, V. P., Efremenko, V. V., Kolosov, M. A., Pozhidaev, V. N., Sokolov, A. V., Strelkov, G. M., and Fedorova, L. V., 1983, "Propagation of Laser Radiation in a Water Aerosol Under Aerosol Breakup Conditions," Sov. Phys. J., **26**(2), pp. 121–140.
[31] Prishivalko, A. P., and Leiko, S. T., 1984, "Effect of Liquid Surface Layers on the Heat Release and Heating of Water Droplets Under the Action of Radiation," Sov. Phys. J., **5**(2), pp. 301–303.
[32] Park, B.-S., and Armstrong, R. L., 1989, "Laser Droplet Heating: Fast and Slow Heating Regimes," Appl. Opt., **28**(17), pp. 3671–3680.
[33] Singh, P. I., and Knight, C. J., 1980, "Impulse Laser-Induced Shattering of Water Drops," AIAA J., **18**(1), pp. 96–100.
[34] Zuev, V. E., and Zemlyanov, A. A., 1983, "Explosion of a Drop Under the Action of Intense Laser Radiation," Sov. Phys. J., **26**(2), pp. 149–159.
[35] Carls, J. C., and Brock, J. R., 1987, "Explosion of a Water Droplet by Pulsed Laser Heating," Aerosol Sci. Technol., **7**(1), pp. 79–90.
[36] Ivanov, E. V., Korovin, V. Y., and Sedunov, Y. S., 1977, "Motion of Optically Dense Liquid Drops in a Laser Radiation Field," Sov. J. Quantum Electron., **7**(9), pp. 1066–1071.
[37] Autric, M., Vigliano, P., Dufresne, D., Caressa, J. P., and Bournot, P., 1988, "Pulsed $\mathrm{CO_2}$ Laser-Induced Effects on Water Droplets," AIAA J., **26**(1), pp. 65–71.
[38] Incropera, F. P., and DeWitt, D. P., 2002, *Fundamentals of Heat and Mass Transfer*, Wiley, New York.
[39] Seeton, C. J., 2006, "Viscosity–Temperature Correlation for Liquids," Tribol. Lett., **22**(1), pp. 67–78.
[40] Astrakhan, I. M., 1959, "Shock Wave Pressure With an Intense Spark Discharge in Water," News of Higher Institutions of Learning, Petroleum and Gas, No. 10, Baku, pp. 87–92.
[41] Zhuzhukalo, E. V., Kolomifekii, A. N., and Nastoyashchii, A. F., 1981, "Breakdown of Atmospheric Air by Neodymium Laser Radiation Forming

Large-Diameter Focusing Spots," Sov. J. Quantum Electron., **11**(5), pp. 670–671.

[42] Phuoc, T. X., 2005, "An Experimental and Numerical Study of Laser-Induced Spark in Air," Opt. Lasers Eng., **43**(2), pp. 113–129.

[43] Phuoc, T. X., 2006, "Laser-Induced Spark Ignition Fundamental and Applications," Opt. Lasers Eng., **44**(5), pp. 351–397.

[44] Pegau, W. S., Gray, D., and Zaneveld, J. R. V., 1997, "Absorption and Attenuation of Visible and Near-Infrared Light in Water: Dependence on Temperature and Salinity," Appl. Opt., **36**(24), pp. 6035–6046.

[45] Bindhu, C. V., Harilal, S. S., Nampoori, V. P. N., and Vallabhan, C. P. G., 1999, "Studies of Nonlinear Absorption and Aggregation in Aqueous Solutions of Rhodamine 6G Using a Transient Thermal Lens Technique," J. Phys. D, **32**(4), pp. 407–411.

[46] White, F. M., 1991, *Viscous Fluid Flow*, McGraw-Hill, New York.

[47] Ataide, C. H., Pereira, F. A. R., and Barrozo, M. A. S., 1999, "Wall Effects on the Terminal Velocity of Spherical Particles in Newtonian and Non-Newtonian Fluids," Braz. J. Chem. Eng., **16**(4), pp. 387–394.

[48] Chen, S. H., 1999, "Thermocapillary Migration of a Fluid Sphere Parallel to an Insulated Plane," Langmuir, **15**(25), pp. 8618–8626.

[49] Chen, S. H., 2000, "Movement of a Fluid Sphere in the Vicinity of a Flat Plane With Constant Temperature Gradient," J. Colloid Interface Sci., **230**(1), pp. 157–170.

[50] Beduneau, J. L., and Ikeda, Y., 2004, "Spatial Characterization of Laser-Induced Sparks in Air," J. Quant. Spectrosc. Radiat. Transf., **84**(2), pp. 123–139.

[51] Zakharin, B., Stricker, J., and Toker, G., 1999, "Laser-Induced Spark Schlieren Imaging," AIAA J., **37**(9), pp. 1133–1135.

A Lattice Boltzmann Method Based Numerical Scheme for Microchannel Flows

S. C. Fu
Department of Mechanical Engineering,
The Hong Kong Polytechnic University,
P.R.C.

W. W. F. Leung[1]
Department of Mechanical Engineering,
The Hong Kong Polytechnic University,
P.R.C.;
Research Institute of Innovative Products and
Technologies,
The Hong Kong Polytechnic University,
P.R.C.
e-mail: riwl@polyu.edu.hk

R. M. C. So
Department of Mechanical Engineering,
The Hong Kong Polytechnic University,
P.R.C.

Conventional lattice Boltzmann method (LBM) is hyperbolic and can be solved locally, explicitly, and efficiently on parallel computers. The LBM has been applied to different types of complex flows with varying degrees of success, and with increased attention focusing on microscale flows now. Due to its small scale, microchannel flows exhibit many interesting phenomena that are not observed in their macroscale counterpart. It is known that the Navier–Stokes equations can still be used to treat microchannel flows if a slip-wall boundary condition is assumed. The setting of boundary conditions in the conventional LBM has been a difficult task, and reliable boundary setting methods are limited. This paper reports on the development of a finite difference LBM (FDLBM) based numerical scheme suitable for microchannel flows to solve the modeled Boltzmann equation using a splitting technique that allows convenient application of a slip-wall boundary condition. Moreover, the fluid viscosity is accounted for as an additional term in the equilibrium particle distribution function, which offers the ability to simulate both Newtonian and non-Newtonian fluids. A two-dimensional nine-velocity lattice model is developed for the numerical simulation. Validation of the FDLBM is carried out against microchannel and microtube flows, a driven cavity flow, and a two-dimensional sudden expansion flow. Excellent agreement is obtained between numerical calculations and analytical solutions of these flows. [DOI: 10.1115/1.3155993]

1 Introduction

Microchannels/tubes are important components for micro-electro-mechanical systems (MEMS), and they are used to transport fluid in many MEMS devices. The development of these technologies has motivated the study of fluid flows in microscale devices and geometries. Due to their small scale, these flows exhibit many interesting phenomena that are not observed in their large-scale counterparts. In these small-scale flows, the molecular mean free path of the fluid could be of the same order as a typical geometric dimension of the device and the continuum hypothesis, which is the basic assumption of the Navier–Stokes (NS) equations, may break down. The Knudsen number Kn defined as the ratio of the mean free path to the characteristic length of a flow, is one of the main parameter used to classify how rarefied a flow is, and hence how valid the continuum hypothesis is. The four main regimes classified by Kn are the following [1]:

1. $\mathrm{Kn}<10^{-3}$, NS equations applicable with no-slip boundary conditions
2. $10^{-3}<\mathrm{Kn}<10^{-1}$, NS equations still applicable with slip boundary conditions
3. $10^{-1}<\mathrm{Kn}<10^{1}$, transitional flow regime
4. $\mathrm{Kn}>10^{1}$, free molecular flow

Most of the microchannel flows in MEMS devices fall into the second regime. Therefore, it is recognized that for microchannel flows, the NS equations are still applicable when slip-wall boundary condition is used.

The Bhatnagar–Gross–Krook (BGK) model has long played an important role in the development of kinetic-theory based numerical schemes. The derivation of the Euler equations and/or NS equations from the Boltzmann equation with a BGK-type model can be achieved by using the Chapman–Enkog or multiscale expansion with Kn as an expansion parameter. The procedure leads to the development of numerical schemes along this direction for different types of fluid flows. The lattice Boltzmann method (LBM) is the most notable and widely used among these numerical schemes, and it has recently been developed into an alternative and a promising numerical scheme for modeling fluid physics and simulating fluid flows [2]. The equation is hyperbolic and can be solved locally, explicitly, and efficiently on parallel computers. Its simplicity renders the equation easy to program and to incorporate the modeling of additional physical phenomena that closely mimic the real physics. Recently, more researchers attempted to apply this LBM to simulate microscale flows [3–7]. Nie et al. [3] explored the possibility of using LBM to simulate flows with high Kn. They argued that "because LBM is a kinetic method based on the particle distribution function, it can be used to study the flow dependence on Kn, including the slip velocity, the nonlinear pressure drop in microchannel, and the variation in the vortex center in the microcavity." Their approach attempts to find new physics through LBM by making use of its kinetic-theory based nature. Besides, LBM can be considered as a particular discretization for the discrete Boltzmann equation. Consequently, LBM can be treated as a powerful numerical solver for the NS equations [8,9].

Under this approach, LBM is also applicable for microchannel flow simulations if the slip boundary condition can be successfully modeled. Through the simulation of microchannel flows, Lim et al. [4] investigated two common approaches for setting the boundary condition in LBM, namely, a heuristic boundary condition (specular model, including the earlier bounce back condition) and an extrapolation scheme. In their heuristic model, as they have reported, momentum was "deposited" on the wall. The argument and physical meaning of the condition adopted in the heuristic approach are not well defined. There still exist many unclear points for the heuristic approach. The extrapolation scheme approximates the density and velocity at a solid boundary by a second-order polynomial extrapolation form, and then the unknown distribution functions are approximated by their equilib-

---

[1] Corresponding author.

Contributed by the Fluids Engineering Division of ASME for publication in the JOURNAL OF FLUIDS ENGINEERING. Manuscript received September 23, 2008; final manuscript received May 12, 2009; published online July 7, 2009. Assoc. Editor: Neelesh A. Patankar. Paper presented at the 2008 ASME International Mechanical Engineering Congress (IMECE2008), Boston, MA, October 31–November 6, 2008.

rium functions. However, the validity of these approximations remains unclear. Although a number of proposals of the slip-wall condition for the LBM were shown to have varying degrees of success [4–7], there is still a need for the development of an algorithm in LBM that enables the application of a more flexible boundary condition, including a slip condition as a result of the above discussion. A contribution of this paper is to offer a more rigorous approach to address the slip boundary condition. An algorithm is developed by solving the Boltzmann equation using a splitting method that enables the implementation of the slip-wall boundary condition at the channel wall for flows in microfluidic and microscale devices. Hereafter, this algorithm is designated as FDLBM.

Also, LBM has been applied to different kinds of complex flows with varying degrees of success, but mainly for Newtonian fluid. Since then, it has been reported by Loose and Hess [10] that the proportionality between stress and strain rates (the Newtonian assumption) breaks down when the strain rate exceeds approximately twice the molecular interaction frequency, which is possible for microfluidic flows. Therefore, it would be desirable to develop a non-Newtonian FDLBM for microchannel flows. Traditionally, the lattice Boltzmann formulation could be made to recover the NS equations by fixing a number of moments of the equilibrium distribution function. A second contribution of the present paper is that the fluid viscosity is determined as a parameter in the constraints for finding the moments of the equilibrium distribution function, and hence it appears as an additional term in the equilibrium distribution function. This offers the ability for simulating both Newtonian and non-Newtonian fluids.

In simulating microchannel flows for which the channel can have a circular cross section, transformation of coordinates is sometimes essential. For example, a pipe flow is best described by cylindrical coordinates. The governing NS equations, after transformation, are no longer in conservation form. This causes difficulty in the attempt to recover the NS equations from the modeled Boltzmann equation. In this paper, a third contribution is that the FDLBM is extended by modifying the BGK-type modeled Boltzmann equation with an additional source term. This additional source term not only can account for the geometric source term due to coordinate transformation, but can also be used to model certain types of external body forces, e.g., those due to electromagnetic effect, which might be important in the modeling of electronic cooling. Through this new technique in the development of the FDLBM, a large variety of governing equations can be recovered.

In this paper, isothermal flows of an incompressible, isotropic fluid, either Newtonian or non-Newtonian, between two parallel plates through a circular tube in a two-dimensional (2D) driven cavity and in a 2D sudden expansion are investigated. A 2D nine-velocity (D2Q9) lattice model is formulated for the FDLBM. The three aforementioned objectives are incorporated in the present approach. Validations against these 2D flows with known theoretical solutions are carried out.

2 Numerical Method

The starting point of the present analysis is the normalized discrete Boltzmann equation.

$$\frac{\partial f_\alpha}{\partial t}+\xi_\alpha\cdot\nabla_x f_\alpha=-\frac{1}{\varepsilon\phi}(f_\alpha-f_\alpha^{\rm eq}) \tag{1}$$

where ϕ, $\xi_\alpha\equiv(\xi_{\alpha x},\xi_{\alpha y})$, f_α, and $f_\alpha^{\rm eq}$ are the relaxation time, the discrete particle velocity, the discrete particle distribution function, and the discrete particle equilibrium distribution function, respectively; and ε is a small parameter, which is usually taken as $\varepsilon=\mathrm{Kn}$. All equations in this paper are in normalized form. The dimensionless variables are defined as

$$x,y=\frac{\hat{x},\hat{y}}{L},\quad t,\phi=\frac{\hat{t},\hat{\phi}}{L/u_0},\quad \xi_{\alpha x},\xi_{\alpha y}=\frac{\hat{\xi}_{\alpha x},\hat{\xi}_{\alpha y}}{u_0}$$

$$f_\alpha,f_\alpha^{\rm eq},f_\alpha^{(n)}=\frac{\hat{f}_\alpha,\hat{f}_\alpha^{\rm eq},\hat{f}_\alpha^{(n)}}{\rho_0},\quad n\geq 1\quad (\text{see Eq.(3) below for } f_\alpha^{(n)})$$

where L is the characteristic length, which can be the width of the microchannel or the radius of the microcircular pipe, and ρ_0 and u_0 are the characteristic density and speed, respectively. Hereafter, the symbols with a "hat" are used to designate their corresponding dimensional counterparts. The particle velocity is restricted into a finite number of lattice vectors as shown in Fig. 1.

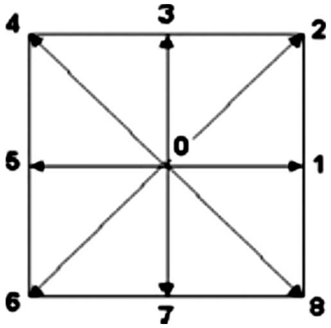

Fig. 1 D2Q9 Lattice velocity model

In this paper, a specific D2Q9 lattice model is used for all simulations (Fig. 1). Therefore, the following derivation uses this D2Q9 model as an example to demonstrate the construction of the numerical method. For a D2Q9 model, the lattice velocities are defined as

$$\xi_0=(0,0),\quad \alpha=0 \tag{2a}$$

$$\xi_\alpha=c(\cos[\pi(\alpha-1)/4],\sin[\pi(\alpha-1)/4]),\quad \alpha=1,3,5,7 \tag{2b}$$

$$\xi_\alpha=\sqrt{2}c(\cos[\pi(\alpha-1)/4],\sin[\pi(\alpha-1)/4]),\quad \alpha=2,4,6,8 \tag{2c}$$

where c is a scaling parameter to be defined later. The index α is used to denote different lattice vectors, ranging from 0 to 8. For other lattice models, such as in a 3D case, the derivation is similar and straightforward. A Chapman–Enskog type expansion is assumed for f_α, such that,

$$f_\alpha=f_\alpha^{\rm eq}+\varepsilon f_\alpha^{(1)}+\varepsilon^2 f_\alpha^{(2)}+O(\varepsilon^3) \tag{3a}$$

where

$$\sum_{\alpha=0}^{8} f_\alpha^{(n)}=\sum_{\alpha=0}^{8} f_\alpha^{(n)}\xi_{\alpha x}=\sum_{\alpha=0}^{8} f_\alpha^{(n)}\xi_{\alpha y}=0,\quad n\geq 1 \tag{3b}$$

is assumed. Multiplying Eq. (1) with respect to $(1,\xi_\alpha)^T$ and taking summation over α, and using the following constraints:

$$\sum_{\alpha=0}^{8} f_\alpha^{\rm eq}=\rho=\text{constant} \tag{4a}$$

$$\sum_{\alpha=0}^{8} f_\alpha^{\rm eq}\xi_{\alpha x}=\rho u \tag{4b}$$

$$\sum_{\alpha=0}^{8} f_\alpha^{\rm eq}\xi_{\alpha y}=\rho v \tag{4c}$$

$$\sum_{\alpha=0}^{8} f_\alpha^{\mathrm{eq}} \xi_{\alpha x}^2 = \rho u^2 + p - \tau_{xx} \tag{4d}$$

$$\sum_{\alpha=0}^{8} f_\alpha^{\mathrm{eq}} \xi_{\alpha y}^2 = \rho v^2 + p - \tau_{yy} \tag{4e}$$

$$\sum_{\alpha=0}^{8} f_\alpha^{\mathrm{eq}} \xi_{\alpha x}\xi_{\alpha y} = \rho uv - \tau_{xy} \tag{4f}$$

the normalized incompressible NS equations are recovered as

$$\frac{\partial \rho}{\partial t} + \frac{\partial \rho u}{\partial x} + \frac{\partial \rho v}{\partial y} = 0 \tag{5a}$$

$$\frac{\partial \rho u}{\partial t} + \frac{\partial \rho u^2}{\partial x} + \frac{\partial \rho uv}{\partial y} = -\frac{\partial p}{\partial x} + \frac{\partial \tau_{xx}}{\partial x} + \frac{\partial \tau_{xy}}{\partial y} + O(\varepsilon) \tag{5b}$$

$$\frac{\partial \rho v}{\partial t} + \frac{\partial \rho uv}{\partial x} + \frac{\partial \rho v^2}{\partial y} = -\frac{\partial p}{\partial y} + \frac{\partial \tau_{xy}}{\partial x} + \frac{\partial \tau_{yy}}{\partial y} + O(\varepsilon) \tag{5c}$$

Here ρ is the density of the fluid, which is specified as constant. Physical quantities (u,v), p, and τ_{xx}, τ_{yy}, τ_{xy} are the x and y direction velocity components, the pressure, and the normal and shear stress components of the flow, respectively. Their dimensionless counterparts are given by

$$\rho = \hat{\rho}/\rho_0, \quad u,v = \hat{u},\hat{v}/u_0, \quad p,\tau_{xx},\tau_{xy},\tau_{yy} = \hat{p},\hat{\tau}_{xx},\hat{\tau}_{xy},\hat{\tau}_{yy}/(\rho_0 u_0^2)$$

For Newtonian fluid, the shear stress components are written as

$$\tau_{xx} = 2\mu\frac{\partial u}{\partial x}, \quad \tau_{yy} = 2\mu\frac{\partial v}{\partial y}, \quad \tau_{xy} = \mu\left(\frac{\partial u}{\partial y} + \frac{\partial v}{\partial x}\right) \tag{6}$$

where μ is the normalized viscosity coefficient. If a suitable f_α^{eq} that satisfies Eqs. (4*a*)–(4*f*) can be found, solving Eq. (1) is equivalent to solving the NS equations with an error term of $O(\varepsilon)$. As a first attempt to develop a viable f_α^{eq} for microscale flows, the traditional approach is not followed, instead, a polynomial series in ξ_α up to the second order is assumed, that is,

$$f_\alpha^{\mathrm{eq}} = A_\alpha + \xi_{\alpha x} Ax_\alpha + \xi_{\alpha y} Ay_\alpha + \xi_{\alpha x}^2 Bxx_\alpha + \xi_{\alpha y}^2 Byy_\alpha + \xi_{\alpha x}\xi_{\alpha y} Bxy_\alpha \tag{7}$$

This lattice f_α^{eq} is different from conventional ones adopted by previous researchers, who normally expand the Maxwellian distribution function up to the second or third order in terms of the products of $\boldsymbol{u}$ and ξ_α [11,12]. The present approach proposes a polynomial in terms of ξ_α and leaves the inclusion of $\boldsymbol{u}$ in the coefficients of the polynomial to be determined through the constraints listed in Eqs. (4*a*)–(4*f*). Assuming parameters with the same magnitude of ξ_α to be equal, the coefficients in Eq. (7), A_α, Ax_α, Ay_α, etc., can be simplified to give the following:

$$A_1 = A_3 = A_5 = A_7$$

$$A_2 = A_4 = A_6 = A_8$$

$$Ax_1 = Ax_3 = Ax_5 = Ax_7$$

$$Ax_2 = Ax_4 = Ax_6 = Ax_8$$

$$Ay_1 = Ay_3 = Ay_5 = Ay_7$$

$$Ay_2 = Ay_4 = Ay_6 = Ay_8$$

$$Bxx_1 = Bxx_3 = Bxx_5 = Bxx_7$$

$$Bxx_2 = Bxx_4 = Bxx_6 = Bxx_8$$

$$Byy_1 = Byy_3 = Byy_5 = Byy_7$$

$$Byy_2 = Byy_4 = Byy_6 = Byy_8$$

$$Bxy_1 = Bxy_3 = Bxy_5 = Bxy_7$$

$$Bxy_2 = Bxy_4 = Bxy_6 = Bxy_8 \tag{8}$$

Using these constraints, one possible set of solution to Eqs. (4*a*)–(4*f*) is

$$A_0 = \rho - \frac{2p}{c^2} - \frac{\rho|\boldsymbol{u}|^2}{c^2} + \frac{\tau_{xx} + \tau_{yy}}{c^2}, \quad A_1 = A_2 = 0 \tag{9a}$$

$$Ax_1 = \frac{\rho u}{2c^2}, \quad Ax_2 = 0 \tag{9b}$$

$$Ay_1 = \frac{\rho v}{2c^2}, \quad Ay_2 = 0 \tag{9c}$$

$$Bxx_1 = \frac{1}{2c^4}(p + \rho u^2 - \tau_{xx}), \quad Bxx_2 = 0 \tag{9d}$$

$$Byy_1 = \frac{1}{2c^4}(p + \rho v^2 - \tau_{yy}), \quad Byy_2 = 0 \tag{9e}$$

$$Bxy_1 = 0, \quad Bxy_2 = \frac{1}{4c^4}(\rho uv - \tau_{xy}) \tag{9f}$$

In order to solve Eq. (1) numerically, the temporal and the spatial derivatives are discretized in the following manner:

$$\frac{f_\alpha(\boldsymbol{x},t+\Delta t) - f_\alpha(\boldsymbol{x},t)}{\Delta t} + \frac{f_\alpha(\boldsymbol{x}+\xi_\alpha\Delta t,t+\Delta t) - f_\alpha(\boldsymbol{x},t+\Delta t)}{\Delta t} = -\frac{1}{\varepsilon\phi}(f_\alpha(\boldsymbol{x},t) - f_\alpha^{\mathrm{eq}}(\boldsymbol{x},t)) \tag{10}$$

where the second term is viewed as a directional derivative. The scaling parameter c in Eqs. (2*b*) and (2*c*) can be chosen such that $\xi_\alpha = \Delta\boldsymbol{x}/\Delta t$ to fit the gird. Further setting $\varepsilon = \Delta t$, the following is obtained:

$$f_\alpha(\boldsymbol{x}+\xi_\alpha\Delta t,t+\Delta t) - f_\alpha(\boldsymbol{x},t) = -\frac{1}{\phi}(f_\alpha(\boldsymbol{x},t) - f_\alpha^{\mathrm{eq}}(\boldsymbol{x},t)) \tag{11}$$

LBM could be considered a particular discretization for the discrete Boltzmann equation, and the resulting Eq. (11) is in line with the conventional LBM [8,9]. Equation (1) can be discretized by any numerical method other than that used in Eq. (10). Even if the same discretization as conventional LBM is employed (i.e., Eq. (10)), the current scheme can still be designated as FDLBM because it is different from the conventional LBM in several ways. These differences are discussed below.

In conventional LBM, the viscous terms in the NS equations are recovered from the second-order (i.e., $O(\varepsilon^2)$) equation of the Chapman–Enskog expansion. Consequently, the relaxation time ϕ is related to the viscosity coefficient, and the resulting shear stress has to be in the Newtonian form. Some researchers attempted to extend the LBM to non-Newtonian fluid flows by allowing the local value of the viscosity to depend on the strain rate tensor [13–16]. However, the relaxation time has critical influence on the numerical stability of the scheme, especially for non-Newtonian fluid flows where numerical instability can occur despite relatively large zero-shear rate viscosity (which is the viscosity as the shear rate tends to zero), e.g., in a non-Newtonian power-law fluid. To avoid this difficulty, Gabbanelli et al. [16] set a lower and upper bounds on the viscosity, but it limits the practical application of the scheme. Also, the recovery of the viscous terms in the second-order expansion implies that the small parameter used for the expansion has to be carefully chosen. If it is not small enough, the asymptotic expansion might not be appropriate. Thus the relaxation time, and hence the viscosity, has to be controlled to avoid failure of the asymptotic expansion. If the small parameter is too small, this means that the viscous terms are much smaller than other terms and that limits the practical application of the scheme again.

Moreover, He and Luo [11] remarked that, theoretically speaking, LBM usually simulates the compressible NS equations instead of its incompressible counterpart, because the density fluctuation is not necessarily zero in numerical simulations. The compressible effect in conventional LBM models might produce some significant errors in numerical simulations. Therefore, in order to correctly simulate the incompressible NS equations, it has to ensure that the Mach number and the density variation are of $O(\mathrm{Kn})$ and $O(\mathrm{Kn}^2)$, respectively. Unfortunately, this is not easy to control numerically; even if it can be accomplished, the numerical scheme becomes a cumbersome process. The error is significant in numerical simulations such as flow through porous media where a pressure gradient is applied to drive the system, and the pressure gradient is established by maintaining a density gradient in the system [11].

In view of these difficulties, it is desirable to develop an alternative (the present FDLBM) to conventional LBM where some or all of these difficulties are remedied. Unlike conventional LBM where the pressure is assumed to relate to the density by an ideal gas law, the current approach considers pressure as an independent dynamic variable. By considering compressibility relation other than an ideal gas law or explicitly specifying the density profile, flow through porous media or stratified flow can be calculated. Although the present approach has the ability to simulate such flows, in this paper, the density is set as a given constant so that the incompressible NS is recovered. Further explanation will be given in Sec. 2.1.

Instead of recovering the viscous terms in the second order, focus is directed to recover the NS equations only from the first-order equation of the Chapman–Enskog expansion. The shear stress components τ_{xx}, τ_{yy}, τ_{xy}, such as given in Eq. (6) for a Newtonian fluid, are modeled by a central difference scheme with a given viscosity coefficient. Then, the idea of changing f_α^{eq} [17], instead of changing ϕ, can be employed, thus offering the ability to simulate non-Newtonian fluid flows. The shear stress tensor is kept as an arbitrary parameter that depends on the non-Newtonian model employed. It should be pointed out that the present scheme is targeted at the time-independent type of non-Newtonian fluids with isotropic stress tensor and not at the wide ranging class of non-Newtonian fluids.

Up until now, no constraint has been imposed on the relaxation time ϕ. In this work, $\phi=1$ is assumed and this allows the derivation of the following simple relation:

$$f_\alpha(\boldsymbol{x}+\xi_\alpha\Delta t, t+\Delta t) = f_\alpha^{\mathrm{eq}}(\boldsymbol{x},t) \tag{12}$$

Also, as will be shown later, this choice provides convenience in the setting of the boundary condition. In fact, since ϕ is arbitrary in the present method and it always appears together with ε, using an appropriate normalization ϕ can always be treated as unity.

For microfluidic flows, the NS equations can still be used to analyze such flows if a slip velocity boundary condition at the wall is allowed. Consequently, setting the boundary condition correctly is critical if the present FDLBM were to be applicable to microchannel flows. Although Eq. (11) or Eq. (12) is rather simple, it is not convenient to implement for a complicated boundary condition, such as a slip velocity where a corresponding boundary f_α is at times difficult to find. In order to apply the boundary condition in the present FDLBM as conveniently as conventional finite difference scheme used in direct numerical simulation, an improved numerical algorithm is required, and this is proposed below.

Since Eq. (1) can be solved by any numerical methods, a splitting method along the line proposed by Toro [18] is used to solve the equation in two stages. Traditionally, they are interpreted as the freestreaming (or evolution) stage and the collision (or projection) stage [19–22]. For the freestreaming stage, the homogenous hyperbolic equation,

$$\frac{\partial f_\alpha}{\partial t} + \xi_\alpha \cdot \nabla_x f_\alpha = 0 \tag{13}$$

is solved. A number of well-known solvers for Eq. (13) are available. It is understood that different numerical schemes will give rise to different overall numerical stability criteria. Since the main objective of this paper is to demonstrate that Eq. (1) used to recover the incompressible NS equations can be solved using this numerical approach, therefore, a careful analysis of the overall numerical stability of the scheme will be deferred to a later study. In the present work, a numerical scheme that gives a stable solution is presented.

If a discretization scheme similar to Eqs. (10) and (11)(noted that the right hand side is zero now) is chosen, this gives rise to a simple relation.

$$f_\alpha(\boldsymbol{x}+\xi_\alpha\Delta t, t+\Delta t) = f_\alpha(\boldsymbol{x},t) \tag{14}$$

Next, for the collision stage, the results obtained in the first stage act as initial conditions for the differential equation.

$$\frac{\partial f_\alpha}{\partial t} = -\frac{1}{\varepsilon\phi}(f_\alpha - f_\alpha^{\mathrm{eq}}) \tag{15}$$

which is discretized using the Euler method with the choice $\varepsilon=\Delta t$ and $\phi=1$,

$$\frac{f_\alpha(\boldsymbol{x},t+\Delta t) - f_\alpha(\boldsymbol{x},t)}{\Delta t} = -\frac{1}{\varepsilon\phi}(f_\alpha(\boldsymbol{x},t) - f_\alpha^{\mathrm{eq}}(\boldsymbol{x},t))$$

then,

$$f_\alpha(\boldsymbol{x},t+\Delta t) = f_\alpha^{\mathrm{eq}}(\boldsymbol{x},t) \tag{16}$$

It should be noted that the splitting method is only first-order accurate in time [18,23]. Since $\varepsilon=\Delta t$ has been chosen, it is consistent with the asymptotic expansion error, which is given by $O(\varepsilon)=O(\Delta t)$. By splitting the equation and setting $\phi=1$, there are some similarities between the present scheme and the total thermalized transport method [19,20] or the equilibrium flux method [24]. The numerical procedures are summarized below.

Initial setting up step.

(i) Initial conditions for all macroscopic quantities (u_0, v_0, p_0) including the boundary points are given. The initial $f_\alpha^{0,\mathrm{eq}}$ (including the boundary points) is determined using Eqs. (7), (8), and (9*a*)–(9*f*). Thus determined that they are used as initial values to start the calculation.

Freestreaming step.

(ii) With f_α at time t (including the boundary points) known, an intermediate value f_α^I is calculated by solving Eq. (13). This is only applied to the interior grid points in the domain. The result thus obtained gives the intermediate value f_α^I (excluding boundary points).

(iii) Using this f_α^I, the corresponding macroscopic quantities (u_I, v_I, p_I) for all interior grid points are calculated.

(iv) The boundary conditions for the macroscopic level are then set as in any finite difference methods.

(v) Using the macroscopic quantities thus determined (complete domain including the boundary points) and invoking Eqs. (7), (8), and (9*a*)–(9*f*), a corresponding $f_\alpha^{I,\mathrm{eq}}$ is obtained (including all boundary points). It is noted that these $f_\alpha^{I,\mathrm{eq}}$ are different from f_α^I in (ii).

Collision step.

(vi) Due to Eq. (16), the collision step is completed by exactly setting the new f_α (at time $t+\Delta t$) as the $f_\alpha^{I,\mathrm{eq}}$. Since each set of macroscopic quantities will map uniquely to an equilibrium distribution function, and vice versa, the macroscopic quantities thus obtained are, in fact, the values at time $t+\Delta t$, i.e., $(u,v,p)|_{t+\Delta t}=(u_I,v_I,p_I)$. Hence, the collision step, in fact, spends none computing resources.

(vii) Time marching proceeds by repeating steps (ii)–(vi).

This algorithm provides a convenient way for setting the boundary condition but retain all the advantages of conventional LBM, i.e., solving the equation locally, explicitly, and efficiently on parallel computing. The formulation and hence the computation is only a bit more (only the modeling of the shear stress tensor is additional) than the conventional D2Q9 LBM. It is in this sense that the inadequacies of the conventional LBM are remedied.

2.1 Remarks on the Satisfaction of the Continuity Equation. In step (iii) of the numerical procedure outlined above, the macroscopic quantities are obtained from the following:

$$u \equiv \frac{1}{\rho}\sum_{\alpha=0}^{8} f_\alpha \xi_{\alpha x} \tag{17a}$$

$$v \equiv \frac{1}{\rho}\sum_{\alpha=0}^{8} f_\alpha \xi_{\alpha y} \tag{17b}$$

$$p \equiv \sum_{\alpha=0}^{8} f_\alpha \frac{1}{2}(\xi_{\alpha x}^2+\xi_{\alpha y}^2) - \frac{1}{2}\rho|\boldsymbol{u}|^2 + \frac{\tau_{xx}+\tau_{yy}}{2} \tag{17c}$$

Unlike the conventional LBM, the density ρ is not determined by f_α, but rather it is a given constant (in fact, it can be defined by any state equation also). Thus, if there is a deviation between the given ρ and the value of Σf_α, Eq. (3*b*) might not be satisfied and the following relation is observed:

$$\sum_\alpha (f_\alpha - f_\alpha^{\text{eq}})\begin{pmatrix} 1 \\ \xi_{\alpha x} \\ \xi_{\alpha y} \\ \dfrac{\xi_{\alpha x}^2+\xi_{\alpha y}^2}{2}\end{pmatrix} = \begin{pmatrix} \sum_\alpha f_\alpha - \rho \\ 0 \\ 0 \\ 0 \end{pmatrix} \tag{18}$$

Consequently, by multiplying Eq. (1) with respect to $(\xi_\alpha, |\xi_\alpha|^2/2)^T$ and taking summation over α and using Eq. (4), during the numerical manipulation, the solution of Eq. (1) will lead to the satisfaction of

$$\frac{\partial \rho u}{\partial t} + \frac{\partial \rho u^2 + p - \tau_{xx}}{\partial x} + \frac{\partial \rho uv - \tau_{xy}}{\partial y} = O(\varepsilon) \tag{19a}$$

$$\frac{\partial \rho v}{\partial t} + \frac{\partial \rho uv - \tau_{xy}}{\partial x} + \frac{\partial \rho v^2 + p - \tau_{yy}}{\partial y} = O(\varepsilon) \tag{19b}$$

$$\frac{\partial p + \frac{1}{2}\rho|\boldsymbol{u}|^2 - \frac{\tau_{xx}+\tau_{yy}}{2}}{\partial t} + \frac{c^2}{2}\left(\frac{\partial \rho u}{\partial x} + \frac{\partial \rho v}{\partial y}\right) = O(\varepsilon) \tag{19c}$$

The last equation is due to

$$\sum_{\alpha=0}^{8} f_\alpha^{\text{eq}} \frac{\xi_{\alpha x}}{2}(\xi_{\alpha x}^2+\xi_{\alpha y}^2) = \frac{c^2 \rho u}{2} \tag{20a}$$

$$\sum_{\alpha=0}^{8} f_\alpha^{\text{eq}} \frac{\xi_{\alpha y}}{2}(\xi_{\alpha x}^2+\xi_{\alpha y}^2) = \frac{c^2 \rho v}{2} \tag{20b}$$

which is a consequence of the choice of parameters in Eqs. (9*a*)–(9*f*). Up to this point, it has been shown that the momentum equations of the incompressible NS equations (Eqs. (19*a*) and (19*b*)) are satisfied with an error of $O(\varepsilon)$. However, it should be noted that Eq. (19*c*) is not the continuity equation. By solving the equations until a steady state is reached the temporal derivative in Eq. (19*c*) vanishes. At this point, mass conservation is satisfied, because the second term of Eq. (19*c*) vanishes. Therefore, the present scheme is most suited for a steady state problem. The simulation starts by first assuming an initial pressure field; thus, the results may not satisfy mass (or volume) continuity. Then, the pressure (see Eqs. (17*c*) and (19*c*)) and the flow field (see Eqs. (17*a*), (17*b*), (19*a*), and (19*b*)) are "corrected" until the mass conservation equation is satisfied. The criterion given below can be used to monitor this approach to mass conservation,

$$\left|\frac{\partial p + \frac{1}{2}\rho|\boldsymbol{u}|^2 - \frac{\tau_{xx}+\tau_{yy}}{2}}{\partial t}\right| \le O(\varepsilon) \tag{21}$$

This criterion is equivalent to enforcing the divergence-free condition at every time step. In this sense the scheme is, in fact, using the pressure-correction approach and is similar to the semi-implicit method proposed for pressure correction (SIMPLE) in Ref. [25]. The scheme can be extended to a time-accurate one by using a pseudotime term, which vanishes at convergence at each physical time step. The extension to unsteady problems is currently underway.

The present scheme is basically following the same approach as the kinetic scheme [22] but with a number of unique features. First, the zeroth order moment is not used to recover the density, but instead, the second-order moment is used to recover the pressure. Second, incompressibility is achieved by iteration similar to the pressure-correction method instead of using the "low Mach number" approximation. Third, unlike the kinetic scheme for NS equations, the numerical viscosity is not used as the physical viscosity, but rather the physical viscosity is explicitly imposed. Also, in the present scheme, the streaming and collision steps are explained mathematically by the splitting method.

2.2 Coordinate Transformation. Flow through a circular pipe is best described by a cylindrical coordinate system. Since the flow is axisymmetric, the normalized NS equations become

$$\frac{\partial u}{\partial x} + \frac{\partial v}{\partial y} + \frac{v}{y} = 0 \tag{22}$$

$$\rho\left(\frac{\partial u}{\partial t} + \frac{\partial u^2}{\partial x} + \frac{\partial uv}{\partial y}\right) + \frac{\partial p}{\partial x} - \frac{\partial \tau_{xx}}{\partial x} - \frac{\partial \tau_{xy}}{\partial y} + \frac{\rho uv}{y} - \frac{\tau_{xy}}{y} = 0 \tag{23a}$$

$$\rho\left(\frac{\partial v}{\partial t} + \frac{\partial uv}{\partial x} + \frac{\partial v^2}{\partial y}\right) + \frac{\partial p}{\partial y} - \frac{\partial \tau_{xy}}{\partial x} - \frac{\partial \tau_{yy}}{\partial y} + \frac{\rho v^2}{y} - \frac{\tau_{yy}}{y} = 0 \tag{23b}$$

Here x and y (and the corresponding velocity components u and v) represent the axial and radial directions, respectively. The equations above are not in conservation form and so it is not possible to apply the above FDLBM technique directly. Applying FDLBM to curvilinear coordinates, one can always transform the discrete Boltzmann equation, i.e., Eq. (1), to the desired coordinates and solving it using a suitable finite difference method that is numerically stable [26]. Guo and Zhao [27] proposed an improved scheme to deal with the discrete Boltzmann equation after its transformation to curvilinear coordinates, and a similar scheme is used to simulate natural convection heat transfer in a horizontal concentric annulus [28]. In the transformed form here, in order to avoid the complexity of solving Eqs. (22), (23*a*), and (23*b*), the equations themselves may be considered as conservative equations plus some "source terms." The additional source terms can be handled by considering a modified form of the discrete Boltzmann equation given by

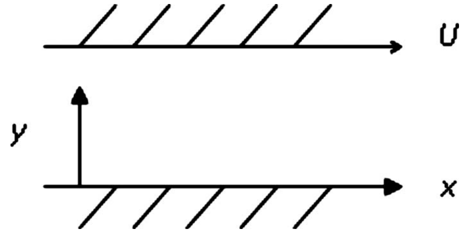

Fig. 2 Schematic of the Couette flow

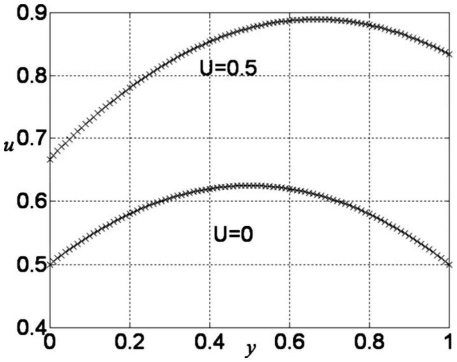

Fig. 3 Newtonian Couette flows with a slip velocity boundary condition: (–) analytical solution and (x) FDLBM solution

$$\frac{\partial f_\alpha}{\partial t} + \xi_\alpha \cdot \nabla_x f_\alpha + g_\alpha = -\frac{1}{\varepsilon\phi}(f_\alpha - f_\alpha^{\mathrm{eq}}) \tag{24}$$

In order to recover Eqs. (22) and (23), the following constraints are required for the distribution function g_α:

$$\sum_{\alpha=0}^{8} g_\alpha = \frac{\rho v}{y} \tag{25a}$$

$$\sum_{\alpha=0}^{8} g_\alpha \xi_{\alpha x} = \frac{\rho u v}{y} - \frac{\tau_{xy}}{y} \tag{25b}$$

$$\sum_{\alpha=0}^{8} g_\alpha \xi_{\alpha y} = \frac{\rho v^2}{y} - \frac{\tau_{yy}}{y} \tag{25c}$$

$$\sum_{\alpha=0}^{8} g_\alpha (\xi_{\alpha x}^2 + \xi_{\alpha y}^2) = 0 \tag{25d}$$

If a minimal form of g_α is assumed such that

$$g_\alpha = A_\alpha + \xi_{\alpha x} A x_\alpha + \xi_{\alpha y} A y_\alpha \tag{26}$$

and employing the same rule as Eq. (8), one possible set of solutions are the following:

$$A_0 = \frac{\rho v}{y}, \quad A_1 = A_2 = 0 \tag{27a}$$

$$A x_1 = \frac{1}{2c^2 y}(\rho u v - \tau_{xy}), \quad A x_2 = 0 \tag{27b}$$

$$A y_1 = \frac{1}{2c^2 y}(\rho v^2 - \tau_{yy}), \quad A y_2 = 0 \tag{27c}$$

A similar splitting method is applied and the freestreaming stage is modified to

$$\frac{\partial f_\alpha}{\partial t} + \xi_\alpha \cdot \nabla_{\boldsymbol{x}} f_\alpha + g_\alpha = 0$$

then,

$$f_\alpha(\boldsymbol{x} + \xi_\alpha \Delta t, t + \Delta t) = f_\alpha(\boldsymbol{x}, t) - \Delta t \cdot g_\alpha(\boldsymbol{x}, t) \tag{28}$$

while the collision stage solves the same Eq. (15) or Eq. (16). In fact, the proposed Eq. (24) is not limited to the circular pipe problem, where geometric source terms appear after coordinate transformation. Whenever external body forces are present in the flow, the governing equation will take on a conservation form plus a source term. By constructing suitable f_α^{eq} and g_α, it is possible to recover the governing equations in the following general forms:

$$\begin{aligned} &\frac{\partial U_1}{\partial t} + \nabla_x U_2 + S_1 = 0 \\ &\frac{\partial U_2}{\partial t} + \nabla_x U_3 + S_2 = 0 \\ &\qquad\vdots \end{aligned} \tag{29}$$

which are useful for modeling certain MEMS devices for which external body forces, such as electromagnetic force, are important. The addition of forcing terms in LBM had been commented and proposed by Guo et al. [29]. Most of the existing methods modify the distribution function; however, the present approach proposes to modify the equation instead. Even though the focus of this paper is in the case of zero applied external body force, but the approach presented here shows potential for extension to flows where there are externally applied body forces.

3 Numerical Results

The proposed FDLBM is validated against Couette and Poiseuille flows, which are common flows in MEMS devices. In addition, it is also tested against 2D flows. Two representative 2D flows are chosen; they are a driven cavity flow and a sudden expansion flow, where internal separation is present in both cases.

3.1 Newtonian Couette Flow With Slip Boundary. The first numerical calculation considers a Newtonian fluid flowing between two parallel plates separated by a distance h (Fig. 2). Slip velocity boundary condition is applied on both walls. The lower wall ($y=0$) is stationary while the upper wall ($y=h$) is moving at speed U (made dimensionless using the characteristic speed u_0). The slip-wall boundary conditions are given by

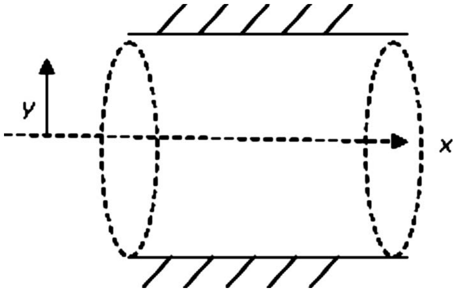

Fig. 4 Schematic of the circular Poiseuille flow

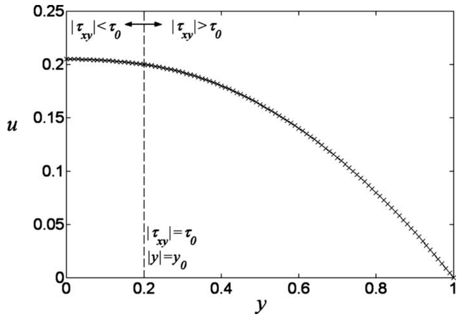

Fig. 5 Non-Newtonian Poiseuille flow with a biviscous model: (–) analytical solution and (x) FDLBM solution

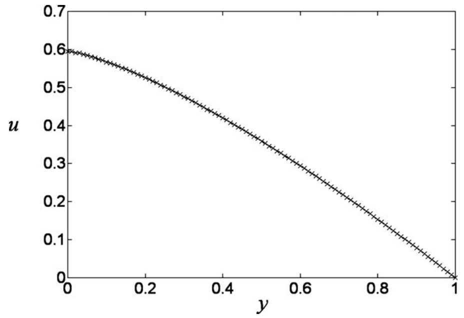

Fig. 7 Non-Newtonian Poiseuille flow with a shear-thickening model ($n=3$ in power-law model): (–) analytical solution and (x) FDLBM solution

$$u(0) = L_s \left.\frac{\partial u}{\partial y}\right|_{y=0}, \quad u(h) = U - L_s \left.\frac{\partial u}{\partial y}\right|_{y=h} \tag{30}$$

where L_s is the Navier-length coefficient [30] normalized by the characteristic length L. It is assumed that the vertical velocity vanishes and the horizontal velocity depends solely on y. If the pressure gradient is assumed constant and $\rho=1$, an analytical solution is obtained.

$$u = \frac{U(y+L_s)}{h+2L_s} + \frac{1}{2\mu}\frac{\partial p}{\partial x}[y^2 - h(y+L_s)] \tag{31}$$

where the normalized viscosity coefficient is given by $\mu = \hat{\mu}/(\rho_0 u_0 L)$.

In the numerical simulation, the computational domain is $0 \le (x,y) \le 1$. The numerical and physical parameters are given by $\Delta x=0.01$, $\Delta t=0.0001$, $\mu=0.1$, $h=1$, and $L_s=1$. The initial condition is set as

$$u|_{t=0} = v|_{t=0} = p|_{t=0} = 0 \quad \forall\, x,y \tag{32}$$

Pressure is specified at the inflow (at $x=0$) and outflow (at $x=1$) boundaries to drive the flow until a steady state is achieved.

$$\begin{gathered} p|_{x=0} = 1.1, \quad p|_{x=1} = 1, \quad \forall\, t>0 \\ \left.\frac{\partial p}{\partial y}\right|_{y=0} = \left.\frac{\partial p}{\partial y}\right|_{y=1} = 0, \quad \forall\, t>0 \end{gathered} \tag{33}$$

The normal derivative of pressure is set to zero at the wall, which is an acceptable approximation for the current problem. For a more general flow, the pressure derivative should be derived from the momentum equations. The derivatives of the inflow and outflow velocities are set to zero, that is,

$$\left.\frac{\partial u}{\partial x}\right|_{x=0} = \left.\frac{\partial v}{\partial x}\right|_{x=0} = \left.\frac{\partial u}{\partial x}\right|_{x=1} = \left.\frac{\partial v}{\partial x}\right|_{x=1} = 0, \quad \forall\, t>0 \tag{34}$$

A constant pressure gradient of –0.1 along x should be calculated. However, this was not specified as input. Instead, a vanishing initial pressure condition as given by Eq. (32) is stipulated everywhere. This way, the pressure field is not assumed a priori, it is correctly calculated in the present numerical scheme.

Two cases, one with $U=0$ and another with $U=0.5$, are simulated. After steady state has been reached, the calculated horizontal velocity u is independent of x, and a correct constant pressure gradient is obtained. In Fig. 3, it is shown that the numerical results agree well with the analytical solution. The slip effect is seen on the boundaries for both cases.

3.2 Non-Newtonian Poiseuille Flow With No-Slip Boundary. In order to validate non-Newtonian effects, three non-Newtonian models, namely, a biviscous model, a shear-thinning model, and a shear-thickening model are simulated. The biviscous model was suggested by Liu and Mei [31] in order to bypass the numerical difficulty encountered in the Bingham model. The fluid of this biviscous model has two constant viscosity coefficients. It exhibits a linear stress-strain relation similar to the Newtonian fluid; however, which viscosity coefficient assumes a linear stress-strain relation is determined by the magnitude of the shear stress τ_{xy} with respect to the yield stress τ_0. The model has the formulation given by

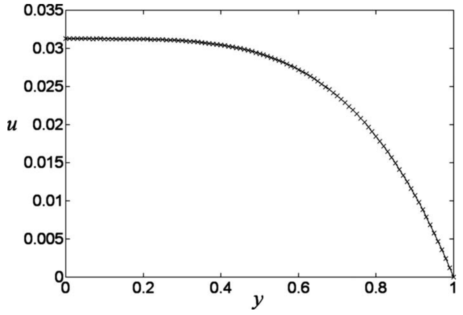

Fig. 6 Non-Newtonian Poiseuille flow with a shear-thinning model ($n=1/3$ in the power-law model): (–) analytical solution and (x) FDLBM solution

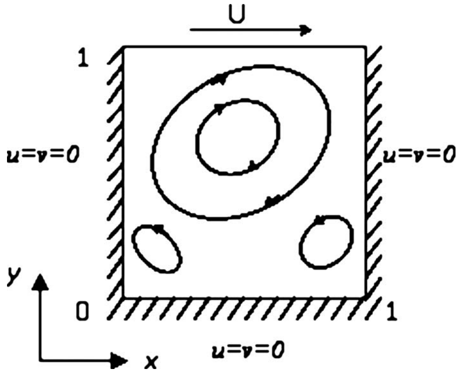

Fig. 8 Schematic of the driven cavity flow

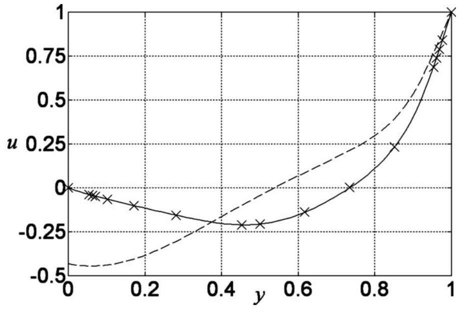

Fig. 9 Horizontal velocity *u* of a driven cavity flow along *y* at *x*=0.5, Re=100: (–) FDLBM solution (no slip), (x) result from Ref. [32], and (- - -) FDLBM solution with slip wall

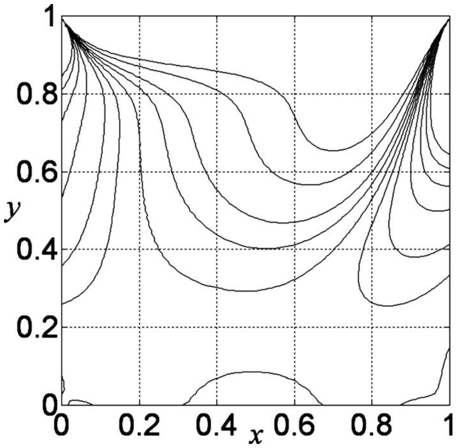

Fig. 11 Vorticity contours for flow in a driven cavity; same contour level setting as that given in Ref. [32]

$$\tau_{xy} = \tau_0\left(1 - \frac{\mu}{\mu_1}\right)\mathrm{sgn}\left(\frac{\partial u}{\partial y}\right) + \mu\frac{\partial u}{\partial y} \quad \text{if } |\tau_{xy}| \geq \tau_0$$

$$\tau_{xy} = \mu_1\frac{\partial u}{\partial y} \quad \text{if } |\tau_{xy}| < \tau_0 \quad \text{with } 0 < \frac{\mu}{\mu_1} < 1 \tag{35}$$

where the normalized yield stress and the viscosity coefficient are given by

$$\tau_0 = \hat{\tau}_0/(\rho_0 u_0^2), \quad \mu, \mu_1 = \hat{\mu}, \hat{\mu}_1/(\rho_0 u_0 L)$$

When $\mu_1 \to \infty$ or $\mu/\mu_1 \to 0$, the biviscous model reduces to the Bingham model limit. The case $\mu_1 = \mu$ recovers the Newtonian fluid. This biviscous model can also be viewed as a simplified version of the shear-thinning and shear-thickening models. Another widely used non-Newtonian model is the power-law model.

$$\tau_{xy} = \mu \ \mathrm{sgn}\left(\frac{\partial u}{\partial y}\right)\left|\frac{\partial u}{\partial y}\right|^n \tag{36}$$

and for this power-law model the normalized viscosity coefficient is given by $\mu = \hat{\mu}/(\rho_0 u_0^{2-n} L^n)$. The case $n < 1$ corresponds to shear-thinning fluids, whereas $n > 1$ corresponds to shear-thickening fluids, and $n = 1$ recovers the Newtonian behavior.

Poiseuille flows through a circular pipe with radius R (Fig. 4) are simulated. The formulation of Eq. (24) is employed. Since the shear stress is always increasing along y (the radial direction, $y = 0$ is the centerline, and $y = R$ is the pipe wall), for constant pressure gradient and $\rho = 1$, with no-slip boundary condition, analytical solutions can be obtained. For the biviscous model, a critical value y_0 can be found where the shear stress reaches the yield stress; this y_0 is given by

$$y_0 = -(2\tau_0)/(\partial p/\partial x) \tag{37a}$$

When $|\tau_{xy}|$ is always smaller than τ_0, then

$$u = \frac{1}{4\mu_1}\frac{\partial p}{\partial x}(y^2 - R^2) \tag{37b}$$

Otherwise, when

$$|\tau_{xy}| > \tau_0 \text{ or } |y| > y_0$$

$$u = \frac{1}{4\mu}\frac{\partial p}{\partial x}(y^2 - R^2) - \frac{\tau_0}{\mu}\left(1 - \frac{\mu}{\mu_1}\right)\mathrm{sgn}\left(\frac{\partial u}{\partial y}\right)(y - R)$$

when

$$|\tau_{xy}| \leq \tau_0 \text{ or } |y| \leq y_0$$

$$u = \frac{1}{4\mu_1}\frac{\partial p}{\partial x}(y^2 - y_0^2) + \frac{1}{4\mu}\frac{\partial p}{\partial x}(y_0^2 - R^2) - \frac{\tau_0}{\mu}\left(1 - \frac{\mu}{\mu_1}\right)\mathrm{sgn}\left(\frac{\partial u}{\partial y}\right)(y_0 - R) \tag{37c}$$

For the power-law model, the analytical solution is

$$u = \mathrm{sgn}\left(\frac{\partial u}{\partial y}\right)\left|\frac{1}{2\mu}\frac{\partial p}{\partial x}\right|^{1/n}\frac{n}{n+1}(y^{n+1/n} - R^{n+1/n}) \tag{38}$$

Three cases are carried out to validate the non-Newtonian counterpart of the FDLBM scheme. The first case is the biviscous model (Fig. 5) with numerical parameters given by $\Delta x = 0.01$, $\Delta t = 0.0001$, $\tau_0 = 0.01$, $\mu = 0.1$, $\mu_1 = 0.2$, and $R = 1$. The second case is a shear-thinning model with $n = 1/3$ (Fig. 6). The other parameters are $\Delta x = 0.01$, $\Delta t = 0.00001$, $\mu = 0.1$, and $R = 1$. The last case is a shear-thickening model with $n = 3$ (Fig. 7) with other parameters specified as $\Delta x = 0.01$, $\Delta t = 0.0001$, $\mu = 0.1$, and $R = 1$. In the three cases considered, the inflow and outflow pressures are specified at 1.1 and 1, respectively, as in Eq. (33). The initial setting and

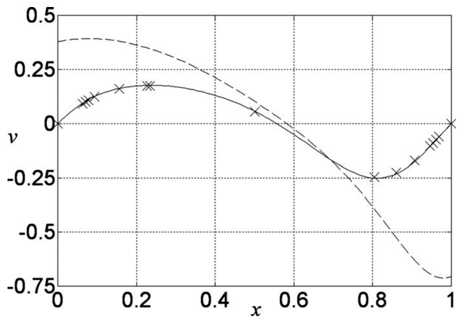

Fig. 10 Vertical velocity *v* of driven cavity flow along *x* at *y* =0.5, Re=100: (–) FDLBM solution (no slip), (x) result from Ref. [32], and (- - -) FDLBM solution with slip wall

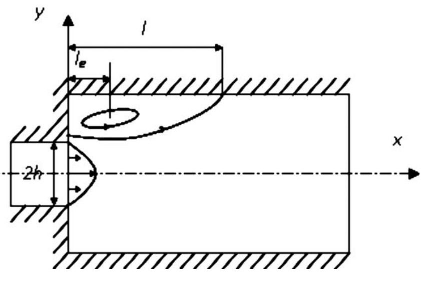

Fig. 12 Schematic of the flow in a channel with sudden symmetric expansion

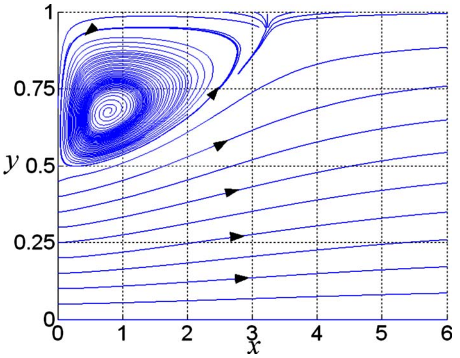

Fig. 13 Streamline plots for flow in a 2D sudden expansion

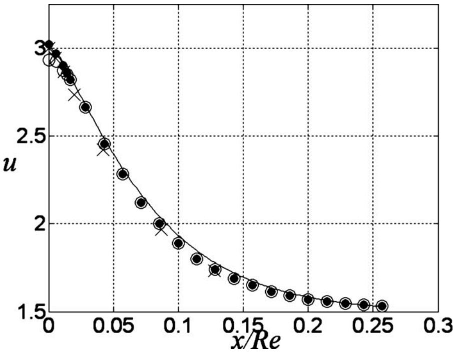

Fig. 14 Centerline ($y=0$) velocity distribution in a sudden expansion flow: (–) FDLBM solution, (x) result from Ref. [34], (○) and (●)·results from Ref. [35] for $N=3$ and $N=5$, respectively

evolution technique are similar to that used in the Newtonian Couette flow case. Figures 5–7 show the comparisons of the analytical solutions and the numerical simulations. Excellent agreement is obtained between the numerical results and the analytical solutions.

3.3 Driven Cavity Flow. A laminar incompressible flow in a square cavity whose top wall moves with a uniform velocity in its own plane is a typical example of steady separated flow. It has served repeatedly as a model problem for testing and evaluating numerical techniques, in spite of the singularities at two of its upper corner [32]. Figure 8 shows the flow behavior in a driven cavity. The flow in a square box with unit length is driven by the upper wall at a normalized horizontal velocity $U=1$.

In the numerical simulation, the computational domain is $0 \leq (x,y) \leq 1$. As mentioned before, there are a number of solvers for Eq. (13) in the freestreaming stage. Instead of using the discretization given in Eq. (14), the Lax and Wendroff [33] scheme is employed. The fluid inside the cavity is Newtonian. The numerical and physical parameters are defined by $\Delta x=0.01$, $\Delta t=0.0001$, $\rho=1$, $c=10$, and $\mu=0.01$, which corresponds to a Reynolds number of 100. The pressure at the boundary is given by

$$\frac{\partial p}{\partial x} = \mu \frac{\partial^2 u}{\partial x^2} \quad \text{at } x=0,1$$
$$\frac{\partial p}{\partial y} = \mu \frac{\partial^2 v}{\partial y^2} \quad \text{at } y=0,1 \tag{39}$$

where a second-order one-sided difference discretization is used in the simulation.

The u and v velocity plots along the center of the axes are shown in Figs. 9 and 10, respectively. These results show good agreement with those of Ghia et al. [32]. In Fig. 11, the vorticity contours are plotted with the same level settings as those given in Ref. [32]. The excellent agreement achieved indicates that the incompressible NS equations recovered from the modeled Boltzmann equation, including the divergence-free condition of the velocity, are correct. It would be interesting to see the slip-wall effect of the driven cavity flow. The dash line in Figs. 9 and 10 shows the same setting of calculation except a slip wall with slip length $L_s=1$ is applied. A vortex still appears in the cavity and the flow amplitude is larger. The behavior of v is influenced by the slip boundary while that of u is much less affected.

Table 1 Comparison of calculated *l* and l_e with data

	l/Re	l_e/Re	$\omega_{\min}$
FDLBM result	0.069	0.017	−2.36
Agarwal [34]	0.068	0.016	−2.26
Kumar and Yajnik ($N=3$) [35]	0.064	0.014	−2.19
Hung and Macagno [36]	0.066	0.013	−2.82

3.4 Sudden Expansion Flow. A channel with a symmetric sudden expansion results in an internal separated flow. The geometry for this flow is shown in Fig. 12. The entry flow (at $x=0$) is taken to be parabolic.

$$u|_{x=0} = \frac{3}{2h}\left[1-\left(\frac{y}{h}\right)^2\right], \quad 0 \leq y \leq h = 0, \quad h \leq y \leq 1 \tag{40}$$

where h is the half-width of the channel upstream of the expansion. The width of the channel is taken to be two; hence the ratio of expansion is given by $1/h$. The entire channel is symmetric about the x-axis ($y=0$). A computational domain of $0 \leq x \leq 12$, $0 \leq y \leq 1$ is used. Similar numerical techniques as used in the Newtonian Couette flow case are adopted. However, in the current case, the Lax and Wendroff [33] scheme is used to solve Eq. (13). The numerical and physical parameters are given by $\Delta x=0.05$, $\Delta t=0.00001$, $h=0.5$, and $c=100$. The flow is assumed to be Newtonian with $\mu=1/(46.6)$ specified. This specification gives rise to a Reynolds number of $\mathrm{Re}=46.6$. The above settings match with those used by Agarwal [34].

Figure 13 shows the streamline plot of the flow. Certain important characteristics, such as the reattachment length l, the location

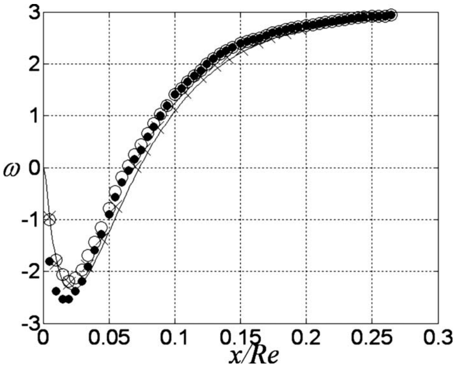

Fig. 15 Vorticity distribution at the upper wall ($y=h$) for flow in a channel with sudden symmetric expansion: (–) FDLBM solution, (x) result from Ref. [34], (○) and (●)·results from Ref. [35] for $N=3$ and $N=5$, respectively

Table 2 Maximum error norm against Δt

Δt	5×10^{-4}	1×10^{-4}	5×10^{-5}	1×10^{-5}
Max error norm	3.24×10^{-3}	6.47×10^{-4}	3.23×10^{-4}	6.46×10^{-5}

Table 3 Maximum error norm against Δx

Δx	0.1	0.05	0.02	0.01	0.005
Max error norm	6.25×10^{-4}	6.46×10^{-4}	6.47×10^{-4}	6.25×10^{-4}	6.25×10^{-4}

Table 4 Maximum error norm against c

C	2	5	10	20	50
Max error norm	6.58×10^{-5}	5.89×10^{-4}	6.47×10^{-4}	6.61×10^{-4}	6.65×10^{-4}

of the eddy-center l_e, and the minimum vorticity $\omega_{\min}$ at the upper wall of the channel are determined from Fig. 13 and tabulated for comparison with other known data in Table 1. Figure 14 shows a comparison of the velocity distribution at the centerline ($y=0$) of the channel, and Fig. 15 shows the comparison of vorticity distribution at the upper wall ($y=h$). The excellent agreement shown in these figures indicates that the incompressible NS equations are recovered correctly.

3.5 Accuracy Analysis. The first case, Newtonian Couette flow with slip boundary is chosen to study the accuracy of the scheme with varying parameters in detail. The Lax–Wendroff scheme [33], which is second-order accurate in space, is employed to solve Eq. (13). The convergence criteria is defined as

$$\max\left\|\partial\left(p+\frac{1}{2}\rho|\boldsymbol{u}|^2-\frac{\tau_{xx}+\tau_{yy}}{2}\right)\right\|_{\text{whole domian}} \leq \Delta t^2 \qquad (41)$$

which ensures an accurate satisfaction of the continuity equation. The operator ∂ means the difference between successive time steps. The parameters Δt, Δx, and c are tested and shown in Tables 2–4. All remaining parameters are kept unchanged as in previous calculations. Numerical instability is found outside the range of the parameters tested. The maximum error norm is taken for the whole domain between the analytical solution and the numerical solution. It is shown that all the results are better than the estimated error $O(\Delta x^2, \Delta t)$. Better result is obtained for smaller Δt. The refinement of Δx seems to have no effect on the accuracy. Also, it is shown that c should be chosen as small as possible and it is problem dependent, but the result is still acceptable when it is large, as long as the calculation is stable.

4 Conclusions

A FDLBM has been formulated. In order to render the numerical scheme more user friendly, a convenient algorithm has been suggested for setting the wall boundary condition, which is critical for microchannel flows. Flows of Newtonian fluids, non-Newtonian fluids with a biviscous model, and a power-law model were simulated. Furthermore, a new formulation has been put forth that allows external body forces and flow in a circular pipe to be studied within the proposed FDLBM framework. Validation against analytical solutions of Couette flows with and without slip boundary, non-Newtonian Poiseuille flows, a two-dimensional driven cavity flow with and without slip boundary, and a two-dimensional sudden expansion flow were carried out; excellent agreement between analysis and simulations was obtained.

Acknowledgment

S.C.F gratefully acknowledges funding support in the form of a Ph.D. studentship awarded him by the Hong Kong Polytechnic University. R.M.C.S. wishes to acknowledge support given him by the Research Grants Council of the Government of the Hong Kong Special Administrative Region under Grant No. PolyU1/02C.

Nomenclature

c = scaling parameter in the lattice model
f_α = discrete distribution function
f_α^{eq} = discrete equilibrium distribution function
g_α = discrete distribution function for source term
h = height between plates in Couette flow
Kn = Knudsen number
L = characteristic length
L_s = Navier-length coefficient
p = pressure
R = radius of pipe in Poiseuille flow
$\boldsymbol{u}\equiv(u,v)$ = flow velocity
u_0 = characteristic speed
U = speed of plate in Couette or driven cavity flow
$\boldsymbol{x}\equiv(x,y)$ = position vector
Δt, Δx = temporal and spatial step size in numerical calculation
ε = small parameter for expansion
μ, μ_1 = viscosity coefficient
ρ = density
ρ_0 = characteristic density
τ_0 = yield stress in the biviscous model
τ_{xx}, τ_{yy}, τ_{xy} = normal and shear stress components of the flow
ϕ = relaxation time
$\xi_\alpha\equiv(\xi_{\alpha x},\xi_{\alpha y})$ = discrete particle velocity

References

[1] Nguyen, N. T., and Wereley, S. T., 2002, *Fundamentals and Applications of Microfluidics*, Artech House, Boston, MA, Chap. 2.
[2] Chen, S., and Doolen, G. D., 1998, "Lattice Boltzmann Method for Fluid Flows," Annu. Rev. Fluid Mech., **30**, pp. 329–364.
[3] Nie, X., Doolen, G. D., and Chen, S., 2002, "Lattice-Boltzmann Simulations of Fluid Flows in MEMS," J. Stat. Phys., **107**(1/2), pp. 279–289.
[4] Lim, C. Y., Shu, C., Niu, X. D., and Chew, Y. T., 2002, "Application of Lattice Boltzmann Method to Simulate Microchannel Flows," Phys. Fluids, **14**(7), pp. 2299–2308.
[5] Zhou, Y., Zhang, R., Staroselsky, I., Chen, H., Kim, W. T., and Jhon, M. S., 2006, "Simulation of Micro- and Nano-Scale Flows Via the Lattice Boltzmann Method," Physica A, **362**, pp. 68–77.
[6] Tian, Z.-W., Zou, C., Liu, H.-J., Guo, Z.-L., Liu, Z.-H., and Zheng, C.-G., 2007, "Lattice Boltzmann Scheme for Simulating Thermal Micro-Flow," Physica A, **385**, pp. 59–68.
[7] Niu, X. D., Shu, C., and Chew, Y. T., 2007, "A Thermal Lattice Boltzmann Model With Diffuse Scattering Boundary Condition for Micro Thermal Flows," Comput. Fluids, **36**, pp. 273–281.
[8] Wolf-Gladrow, D. A., 2000, *Lattice-Gas Cellular Automata and Lattice Boltzmann Models: An Introduction*, Springer-Verlag, Berlin, Chap. 5.
[9] Sterling, J. D., and Chen, S., 1996, "Stability Analysis of Lattice Boltzmann Methods," J. Comput. Phys., **123**, pp. 196–206.
[10] Loose, W., and Hess, S., 1989, "Rheology of Dense Model Fluids Via Nonequilibrium Molecular Dynamics: Shear Thinning and Ordering Transition," Rheol. Acta, **28**, pp. 91–101.
[11] He, X., and Luo, L. S., 1997, "Lattice Boltzmann Model for the Incompressible Navier–Stokes Equation," J. Stat. Phys., **88**, pp. 927–944.
[12] Tsutahara, M., Kataoka, T., Takada, N., Kang, H. K., and Kurita, M., 2002, "Simulations of Compressible Flows by Using the Lattice Boltzmann and the Finite Difference Lattice Boltzmann Methods," Comput. Fluid Dyn. J., **11**(1),

pp. 486–493.
[13] Aharonov, E., and Rothman, D. H., 1993, "Non-Newtonian Flow (Through Porous Media): A Lattice Boltzmann Method," Geophys. Res. Lett., **20**, pp. 679–682.
[14] Rakotomalala, N., Salin, D., and Watzky, P., 1996, "Simulation of Viscous Flows of Complex Fluids With a Bhatnagar, Gross, and Krook Lattice Gas," Phys. Fluids, **8**(11), pp. 3200–3202.
[15] Boek, E. S., Chin, J., and Coveney, P. V., 2003, "Lattice Boltzmann Simulation of the Flow of Non-Newtonian Fluids in Porous Media," Int. J. Mod. Phys. B, **17**, pp. 99–102.
[16] Gabbanelli, S., Drazer, G., and Koplik, J., 2005, "Lattice Boltzmann Method for Non-Newtonian (Power-Law) Fluids," Phys. Rev. E, **72**, p. 046312.
[17] Yoshino, M., Hotta, Y., Hirozane, T., and Endo, M., 2007, "A Numerical Method for Incompressible Non-Newtonian Fluid Flows Based on the Lattice Boltzmann Method," J. Non-Newtonian Fluid Mech., **147**, pp. 69–78.
[18] Toro, E. F., 1999, *Riemann Solvers and Numerical Methods for Fluid Dynamics: A Practical Introduction*, 2nd ed., Springer-Verlag, Berlin, Chap. 15.
[19] Xu, K., 1998, "Gas-Kinetic Schemes for Unsteady Compressible Flow Simulations," 29th CFD Lecture Series at von Karman Institute for Fluid Dynamics, Belgium.
[20] Xu, K., 1998, "Gas-Kinetic Schemes for Unsteady Compressible Flow Simulations," VKI Report No. 1998-03.
[21] Yu, D., Mei, R., Luo, L.-S., and Shyy, W., 2003, "Viscous Flow Computations With the Method of Lattice Boltzmann Equation," Prog. Aerosp. Sci., **39**, pp. 329–367.
[22] Junk, M., 1999, "Kinetic Schemes in the Case of Low Mach Numbers," J. Comput. Phys., **151**, pp. 947–968.
[23] Strang, G., 1968, "On the Construction and Comparison of Difference Schemes," SIAM (Soc. Ind. Appl. Math.) J. Numer. Anal., **5**(3), pp. 506–517.
[24] Pullin, D. I., 1980, "Direct Simulation Methods for Compressible Inviscid Ideal Gas Flow," J. Comput. Phys., **34**, pp. 231–244.
[25] Patankar, S. V., and Spalding, D. B., 1972, "A Calculation Procedure for Heat, Mass and Momentum Transfer in Three-Dimensional Parabolic Flows," Int. J. Heat Mass Transfer, **15**, pp. 1787–1806.
[26] Mei, R., and Shyy, W., 1998, "On the Finite Difference-Based Lattice Boltzmann Method in Curvilinear Coordinates," J. Comput. Phys., **143**, pp. 426–448.
[27] Guo, Z., and Zhao, T. S., 2003, "Explicit Finite-Difference Lattice Boltzmann Method for Curvilinear Coordinates," Phys. Rev. E, **67**, p. 066709.
[28] Shi, Y., Zhao, T. S., and Guo, Z. L., 2006, "Finite Difference-Based Lattice Boltzmann Simulation of Natural Convection Heat Transfer in a Horizontal Concentric Annulus," Comput. Fluids, **35**, pp. 1–15.
[29] Guo, Z., Zheng, C., and Shi, B., 2002, "Discrete Lattice Effects on the Forcing Term in the Lattice Boltzmann Method," Phys. Rev. E, **65**, p. 046308.
[30] Navier, C. L. M. H., 1822, "Memoire sur les lois du mouvement des fluides," Mem. de l'Acad. des Sci., **6**, pp. 389–440.
[31] Liu, K. F., and Mei, C. C., 1994, "Roll Waves on a Layer of a Muddy Fluid Flowing Down a Gentle Slope—A Bingham Model," Phys. Fluids, **6**(8), pp. 2577–2590.
[32] Ghia, U., Ghia, K. N., and Shin, C. T., 1982, "High-Re Solutions for Incompressible Flow Using the Navier–Stokes Equations and a Multigrid Method," J. Comput. Phys., **48**, pp. 387–411.
[33] Lax, P. D., and Wendroff, B., 1960, "Systems of Conservation Laws," Commun. Pure Appl. Math., **13**, pp. 217–237.
[34] Agarwal, R. K., 1981, "A Third-Order-Accurate Upwind Scheme for Navier-Stokes Solutions at High Reynolds Numbers," AIAA Paper No. 81-0112.
[35] Kumar, A., and Yajnik, K. S., 1980, "Separated Flows at Large Reynolds Numbers," J. Fluid Mech., **97**, pp. 27–51.
[36] Hung, T. K., and Macagno, E. O., 1966, "Laminar Eddies in a Two-Dimensional Conduit Expansion," La Houille Blanche, **21**, pp. 391–401.

Wolfgang Wulff[1]
Mem. ASME
11 Hamilton Road,
Setauket, NY 11733
e-mail: wolfgangwulff@optonline.net

Novak Zuber
Mem. ASME
703 New Mark Esplanade,
Rockville, MD 20850
e-mail: wulff@bnl.gov

Upendra S. Rohatgi
Mem. ASME
Brookhaven National Laboratory,
Building 197D,
Upton, NY 11973
e-mail: rohatgi@bnl.gov

Ivan Catton
Mem. ASME
UCLA-MAE,
P.O. Box 951597,
48-121 Engineering IV,
Los Angeles, CA 90195-1597
e-mail: catton@ucla.edu

Application of Fractional Scaling Analysis to Loss of Coolant Accidents, System Level Scaling for System Depressurization

Fractional scaling analysis (FSA) is demonstrated at the system level. The selected example is depressurization of nuclear reactor primary systems undergoing large- and small-break loss of coolant accidents (LOCA), specifically in two integral test facilities of different sizes and shapes, namely, LOFT and Semiscale. The paper demonstrates (1) the relation between pressure and volume displacement rates in analogy to generalized "effort" and "flow" in interdisciplinary analysis of complex systems and (2) using experimental data that a properly scaled depressurization history applies to both large- and small-break LOCA in two different facilities. FSA, when applied at the system, component, and process levels, serves to synthesize the worldwide wealth of results from analyses and experiments into compact form for efficient storage, transfer, and retrieval of information. The demonstration at the system level shows that during LOCAs the break flow dominates for break sizes between 0.1% and 200% of cold-leg flow cross-sectional area, and that FSA ranks processes quantitatively and thereby objectively in the order of their importance. FSA supersedes the hereunto subjectively implemented phenomena identification and ranking table. FSA readily quantifies scale distortions. FSA reduces significantly the need for and current cost of experiments and analyses.
[DOI: 10.1115/1.3155994]

Keywords: fractional scaling, fractional rate of change, fractional change metric, hierarchy of complex system processes, scale distortion, information synthesis, holistic scaling approach

1 Introduction

1.1 Background. This paper presents a *system-level* application of the fractional scaling analysis (FSA), the *principle* of which was introduced by Zuber et al. [1]. Zuber et al. [1] explained the need for coordinated FSA scaling at the system, component, and process levels. Catton et al. [2] applied FSA in a related paper at the *component level*. The application in this paper encompasses the fluid in a complex multicomponent system such as the entire primary system or the containment building of a nuclear power plant. FSA applies to any system, component, and process; it is shown here with available data for loss of coolant accidents (LOCAs) in light water reactors (LWRs). The system is modeled from the holistic point of view and consequently, the scaling is carried out at the system level.

The holistic (as opposed to the reductionist) approach to thermohydraulic system analysis and especially scaling encompasses a system as a whole and reveals (a) the *common response of its components* to all external effects through the overall system depressurization, and (b) the *component interaction* as the dynamic fluid exchange between components. The system pressure is (in interdisciplinary system analysis) the generalized effort [3] *affecting simultaneously all components* and accounting not only for the fluid inventory but, more importantly, for the mechanical energy stored in the compressed fluid. This paper demonstrates the system pressure variation to be a consequence only of volume displacements or generalized flows [3] that are caused by six types of agents of change, which can act anywhere across the pressure boundary (see Sec. 2 below). The combined *global* mass and energy balances have been used before by Solberg and Bakstad [4], Lahey and Moody [5], and many others in an Eulerian approach to predict the depressurization rate and to obtain the scaling criteria of system depressurization [6–11].

Here we use the more direct Lagrangian approach (see Appendix A). We demonstrate the relation between pressure and volume displacement rates (rates of elastic dilation) and show FSA for the common response of components in a hydraulic system.

The component interaction is described by the system of loop momentum balances (coupled ordinary differential equations), which is based on the integral momentum balance for transient fluid flow [12]. Loop momentum balances complete the description of *global system response*. They have been used in only three but fast-running and highly efficient computer codes [4,13] for analyzing system transients in boiling water reactors and in Ref. [14] for pressurized water reactors. These balance equations reveal *inertia and impedance cross coupling* between any number of interconnected loops mathematically through inertia and impedance matrices, and the global system response to all agents of change through the vectors of gravity, friction, and pumping pressures. Scaling of the loop momentum balances provides characteristic loop response times and similarity criteria for component interaction [8,9,11].

Notice that the reductionist approach based on scaling the *local* mass, energy, and momentum balances, expressed through partial differential equations, does not incorporate appropriate boundary conditions. Local scaling provides at most similarity of *distributions* at the process level but not similarity criteria of global system responses and component interactions. It cannot reveal the overall insights afforded by the holistic approach. A nonlinear

---

[1] Corresponding author.

Contributed by the Fluids Engineering Division of ASME for publication in the JOURNAL OF FLUIDS ENGINEERING. Manuscript received October 24, 2008; final manuscript received April 16, 2009; published online July 20, 2009. Assoc. Editor: Malcolm J. Andrews.

system is more than the sum of its parts. Because of space limitation, we demonstrate FSA here only for system depressurization, i.e., the common response of system components.

Reactor coolant systems and related test facilities are *physically similar* because a compressed fluid transfers thermal power in all of them from (perhaps simulated) nuclear fuel elements to a prime mover. Properly scaled systems depressurize similarly because one scaled equation governs their depressurizations. Inordinately many expensive tests and computer simulations have been performed, one for every break size, location, and orientation in every test facility and power plant. Test and computer results (time histories) have been presented in terms of *absolute variables* in individual widely scattered reports. The results were never synthesized and interpreted with regard to their common features or different patterns and related physical causes. Many tests and computations have been unnecessary duplications. FSA avoids such duplications, guarantees efficiency, and conserves resources in the future.

1.2 Purpose of Paper. It will be shown how FSA provides two distinct and important system characteristics introduced by Zuber et al. [1]: (i) the *fractional rates of change* ω (FRC) to quantify the intensity of each transfer process (or agent of change), which changes a state variable (here the pressure) by a fraction of its total change (see Sec. 3.1), and to *rank* these agents of change in the order of their impact on a given system; and (ii) the *fractional change metric* Ω for scaling the fractional change in a system state variables (see Sec. 3.4). The fractional change metric Ω must be the same in two similar systems to produce *the same fractional change at the correctly scaled time*. It will be shown how the difference between FRCs of the same agent of change in two different facilities is a quantitative measure of scale distortion between the facilities. A central feature of FSA is that the system of six subvolumes has a *single* FRC $\bar{\omega}$ and a single fractional change metric Ω *for the aggregate*. Sections 3.1 and 3.2 below demonstrate the ranking. Section 3.4 shows the fractional change metric Ω as the correct basis for time scaling and its role in data synthesis.

Specifically, we shall apply FSA at the system level and demonstrate through data synthesis that a properly scaled depressurization history is the same for large- and small-break loss of coolant accidents in two test facilities of different shapes and sizes: loss-of-fluid test (LOFT) and Semiscale. Consequently, a single experiment or trustworthy computer simulation, when properly scaled, suffices for LOCAs of all break sizes and orientations in the primary system of a particular power plant (PWR or BWR) and of all related test facilities. FSA can realize similar savings for reactor secondary systems and containments. Thus, we shall show how FSA *saves resources* and, by example, that FSA recasts experimental data in the most compact form, which reveals plant differences or scale distortions as well as common plant features. This will demonstrate in principle that through FSA one can synthesize the worldwide wealth of experiences from analyses and experiments into displays that provide for efficient evaluation, storage, transfer, and retrieval of information.

2 Depressurization

The system pressure changes due to coolant loss through break(s), relief valves and leaks, and due to the transfer of thermal and mechanical energies (heating, cooling, or stirring) anywhere across the primary system's fluid boundary. Heat transfer to or from fluid regions (subvolumes) occupied by two-phase mixture produces phase change. Heat transfer to or from regions filled by compressed liquid or superheated vapor causes thermal expansions or contractions. Pumping power $P_{PP}=\dot{Q}_{PP}$ also causes fluid expansion. As the inert cover gas (N_2) in the accumulator ejects emergency coolant, it cools by expansion and receives heat from the accumulator walls, which further expands the gas and decreases the rate of depressurization. All causes contributing to the rate of pressure change are the boundary conditions of the system and collectively called *agents of change*. Each of the six contributors to the rate of pressure change is a *rate of volume change* $\dot{V}_j$ or rate of dilatation/contraction or simply *volume rate* or flow according to Layton [3].

The time rate of depressurization of fluid in the system volume V, derived in Appendix A, is given by

$$\frac{dp}{dt}=\frac{1}{V\mathrm{K}_{s,\mathrm{sys}}}\left[-\sum_{j=\mathrm{bk},vl}\dot{V}_j+\frac{v_{\mathrm{fg}}}{h_{\mathrm{fg}}}(\dot{Q}_{2\varphi})_{\mathrm{net}}+\sum_{j=l,v}\left(\frac{\beta}{\rho c_p}\dot{Q}_{\mathrm{net}}\right)_j+\left(\frac{\beta}{\rho\cdot c_p}\right)_l P_{\mathrm{PP}}+\frac{\gamma-1}{\gamma}\frac{\dot{Q}_{\mathrm{N}_2}}{p}\right]=\frac{\sum_j\dot{V}_j}{VK_{s,\mathrm{sys}}}$$

$$=\sum_j\Phi_j,\ \ldots\ \text{summation over all agents of change} \quad (1)$$

Equation (1) defines the individual generalized rates of volume dilation or contraction $\dot{V}_j$ and the individual rates of pressure change Φ_j. The denominator $K_{s,\mathrm{sys}}$ is the aggregate isentropic compressibility of the global system, i.e., the sum of the volume fraction-weighted isentropic compressibilities of the aggregate subvolumes.

$$K_{s,\mathrm{sys}}=\sum_{j=l,v,2\phi,\mathrm{N}_2}\frac{V_{\mathrm{sub},j}}{V}(\kappa_s)_{\mathrm{sub},j} \quad (2)$$

The six terms in the square bracket of Eq. (1) represent all the possible agents of change affecting primary system depressurization, at some time phase or during the entire blow down. The first term is the rate of *net* discharge through breaks, leaks, and safety or relief valves. The second term accounts for volume generation or annihilation by phase change (evaporation or condensation). The next two terms are thermal expansion or contraction in single-phase liquid (index l) and superheated vapor (index v). The fifth term accounts for the pumps heating single-phase liquid, and the last term accounts for thermal expansion of inert gas caused by wall heating. The break and valve discharge terms are zero during steady-state operation, while heating from the reactor, by the pumps and the pressurizer heater, is balanced by cooling in steam generators and by general heat losses to the environment. The heating and compressibility terms of inert gas (index N_2) in, respectively, the numerator and denominator of Eq. (1), remain zero until the accumulators discharge emergency coolant that is pressurized by nitrogen gas. This means that the *net break flow* (first term in square bracket of Eq. (1)) is the *only uncancelled* and *effective agent of change at the beginning of a blow-down from steady-state conditions*.

The denominator $V\mathrm{K}_{s,\mathrm{sys}}$ of Eq. (1) is the *fluid system elasticity* or the *compliance* of all subsonically communicating components combined. The reciprocal $1/V\mathrm{K}_{s,\mathrm{sys}}$ is the fluid stiffness, analogous to an aggregate "spring constant" of six springs in series, which are subject to the same force. During subsonic surge line flow in small-break LOCAs, the system compliance is dominated by the compliance of the pressurizer, even though the pressurizer volume is only 12% of the primary system volume. The specific compressibilities of saturated liquid and vapor are, respectively, 100 and 45 times as large as that of compressed liquid. The initial vapor volume in the pressurizer controls the initial system compliance and depressurization rate.

Next to the break flow, the strongest agent of change is the heating of the two-phase mixture. A given heating or cooling power produces 12.5 times as much volume displacement in the mixture as in compressed liquid. This retards the rate of depressurization as more and more of the fluid in the primary system

Table 1 Definitions of scaled rates of pressure change and initial fractional rates of change (indices *j* in first column are used in summations)

Agents of change system boundary effects	Scaled agents of pressure change, $\Phi_j^* = \dot{V}_j^* / K_{s,\text{sys}}^*$	Initial fractional rates of change, ω_j
Break flow, $j=1$	$\Phi_{\text{bk}}^* = \dfrac{-\dot{V}_{\text{bk}}^*}{K_{s,\text{sys}}^*}$	$\omega_{\text{bk}} = \dfrac{(\dot{V}_{\text{bk}})_0}{V\Delta p(K_{s,\text{sys}})_0}$
Phase change by heating $(>0)/\text{cooling}(<0)$, $j=2$	$\Phi_{\dot{Q}_{2\phi}}^* = \dfrac{(v_{\text{fg}}/h_{\text{fg}})^*}{K_{s,\text{sys}}^*}\dot{Q}_{2\phi}^*$	$\omega_{\dot{Q}_{2\phi}} = \dfrac{\left(\dfrac{v_{\text{fg}}}{h_{\text{fg}}}\right)_0 (\dot{Q}_{2\phi})_{\max}}{V\Delta p(K_{s,\text{sys}})_0}$
Single-phase thermal expansion/contraction by heating/cooling, $j=3,4$	$\Phi_{\dot{Q}_{1\phi}}^* = \dfrac{[\beta/(\rho c_p)]_{1\phi}^*}{K_{s,\text{sys}}^*}\dot{Q}_{1\phi}^*$	$\omega_{\dot{Q}_{1\phi}} = \dfrac{\left(\dfrac{\beta}{\rho c_p}\right)_{1\phi,0} (\dot{Q}_{\text{net},1\phi})_{\max}}{V\Delta p(K_{s,\text{sys}})_0}$
Expansion due to heating by recirculation pumps, $j=5$	$\Phi_{\text{PP}}^* = \dfrac{[\beta/(\rho c_p)]_l^*}{K_{s,\text{sys}}^*}P_{\text{PP}}^*$	$\omega_{P_{\text{PP}}} = \dfrac{\left(\dfrac{\beta}{\rho c_p}\right)_{l,0} (P_{\text{PP}})_0}{V\Delta p(K_{s,\text{sys}})_0}$
Expansion of inert gas due to wall heating, $j=6$	$\Phi_{\dot{Q}_{\text{N}_2}}^* = \dfrac{1}{p^* + \dfrac{p_{\text{env}}}{\Delta p}}\dot{Q}_{\text{N}_2}$	$\omega_{\dot{Q}_{\text{N}_2}}^* = \dfrac{\gamma - 1}{\gamma}\dfrac{(\dot{Q}_{\text{N}_2})_{\max}}{V(\Delta p)^2(\text{K}_{s,\text{sys}})_0}$

reaches saturation. The reductionist cannot discern such salient facts from these local balance equations, either in dimensional or in scaled form.

3 Fractional Scaling on the System Level

With system pressure being the system-wide state variable (effort), we define first the normalized pressure, or *fractional change in pressure* by

$$1 \geq p^* = \frac{p(t) - p_{\min}}{p_{\max} - p_{\min}} = \frac{p(t) - p_{\text{env}}}{p_0 - p_{\text{env}}} = \frac{p(t) - p_{\text{env}}}{\Delta p} \geq 0 \tag{3}$$

The definition renders p^* of the order of unity during blow down from initial pressure p_0 to environmental pressure p_{env} (i.e., pressure in the containment, or in the pressure suppression tank of a test facility); the definition satisfies the first scaling principle (Ref. [8], p. 362). The first one in Eq. (3) is general and applies to any pressure variation in any one or a combination of contiguous time phases of a transient. The second equation is specialized for the complete depressurization $1 \geq p^* \geq 0$, and the last one in Eq. (3) defines the reference total pressure change Δp for the whole blow down. Equation (3) gives also the absolute pressure $p(t) = \Delta p \cdot p^* + p_{\text{env}}$, which is needed later in Eq. (5) for normalizing the last term in the square bracket of Eq. (1).

Under standard scaling procedures, the term for each agent of change on the right-hand side of Eq. (1) is normalized such that their nondimensional variables, recognized by an asterisk superscript, are also of the order unity (Ref. [8], p. 362). All combinations Y of thermophysical properties and the time-dependent heating rates are normalized with their *estimated maximum value* $Y_{\max}$ or, for all monotonically decreasing Y_s, by their *known initial value* Y_0 as follows:

$$Y^*(t) = \frac{Y(t)}{Y_{\max}} = \frac{Y(t)}{Y_0} \tag{4a}$$

The normalizing coefficients Y_0 are formed only with known *initial values*, *fixed operating conditions, and design parameters*. Y_0 embodies the magnitude of the respective agent of change represented by the variable $Y(t)$. We then define in Table 1 above for system depressurization the *fixed* initial FRCs, or ω_j, and the *time-dependent* nondimensional agents of pressure change Φ_j^*. The index j runs from 1 to 6 as shown in Table 1. The generalized rates of *volume change* $\dot{V}_j(t)$ (dilatation or contraction) are due to break flow, phase change, and single-phase fluid dilation. Their scaled variables are

$$\dot{V}_j^* = \dot{V}_j(t)/\dot{V}_j(0) \tag{4b}$$

The normalizations according to Eqs. (4*a*) and (4*b*) are suitable for deriving the individual FRCs, or ω_j, in Table 1, but not for the direct derivation of the aggregate FRC $\bar{\omega}$, which is shown in Sec. 3.4. The individual FRCs provide scaling criteria for test facility design; they serve to rank individual agents of change. The aggregate FRC is needed for data synthesis.

Equation (1) becomes with the definitions of Eq. (3) through Eq. (4*b*), after dividing by Δp, the equation for the rate of change in fractional pressure p^* with respect to actual time (dimensional time).

$$\begin{aligned}\frac{dp^*}{dt} &= -\omega_{\text{bk}}\frac{\dot{V}_{\text{bk}}^*}{K_{s,\text{sys}}^*} + \omega_{2\phi}\frac{\left(\dfrac{v_{\text{fg}}}{h_{\text{fg}}}\right)^*}{K_{s,\text{sys}}^*}(\dot{Q}_{2\phi,\text{net}})^* + \sum_{j=l,v,\text{PP}} \omega_j \frac{\left(\dfrac{\beta}{\rho c_p}\right)_j^*}{K_{s,\text{sys}}^*}(\dot{Q}_{\text{net}})_j^* \\ &\quad + \omega_{\text{N}_2}\frac{\dot{Q}_{N_2}^*}{K_{s,\text{sys}}^*\left(p^* + \dfrac{p_{\text{env}}}{\Delta p}\right)} = \omega_{\text{bk}}\frac{\dot{V}_{\text{bk}}^*}{K_{s,\text{sys}}^*} + \omega_{2\phi}\frac{\dot{V}_{2\phi}^*}{K_{s,\text{sys}}^*} + \omega_l\frac{\dot{V}_l^*}{K_{s,\text{sys}}^*} \\ &\quad + \omega_v\frac{\dot{V}_v^*}{K_{s,\text{sys}}^*} + \omega_{\text{PP}}\frac{\dot{V}_{\text{PP}}^*}{K_{s,\text{sys}}^*} + \omega_{\text{N}_2}\frac{\dot{V}_{\text{N}_2}^*}{\text{K}_{s,\text{sys}}^*} = \omega_{\text{bk}}\Phi_{\text{bk}}^* + \omega_{2\phi}\Phi_{2\phi}^* \\ &\quad + \omega_l\Phi_l^* + \omega_v\Phi_v^* + \omega_{\text{PP}}\Phi_{\text{PP}}^* + \omega_{\text{N}_2}\Phi_{\text{N}_2}^*\end{aligned} \tag{5}$$

Equation (5) shows in standard form the individual FRCs of each agent of change, but not an FRC for the aggregate. Therefore, by using Eq. (5), one cannot account for the combined action of all agents of change in the time scale. See also Appendix A in Ref. [1]. The respective FRCs in Eq. (5) represent only the percentage rate of fractional pressure change per second if *one agent of*

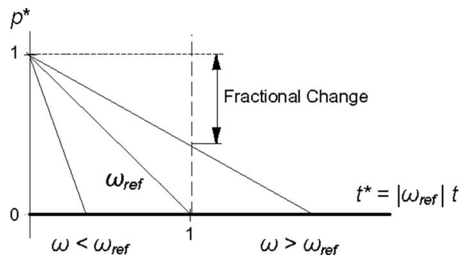

Fig. 1 Fractional change in pressure for different negative FRCs

change acted alone. Aggregate time scaling is presented in Sec. 3.4 below.

In Table 1, the symbol $(\dot{Q}_{2\varphi})_{\max}$ is the maximum electrical heating power in the pressurizer, the only volume having initially two-phase mixture. $(\dot{Q}_{\mathrm{N}_2})_{\max}$ is the maximum possible heating rate in the accumulators. Appendix A identifies the source for thermophysical properties used for Eq. (5) and Table 1. Table 1 defines indices $j=1,\ldots,6$ used later in Eqs. (6), (7*a*), (7*b*), (8), and (10)–(13).

3.1 Fractional Rate of Change. Every agent of change (with subscript j) is represented in Eq. (5) by the product of a fixed FRC, i.e., the initial ω_j defined in Ref. [1], and a time-dependent *ratio* Φ_j^* of dimensionless rate of volume change over dimensionless specific system elasticity. The FRCs measure the intensity of their respective agents of change. Figure 1 shows the relation between ω and the fractional change in the state variable. The time-dependent Φs vary with time between -1 and $+1$. The FRCs could have been derived directly from known relations between system boundary conditions and fluid dilatations. But the approach using conservation equations is more familiar to most readers.

The facility characteristic $V\mathrm{K}_{s,\mathrm{sys}}$ and operating conditions Δp and $(\dot{V}_{\mathrm{bk}})_0$ are now included in the fixed fractional rates of change ω_j. The products of these with a selected reference time are individual *fractional change metrics* $\Omega_j=\omega_j t_{\mathrm{ref}}$ and must be common to all scaled facilities of any volume size, system elasticity, break size, break orientation, and initial pressure. Congruence of pressure histories from different facilities, however, requires also equality of time-dependent normalized change rates Φ_j^* unless compensating inequalities happen to produce spurious congruence.

3.2 Agent of Change Hierarchy. As explained in Ref. [1] and seen from Eq. (5), every active agent of change affects the rate of change in the *fractional pressure* p^*, and the rate is measured by the respective FRC ω_j, since Φ_j^* are of the order of unity (perhaps initially *equal* to one). The magnitudes $|\omega_j|$ of the FRCs, or of the fractional change metrics $|\Omega_j|=|\omega_j t_{\mathrm{ref}}|$, with any common t_{ref}, order the agents of change in one and the same facility (entries in the row of Table 2) according to their importance. The agent with the largest magnitude is most important, as it causes the greatest rate of pressure change. Ordering the agents of change by magnitude of $|\omega_j|$ or $|\Omega_j|$ establishes a *quantitatively based hierarchy of agents* or an objective phenomena identification and ranking table (PIRT). This facilitates effectively uncertainty analyses and judicious resource allocations for experiments and computer code development (see Table 2 below).

An agent of change may be active or even dominant during specific time phases of the blow down and inactive (zero) during others. Thus, it may be necessary to break up the transient in phases to determine for each phase the hierarchy of agents of change.

3.3 Standard Approach to Time Scaling. The time t on the left-hand side of Eq. (5) is not scaled. Depending on the aim of scaling Eq. (5), there are two preferred options for scaling time. If the *hierarchy* of agents of change is sought *relative to the dominant agent of change* then one can divide Eq. (5) by the FRC of the agent of change that dominates the process (here the depressurization), as shown in Eq. (6) of Sec. 3.3.1 below. This standard scaling method does not scale time correctly for the system as an aggregate. If, on the other hand, *time scaling* is the aim of (FSA) then one scales the aggregate with all active agents of change and divides Eq. (5) by the aggregate FRC $\bar{\omega}$ of the depressurization process. This is shown in Sec. 3.4.

3.3.1 Time Scaling for Relative Importance of Agents. We have described in Sec. 3.2 the ranking of agents of change on the basis of the magnitude of their respective FRCs ω_j. Here, we express the hierarchy of agents of change *relative to break flow*, the *dominant agent of change* at the start of LOCA. This approach distorts the time scale unless all agents of change other than the dominant one are relatively insignificant. The *hierarchy* of the agents of change is identical to the one obtained on the basis of the ω_j as discussed in Sec. 3.2. We divide Eq. (5) by the FRC of the net break flow ω_{bk} and obtain the scaled differential equation in standard form for the system pressure as a function of scaled time $t^*=|\omega_{\mathrm{bk}}|t=t_{\mathrm{bk}}^*$.

$$\frac{dp^*}{dt^*} = -\frac{\dot{V}_{\mathrm{bk}}^*}{K_{s,\mathrm{sys}}^*} + \hat{\omega}_{\dot{Q}_{2\phi}}\frac{\dot{V}_{\dot{Q}_{2\phi}}^*}{K_{s,\mathrm{sys}}^*} + \hat{\omega}_{\dot{Q}_{1\phi}}\frac{\dot{V}_{\dot{Q}_{1\phi}}^*}{K_{s,\mathrm{sys}}^*} + \hat{\omega}_{PP}\frac{\dot{V}_{\mathrm{PP}}^*}{K_{s,\mathrm{sys}}^*}$$

$$= -\Phi_{\mathrm{bk}}^* + \sum_{j=2}^{6}\hat{\omega}_j\Phi_j^*, \quad p^*(0) = 1 \tag{6}$$

where the ratios of the fractional rates of change are defined for the start of LOCA by

$$\hat{\omega}_j = \frac{\omega_j}{|\omega_{\mathrm{bk}}|}, j = 2, \ldots, 6, \quad |\hat{\omega}_j| < 1, \quad \hat{\omega}_1 = \hat{\omega}_{\mathrm{bk}} = 1 \tag{7a}$$

They are the familiar Π-groups of traditional scaling [8,11]. It is interesting to note that these Π-groups are always ratios of fractional change rates, but independent of system elasticity. Table 2 and Sec. 4.2 show that break flow dominates depressurization. The reciprocal of ω_{bk}, $1/\omega_{\mathrm{bk}}$, therefore approximates the characteristic time t_{bk} of depressurization and the scaled time $t^*=t/t_{\mathrm{bk}} = t_{\mathrm{bk}}^*$ reflects system elasticity. Notice that vapor and inert gas

Table 2 Fractional rate of change ω in %/s for large-break LOCAs in LOFT and Semiscale for the start of depressurization (j=3 for compressed liquid, 4 for superheated vapor (N.A.))

	Net break flow	Net two-phase mixture heating	Net liquid heating or cooling	Pumping power	Accumulator cover gas heating
	ω_{bk}	$\omega_{\dot{Q}_{2\phi}}$	$\omega_{\dot{Q}_{1\phi}}$	$\omega_{P_{\mathrm{PP}}}$	$\omega_{\dot{Q}_{\mathrm{N}_2}}$
Summation index, j	1	2	3, 4	5	6
LOFT	−577.3	1.41	−0.63	0.63	N.A.
Semiscale	−602.6	1.41	−0.52	0.52	N.A.

terms are omitted in the first in Eq. (6). No superheated vapor exists and accumulators are valved off initially.

Each agent of change is represented in Eq. (6) by a quotient $\hat{\omega}_j$ of fixed FRCs ω_j (see Table 1), multiplied by a time-varying normalized change rate Φ_j^*, which has the *magnitude of order* 1. The ratios of fixed fractional rates of change $\hat{\omega}_j$ *relate the importance of their respective agent of change to that of the break flow*, which has automatically $\hat{\omega}_1 = \hat{\omega}_{\text{bk}} = 1$. The $\hat{\omega}_j$ can be ordered in a hierarchy, but a criterion, such as $|\hat{\omega}_j| < 0.1$, must be defined by convention for separating unimportant agents of change from important ones [11]. The ratios $\hat{\omega}_j = (\dot{V}_{j,0}/\dot{V}_{\text{bk},0})$ are, respectively, for single-phase fluids modified Stanton numbers, $(\dot{Q}/\dot{V})\beta/(\rho c_p) \to q''/(\rho c_p u \Delta T)$, and for two-phase mixture a modified Zuber number, $(v_{\text{fg}}/h_{\text{fg}})\dot{Q}/\dot{V}$. Transients with only one agent of change have no free scaling parameter in Eq. (6); the corresponding equation is always self-scaling. Equation (6) imposes one scaling criterion less than Eq. (5), but provides in each scaling criterion the largest possible number of adjustable design and operating parameters and therefore the maximum flexibility for satisfying scaling requirements for each agent of change.

3.3.2 Time for Quantification of Scale Distortion. We have pointed out in Sec. 3.1 that the individual fractional change metric $\Omega_j = \omega_j t_{\text{ref}}$ must be common to any facilities with individually scaled agents of change. Time need not to be preserved. Facilities with small values of $|\omega_j|$, especially of the significant FRCs, need a longer time t_{ref} to achieve a given fractional change in pressure. A convenient choice for reference time t_{ref}, which is readily available to facility designers and experimenters is the time $t_{\text{ref}} = 1/|\omega_{\text{bk}}|$ from the dominant agent of change, as in Eq. (6). Therefore, we obtain one choice of fractional change metrics for quantifying scale distortion of individual agents of change directly from

$$\hat{\omega}_j = \frac{\omega_j}{|\omega_{\text{bk}}|} = \Omega_j, \quad j = 2, \ldots, 6, \quad |\Omega_j| < 1, \quad |\Omega_1| = |\Omega_{\text{bk}}| = 1 \tag{7b}$$

The quantification of scale distortion requires in a table such as Table 2, with the above Ωs as entries, a comparison of entries in a column (recall the comparison in Sec. 3.2 of entries in a row for ranking purposes). The difference between two entries in a column equals the difference in fractional change in the state variable by a specific agent of change acting alone, as it would be observed in the corresponding facilities during the time $t_{\text{ref}} = 1/|\omega_{\text{bk}}|$. This difference is a measure of scale distortion.

3.4 Fractional Change Metric for an Aggregate and Aggregate Response Time.

Following the method of fractional scaling introduced by Zuber et al. [1], the *aggregate fractional rate of change* $\bar{\omega}$ is obtained by adding all positive FRCs related to *pressurizing* agents of change to the sum of all negative FRCs related to *depressurizing* agents of change. The aggregate fractional rate of change $\bar{\omega}$ gives the correct aggregate response rate and scales time correctly for the aggregate of all subvolumes under the action all agents of change combined. It includes the action of all agents of change, which are active during the scaled time phase.

Depressurizing agents of change are break (subscript bk) and valve discharge flows, leaks, and steam generator cooling or heat losses that cause fluid contraction or condensation. Pressurizing agents of change are coolant injection, driven coolant pumps and heating in core and pressurizer, and possibly from solid structures. Thus, by summing over net outflows and the remaining active (possibly five types of) agents of change (see Table 1 above), or by scaling according to Eq. (11) below, one obtains the aggregate's effective fractional rate of change $\bar{\omega}$ for the *response rate of the aggregate*.

$$\bar{\omega} = \omega_{\text{bk}} + \sum_{j=2}^{6} \omega_j \tag{8}$$

The fractional change metric Ω of the aggregate for a scaled time phase is then defined as $\Omega = \bar{\omega}t$ and is the measure of fractional change in a state variable (pressure) during the time phase to which $\bar{\omega}$ applies. The fractional change metric Ω is negative during depressurization and positive for a pressure excursion when net overheating overwhelms cooling and loss of coolant. If the effective fractional rate of change $\bar{\omega}$ is close to zero for a time phase, then the fractional change metric also approaches $\Omega = 0$, and the associated time phase has nearly constant pressure. This occurs when in a time phase the steam generators and structural components act as heat sources and support decay heating in the core to compensate for break flow. Equation (8) corresponds to Eq. (A20) in Appendix A of the paper by Zuber et al. [1].

The *scaled time for the aggregate depressurization* and system-level *data synthesis* is as follows:

$$t^* = |\bar{\omega}|t, \quad |\bar{\omega}| > 0 \tag{9}$$

where the time counts from the beginning of the time phase. According to Eq. (9) the scaled time t^* is stretched during rapid and compressed during slow depressurization, always in accordance with the net dilatation of the fluid caused by *all active agents of change combined*. This is the reason for large- and small-break loss of coolant accidents to have a common scaled depressurization history.

Since the FRCs in Eq. (5) are *initial* rates of change obtained with *initial maximum full-power conditions*, and since the system is at steady state before the burst of the break, all agents of change except the break flow are initially balanced. Therefore, for the *special case of* a LOCA starting from full-power steady-state conditions, the sum in Eq. (8) is zero and $\bar{\omega} = \omega_{\text{bk}}$ as the break flow dominates initially the blow down.

Instead of scaling time in Eq. (1) via Eqs. (5) and (9), and by factoring out the effective fractional rate of change $|\bar{\omega}|$ on the right-hand side of Eq. (5), one gets exactly the same scaled equation directly by normalizing each dilation rate with the *effective dilation rate of the aggregate* (see Eq. (A17) in Ref. [1]), i.e., the magnitude of the algebraic sum of all (active) dilatation rates.

$$\dot{\mathbf{V}}_{\mathbf{j}}^* = \frac{\dot{V}_j(t)}{\left|\sum_{j=1}^{6} \dot{V}_j\right|_{t=0}}, \quad \left|\sum_{j=1}^{6} \dot{V}_j\right| \neq 0 \tag{10}$$

This replaces the normalization of the volume change rates in Eqs. (4*a*) and (4*b*). Here, the $\dot{\mathbf{V}}_j^*$ are no longer of order of unity. Return with Eq. (10) to the second equation of Eqs. (1) and get *directly*

$$\frac{dp^*}{dt} = \frac{\left|\sum_{j=1}^{6} \dot{V}_j\right|_0}{V\Delta p(K_{s,\text{sys}})_0} \frac{\sum_{j=1}^{6} \dot{\mathbf{V}}_{\mathbf{j}}^*}{K_{s,\text{sys}}^*} = \left|\sum_{j=1}^{6} \omega_j\right| \frac{\sum_{j=1}^{6} \dot{\mathbf{V}}_{\mathbf{j}}^*}{K_{s,\text{sys}}^*} = |\bar{\omega}| \sum_{j-1}^{6} \varphi_j^* \tag{11}$$

Dividing Eq. (11) by $|\bar{\omega}|$ gives

$$\frac{dp^*}{dt^*} = \sum_{j=1}^{6} \frac{\dot{\mathbf{V}}_{\mathbf{j}}^*}{K_{s,\text{sys}}^*} = \sum_{j=1}^{6} \varphi_j^*, \quad p^*(0) = 1 \tag{12}$$

The time t^* is defined in Eq. (9) and approaches that of Eq. (6) *only* if $\bar{\omega} \to \omega_{\text{bk}}$. Equation (12) replaces Eq. (6) and is self-scaling because it has no free scaling parameters $\hat{\omega}_j$. The fractional change metric $\Omega = \bar{\omega}t$ denotes the *aggregate fractional change in pressure by all agents of change*. Time t^* in Eq. (12) is stretched or compressed according to the net dilation caused by all agents of change active during a time phase, as explained below Eq. (9).

Table 3 Fractional rate of change for break flow at the start of large-break and small-break LOCAs in LOFT and Semiscale

	LOFT				Semiscale			
	Break size	Residence time, $V/\dot{V}_{\mathrm{bk},0}$ (s)	$\Delta p(K_s)_0$	ω_{bk} (%/s)	Break size (%)	Residence time (s)	$\Delta p(K_s)_0$	ω_{bk} (%/s)
Large-break	200%	7.24	0.0241	−577	200	6.53	0.0257	−603
Small-break (PRZ included)	1 in. diameter, 0.1%	2,842	0.262	−0.134	$2\frac{1}{2}$	471	0.245	−0.866
					5	277		−1.48
					10	98.8		−4.13

The scaled variable of the jth agent of change φ_j^* in Eq. (12) now depends on the FRCs of all active agents of change because the φ_j^* obtained by scaling via Eq. (10) is the product of the jth normalized variable Φ_j^* in Eq. (5) and obtained via Eq. (4*b*), times the ratio of two FRCs as follows:

$$\varphi_j^* = \frac{\omega_j}{|\bar{\omega}|}\Phi_j^* \tag{13}$$

The hierarchical order of the *variables* φ_j^* differs from that of the individual fractional change metrics Ω_j of Eq. (7*b*), unless the normalized variables Φ_j^* have the same value at some known time. Equation (6) is used therefore for ranking agents of change according to their importance, while Eq. (12) has the correct time scaling for data synthesis and for computer simulation of blowdown pressure history.

Equation (12) without free parameters is *far simpler* than Eq. (6). The inequality behind Eq. (9) may be needed in Eq. (12) but may not be met in the scaling of transients without directly initiating agents of change, such as the transient in the reactor primary system that starts from full-power steady state and follows a turbine trip. The inequality may not be met even when estimated maxima are used as reference values in Eq. (10). Because of Eq. (13), the pressure history obtained from Eq. (12) depends on each FRC seen in Eqs. (6) and (7*a*), even though Eq. (12) shows no free parameters.

4 Application

FSA at the system level is demonstrated here in two ways, namely, for establishing *a process hierarchy* and *assessing scale distortion* based on the FRC and for data synthesis based on the fractional change metric. The demonstration is for two PWR integral effects test facilities, namely, the LOFT facility with its primary system fluid volume said to equal 1/48 of that of a 3000 MW (thermal) Westinghouse PWR, and the Semiscale test facility, whose volume is 1/1700 of that of the Westinghouse reference PWR. For large-break LOCA in LOFT and Semiscale the demonstration is made with the break size of 200% of flow area in one cold leg. The small-size break in LOFT simulates a 1 in. pipe break (25.4 mm diam.) at the cold leg in the reference plant, representing a 0.1% break size. For Semiscale the FSA demonstration is with Semiscale Mod-1 for large-break LOCA in the cold leg, and Mod-2A for small-break LOCA simulations of $2\frac{1}{2}$%, 5%, and 10% break sizes. For data source references see Appendix B.

The FRC-based hierarchy of agents of change, or transfer processes across the system boundaries, is an *objectively quantified* alternative for the hereunto subjectively implemented PIRT. Moreover, the FRCs serve to *identify* and *quantify scale distortion*.

The graph $p^*(|\Omega|)=p^*(t_{\mathrm{bk}}^*)$ should reveal whether the fractional change in pressure p^* during blow-down tests is the same at the same value of the fractional change metric of the break, Ω, regardless of plant or test facility size or break size and actual blowdown time. Congruence of curves $p^*(|\Omega|)$ indicates that break flow governs the entire blow down and that system volume, system elasticity (dominated by saturated liquid volume in the pressurizer), break size, and initial pressure are properly scaled; differences reveal scale distortions. The initial slope of $p^*(|\Omega|)$ should be always (-1).

4.1 Establishing Process Hierarchy and Assessing Scale Distortion. The break flow is the *net flow* from all breaks, leaks, and possible injections. The net flow leaving the system is the dominant agent of change. Table 3 lists associated numerical values of the initial *fractional rates of change* ω_{bk} defined in Table 1, along with the break size, the residence or turn-over time defined as $V/\dot{V}_{\mathrm{bk},0}$, and the fractional volume compression $\Delta p(K_s)_0$. It takes the residence time to displace the control volume V at the initial volumetric flow rate $\dot{V}_{\mathrm{bk},0}$ of the break.

The residence time dominates the differences of ω_{bk}, the FRC of break flow, in facilities of different sizes, when the same fluid is used at the same pressure, because it is dominated by the *characteristic length for system depressurization by break flow* ($\lambda = V_{\mathrm{sys}}/A_{\mathrm{bk}}$). The fractional volume compression $\Delta p(K_s)_0$ is the fractional reduction in fluid volume when it is adiabatically compressed by Δp.

The large-break entries in Table 3 are for the primary system with no pressurizer in the control volume, because the surge line flow is choked and must be treated as injection flow into the primary system control volume at the start of LOCA. The small-break entries are for a control volume that includes the pressurizer, since the surge line flow is subsonic for small breaks.

Table 2 exhibits in its last two *rows* for each of the two facilities the *hierarchy* of all agents of change in Eq. (6) that are active at the start of the blow down. The agents of change are ordered from left to right according to the magnitudes $|\omega_j|$ of their respective fractional rates of change, given in %/s, at the start of depressurization. The break flow leads and is followed by the expansion of a two-phase mixture due to phase change in the pressurizer. If $|\hat{\omega}_j|<0.1$ is accepted as the threshold criterion for unimportant agents, only the break flow is important.

Comparing in *columns* the values in the last two rows, one observes that initially there is little or no *scale distortion* for lbLOCAs and LOFT versus Semiscale. The single-phase liquid cooling is the difference in core heating plus pump heat additions, minus steam generator cooling and heat losses to the environment. The accumulators are initially valved off and therefore not active at the start of depressurization. There is no superheated vapor at the start of depressurization. Table 2 shows also the summation indices j introduced in Table 1 and used in Eqs. (6), (7*a*), (7*b*), (8), and (10)–(13).

A practical working criterion for scale distortion is needed for declaring an important process to be distorted in one test facility relative to another facility or a full-size plant, just as one needs a criterion for separating "important" from "unimportant" agents of change [11]. The criterion for scale distortion cannot be tighter than is permitted by the compound of pertinent experimental uncertainties, manufacturing tolerances, and operational uncertainties, or else no important process can ever be found to be without scale distortion. If one accepts a 10% difference between two corresponding FRCs as the lower limit for "scale-distorted" then

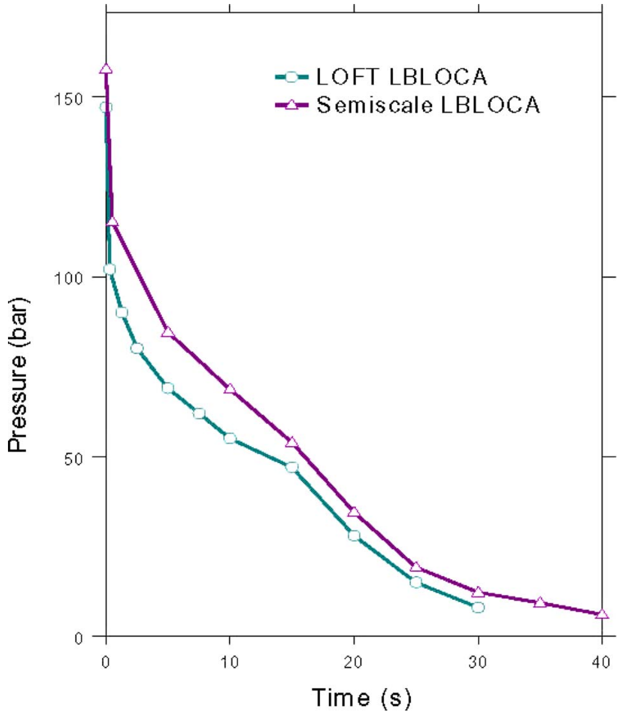

Fig. 2 Measured large-break LOFT and Semiscale depressurizations: facility effects are scaled to preserve blow-down time

the last two rows in Table 2 show no large-break LOCA depressurization process of importance that is distorted.

4.2 Data Synthesis. Figures 2 and 3 show, in currently prevailing and familiar format, measured blow-down pressure histories, i.e., pressures versus actual time, for LOFT and Semiscale, during large-break LOCAs (200% break size) and small-break LOCAs (1 in. pipe break for LOFT and $2\frac{1}{2}\%$, 5%, and 10% break sizes for Semiscale). Discrete points were read from the graphs cited in Section (3) of Appendix B, digitized, tabulated, and plotted with AXUM6 software.

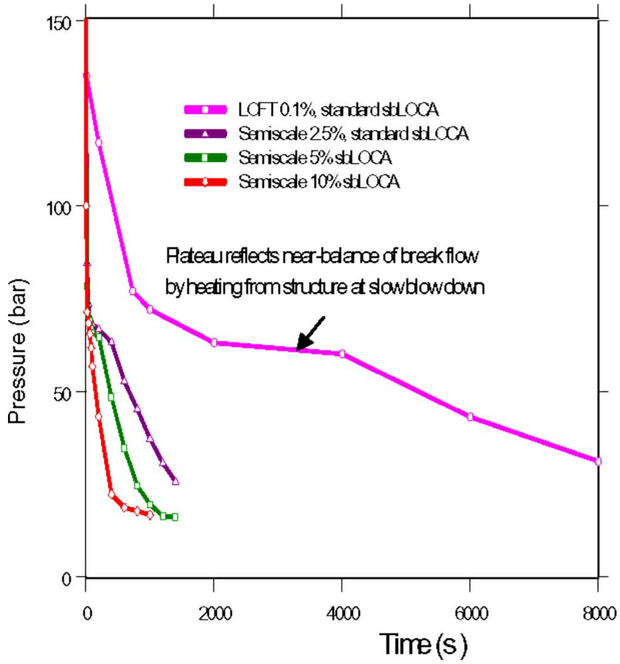

Fig. 3 Measured small-break LOFT and Semiscale depressurizations show effects of facility and break sizes on blow-down time

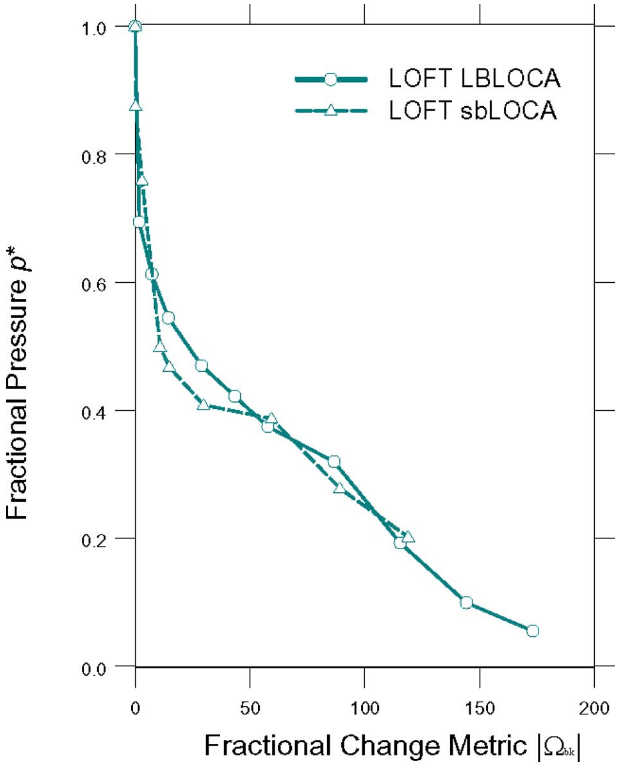

Fig. 4 Scaled large- and small-break LOCAs in LOFT: effects of break size on blow-down time is scaled

The comparison of the figures reveal the large spread of blow-down times on account of break size, from a short 30 s for large-break LOCA (see Fig. 2) to the long time of 8000 s for the LOFT small-break LOCA (see Fig. 3). Notice that the rates of depressurization in Fig. 3 are consistent with the magnitudes of the fractional rates of change shown in Table 1 for all small breaks. The small-break LOCA tests with the smallest magnitude $|\omega_{\mathrm{bk}}|$ of its break flow FRC has the smallest break size and the longest blow-down time (LOFT sbLOCA with 0.1% break size), while the small-break LOCA tests with the largest magnitude $|\omega_{\mathrm{bk}}|$ of its break flow FRC has the largest break size and the shortest blow-down time (Semiscale sbLOCA with 10% break size). Figure 2 shows a faster depressurization for LOFT than for Semiscale, even though LOFT's FRC of $|\omega_{\mathrm{bk}}|$ of 577%/s is less than the 603%/s of Semiscale. The explanation of this reversal is that LOFT started from a lower pressure and that the 4.5% difference between the two FRCs is much less than the uncertainties in drag disk measurements of break flows and their graphical determinations from the recorded flow rates.

Figures 2 and 3 present the effects of facility differences on pressure history. Evidently, the scaling of LOFT and Semiscale nearly *preserved time* for large-break LOCA (see Fig. 2) but not for small-break LOCA (see Fig. 3). Only for large-break LOCA are the fractional rates of change ω_{bk} of break flow, namely, $-603\%/\mathrm{s}$ for Semiscale and $-577\%/\mathrm{s}$ for LOFT (Table 3), close and within the uncertainty range of initial break flow determination. The FRCs in Table 3 were used to form the fractional change metric Ω and to scale the time of the experimental results in Figs. 2 and 3 according to Eq. (9), where $\bar{\omega}=\omega_{\mathrm{bk}}$, because the sum in Eq. (9) is zero at the beginning of the blow-down. The pressure is scaled according to Eq. (3). This leads to the plots of $p^*(|\Omega|)$ in Figs. 4–7, which show the effects of scaling parameters $\hat{\omega}_k$ and scaled variables Φ_k^* as well.

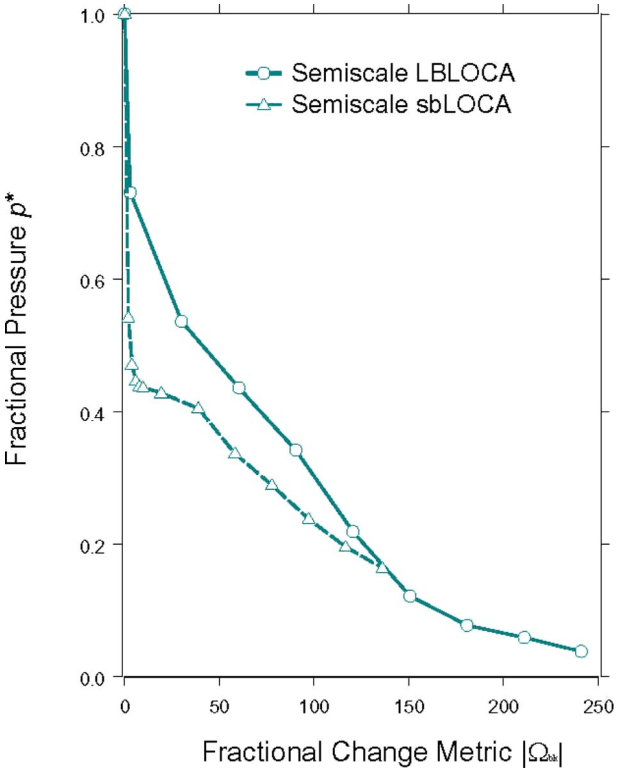

Fig. 5 Scaled large- and small-break LOCAs in Semiscale: effects of break size on blow-down time is scaled

4.2.1 Scaling of Break Size. For the *LOFT facility*, the effect of break size is scaled, because the two curves in Fig. 4 collapse into one, even though the times of blow-down differ by the factor of 267. It must be noted that the break size is represented by the initial total volumetric flow rate, rather than by the total break area. There are two breaks for the large-break LOCA, one on the vessel and the other on the pump side. The volumetric flow rate was computed from the total measured initial critical mass flow rate at the break(s) and respective upstream fluid density. Fluid density had to be taken from upstream of the break plane(s), to meet the condition of $\nabla p=0$ in the control volume V (see Appendix A).

For the selected *Semiscale facility*, the effect of break size is also scaled, because the two curves in Fig. 5 collapse nearly into one later in the blow-down, even though the actual blow-down times differ by the factor of 71.

The more pronounced shape difference between the Semiscale curves in Fig. 5 suggests dissimilar processes during large- and small-break Semiscale depressurizations. The convergence of the curves late in the blow down reflects proper scaling of the system volume and break flow, but the small-break LOCA fluid is initially disproportionately stiffer (smaller isentropic compressibility of the system, see Eq. (2)) than the large-break LOCA fluid system. The pressurizer compressibility is, for large breaks, not part of system compressibility in the denominator of Eq. (1) but affects the surge line flow, and with that the net discharge in the numerator of Eq. (1). Conflicting records of the initial pressurizer liquid level in Semiscale suggests that insufficient care was exercised in monitoring and recording the level, and that the level records may be uncertain. A PWR *system* compressibility will vary approximately from 120% to 54% of the recorded value $K_{s,\mathrm{sys}}=1.7\cdot 10^{-8}$ Pa^{-1} with a pressurizer full of liquid and full of vapor, respectively. It appears however, that saturation temperature and flashing were reached at higher pressure during large-break than during the small-break LOCAs.

The blow-down passes through time phases, each of which has its set of initial fractional rate of change ratios $\hat{\omega}_j$ (see Ref. [11].). The ratios $\hat{\omega}_j$ associated with the heat transfer from the solid structures and from the secondary side will reflect facility differences in structural heat capacities and will serve to quantify scale distortions. In general, the hierarchy of agents of change will change from time phase to time phase, as fission heat and cooling in the steam generators decrease and the compressed liquid reaches saturation. This will introduce sectionally separate time scales for each time phase according to Eqs. (7*a*) and (7*b*) or ratios $\hat{\omega}_j$ of fractional rates of change as parameters in Eq. (6), and thereby relate scale distortions to specific agents of change. Unfortunately, the necessary data could not be obtained to calculate the additional ratios of fractional rate changes $\hat{\omega}_j$ for later time phases in sbLOCAs.

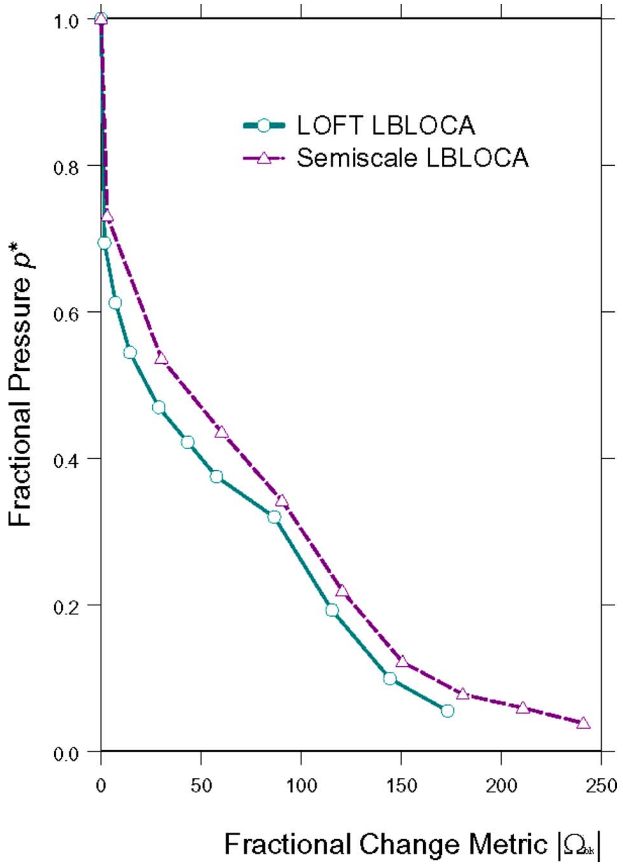

Fig. 6 Scaled large-break LOFT and Semiscale depressurization: facility effects are scaled for 200% break size

4.2.2 Scaling of Facility Size. Figure 6 demonstrates the scaling of large-break LOCA Depressurization for two facilities: LOFT and the 37 times smaller Semiscale test facilities. The blow-down times differ by one-third. Figure 6 resembles Fig. 2, because LOFT and Semiscale were scaled to preserve time for large-break LOCA.

Figure 7 shows the scaling of the small-break LOCA blow down for two facilities of very different sizes and shapes, LOFT and Semiscale, but now with the blow-down times differing by the factor of 4.7. Figure 7 shows also the shape differences discussed in connection with Fig. 5 above.

4.2.3 Scaling of Small-Break and Facility Sizes. The four small-break LOCA depressurization histories shown above in Fig. 3 with depressurization times between 600 s and 8000 s have been scaled by FSA. Compare Fig. 3 with Fig. 8 below, where the scaled histories are demonstrated to collapse almost into a single curve. The curve for LOFT is for a 1 in. pipe break (1%), and the

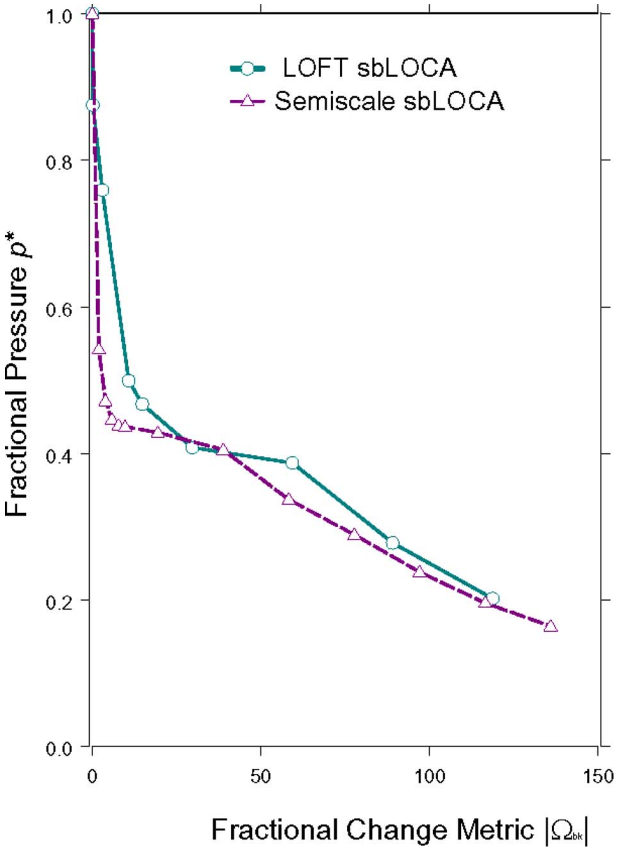

Fig. 7 Scaled small-break LOFT and Semiscale depressurization: facility effects are scaled for 1 in. and $2\frac{1}{2}$% break sizes, respectively

three Semiscale curves are for break sizes of $2\frac{1}{2}$%, 5%, and 10% of the cold-leg cross-sectional area. All Semiscale tests were performed as base cases in the same Mod-2A configuration *prior* to the upper-head injection tests.

The measured Semiscale pressure histories are consistent, in that the largest break produces the fastest, and the smallest break the slowest blow-down (Fig. 3). However, the scaled curve from the 5% break size test did not fall, as expected, between the test curves from the $2\frac{1}{2}$% and 10% break sizes because of the uncertainty in the initial break flow.

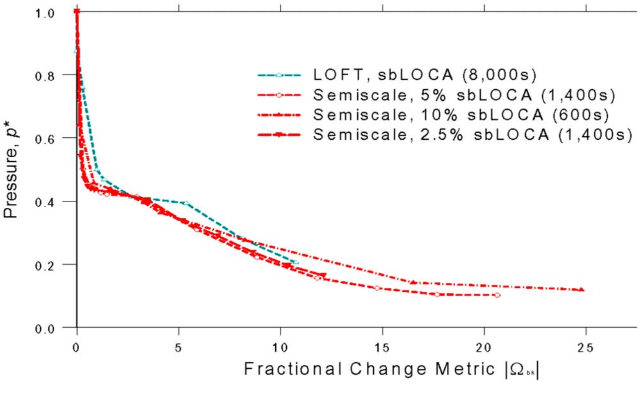

Fig. 8 Small-break LOCA blow-down in LOFT and three break sizes in Semiscale. Pressurizer volume included in primary system volume. The legend shows break sizes for Semiscale and, in parentheses, recorded test durations. Compare with unscaled curves in Fig. 3.

The four curves in Fig. 8 display a common partition of the small-break LOCA blow down in a high-pressure Phase I of fast depressurization, an intermediate-pressure Phase II of nearly no depressurization, and a low-pressure Phase III of slow depressurization. The fluid is stiffest in Phase I, where most of it is compressed liquid having the smallest compressibility; it starts with a sharp depressurization while subcooled liquid enters the break. Heat addition from the secondary system and emergency injection almost balances the break flow effects during Phase II. Emergency injection during Phase III retards the depressurization during Phase III.

LOFT appears in Phase I to have its sbLOCA depressurization rate strongly reduced relative to Semiscale. That must have been caused primarily by LOFT's relative small-break size (only 0.13% of cold-leg cross-sectional area) permitting more time for effective heat transfer from structures, but also possibly by greater fluid elasticity in the pressurizer, earlier system-wide flashing, or less cooling in steam generators, or more boiling in the core.

Semiscale with the 10% break size appears to have greater heat transfer from the solid structures than LOFT during Phase III, as its depressurization is retarded late in the blow-down. This may be attributed to delays in loop seal clearing. However, the pressure differences are small compared with the reference data uncertainties.

The scaled abscissa $0 \leq (t_{bk}) \leq 25$ in Fig. 8 is shorter than that in Figs. 4–7 ($0 \leq (t_{bk}) \leq 250$). Figure 8 is based on the primary system volume, including the pressurizer volume, and only the break discharge, as there is no choking in the surge line during small-break LOCAs. Figures 4–7 are based on the volume of the primary system without the pressurizer, and on the break flow minus the surge line flow. The resulting flow reduction is more than compensated for by the increase in fluid stiffness (refer to Table 3).

5 Conclusions

We have applied FSA at the system level, first on the basis of FRC ω to identify, quantify, and prioritize in the order of their impact all transfer processes responsible for system depressurization (see Tables 2 and 3); and second, based on the fractional change metric Ω to synthesize experimental data (compare Figs. 2 and 3 with Figs. 4–8). We have demonstrated quantitatively for large- and small-break LOCAs in test facilities of widely different sizes and geometric shapes and for break sizes between 0.1% and 200% of cold-leg flow area that the break flow is the leading agent of change for global depressurization. It turned out that the absolute value of the break flow-related fractional change metric $|\Omega_{bk}| = t^*_{bk}$ alone synthesizes the pressure histories. We have found that a successful data synthesis requires reliable and complete plant specifications and test data. The synthesis is therefore performed most efficiently and reliably during testing or computer simulation, when data can be easily retrieved.

- We have also shown based on ratios of FRCs $\hat{\omega}_k$, i.e., one particular form of fractional change metric, that FSA serves to rank agents of change relative to the dominant agent of change. The FRC ratios facilitate the application of relative importance criteria. All agents of change for depressurization are exclusively volume contractions or dilations due to break flow, phase change, and thermal expansion or contraction. Ratios of FRCs ($\hat{\omega}_k = (\dot{V}_k / \dot{V}_{bk})_0$) are ratios of dilation rates over initial break volumetric flow rate and, unlike FRCs, independent of system elasticity.
- Depressurization, on the hierarchical system level, has its own *single process-specific response time*, as given by Eq. (9). This is a specific and important result of FSA and distinguishes FSA from standard scaling analyses.
- The transfer processes prioritized by FSA provide (i) the quantitative hierarchy that supersedes the widely used, but

subjectively generated PIRT; and (ii) the identification of scale distortions and a quantitative assessment of their impact on system depressurization. The hierarchy is, in general, important for any reactor design, safety analyses, code development, and for *greatly reduction in* design and development costs *without compromise of safety*.

- FSA affords, in general, simple and compact *syntheses* of experimental and analytical results that are efficient and economical for storing, preserving, and for retrieving information. FSA facilitates *efficient* and *quantified* sensitivity and uncertainty analyses without costly computer calculations. Through quantified prioritization, FSA serves to simplify computer codes while directing code development toward important needs. By sharply reducing the number of needed experiments and computations, FSA strongly reduces expenditures.
- Data synthesis by FSA serves, in general, to exhibit facility-related differences of process patterns or scale distortions in a component. FSA serves to *quantify the effect of scale distortion*.
- The partitioning of a transient into time phases accommodates in principle reordering at different times the agents of change as processes exchange the role of dominance, retarding (by evaporation or single-phase expansion) or accelerating (by condensation or contraction) the depressurization rate. This shows up either in sectionally different effective fractional rate changes $|\bar{\omega}|$, stretching or shortening the time scale (according to Eq. (12)) or by introducing scaling parameters $\hat{\omega}_j$ (according to Eq. (6)). If depressurization ceases in some time phase as the agents of change balance and cancel each other, that time phase disappears from the pressure history if scaled according to Eq. (12) because the scaled time of the phase becomes $t^* \rightarrow 0$.
- The elasticity of the two-phase mixture in the pressurizer dominates initially the system elasticity $\mathrm{K}_{s,sys}$ for small-break sizes. The scaling criteria imposed on the water level in the pressurizer must be met for global similarity (expected time scale). The pressurizer affects the system depressurization also for large breaks via the critical surge line flow, which subtracts from the break flow.
- Large-break LOCAs must be modeled and scaled with two control volumes, because the pressurizer and primary system have separate depressurization rates. The pressurizer and the primary system communicate by critical flow (during most of the blow down). This is true for all other systems with critical flow between components.
- Depressurization is independent of coolant flows within and between system components so long as the flows are at low-Mach numbers. The depressurization rate is determined only by rates of volume displacement imposed *across the system boundary*, either directly by loss or by injection of coolant or indirectly by fluid expansion or contraction due to energy transfer across the pressure boundary.
- Holistic models for some aspects of *system simulation* are already proven superior to reductionist's models. Holistic modeling combined with FSA provides similarity criteria for both common response of and interactions between components of a complex thermohydraulic system.
- This application is only a first exploratory effort to demonstrate, on an example, the potential of FSA for analysis, data synthesis, and to gain in-depth understanding of complex systems at *minimal* cost. FSA is not limited to the selected examples, but applies to simple and complex systems in general. More data are needed to include other facilities and to extend FSA to the analysis of system component interactions. Ignoring the benefits from FSA in the future would result without a doubt in *unnecessary financial losses to industry and taxpayers*.
- FSA is a scaling analysis, not a prediction tool. However, the *combination of FSA and scaled experiments* can sharply reduce the need for computer code calculations. The combination would be more trustworthy than most currently used computer codes.
- FSA is demonstrated here without any LOCA-specific assumptions. FSA provides the demonstrated features and capabilities equally well for any scenario in past, current, and future reactor designs, in fact, for complex systems in general, since FSA scales any modeling equation [2].

Nomenclature

a = isentropic speed of sound
A = cross-sectional area
c_p = isobaric specific heat
c_v = isochoric specific heat
h_{fg} = enthalpy of phase change
M = fluid mass
p = pressure
P_{PP} = pumping power
$\dot{Q}$ = heating power
s = specific entropy
S = entropy
t = time
T = absolute temperature
T_{sat} = saturation temperature
v_{fg} = specific volume of phase change
$\boldsymbol{v}$ = fluid velocity
V = volume
V_{sub} = phasic subvolume
V_{sys} = total system volume
v = specific volume
$\dot{V}$ = volumetric flow rate
$\dot{\mathbf{V}}_k^*$ = kth normalized rate of volume change, see Eq. (10)
W = mass flow rate
$Y(t)$ = general variable or variable expression

Greek Symbols

α = vapor volume fraction
β = isobaric thermal expansion coefficient
γ = specific heat ratio, isentropic exponent
Δp = range of pressures, Eq. (3)
ρ = density
$K_{s,\mathrm{sys}}$ = system isentropic compressibility, Eq. (2)
κ = specific isothermal compressibility
κ_s = specific isentropic compressibility, Eq. (A3)
λ = $V_{\mathrm{sys}}/A_{\mathrm{bk}}$ characteristic length of depressurization by break flow
Φ_k = rate of pressure change effect from kth agent of change, Eq. (5) and Table 1
φ_k^* = rate of pressure change scaled to include fixed ratio of fractional change rates, Eq. (13)
Ω = ωt, fractional change metric of state variable (-)
ω = rate of fractional change, Eq. (5) and Table 1 (%/s)
$\bar{\omega}$ = effective (compound) rate of fractional change, Eq. (8) (%/s)
$\hat{\omega}_k$ = kth ratio of rates of fractional change, Eq. (7)

Subscripts

bk = break(s)
crit = critical, choked flow
env = environmental, suppression tank
f = saturated liquid
j = summation index, see Tables 1 and 2
g = saturated vapor

l = liquid, compressed liquid
max = maximum value
min = minimum value
N_2 = inert gas, nitrogen
net = net, heating minus cooling
$\dot{Q}$ = due to heat transfer
sub = subvolume
sys = total system with volume V
v = vapor, superheated vapor
vl = valve(s)
0 = initial value
1φ = single-phase liquid or vapor
2φ = two-phase mixture

Superscripts

* = scaled
‘ = differentiation w/r pressure, along saturation line
$^\bullet$ = time derivative, time rate of change

Appendix A: The Depressurization Rate Equation

Published depressurization rate equations have been derived by combining the mass and energy balances, predominantly local balances in the form of partial differential equations, supplemented by caloric and thermal equations of state, and by using thermodynamic identities [4–10]. The derivation from local balance equations is greatly simplified by converting the mass balance into the flux divergence equation and by retaining the normally neglected, but for depressurization essential mechanical energy term $p\nabla\cdot\boldsymbol{v}$ in the energy equation (Ref. [11], pp. 5–7). One cannot get the depressurization in terms of subvolume dilations and aggregate isentropic compressibility without the mechanical energy term. The approach relates the variation of pressure to all active agents of change through their effect of volume displacement, that is, it relates “effort” to “flows” in Layton’s terms of multidisciplinary system variables [3]. It shows also how isentropic and isobaric expansions combine into any system depressurization.

To obtain the depressurization rate equation, we consider the primary system enclosed by its rigid pressure boundary with specified openings and containing the time-dependent volume $V(t)$ of coolant. $V(t)$ consists of up to four types of time-dependent subvolumes V_{sub}, namely, three for single-phase liquid, vapor, and inert gas, $V_{1\varphi,j}$, $j=l,v,\mathrm{N}_2$, respectively, and one for two-phase vapor-liquid mixture $V_{2\varphi}$. Each subvolume present in V may be anywhere in the primary system and need not to be contiguous. The boundaries separating the subvolumes move in time such that there is no mixing across or phase change in the interfaces. This implies that the mass M_{sub} in each subvolume remains constant, even though the fluid may switch from subcooled to saturated liquid, to two-phase mixture and superheated vapor.

If the components in the control volume V communicate only by low-Mach number flows (having fluid velocity $\boldsymbol{v}$ and pressure p) then the effect of $\boldsymbol{v}\cdot\nabla p$ on density ρ is negligible compared with that of $\partial p/\partial t$, and a single time-dependent volume-averaged pressure $p(t)$ represents the entire primary system. The momentum balances of the primary system loops are then decoupled from mass and energy balances. However, when a component, such as the pressurizer, interacts with the primary system through choked flow, that component has a different depressurization rate and requires its own depressurization equation.

The net outflow (or break flow) across the system’s pressure boundary is choked flow. The critical mass flow rate W_{crit} is known from measurement or computed from a correlation. The break is idealized here by a shock plane, upstream of which thermophysical properties, such as the upstream fluid density $\bar{\rho}$, equal the volume-averaged properties of the upstream subvolume, and downstream of which is critical flow. This and the mass balance $dM_{\mathrm{sub}}/dt=0$ imply for the fluid in the control volume V (Lagrangian system) that the rate of change in volume equals the volumetric break flow rate.

$$\frac{dV}{dt}=\frac{d}{dt}\sum_j V_{\mathrm{sub},j}=\frac{d}{dt}\sum_j (Mv)_{\mathrm{sub},j}=\sum_j\left(\frac{V}{v}\right)_{\mathrm{sub},j}\frac{dv_{\mathrm{sub},j}}{dt}=\frac{W_{\mathrm{crit}}}{\rho^{-}}$$
$$=\dot{V}_{\mathrm{crit}} \qquad \text{(A1)}$$

Recognizing that even for the large-break LOCA the depressurization (with approximately −3 bar/s) follows an equilibrium path sufficiently close, we approximate the general change in any one of the subvolumes with average specific volume v, average pressure p and average entropy s by (omitting here the subscript “sub”)

$$\frac{dV}{dt}=\frac{V}{v}\frac{dv}{dt}=\frac{V}{v}\left(\frac{\partial v}{\partial p}\right)_s\dot{p}+\frac{V}{v}\left(\frac{\partial v}{\partial s}\right)_p\frac{ds}{dt}=-V\kappa_s\dot{p}+\left(\frac{\partial v}{\partial s}\right)_p\frac{d(Ms)}{dt}$$
$$=-V\kappa_s\dot{p}+\left(\frac{\partial v}{\partial s}\right)_p\frac{\dot{Q}}{T} \qquad \text{(A2)}$$

Where $\dot{p}=\partial p/\partial t$, $\dot{Q}$ is the net heat added to the subvolume, and the isentropic compressibility is given by

$$\kappa_s=-\frac{1}{v}\left(\frac{\partial v}{\partial p}\right)_s=\frac{1}{\rho a^2} \quad \ldots\text{in general}$$
$$=\frac{c_v}{c_p}\kappa \quad \ldots\text{liquid, vapor}$$
$$=\sum_{k=f,g}\alpha_k\left[\frac{v_{\mathrm{fg}}}{h_{\mathrm{fg}}}(\rho_k h'_k-1)+\frac{\rho'_k}{\rho_k}\right] \quad \ldots\text{two-phase mixture}$$
$$=\frac{1}{\gamma p} \quad \ldots\text{inert gas} \qquad \text{(A3)}$$

in familiar terms of density ρ and isentropic speed of sound a for all fluids; in terms of isochoric and isobaric specific heats c_v and c_p, and isothermal compressibility κ for single-phase liquid and vapor; then in terms of specific volume change and enthalpy of evaporation, v_{fg} and h_{fg}, respectively, of phasic volume fractions α_k, $k=f$, g, phasic densities ρ_k, and the derivatives with respect to pressure along the saturation lines of phasic densities and enthalpies ρ'_k and h'_k, respectively; and finally in terms of the isentropic expansion coefficient γ and pressure p for inert gases.

For *single-phase fluids*, i.e., liquid, vapor, and inert gas, the last derivative in Eq. (A2) is easily read from the third *Tds* equation (see Ref. [15], p. 330). It is

$$\left(\frac{\partial v}{\partial s}\right)_p=\frac{\beta T}{\rho c_p} \qquad \text{(A4}a\text{)}$$

which reduces to

$$\left(\frac{\partial v}{\partial s}\right)_p=\frac{1}{\rho c_p}=\frac{\gamma-1}{\gamma}\frac{T}{p} \qquad \text{(A4}b\text{)}$$

for a *perfect gas* and for the equilibrium *two-phase mixture* to,

$$\left(\frac{\partial v}{\partial s}\right)_p=\frac{T_{\mathrm{sat}}v_{\mathrm{fg}}}{h_{\mathrm{fg}}} \qquad \text{(A4}c\text{)}$$

In Eqs. (A4*a*)–(A4*c*), the symbols β and T_{sat} denote, respectively, isobaric thermal expansion coefficient and saturation temperature. Substitute Eqs. (A3) and (A4*a*)–(A4*c*) into Eq. (A2), once each for two-phase mixture, for liquid, vapor, and inert gas. Add a separate term for heat addition by the total pumping power P_{PP} to the appropriate subvolume (liquid at the beginning of depressurization). Substitution of the result into Eq. (A1) and solving for the time rate of depressurization $\dot{p}$ gives the following desired system depressurization equation:

$$\frac{dp}{dt}=\frac{1}{VK_{s,\mathrm{sys}}}\left[-\sum_{j=\mathrm{bk},vl}\dot{V}_j+\frac{v_{\mathrm{fg}}}{h_{\mathrm{fg}}}(\dot{Q}_{2\varphi})_{\mathrm{net}}+\sum_{j=l,v}\left(\frac{\beta}{\rho c_p}\dot{Q}_{\mathrm{net}}\right)_j+\left(\frac{\beta}{\rho c_p}\right)_l P_{\mathrm{PP}}+\frac{\gamma-1}{\gamma}\frac{\dot{Q}_{\mathrm{N}_2}}{p}\right] \tag{A5}$$

Here, $K_{s,\mathrm{sys}}$ is the aggregate isentropic compressibility of the global system, which is the sum of the volume fraction-weighted isentropic compressibilities of those subvolumes that are present and communicating by subsonic flow within the primary system:

$$K_s=\sum_{j=l,v,2\varphi,\mathrm{N}_2}\frac{V_{\mathrm{sub},j}}{V}(\kappa_s)_{\mathrm{sub},j} \tag{A6}$$

Equations (A5) and (A6) are Eqs. (1) and (2) of the paper. Wulff and Rohatgi (Ref. [11], pp. 5.7–8) derived the same result earlier from *local* mass and energy balances for single-phase fluids, from the flux divergence and equilibrium phase change equations for two-phase flow and by applying the Gauss divergence theorem to integrals of the resulting partial differential equations. That derivation requires only continuous mixture volumetric flow rates across subvolume boundaries.

The NBS standard reference database of steam tables [16] provides all the standard thermophysical properties of water appearing in Eqs. (A3), (A5), and (A6), including isothermal compressibility κ and isentropic speed of sound a. Three exceptions are the thermal expansion coefficient β and the derivatives along the saturation lines of phasic densities and enthalpies ρ_k' and h_k'. The NBS steam tables yield two partial derivatives of pressure with respect to density and temperature. These must be used to compute the following:

$$\beta=\frac{1}{\rho}\frac{\left(\frac{\partial p}{\partial T}\right)_\rho}{\left(\frac{\partial p}{\partial \rho}\right)_T}=\kappa\left(\frac{\partial p}{\partial T}\right)_\rho \tag{A7}$$

Using Clapeyron's equation, one finds the derivatives with respect to pressure, along both saturation curves, first of phasic density as follows:

$$\rho_k'=\left(\frac{\partial \rho_k}{\partial p}\right)_T\left[1-T_{\mathrm{sat}}\frac{v_{\mathrm{fg}}}{h_{\mathrm{fg}}}\left(\frac{\partial p}{\partial T}\right)_{\rho_k}\right],\quad k=g,f \tag{A8}$$

and then of phasic enthalpy as follows:

$$h_k'=\frac{1}{\rho_k}+T_{\mathrm{sat}}\left[(c_p)_k\frac{v_{\mathrm{fg}}}{h_{\mathrm{fg}}}-\frac{\beta_k}{\rho_k}\right],\quad k=g,f \tag{A9}$$

Inert gas does not enter the present application, since the formation of scaling groups is for conditions at the start of the blowdown with closed accumulators.

Appendix B: Identification of Data Source Documentation

Scaling requires (1) facility specifications, (2) specified initial test and operating conditions, and (3) initial boundary conditions, such as break flows. Data synthesis implies availability of some test data. Scaling and data syntheses are achieved in the absence of some or all test data, before a facility design, for example, by using know and confirmed correlations consistently for small- and full-size facilities. This appendix presents the sources of data needed to compute the fractional rates of change listed in Table 1 and used in Chapter 4. The information enables the reader to reproduce and scrutinize the results in this paper and to recognize the inadequacy of published reports on important and costly experiments. Standard NBS/NRC steam tables (a FORTRAN code [16]) provided thermophysical properties of water.

(1) *Facility specifications* for LOFT and experimental objectives are described by Reeder [17]; Nalezny [18] summarized the LOFT experiments. There are at least eight modifications of the Semiscale facility, namely, Semiscale Mod-1, 2, 2A, and 2C, and Mod-3–6 [19]. No reference could be found to a systematic and comprehensive documentation for plant specifications, initial test, and operating conditions. Different reports for the same Mod-version, and descriptions of code input data, contain contradictory data; yet no single report describes a specific facility version completely. Buckingham's Π-theorem was unofficially and unsuccessfully tried. "Power to volume scaling" is alluded to, but no reference could be found to a systematic scaling analysis or to a list of scaling criteria, not even to the ubiquitously cited so-called reference Westinghouse power plant: The LOFT reference cites a 3000 MW power plant; the Semiscale documentation implies a 3400 MW plant. The primary system volume of LOFT should be 1700/48 =35.4 times larger than that of Semiscale, but for Mod-1 it is 37 times larger. Semiscale primary system volumes of different Mod-versions differ by 13%, yet no scaling criteria were found to be maintained while the volume was varied. The strongest effect on initial primary system elasticity $\mathrm{K}_{s,\mathrm{sys}}$ comes from the initial vapor volume in the pressurizer. Semiscale documentation reports initial vapor volume fraction values between 0.613 (p. 284 in Ref. [20]) and 0.367 on (p. 385 in Ref. [21]).

The Semiscale *test series 1* is called "Isothermal blowdown tests" and "Mod-1 isothermal tests;" yet there is no (core) heating to keep the fluid temperature constant during large-break LOCA depressurizations. Instead, the tests are rapid and therefore nearly *adiabatic* blow-down tests. Semiscale documentation is obviously and quite generally haphazard and often bewildering.

Fractional scaling at the system level is demonstrated here for Semiscale with Semiscale Mod-1 for large-break LOCA simulation (with the break size being 200% of cold-leg flow area) [22]; and with Semiscale Mod-2A for small-break LOCA simulations of 2.5%, 5%,and 10% break sizes [23,24].

(2) *Initial test and operating conditions* were found for LOFT large-break LOCA tests in the report by Bayless and Divine [25] (pp. 185–187) and for LOFT small-break LOCA tests in the report by Addessio and Boyak [26] (pp. 83 and 85). Semiscale initial test and operating conditions came for the large-break LOCA test from Ref. [27] (pp. 141, 160, 163, 173, and 176) and for the small-break LOCA tests from Refs. [23] (pp. 11 and 16) and [28] (pp. 17 and 21).

(3) *Test data* in the form of pressure histories were taken for the LOFT Large-break LOCA test L2–5 also from the report by Bayless and Divine [25] (p. 94) and for LOFT small-break LOCA tests L3–7 from Sahota and Addessio [24] (p. 91). The Semiscale test data came for the large-break LOCA test S-06–3 [27] (p. 92) and for the small-break LOCA tests S-UT-4 ($2\frac{1}{2}$% break size), S-UT-6 (5%), and S-UT-1 (10%) from Shimeck [23] (p. 11). The three tests used here for scaling are the base case tests performed without upper-head injection.

References

[1] Zuber, N., Catton, I., Rohatgi, U. S., and Wulff, W., 2007, "Application of Fractional Scaling Analysis (FSA) to Loss of Coolant Accidents (LOCA): Methodology Development," Nucl. Eng. Des., **237**, pp. 1593–1607.

[2] Catton, I., Wulff, W., Zuber, N., and Rohatgi, U. S., 2005, "Application of Fractional Scaling Analysis to Loss of Coolant Accidents (LOCA), Part 3: Component Level Scaling for Peak Clad Temperature," Proceedings of the 11th International Topical Meeting on Nuclear Thermal Hydraulics (NURETH-11), Popes' Palace Conference Center, Avignon, France.

[3] Layton, R. A., 1998, *Principles of Analytical System Dynamics* (Mechanical Engineering Series), Springer-Verlag, New York.

[4] Solberg, K. O., and Bakstad, P., 1967, "A Model for the Dynamics of Nuclear Ractors With Boiling Coolant With a New Approach to the Vapor Generating

Process," *Symposium on Two-Phase Flow Dynamics*, Institute for Atomenergi, Kjeller, Norway Sept. 4–9, Commission of the European Communities, Brussels.

[5] Lahey, R. T., Jr., and Moody, F. J., 1993, *The Thermal Hydraulics of a Boiling Water Nuclear Reactor* (Monogram Series on Nuclear Science and Technology), 2nd ed., American Nuclear Society, LaGrange Park, IL.

[6] Reyes, J. N., Hochreiter, L. E., Lau, L. K.. and Lafi, A. Y., 1995, "Low Pressure Integral System Test Facility Scaling Report," Westinghouse Proprietary Class 2, WCAP 14270.

[7] Banerjee, S., Reeder, D. L., Ortiz, M. G., and Larson, T. K., 1996, "Top-Down Scaling Analysis for AP600 Integral Tests," Idaho National Engineering Laboratory, Report No. INEL-96/0040.

[8] Wulff, W., 1996, "Scaling of Thermohydraulic Systems," Nucl. Eng. Des., **163**, pp. 359–395.

[9] Wulff, W., 1998, "Integral Methods for Two-Phase Flow in Hydraulic Systems," *Advances in Heat Transfer*, J. P. Hartnet, T. F. Irvine, Jr., Y. I. Cho, and G. A. Greene, eds., Academic Press, San Diego, CA, Vol. 31, pp. 105–158.

[10] Ortiz, M. G., Larson, T. K., Reeder, D. G., and Banerjee, S., 1997, "Top-Down Scaling Studies to AP600 Facilities," ACRS Thermal Hydraulics Subcommittee Meeting, Los Angeles, CA.

[11] Wulff, W. and Rohatgi, U. S., 1998, "System Scaling for the Westinghouse AP600 Pressurized Water Reactor and Related Test Facilities," Brookhaven National Laboratory, Report No. NUREG/CR-5541.

[12] Meyer, J. E., and Williams, J. S., 1962, "A Momentum Integral Model for the Treatment of Transient Fluid Flow," Report No. WAPD-BT-25.

[13] Wulff, W., Cheng, H. S., Lekach, S. V., and Mallen, A. N., 1984, "The BNL Plant Analyzer," Brookhaven National Laboratory, Report Nos. NUREG/CR-3943 and BNL-NUREG-51812.

[14] Wulff, W., 1996, "High-Speed Interactive Computer Simulation for PWR Power Plants," Brookhaven National Laboratory, Research Report No. EP88-19.

[15] Zemanski, M. W., 1968, *Heat and Thermodynamics*, 5th ed., McGraw-Hill, New York.

[16] Haar, L., Gallagher, J. S., and Kell, G. S., 1984, *NBS/NRC Steam Tables, Thermodynamic and Transport Properties and Computer Programs for Vapor and Liquid States of Water*, Hemisphere, New York.

[17] Reeder, D. L., 1978, "LOFT System and Test Description (5.5-ft Nuclear Core 1 LOCES)," EG&G Idaho, Inc., Report Nos. NUREG/CR-0247 and TREE-1208.

[18] Nalenzy, C. L., 1983, "Summary of Nuclear Regulatory Commission's LOFT Program Experiments," Idaho National Engineering Laboratory, Report Nos. NUREG/CR-3214 and EG&G-2248.

[19] Ball, L. J., Dietz, K. A., Hanson, D. J., and Olson, D. J., 1978, "Semiscale Program Description," EG&G Idaho, Inc., Idaho National Engineering Laboratory, Report No. TREE-NUREG-1210.

[20] Bott, T., Gilbert, J., Mandell, D., Meier, J., and Sicilian, J., 1985, "TRAC-PD2 Developmental Assessment," Los Alamos National Laboratory, Report No. LA-9700-MS and NUREG/CR-3208.

[21] LA Development Group, 1984, "Computer Program for Pressurized Water Reactor Analysis," Los Alamos National Laboratory, Report Nos. LA-9944-MS and NUREG/CR-3567.

[22] Liang, K. S., Kao, L., Chiou, J. L., Liao, L. Y., Wang, S. F., and Chen, Y. B., 1992, "Assessment of RELAP5/MOD2 Using Semiscale Large Break Loss-of-Coolant Experiment S-06-3," Institute of Nuclear Energy Research, Report No. NUREG/IA-0046.

[23] Shimeck, D. J., 1983, "Analysis of Semiscale Mod-2A System UHI/SBLOCA Experiments," Idaho National Engineering Laboratory, Report Nos. NUREG/CR-3195 and EGG-2246.

[24] Sahota, M. S., and Addessio, F. L., 1985. "TRAC-PF1 Developmental Assessment," Los Alamos National Laboratory, Report Nos. NUREG/CR-4278, and LA-10445-MS.

[25] Bayless, P. D., and Divine, J. M., 1982, "Experimental Data Report for LOFT Large Break Loss-of-Coolant Experiment L2-5," Report Nos. NUREG/CR-2826 and EGG-2210.

[26] Addessio, F. L., and Boyack, B. E., 1983, "TRAC-PF1 Development Assessment," Los Alamos National Laboratory, Report Nos. NUREG/CR-3280, and LA-9704-M.

[27] Collins, B. L., and Patton, M. L., Jr., 1978, "Experiment Data Report for Semiscale Mod-1 Test S-06-3 (LOFT Counterpart Test)," EG&G Idaho, Inc., Report Nos. NUREG/CR-0251 and TREE-1123.

[28] Loomis, G. G., and Streit, J. E., 1985, "Results of Semiscale Mod-2C Small-Break (5%) Loss of Coolant Accident Experiments S-LH-1 and S-LH-2," Idaho National Engineering Laboratory, Report Nos. NUREG/CR-4438 and EGG-2424.

Fluid Streaming in Micro/ Minibifurcating Networks

Z. Zhang[1]
e-mail: zhang@egr.uri.edu

A. Fadl

C. Liu

D. M. L. Meyer

Department of Mechanical Engineering and Applied Mechanics,
University of Rhode Island,
Kingston, RI 02881

M. Krafczyk
Department of Architecture, Civil Engineering and Environmental Sciences,
Institute for Computational Modeling in Civil Engineering,
TU Braunschweig,
38023 Braunschweig, Germany

In this study, we investigate the phenomena of flow streaming in micro-/minichannel networks of symmetrical bifurcations using computer simulations with analytical validation. The phenomena of the flow streaming can be found in zero-mean velocity oscillating flows in a wide range of channel geometries. Although there is no net mass flow (zero-mean velocity) passing through the channels, the discrepancy in velocity profiles between the forward flow and backward flow causes fluid particles near the walls to drift toward one end while particles near the centerline to drift toward the opposite end. The unique characteristics of flow streaming could be used for various applications. The advantages include enhanced mixing, pumpless fluid propulsion, multichannel fluid distribution, easy system integration, and cost-effective operation. The results of computer simulations showed that oscillation amplitude is the dominant effect on streaming velocity in channel networks. Streaming velocity was directly proportional to the oscillation frequency and can be used as a cost-effective and reliable convective transport means when the particle diffusivity is less than the fluid kinematic viscosity. A considerable amount of work is needed to further study and understand the flow streaming phenomenon. [DOI: 10.1115/1.3176973]

1 Introduction

Many papers on steady streaming in macrochannel oscillatory flows [1–15] were published in the last few decades. Various geometry and flow arrangements were covered in the literature, including streaming flow induced by a torsionally oscillated disk [2,3,6], streaming adjacent to a cylinder oscillating along its diameter [4,5], streaming in oscillating flow along a curved tube [7], pressure-driven oscillatory flow within a tapered tube [11,12], oscillatory flow through bifurcations [8,9,15], and streaming in the channel entrance region [14].

These previous studies showed that flow streaming during flow oscillation can occur at various simple geometries. However, still a considerable number of issues have not been studied. There is a need for the fundamental understanding of the flow streaming dynamics and for the full exploration of its potential applications, both in macro- and microscales. Many important research questions, including flow streaming in networked or combined streaming flow geometries, suspended particle behaviors in streaming flows, and practical applications of flow streaming, have not been addressed. This is particularly true for streaming flow in micro- and minichannels; very few studies have been reported to-date in the literature.

In this study, we investigate the phenomena of flow streaming in the networks of micro-/minibifurcation channels. This research topic is new and has many potential applications including micro-/minichannel convective heat and mass transport, fluid mixing, propulsion, multichannel distribution, and heat pipe technology.

2 Research Methods

2.1 Mechanisms of Flow Streaming in Bifurcations. The mechanisms of flow streaming in a bifurcating channel are illustrated in Fig. 1. It shows a qualitative picture of the axial velocity profiles of a Newtonian fluid in a macrochannel bifurcation tube based on the works of Haselton and Scherer [8] and Zhang et al. [15]. During inflow (toward the right), the parabolic velocity profile in the mother tube is split in half at the location of $U_{\max}$ when entering the daughter tubes, resulting in a nonsymmetrical profile with the maximum velocity skewed to the inner wall of the daughter tubes. During backflow (toward the left), two fully developed parabolic flow profiles in the daughter tubes merge at the center of the bifurcation and result in an ε-shaped symmetrical profile in the mother tube with a zero velocity at the center. A discrepancy in velocity profiles between inflow and backflow causes fluid elements near the walls to drift toward the mother tube (negative drift) while fluid near the centerline to drift toward the daughter tubes (positive drift). We would like to apply this unique flow streaming phenomenon from a single "macro" sized bifurcation to problems of fluid propulsion, mixing, and distribution in the networks of micro-/mini channels.

It is noted that the mechanisms of flow streaming we studied are different from those of acoustic streaming. Acoustic flow streaming originates from attenuation of the acoustic field. The attenuation spatially reduces the vibrating amplitude of the acoustic wave and hence generates Reynolds stress distributions and drives the flow to form the acoustic streaming. Acoustic streaming occurs in most geometries when an acoustic field exists, while the streaming flows we study are induced by the pressure-driven asymmetrical oscillating flows. In addition, oscillating parameters are quite different. In most cases, the acoustic vibration has much higher frequency (>100 kHz versus <0.1 kHz) and much smaller amplitude (<0.1 mm versus >0.1 mm).

2.2 Dimensional Analysis. There are six major independent variables that characterize a flow streaming process, e.g., oscillation amplitude A, oscillation frequency f, fluid kinematics viscosity ν, mother channel width r, fluid streaming velocity V, and one or more geometry variables. These additional geometry variables could be the length of the mother or daughter channels L, the daughter channel width r_1, the aspect ratio of the channel to width L/r, the bifurcation angle or the slope of the tapered channel, and others. There is a wide range of selections and variations among these geometry variables. For example, the curvature and branching angles of both curved and y-shaped channels will certainly affect the magnitude of secondary flow (transverse flow in a cross section) [16]. Work is needed to identify the effects of these vari-

---

[1] Corresponding author.

Contributed by the Fluids Engineering Division of ASME for publication in the JOURNAL OF FLUIDS ENGINEERING. Manuscript received September 19, 2008; final manuscript received May 19, 2009; published online July 24, 2009. Assoc. Editor: Neelesh A. Patankar.

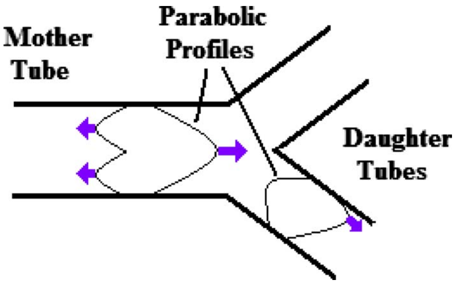

Fig. 1 Mechanisms of flow streaming in a bifurcation channel

ables and is not the focus of this study. It is assumed that the fluid is in a single phase and surface tension and other surface forces are neglected.

There are several methods of reducing a number of dimensional variables into a smaller number of dimensionless groups [17]. The Buckingham Pi Theorem was used in this study. The problem of flow streaming contained six variables described by three dimensions, e.g., mass, length, and time. According to the Buckingham Pi Theorem, the minimum Pi groups will then be three (i.e., the number of minimum Pi groups$=6-3$). However, it took one more Pi group than the minimum in this case since two geometry variables, i. e. mother channel width r and another geometry variable, had the identical dimensions. We selected the fluid viscosity ν and mother channel width r as the repeating variables in the Pi groups, since both ν and r were used in the conventional Pi groups, such as flow Reynolds and Womersley numbers. The Womersley number α is a nondimensional oscillation frequency defined as $\alpha = r(2\pi f/\nu)^{1/2}$.

Based on the above discussion, we combined the six flow streaming variables to yield four chosen nondimensional groups; $\mathrm{Re}_{\mathrm{st}}$=function (Womersley number, nondimensional oscillation amplitude, and nondimensional geometry factor), where $\mathrm{Re}_{\mathrm{st}}$ is the streaming flow Reynolds number or nondimensional streaming velocity, defined as $V(r/\nu)$ and the nondimensional oscillation amplitude is defined as A/r.

2.3 Computer Simulations. Haselton and Scherer [8] conducted the photographic streaming oscillating flow visualization experiments in a large-scale (2 m in length and 3.5 cm inside diameter) *Y*-shaped tube model. Zhang et al. [15] conducted the computer simulations of flow streaming in a *Y*-shaped channel. No other experimental work or computer simulations of flow streaming in a bifurcation were reported based on our knowledge. In this study, we conducted computer simulations of streaming flow in multigeneration microbifurcation channels using commercial computational fluid dynamics (CFD) software FLUENT V.6.2 (ANSYS, Inc., Canonsburg, PA). The computer simulation is a necessary tool to display the dynamics distribution patterns of fluid streak lines in microchannels and, in particular, to theoretically eliminate mass diffusion in the fluid. These simulated streaming flow patterns are essential in understanding the physics of flow streaming but not yet possible to obtain experimentally based on current experimental techniques.

The configuration of the bifurcation network model used in the computer simulation is shown in Fig. 2. The symmetrical bifurcation channel network consisted of four generations and fifteen channels. All channels had the length of 1 mm except the length of 1.5 mm for the mother channel. The width of the mother tube was 1 mm and it decreased by one-half after each bifurcation. As a result, mean oscillation velocities of the fluid in all channels were maintained at the same value thus providing a meaningful comparison of results. After three bifurcations, the width of the tube at the fourth generation became 125 μm. The bifurcating angle was 60 deg for all bifurcations.

The fluid was modeled as an incompressible Newtonian fluid.

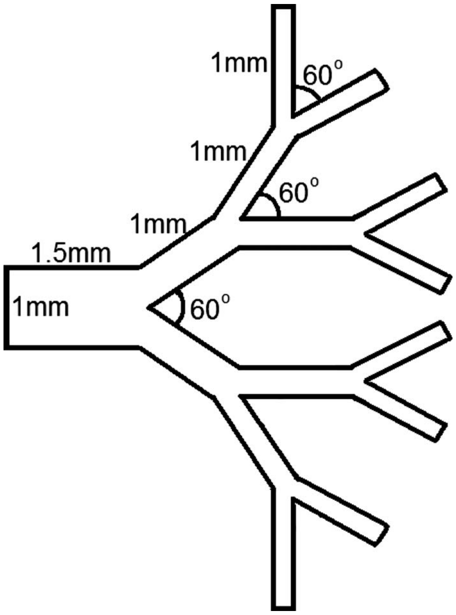

Fig. 2 Bifurcation channel networks used in the computer simulation

Two-dimensional flows were simulated for the sake of simplicity. Fluid motion was governed by the Navier–Stokes (N–S) equations and the continuity equation. The second-order implicit, semi-implicit method for pressure-linked equations, consistent (SIMPLEC) numerical scheme was used. The flows were considered to be laminar. The convective mass transport equation was numerically solved simultaneously with the N–S equations. Mass diffusivity D of the fluid was set to zero, so that the effect of mass diffusivity would be theoretically eliminated and the resultant mass concentration distribution patterns were purely created by fluid streaming. Mass concentration of the fluid inside the channel network was initially zero. At time $t>0$, fluids with constant properties and a high mass concentration entered the mother channel. A time-dependent parabolic velocity profile, in which the center velocity U_c is defined as $U_c=U_{\max}\sin(2\pi\ f\,t)$, was applied at the inlet of the mother tube. Zero-gradient velocity and mass concentration boundary conditions were applied at the outlet of eight daughter channels. Zero mass flux boundary conditions were applied on all wall surfaces. Since mass diffusions between fluids were artificially eliminated in the computer simulations, the unsteady mass concentration patterns mimic the patterns of fluid streak lines, displaying the vivid picture of flow streaming.

We used the total friction loss as the benchmark for grid converging tests since wall shear stress was susceptible to mesh size used in the simulations. This friction loss is the numerical integration of wall shear stress over the entire channel network surface and over an oscillation cycle at oscillation frequency $f=10$ Hz and amplitude $A/r=0.8$. Three element mesh sizes were examined including (A) $40(H)\times 100(L)$, (B) $80(H)\times 200(L)$, and (C) $160(H)\times 400(L)$. The difference in the calculated total friction loss between sizes A and B was 8.5% and 2.5 % between sizes B and C. The distribution of mesh sizes $80(H)\times 200(L)$ among four channel generations was as follows: generation 1, $80(H)\times 40(L)$; generation 2, $40(H)\times 40(L)$; generation 3, $20(H)\times 50(L)$; and generation 4, $10(H)\times 70(L)$. Figure 3 shows the fluid center axial velocity at the inlet as a function of time using time steps per oscillation cycle of 8, 16, 32, and 64 using the oscillating pressure inlet boundary condition. The maximum differences between the time steps of 8, 16, and 32 compared with 64 were 19%, 9%, and 3%, respectively. As a compromise between computational accuracy and central processing unit (CPU) time, mesh size B and a

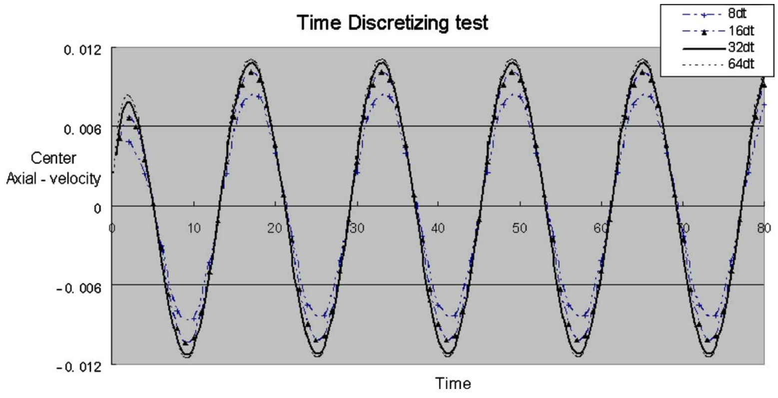

Fig. 3 Center velocity at $x=1.2$ mm as function of time. Time steps of 8, 16, 32, and 64 per oscillation cycle were used.

time step of 32 per oscillation cycle (the thick line in Fig. 3) were used in all simulations. The residual tolerance for continuity and velocities was 10^{-4} and 10^{-6} for the mass transport equation.

The numerical scheme was validated by analytical solutions since there was no experimental data of oscillating velocity profiles in bifurcation networks available in the literature. Computer simulations of straight, long, pipe flow due to an oscillating pressure gradient at the oscillation frequency of $f=10$ Hz and $r=0.5$ mm were conducted. Velocity profiles were then compared with the analytical solution of unsteady duct flows due to an oscillating pressure gradient [17]. The maximum difference between velocity values computed from the computer simulations and the approximated high frequency analytical solution for oscillating pressure-driven pipe flow described in Ref. [17] was less than 4.7%. Simulated velocity profiles clearly demonstrated the unique features of velocity overshoot for an unsteady oscillating pipe flow.

2.4 Results and Discussion. Figure 4 illustrates the effects of oscillation amplitude and frequency on streaming velocities. Streaming flow Reynolds numbers were presented as a function of Womersley number (dimensionless frequency) using nondimensional oscillation amplitudes as references. Streaming velocity was the rate of fluid streak line advancement or the rate of streaming front movement from one end to another. The discussions on streaming velocity were rare in the literature as is its measurement. For lack of a unified definition as well as for simplicity, we employed the position of the 20% mass concentration contour to represent the front of the streaming flow. The rate of this contour line advancement was reported as the streaming velocity. The average streaming velocity in a channel generation was calculated based on the channel length and time elapsed for the streaming flow traveling from one end to the other. In Fig. 4, panels A, B, and C display the streaming flow Reynolds number as a function of the Womersley number using oscillation amplitude as the reference parameter for the first, second, and third channel generations, respectively. The mother channel width r was used as the characteristic length in both streaming flow Reynolds and Womersley numbers. Since mass diffusivity of the fluid was set to zero in the simulations, the resultant streaming patterns were supposedly free of diffusion. Meanwhile, it is also noted that there was always a finite amount of numerical diffusion in the simulations due to inherent errors of the numerical method.

Computer simulations revealed that the streaming flow velocities highly depended on the location within the network. The streaming Reynolds numbers presented in Fig. 4, panels A, B, and C are the mean velocity values averaged over the entire channel generations. Neglecting the end effects (inlet and outlet), bifurcations were the only sources of fluid disturbances that created flow streaming. It was observed from dynamics simulation results that at a distance away from the bifurcation, flow disturbances induced at the bifurcation diminished, and the streaming flow slowly dissipated. At a distance closer to the bifurcation, the streaming flow accelerated. Bifurcation configurations practically served as pumps in the channel networks to move the streaming flows forward.

Figure 4 shows that at the fixed oscillation amplitude, streaming velocity increased proportionally with the oscillation frequency

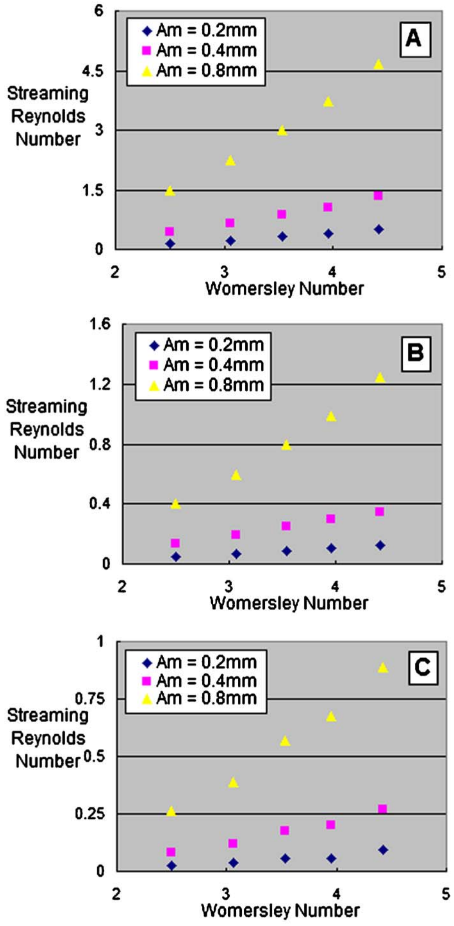

Fig. 4 Effects of Womersley number and oscillation amplitude on streaming velocity. Panel A: channel generation 1, panel B: channel generation 2, and panel C: channel generation 3.

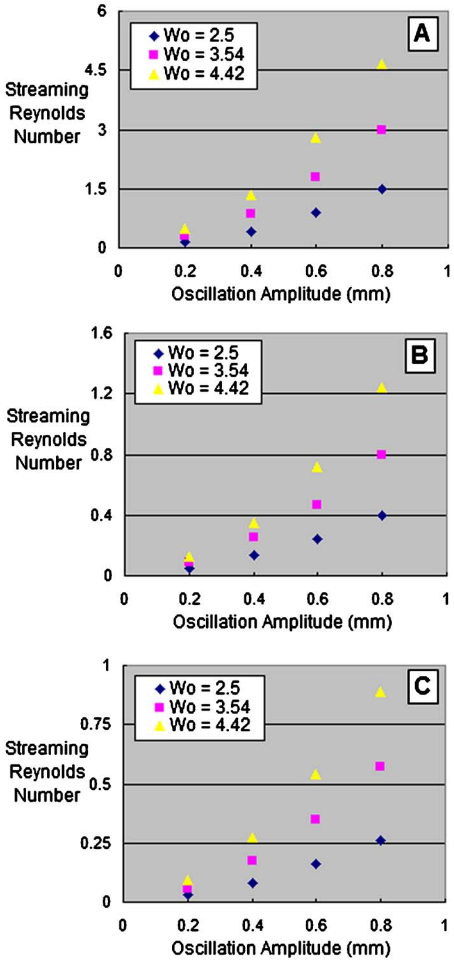

Fig. 5 Effects of oscillation amplitude on flow streaming. Panel A: channel generation 1, panel B: channel generation 2, and panel C: channel generation 3.

for all parameters we simulated. This suggested that the streaming flow velocity had a linear relation with the oscillation frequency. Oscillation frequency varied from 1 Hz to 12.5 Hz in the simulations.

Panels A, B, and C in Fig. 4 also show that oscillation amplitude had a dominant effect on streaming velocity as compared with effects from the oscillation frequency. In Fig. 5, panels A, B, and C display the effects of oscillation amplitude on flow streaming in generations 1, 2, and 3, respectively, using oscillation frequency as a reference. In the entire range of the frequency we studied, the rate of streaming velocity enhancement accelerated from low to high amplitude. For example, at an oscillation frequency of 8 Hz, the enhancement in streaming flow Reynolds number from an oscillation amplitude of 0.2–0.4 mm and then to 0.8 mm increased from 171% to 251% in generation 1, from 199% to 220% in generation 2, and from 214% to 229% in generation 3. This may be attributed to the fact that high oscillation amplitudes pushed the fluid directly close to the location of the channel bifurcation (e.g., source of streaming), bypassed or reduced the zone of low streaming, and therefore, enhanced the average streaming velocity.

Figures 4 and 5 show that streaming velocity decreased from mother channels to daughter channels. This may be caused by two factors: (a) Streaming flow is a bidirectional flow as streaming flow traveled from mother to daughter channels, mass concentration decreased as well. Consequently, the spreading rate of the mass concentration contour line decreased, and (b) flow disturbances induced at the bifurcation would dissipate within a distance equivalent to the flow entrance length. Flow entrance length was proportional to the square of the channel diameter [17].

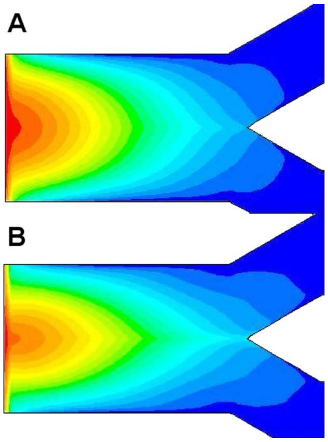

Fig. 6 Effects of mean oscillation fluid velocity on streaming flow distribution patterns. Mean oscillation velocity $u=0.004$ and 0.016 m/s in panels A and B, respectively.

The effects of mean fluid oscillation velocity on streaming distribution patterns are shown in Fig. 6. The mean oscillation fluid velocity was calculated as $u=2Af$. Streaming flow profiles with mean oscillation velocities of 0.004 m/s and 0.016 m/s (Panel A: $A=0.2$ mm, $f=10$ Hz; Panel B: $A=0.8$ mm, $f=10$ Hz). Three distinct features of the streaming flow could be observed in Fig. 6, namely: (i) The layered mass concentration contours displayed shadowed footprints of the matching streaming flow remaining during oscillation cycles; (ii) the skewed velocity profile at the entrance of the daughter tubes: During the inflow, the parabolic velocity profile in the mother tube was split in half at the ridge of bifurcation with the maximum velocity $U_{\max}$ at that location when entering the daughter tubes, resulting in a nonsymmetrical profile with the maximum velocity skewed to the inner wall of the daughter tubes. At a low velocity, the daughter channel velocity profile was blunt as shown in panel A. The degrees of skewness increased with the mean oscillation velocity u as shown in panel B; and (iii) the demonstration of the ε-shaped streaming profile in the mother channel: During the backflow, two fully developed, parabolic flow profiles in the daughter tubes merge at the center of the bifurcation and result in an ε-shaped symmetrical profile in the mother tube with a zero velocity at the center. The ε-shaped backflow produces layers of sharp-tongue-like concentration profiles at the centerline as shown in Fig. 6. Both the sharp-tongue and ε-shaped streaming phenomena were reported by Haselton and Scherer [8].

Next, we considered the total mass transport by mass diffusion and mass streaming convection. Figure 7 shows the effects of mass diffusivity on the effective (overall) streaming velocity. With

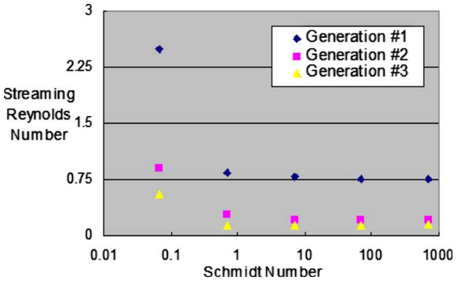

Fig. 7 Effects of mass diffusivity on convective mass transport process under flow streaming

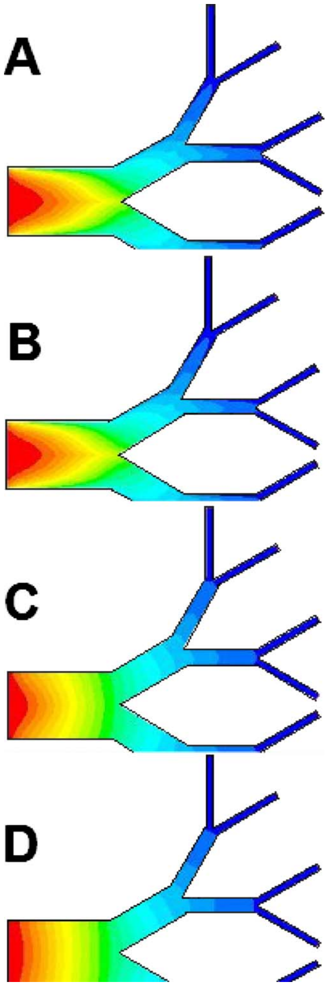

Fig. 8 Effects of mass diffusivity on concentration profiles under flow streaming. Panel A: Sc=∞, *t*=6.15 s; panel B: Sc =700, *t*=6.15 s; panel C: Sc=0.7, *t*=4.95 s; and panel D: Sc =0.07, *t*=1.45 s.

a nonzero mass diffusivity, mass transport mechanisms included both streaming advection and mass diffusion. The effective streaming velocity, again defined as the rate of 20% mass concentration contour traveling down the channel network, as a function of the Schmidt number ($\mathrm{Sc}=\nu/D$), was presented. Oscillation amplitude $A=0.3$ mm and frequency $f=10$ Hz were used in the simulation while the Schmidt number varied from 0.07 to 700. Figure 7 shows that there were no significant changes in the streaming flow Reynolds number for the entire range of Schmidt numbers that were greater than one and for all channel generations. In other words, mass transport by convective flow streaming was the dominant transport mechanism if mass diffusivity of the fluid was less than the kinematic viscosity of the fluid. Due to similarities between the mass and heat transport, this finding may be extended to other applications involving fluid/particle transport. For example, the streaming flow can be used as a convective heat transfer means when the Prandtl number is greater than one or as an effective means to transport particles entrained in fluids (such as cells, bacteria, and other fluid suspensions) when the particle diffusivities in fluids are less than the fluid kinematic viscosity.

Effects of the Schmidt number on mass concentration patterns during streaming are shown in Fig. 8. Oscillation amplitude $A=0.3$ mm and frequency $f=10$ Hz were used. The Schmidt number and elapsed time in panels A, B, C, and D were Sc=∞, 700, 0.7, and 0.07, and $t=6.15$ s, 6.15 s, 4.95 s, and 1.45 s, respectively. Figure 8 shows that there were virtually no differences between the concentration patterns between Sc number of ∞ and 700 due to the dominance of the convective streaming mechanism in total mass transport as shown in panels A and B. The transition between the convection dominance to diffusion dominance started around Sc=1. Although there was no significant difference in effective streaming Reynolds number for Sc=700 and Sc=0.7 as demonstrated in Fig. 7, mass concentration distribution patterns were starting to change around Sc=1. The concentration profiles shown in panel B (Fig. 8) were dominated by convective streaming, where the skewed concentration profiles toward the inner wall in the daughter channel are clearly visible. The concentration profiles shown in panel C were dominated by diffusion, where the concentration contours were smooth and uniformly distributed in all directions. There were no visible differences between concentration profiles shown in panels C and D with both concentration patterns dominated by diffusion. However, the elapsed times were quite different. Elapsed times in panels C and D were 4.95 s and 1.45 s, respectively. The effective streaming velocity for Sc =0.07 in Panel D was about 340% of that for Sc=0.7 in Panel C.

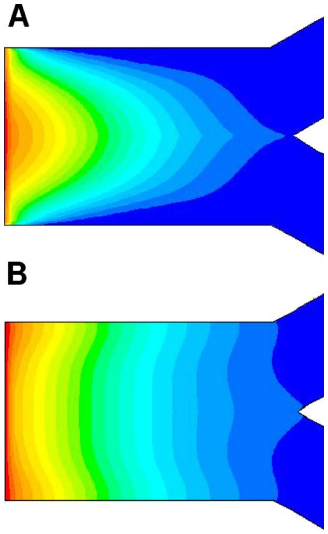

Fig. 9 Comparison of streaming patterns under different entrance boundary conditions: Panel A is parabolic velocity boundary condition and panel B is pressure boundary condition; *t*=1 s, *f*=10 Hz, and *A*=0.414 mm

Fluid entrance boundary conditions have crucial effects on downstream fluid velocity patterns. Therefore, it will certainly impact the streaming flow patterns as well. A pure pulsating flow in a circular pipe driven by a periodic pressure difference was investigated experimentally by Richardson and Tyler [18], and its exact analytical solution was obtained by Sexl [19] and Uchida [20]. The nontrivial feature of this flow was that for a high flow oscillation frequency, the time-mean velocity squared had a maximum, which occurs near the wall instead of the center. This overshoot phenomenon was called Richardson's annular effect, which also took place for oscillating flows in ducts of arbitrary cross-sectional shapes including the geometry we simulated [19]. Figure 9 displays the instantaneous fluid streaming patterns for oscillation frequency $f=10$ Hz, oscillation amplitude $A=0.414$ mm, and time at the end of 10 cycles or $t=1$ s for two different boundary conditions. Panel A is the parabolic velocity boundary condition and panel B is the pressure boundary condition. The sharp-tongue and ε-shaped streaming phenomena are shown in panel A. For pressure boundary conditions, the streaming pattern was blunt and uniform. This was caused by the Richardson's annular effect. Velocity overshoot near the wall enhanced the flow velocity in the

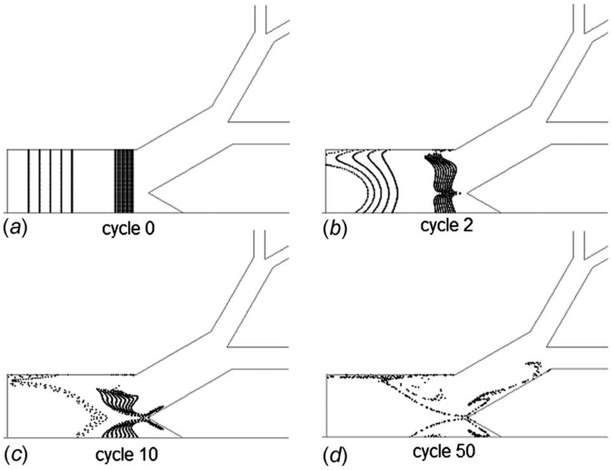

Fig. 10 Streak lines of air bubbles suspended in oscillation flows: (*a*) $t=0$ s (cycle 0); (*b*) $t=0.2$ s (cycle 2); (*c*) $t=1$ s (cycle 10); and (*d*) $t=5$ s (cycle 50). Oscillation amplitude $A=0.6$ mm and frequency $f=10$ Hz were simulated.

peripheral region and reduced the flow velocity near the center.

Compared with the oscillating pressure inlet boundary condition, the parabolic velocity boundary condition was less realistic since two profiles will be identical only at low oscillating frequencies. However, the differences in streaming velocity values were negligible for the frequency range we simulated ($f<12$). The maximum difference in streaming velocity between the two boundary conditions was less than 5% with the oscillating pressure inlet conditions consistently having a slightly greater streaming velocity. It was also noted that the maximum oscillation amplitude of the velocity profile for an oscillating pressure inlet boundary condition was not only a function of pressure but also a function of frequency as well as a function of latitudinal position due to the Richardson's annular effect. It posed a challenge for us to compare the streaming flow results using the oscillation amplitude as the (fixed) reference parameter. Based on the above small differences, even though the oscillating pressure inlet boundary condition is more realistic, parabolic velocity inlet boundary conditions were used mainly for computer simulations and discussions.

The influences of Richardson's annular effect on streaming increased with the frequency. Also, as discussed in the dimensional analysis, there is a wide range of variations among geometry variables to construct a bifurcation network. The potential interaction or resonance of overshoot velocity with the bifurcating network structure should create different streaming flow patterns to make this topic interesting and challenging.

The streak lines of particles suspended in oscillation streaming flow are shown Fig. 10, panel A: $t=0$ s (cycle 0), panel B: $t=0.2$ s (cycle 2), panel C: $t=1$ s (cycle 10), and panel D: $t=5$ s (cycle 50). A particle diameter of 1 μm and a density of 1.2 kg/m^3 (simulated a microsized air bubble) were used in this example. For simplicity, effects of buoyancy and diffusion were neglected in the particle trajectory model. Oscillation amplitude $A=0.6$ mm and frequency $f=10$ Hz were simulated. At time $t=0$, two bands of particles (left and right) were introduced into the mini-/microchannel as shown in panel A. Panel B displays the air bubble positions at the end of the second oscillation cycle. Two distinguished features of streaming can be observed: (1) the ε-shape of the right particle band near the bifurcation, and (2) the effects of the bidirectional streaming profile of the left band, from which a fraction of the particles was completely eliminated from the channel in the upstream direction. The bidirectional particle flow was demonstrated further in panel C at time $t=1$ s. Strong and local particle mixing occurred within the left band of particles while there was little mixing taking place at the right band although the shape of the right band was compressed. At time $t=5$ s, the front of the particles was propelled to the second bifurcation as shown in panel D. Panel D also showed that particles were mostly pushed along the wall. Figure 10 shows that the transport profiles of particles were more complicated than the fluid velocity profiles. Further confirmation is needed beyond the scope of this work, by way of a systematic and parametric study on particle-fluid interaction, particularly the sensitivity of time steps and grid sizes on particle trajectory.

Figure 11 displays the axial velocity profiles at various cross sections of the bifurcation networks for $t=3.025$ s (1/4 of an oscillation cycle, forward flow) and $t=3.075$ s (3/4 of an oscillation cycle, backward flow). Oscillation amplitude $A=0.6$ mm and frequency $f=10$ Hz were simulated. The asymmetry of axial velocity profiles along the transverse position between the forward and reverse flow at various sections of the bifurcation networks during the oscillation is the driving force of the bidirectional flow streaming.

2.5 Discussions on Applications. The proposed streaming flow-based fluid propulsion technique in micro-/minichannel has both limitations and advantages. The major disadvantage is its low efficiency in transport of sample flows. Compared with the main current of the oscillating channel flow, flow streaming is always a second-order flow. Oscillatory flow increases friction losses. Clearly, this inefficiency could limit its applications where direct pumping can be easily applied. However, it has a great potential in micro-/minichannels where various cost-effective and reliable micropumps are still under development.

Oscillation flow in micro-/minichannels can be generated by piezoelectric (PZT) diaphragms. Streaming flow-based microfluidics-driven PZT diaphragms provide many potential advantages. It will be valveless (no check valves needed), low cost (under $1/piece for a dime-sized PZT under mass production conditions and no need for looped piping), reliable (no moving parts except for the motion of the PZT), regular battery compatible, and easy system integration.

Flow streaming in channel networks can also be used in laboratory-on-chip (LOC) devices, for microcooling, microreactors, micromixers, and microheat pipes. Streaming flow will not only preserve the high heat transfer coefficients near the entrance and exit regions as conventional oscillation flow does but it also has higher heat/mass transfer coefficients in the middle section of the channel. The bidirectional flow streaming or the sliding of the warmer (or high concentration) liquid layer near the channel circumference region over the cooler (or low concentration) liquid layer near the channel core region should effectively disrupt the low laminar heat/mass transfer gradient, stretch the total surface area of the heat/mass transfer interface, and therefore enhance heat/mass transfer in microchannels.

3 Conclusions

Computer simulation results showed that oscillation amplitude had a dominant effect on streaming velocity in channel networks. Streaming velocity was directly proportional to the oscillation frequency. Streaming flow can be used as a cost-effective and reliable convective transport means when the particle diffusivity was less than the fluid kinematic viscosity. A considerable amount of work is needed to further study and understand the flow streaming phenomenon.

Acknowledgment

The research described in this paper was supported by the National Science Foundation, with Grant No. OISE-0530203.

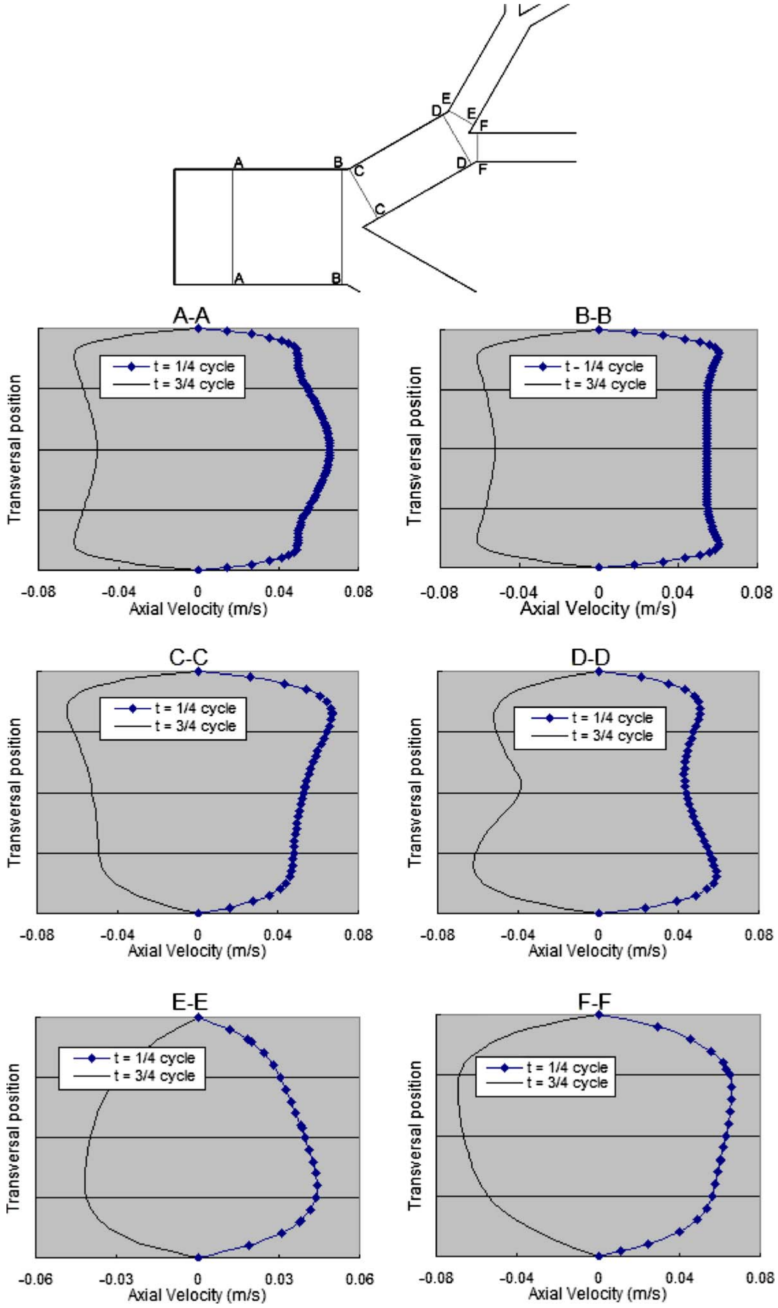

Fig. 11 Axial velocity profiles at various cross sections of the bifurcation networks for $t=3.025$ s (1/4 of an oscillation cycle) and $t=3.075$ s (3/4 of an oscillation cycle). Oscillation amplitude $A=0.6$ mm and frequency $f=10$ Hz were simulated.

Nomenclature

A = oscillation amplitude (mm)
D = mass diffusivity (m^2/s)
f = oscillation frequency (Hz)
L = length of the mother or daughter channels (mm)
r = mother channel width (mm)
r_1 = daughter channel width (mm)
Re_{st} = streaming flow Reynolds number or nondimensional streaming velocity
Sc = Schmidt number ($\mathrm{Sc}=\nu/D$)
U_c = center velocity (m/s)
$U_{\max}$ = maximum inlet velocity (m/s)
V = fluid streaming velocity (m/s)
α = Womersley number or nondimensional oscillation frequency
ν = fluid kinematic viscosity (m^2/s)

References

[1] Nyborg, W. L., 1953, "Acoustic Streaming Due to Attenuated Plane," J. Acoust. Soc. Am., **25**(1), pp. 68–75.
[2] Rosenblat, S., 1959, "Torsional Oscillation of a Plane in Viscous Fluids," J. Fluid Mech., **6**, pp. 206–220.
[3] Rosenblat, S., 1960, "Flow Between Torsional Oscillating Disks," J. Fluid Mech., **8**, pp. 388–399.
[4] Riley, N., 1965, "Oscillating Viscous Flows," Mathematika, **12**, pp. 161–170.
[5] Riley, N., 1967, "Oscillating Viscous Flows, Review and Extension," J. Appl.

Math., **3**, pp. 419–434.
[6] Jones, A. F., and Rosenblat, S., 1969, "The Flow Induced by Torsional Oscillations of Infinite Planes," J. Fluid Mech., **37**(2), pp. 337–347.
[7] Lyne, W. H., 1970, "Unsteady Viscous Flow in a Curved Tube," J. Fluid Mech., **45**(13), pp. 15–31.
[8] Haselton, F. R., and Scherer, P. W., 1982, "Flow Visualization of Steady Streaming in Oscillatory Flow Through a Bifurcation Tube," J. Fluid Mech., **123**, pp. 315–333.
[9] Simon, B., Weinmann, G., and Mitzner, W., 1982, "Significance of Mean Airway Pressure During High Frequency Ventilation," Physiologist, **25**, pp. 282–293.
[10] Tarbell, J. M., Ultman, J. S., and Durlofsky, L., 1982, "Oscillatory Convection Dispersion in a Branching Tube Network," J. Biomech. Eng., **104**(4), pp. 338–342.
[11] Grotberg, J. B., 1984, "Volume Cycled Oscillatory Flow in a Tapered Channel," J. Fluid Mech., **141**(1), pp. 249–264.
[12] Gaver, D. P., and Grotberg, J. B., 1986, "An Experimental Investigation of Oscillating Flow in a Tapered Channel," J. Fluid Mech., **172**(1), pp. 47–61.
[13] Briant, J. K., and Lippmann, M., 1992, "Particle Transport Through a Hollow Canine Airway Cast by High-Frequency Oscillatory Ventilation," Exp. Lung Res., **18**(3), pp. 385–407.
[14] Goldberg, I. S., Zhang, Z., and Tran, M., 1999, "Steady Streaming of Fluid in the Entrance Region of a Tube During Oscillatory Flow," Phys. Fluids, **11**(10), pp. 2957–2962.
[15] Zhang, Z., Fadl, A., Liu, C., and Meyer, D. M. L., 2008, "A Streaming Flow Based Lab-On-Chip Platform Technology," Proceedings of ASME Micro/Nanoscale Heat Transfer International Conference (MNHT08), Tainan, Taiwan, Paper No. MNHT2008-52283.
[16] Fresconi, F. E., Wexler, A. S., and Prasad, A. K., 2003, "Expiration Flow in a Symmetric Bifurcation," Exp. Fluids, **35**(5), pp. 493–501.
[17] White, F., 2003, *Fluid Mechanics*, McGraw-Hill, New York, pp. 296–306.
[18] Richardson, E. G., and Tyler, E., 1929, "The Transverse Velocity Gradient Near the Mouths of Pipes in Which an Alternating or Continuous Flow of Air Is Established," Proc. Phys. Soc., **42**(1), pp. 1–15.
[19] Sexl, T., 1930, "Uber Den Von E. G. Richardson Entdeckten Annular Effekt," Z. Phys., **61**(5–6), pp. 349–362.
[20] Uchida, S., 1956, "The Pulsating Viscous Flow Superposed on the Steady Laminar Motion of Incompressible Fluid in a Circular Pipe," Z. Angew. Math. Phys., **7**(5), pp. 403–421.

Modeling of Pumping Performance of Labyrinth Screw Pump (LSP) by 2D Reynolds Stress Equations

Runmei Ma[1]
e-mail: marm@mail.buct.edu.cn

Kuisheng Wang

Department of Mechanical and Electrical Engineering,
Beijing University of Chemical Technology,
Beijing 100029, China

By using Prandtl's mixing length theory to model two-dimensional Reynolds stress equations, the pumping performance of a labyrinth screw pump (LSP) is studied and several key parameters are empirically determined. As a result, two innovative concepts, a cell head coefficient K_f and a pump total head coefficient K_b, are proposed. A simple empirical equation quantifying the effects of the main geometric parameters of the threads on the pump performance is obtained and compared with Golubiev's experimental results (1965, "Studies on Seal for Rotating Shafts of High-Pressure Pumps," Wear, ***8****, pp. 270–288; 1981, Labyrinth-Screw Pumps and Seals for Corrosive Media, 2nd ed., Mashinostroenie, Moscow, pp. 34–49). Both theoretical study and Golubiev's results indicate that with an increase in screw lead, K_f increases while K_b decreases. K_f is inversely proportional to power of screw-sleeve relative diametrical clearance, and the power exponent varies with different shapes of thread. Finally, K_f decreases with an increase in the relative depth of the thread groove over a wide range. Furthermore, some empirical relations between K_f and screw lead, the screw-sleeve relative diametrical clearance and the relative depth of thread groove are fitted, respectively, based on the derived relation between K_f and thread geometric parameters and Golubiev's experimental data, which would provide a theoretical basis for LSP design.*
[DOI: 10.1115/1.3129128]

Keywords: labyrinth screw pump (LSP), pumping performance, cell head coefficient, pump total head coefficient

1 Introduction

A labyrinth screw pump (LSP) is a very low specific speed pump with small capacity and high lift and is now primarily used for pumping dilute acids and alkalis in chemical engineering. The pump has a simple structure and relatively high efficiency, up to 20–30% within the range of flow rate $1-4\ \mathrm{m^3/h}$, which could not be achieved by other small capacity and high head pumps. Therefore, over the recent decade, LSP has been gradually receiving more and more attention from pump manufacturers and users and becoming more common for applications in petrochemical and chemical engineering.

Golubiev [1,2] first proposed the labyrinth screw pump or seal structure and noted that the turbulent friction force between the fluid in the screw grooves and the fluid in the sleeve grooves acts on the thread walls and consequently creates the pump head. He then derived a pump head expression with head coefficient K for his pumping mechanism and investigated the qualitative relationships between K and the geometric parameters of the screw. These parameters include the screw lead, the relative fitting clearance of the screw to the sleeve, and the relative depth of the thread groove. According to the momentum principle, Bilgen and Akgungor [3] also derived a pump head equation with a cell form factor. Yet they did not discussed this factor. Later, Yizheng and coworkers [4,5], investigated the methods to determine the pump head coefficient K and the factors that influence it. However, since the function of the LSP has not been fully understood, the head coefficient of Golubiev and the cell form factor of Bilgen and Akgungor were not given clear physical meanings and this causes uncertainty for pump designers: What is the basis of the pump design? In order to answer the above question, we define two new concepts: a cell head coefficient K_f and a pump total head coefficient K_b based on the pumping principle of LSP put forward by Runmei et al. [6], to provide a design basis for pump designers who are interested in LSP.

2 Modeling of Pumping Performance of LSP

2.1 The Pumping Mechanism of LSP. Based on computational fluid dynamics (CFD) numerical simulation, the following LSP pumping mechanism was proposed by Runmei et al. [6]. The screw rotation creates intense turbulent friction at a nominal clearance interface between the screw and the sleeve. Due to the viscous action of the fluid and shears on the thread side walls of the screw and sleeve, two pressure sides and two suction sides are separately produced on the side walls in a cell formed momentarily by two cylinder threads and two sleeve threads. Along the radial direction, the pressure side of the screw faces the suction side of the sleeve, while the suction side of the screw faces the pressure side of the sleeve (Fig. 1). Having gained pressure and kinetic energy from the screw, the liquid flows from the cylinder grooves to the sleeve grooves under the pressure difference between the pressure side of the rotor and the suction side of the stator, and transfers momentum and energy into the fluid elements in sleeve grooves. In addition, because of the increase in the tangential sectional area of the sleeve grooves, some kinetic energy is converted into pressure energy. At the same time, the fluid elements near the pressure side of the stator flows back to the rotor grooves under the pressure difference between the pressure side of the stator and the suction side of the rotor, and again obtain momentum and energy from the rotor. So the cell actually plays a role similar to a single stage micro-impeller pump. The screw threads work on the fluid like impeller blades while the sleeve grooves provide the fluid with space to transfer momentum and also change fluid kinetic energy into pressure energy, much like a diffuser. The fluid elements obtain energy from the screw again and again while flowing along the axial direction, and consequently the pumping pressure increases linearly along the pump axis [7]. The frequency for which the fluid obtains energy is supposed to be proportional to the axial cell number.

2.2 Pumping Performance of LSP. To determine the pump performance, a coordinate system establishes the tangential, radial, and axial directions as x, y, and z axes, respectively, and fixes the zero point on the nominal clearance interface between the screw and the sleeve (Fig. 2). It is assumed [3] that the fluid average velocity and Reynold's stresses are functions of y only, and the radial average velocity is zero. Neglecting the effects of eccentricity and curvature of screw and the influence of the entrance and exit sections of the pump, the fluid flow in the pump is approximated as a steady incompressible turbulent flow between infinite parallel planes, both of them with grooves. Equations of motion for above flow are given by

$$-\frac{1}{\rho}\frac{\partial p}{\partial x}+\nu\frac{\partial^2 u}{\partial y^2}+\frac{\partial}{\partial y}(-\overline{u'v'})=0 \tag{1}$$

---

[1] Corresponding author.

Contributed by the Fluids Engineering Division of ASME for publication in the JOURNAL OF FLUIDS ENGINEERING. Manuscript received March 19, 2008; final manuscript received March 27, 2009; published online July 15, 2009. Review conducted by Joseph Katz.

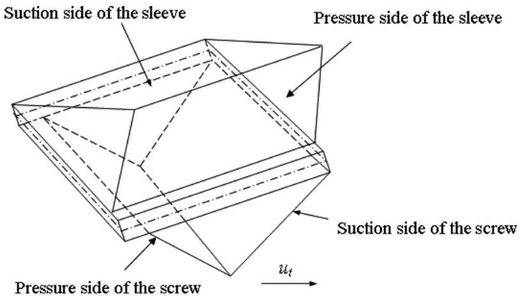

Fig. 1 The cell shape

$$-\frac{1}{\rho}\frac{\partial p}{\partial z}+\nu\frac{\partial^2 w}{\partial y^2}+\frac{\partial}{\partial y}(-\overline{w'v'})=0 \tag{2}$$

Assuming the fluid flow to be a well developed turbulent flow and neglecting the viscous friction, both Eqs. (1) and (2) are further simplified as follows by adopting Prandtl's mixing length theory [8]:

$$-\frac{\partial p}{\partial x}+\frac{\partial}{\partial y}\left(\rho l_{xy}^2\frac{\partial u}{\partial y}\cdot\frac{\partial u}{\partial y}\right)=0 \tag{3}$$

$$-\frac{\partial p}{\partial z}+\frac{\partial}{\partial y}\left(\rho l_{zy}^2\frac{\partial u}{\partial y}\cdot\frac{\partial w}{\partial y}\right)=0 \tag{4}$$

For periodicity of tangential and axial flows, let both $\partial p/\partial x$ and $\partial p/\partial z$ be constants. Integrated along the radial direction, Eqs. (3) and (4) are transformed as

$$\int_{-(h+(c/2))}^{0}\frac{\partial p}{\partial x}dy=\rho l_{xy}^2\frac{\partial u}{\partial y}\cdot\frac{\partial u}{\partial y}\bigg|_{y=0} \tag{5}$$

$$\int_{-(h+(c/2))}^{0}\frac{\partial p}{\partial z}dy=\rho l_{zy}^2\frac{\partial u}{\partial y}\cdot\frac{\partial w}{\partial y}\bigg|_{y=0} \tag{6}$$

where turbulent stresses on thread walls of screw and sleeve are zero [6].

Using direct numerical solution of the above two equations, it is difficult to obtain a single generalized equation for the pump head. As an approximation, we can presume that both planes have many threads and that the screw and the sleeve rotate in opposite directions with equal tangential velocity of $u_t/2$. We also assume that the motion of the liquid in the screw grooves can be regarded as being identical to the motion in the sleeve grooves. Neglecting the thickness of thread, which means the width of the thread land is zero, the tangential velocity of the liquid in both screw and sleeve grooves is approximately expressed as [1,2]

$$c_u=\frac{u_t}{2}-\frac{Q}{2S_c\tan(\alpha)} \tag{7}$$

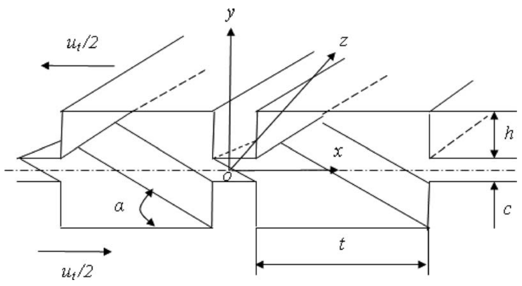

Fig. 2 Geometry of LSP and coordinate system

The average rate of strain between rotor-stator clearance is approximately written as

$$\frac{\partial u}{\partial y}\approx\left(u_t-\frac{Q}{S_c\tan(\alpha)}\right)/c \tag{8}$$

The fitting clearance is so small that Eq. (8) could be used as an approximation for the strain rate of $\partial u/\partial y$ at the nominal clearance interface. In addition, the head of the LSP increases with a decrease in flow rate and reaches a maximum when the pumping flow rate is zero. Thus we conclude that at the nominal clearance interface, the axial strain rate of $\partial w/\partial y$ has the same tendency to vary with flow rate as that of $\partial u/\partial y$, that is,

$$\frac{\partial w}{\partial y}\propto\left(u_t-\frac{Q}{S_c\tan(\alpha)}\right)/c \tag{9}$$

Let the axial length of the screw be L, and $\partial p/\partial z$ be approximately equal to $\Delta p/L$. Substituting Eqs. (8) and (9) into Eq. (6), we obtain

$$\Delta p_z\propto\rho l_{zy}^2\frac{L}{c^2\left(h+\frac{c}{2}\right)}\left(u_t-\frac{Q}{S_c\tan(\alpha)}\right)^2 \tag{10}$$

Neglecting the width of the thread land, then the tangential width of thread groove is $t=\pi D/z_1$. According to the head generation mechanism of LSP [6], Eq. (10) can further be transformed as

$$H=\frac{K_f}{g}\frac{z_1L}{\pi D\tan(\alpha)}\left(u_t-\frac{Q}{S_c\tan(\alpha)}\right)^2 \tag{11}$$

where

$$K_f\propto\rho l_{zy}^2\frac{\tan(\alpha)}{c^2\left(1+\frac{c}{2h}\right)\left(\frac{h}{t}\right)} \tag{12}$$

Equation (11) has almost the same form as Golubiev's head equation, but the basis for the pumping mechanism and the method of deduction are different from that of Golubiev. The physical meaning of coefficient K_f is therefore also different from that of head coefficient K. K_f in Eq. (12) is named a cell head coefficient. It, in fact, reflects the degree to which the fluid elements get the effective pressure energy from a cell. Thus K_f is determined mainly by the pressure transferred from cell walls minus energy losses related to the impinging, mixing, and friction between fluid elements as well as between fluid elements and cell walls. A larger K_f means that more pressure is transferred from cell walls, the momentum between fluid elements is transferred more effectively, and that energy losses for liquid mixing are smaller. Therefore, K_f may be taken as a criterion for evaluating the hydraulic performance of a cell.

To evaluate the influence of the cell hydraulic performance and the axial number of cells on pump characteristics, let coefficient $K_b=K_f\cdot m$, where $m=z_1L/\pi D\tan(\alpha)$, as the axial cell number, and K_b is the pump total head coefficient. K_b directly indicates the relative level of the pump head for pumps having the same main dimensions. In some cases of seal or pumping liquid, if a high head is required, then the larger K_b should be selected. In general, both K_f and K_b should be taken into account in design of LSP.

K_f, K_b, and Golubiev's K satisfy

$$K_f=\frac{K}{4}\tan(\alpha)=K_b/\left(\frac{z_1L}{\pi D\tan(\alpha)}\right) \tag{13}$$

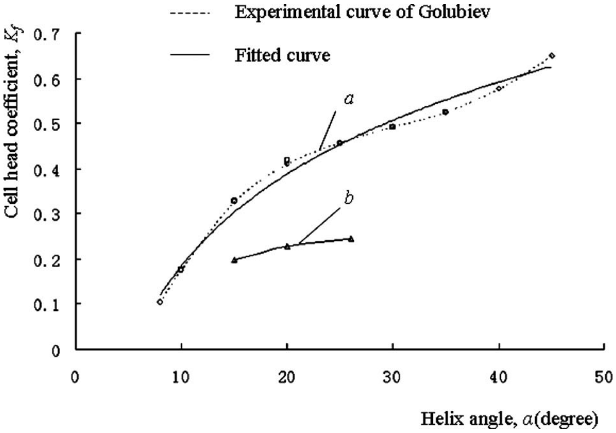

Fig. 3 Variation of the cell head coefficient with thread angle: (*a*) for trapezoidal and semicircular thread and (*b*) for triangular thread

3 Effects of Some Thread Geometric Parameters on K_f

Equation (12) is an approximation of the relationship between K_f and the thread geometric parameters. Therefore, it could be used as a theoretical basis for analyzing the effects of the thread geometric parameters on K_f.

3.1 Thread Lead. Equation (12) shows that with an increase in thread lead, K_f also increases. That means the effective pressure transferred from the walls of every cell into the fluid increases and energy losses are relatively less during fluid momentum exchange. Figure 3 shows how K_f varies with thread lead. In this figure, K_f is calculated from Golubiev's experimental data [2,9] on trapezoidal, semicircular, and triangular thread geometries by using Eq. (13). For trapezoidal and semicircular threads, K_f varies gradually with helix angle from 20 deg to 40 deg. When the helix angle is below 20 deg or exceeds 40 deg, K_f decreases or increases rapidly. For the triangular thread, K_f changes slowly in the range of spiral angle from 15 deg to 26 deg. Figure 4 shows the experimental results of triangular thread pumps with thread leads of 80 mm, 112 mm, and 160 mm, respectively. The pumps have the same diameter of 100 mm, screw length of 150 mm, thread number of 27, and screw-sleeve radial clearance of 0.2 mm [2]. Their axial cell numbers are 50, 36, and 25, respectively, the corresponding cell head coefficients K_f are 0.22, 0.23, and 0.25, and the corresponding pump total head coefficients K_b are 11.11, 8.41, and 6.31, respectively. It is obvious that since the axial cell number decreases much more rapidly than the cell head coefficient increases, the pump total head coefficient and the maximum head of the pump decrease.

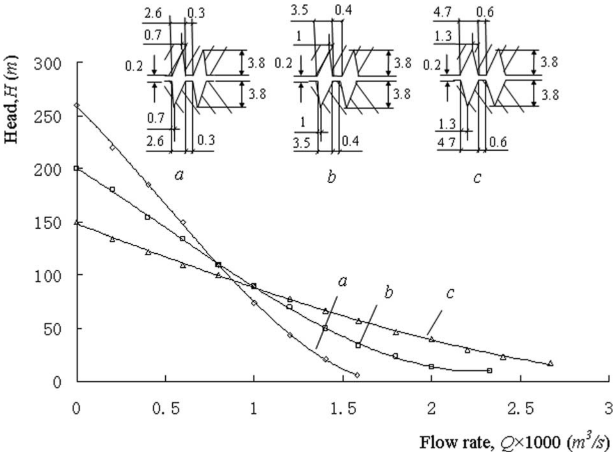

Fig. 4 Characteristics of triangular thread pumps with different thread lead (*n*=2900 rpm): (*a*) for *ϕ* 100 mm×80 mm ×27(*D*×*b*×z_1), *L*=150 mm; (*b*) for *ϕ* 100 mm×112 mm×27, *L*=150 mm; and (*c*) for *ϕ* 100 mm×160 mm×27, *L* =150 mm

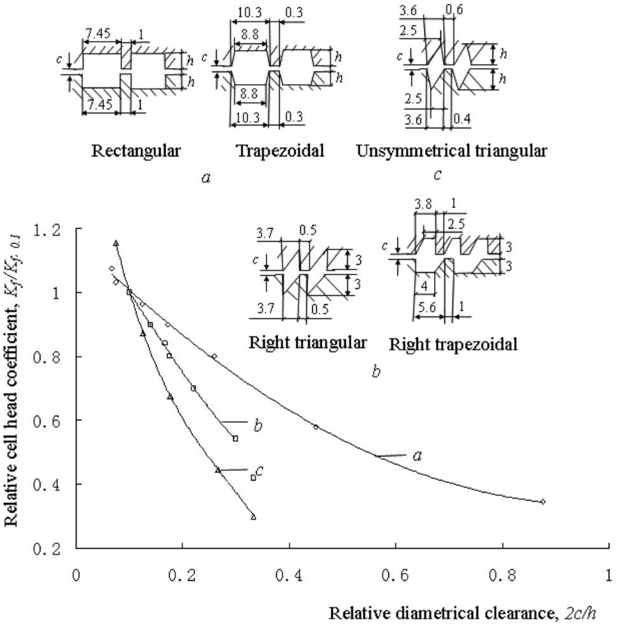

Fig. 5 Variation of the relative cell head coefficient ($K_f/K_{f,0.1}$) with the relative diametrical clearance (2*c*/*h*) for LSP with different shape thread ($K_{f,0.1}$—the cell head coefficient at the relative diametrical clearance of 0.1)

The relationship between K_f and the thread lead is given by fitting experimental data in Fig. 3. For the trapezoidal and semicircular threads,

$$K_f = 0.2573 \ln(\tan(\alpha)) + 0.6413 \tag{14}$$

For the triangular thread,

$$K_f = 0.0844 \ln(\tan(\alpha)) + 0.3125 \tag{15}$$

Evidently, K_f increases with $\tan(\alpha)$, but it is not proportional to $\tan(\alpha)$.

3.2 Clearance Between Screw and Sleeve. Equation (12) indicates that K_f decreases with increasing clearance between screw and sleeve. As the clearance increases, the retarding action of the sleeve thread on fluid elements becomes weak, and then the pressure gradient from the pressure side of screw to the suction side of sleeve falls. As a result, the momentum transfer between the fluid elements in the screw grooves and the fluid elements in the sleeve grooves becomes weak. It is as if the clearance is a resistance against the momentum transfer between fluid elements in cells. The experiments of Golubiev [2] and Runmei et al. [7] proved that the cell head coefficient, as well as the pump efficiency, decreases with an increase in clearance.

The performance of LSPs with different shaped threads varies differently with clearance. In Fig. 5, the relative cell head coefficients for rectangular, right trapezoidal and right triangular, and unsymmetrical triangular thread pump are transformed from the corresponding pump head coefficient of Golubiev [2] on the basis of Eq. (13). It is shown that with the increase in clearance, the relative cell head coefficient for unsymmetrical triangular thread falls most rapidly and that for rectangular thread falls most slowly and for right trapezoidal and right triangular thread falls at a rate in between.

The phenomena in Fig. 5 could be explained in terms of the LSP mechanism. The intense turbulent friction between fluid elements in screw grooves and in sleeve grooves causes a complex radial flow and momentum transfer in cells under the actions of thread walls. The straight side walls of the rectangular thread is conducive for fluid to carry out the momentum transfer in the radial direction, while the inclined side walls of triangular thread not only promote radial momentum transfer between liquids in screw grooves and liquids in sleeve grooves but also facilitate liquids in thread grooves to tangentially transfer momentum with liquids in clearance, which consequently produces more energy losses. Consequently, the pressure created in a pump with triangular threads falls more rapidly with increases in screw-sleeve fitting clearance than the pressure in pumps with threads of other shapes such as right trapezoidal, right triangular, and rectangular threads

A relationship between the relative cell head coefficient and the relative diametrical clearance is given by analyzing and fitting experimental data in Fig. 5,

$$K_f/K_{f,0.1} = (1.223 + 0.281i)/(1 + 2c/h)^{2(j+1)} \tag{16}$$

For trapezoidal, rectangular, and semicircular threads (Figs. 5 and 5(*a*)), $i=j=0$; for right trapezoidal and right triangular threads (Figs. 5 and 5(*b*)), $i=j=1$; for unsymmetrical triangular thread (Figs. 5 and 5(*c*)): $i=j=2$.

3.3 Relative Depth of Thread Groove h/t.

The cell provides the space for liquid momentum transfer in both screw grooves and sleeve grooves. Thread groove depth should be properly chosen so as to transfer fluid momentum efficiently and make energy losses minimal. Too shallow a depth will produce too much friction loss caused by impinging between fluid and thread walls, and too deep a depth will result in fluid insufficient momentum transfer. Both of these cases make the cell head coefficient decrease and pump efficiency fall. Neglecting the effects of the mixing length in Eq. (12), K_f is inversely proportional to the relative depth of thread groove. The shallower the relative depth, the higher value K_f has. However, an exceedingly small relative depth can enhance relative losses and lead to the decrease in K_f. As a result, there must exist a maximal K_f with variation of h/t, which is determined only by experiments.

Figures 6(*a*) and 6(*b*), respectively, show the variation of K_f and K_b with the relative depth of rectangular thread groove, where K_f and K_b are calculated from Golubiev's [2] experimental data on pump head coefficient K. Curve *a* keeps the depth of the thread groove and width of thread land fixed, while the width of the thread grooves differ with the number of threads. Curve *b* maintains the width of thread groove and the number of threads constant, and the depth of thread groove changes. Curve *c* keeps the depth of the thread groove and the number of threads unchanged and varies the width of the thread groove. The three curves indicate that K_f decreases with an increase in h/t over a wide range. Comparing curve *a* and curve *b*, there exists a maximal cell head coefficient, separately being $K_{f,a}=0.446$ and $K_{f,b}=0.332$ at $h/t \approx 0.15$. The corresponding pump total head coefficient is $K_{b,a}=1.227$ and $K_{b,b}=3.652$, respectively. Obviously, while having many threads, the LSP with a shallower thread has a larger K_b than that of LSP with few threads, although it has smaller K_f. For curve *a*, with an increase in thread number, K_f decreases but K_b increases and reaches a maximum of 0.245 at $z_1=8$. After that, K_f decreases faster than the increase in thread number and K_b consequently decreases. Curve *c* shows that the wider the thread land, the more the relative friction losses and the less K_f.

For the right portions of curve *a* and curve *b* in Fig. 6(*a*), a relation between K_f and h/t is fitted and given by the following.

For curve *a*,

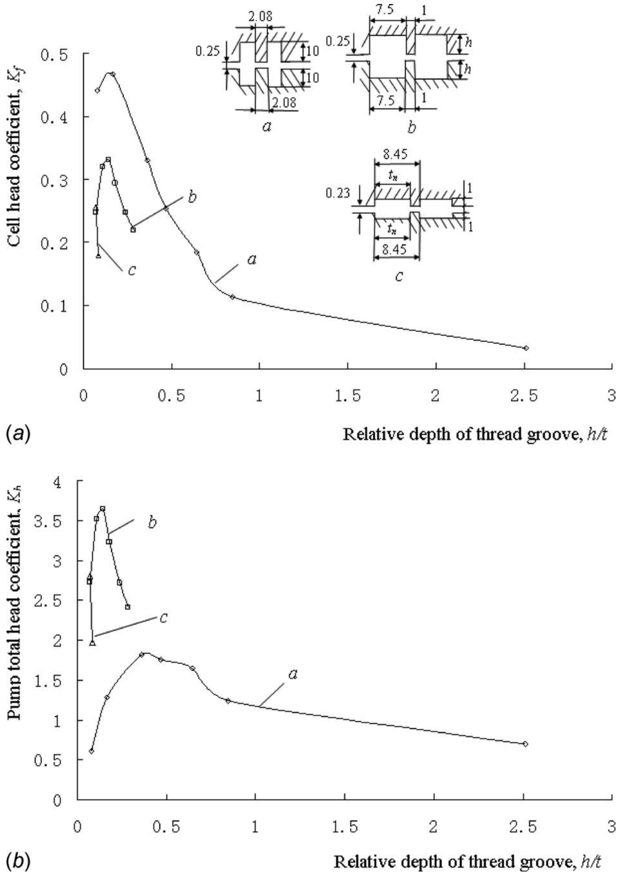

Fig. 6 Variation of (*a*) K_f and (*b*) K_b with the relative depth of rectangular thread groove ($n=2900$ rpm): (*a*) for ϕ 80 mm $\times 160$ mm$\times z_1$, $L=110$ mm, $z_1=2$, $z_1=4$, $z_1=8$, $z_1=16$, and $z_1=32$; (*b*) for ϕ 80 mm$\times$160 mm$\times$16, $L=110$ mm, $h=1$ mm, $h=1.5$ mm, $h=2$ mm, $h=2.5$ mm, $h=3.3$ mm, and $h=4$ mm; and (*c*) for ϕ 80 mm$\times$160 mm$\times$16, $L=110$ mm, $t_n=6.45$ mm, and $t_n=7.45$ mm.

$$K_f = 0.0984(h/t)^{-1.0395} \tag{17}$$

For curve *b*,

$$K_f = 0.104(h/t)^{-0.6022} \tag{18}$$

where K_f with semicircular thread reaches maximum when $(h/t)_n$ at normal cross section is approximately equal to 0.44.

4 Conclusions

The pumping performance of LSP based on its working principle is determined by modeling two-dimensional turbulence equations. Two new concepts, the cell head coefficient K_f and the pump total head coefficient K_b, are proposed. The cell head coefficient Eq. (12) provides a theory for analyzing and fitting experimental data on the effects of thread geometric parameters including thread lead, screw-sleeve fitting clearance, and relative width of groove upon the pump performance. Golubiev's experiments and the cell head coefficient expression both show the following.

(1) With an increase in thread lead, K_f increases but the axial number of threads decreases, thus K_b falls.

(2) With an increase in the fitting clearance, both the pump head and efficiency fall. The head for the triangular thread pump falls most quickly; for rectangular, trapezoidal, and semicircular threads, the head drops most slowly; and, for right triangular and right trapezoidal threads, it decreases at a middle rate.

(3) For either rectangular, semicircular, or trapezoidal thread, K_f decreases with increasing in h/t over most of the range of this variable.

Being in good agreement with Golubiev's experimental results, the cell head coefficient (Eq. (12)) may provide a theoretical basis for thread geometric parameters optimization and LSP design theory, and the two concepts, K_f and K_b, may be used as LSP design criterions. The effects of screw diameter, triangular thread angle, surface roughness, liquid viscosity, and other factors on the cell head coefficient still need further theoretical and experimental investigation.

Nomenclature

b = thread lead
c = fitting clearance between screw and sleeve
c_u = average tangential velocity of fluid in screw and sleeve grooves
D = diameter of screw
g = gravity acceleration
H = pump head
h = groove depth
i,j = constants
K = head coefficient of Golubiev
K_f = cell head coefficient
K_b = pump total head coefficient
L = pump length
l_{xy}, l_{zy} = mixing length for fluid particles
m = number of cells formed by two screw threads and two sleeve threads in axial direction
p = fluid pressure
Q = total flow rate of pump
S_c = cross sectional area of screw grooves
t = circumferential width of groove
u_t = tangential surface velocity of screw
u,w = velocity in tangential and axial direction
$u'v'$, $w'v'$ = Reynolds stresses
x,y,z = coordinate system
z_1 = number of threads in x direction
Δp_z = pumping pressure
α = helix angle
ρ = fluid density

Subscript

n = normal

References

[1] Golubiev, A. I., 1965, "Studies on Seal for Rotating Shafts of High-Pressure Pumps," Wear, **8**, pp. 270–288.
[2] Golubiev, A. I., 1981, *Labyrinth-Screw Pumps and Seals for Corrosive Media*, 2nd ed., Mashinostroenie, Moscow, pp. 34–49.
[3] Bilgen, B., and Akgungor, A. C., 1973, "The Turbulent Double Screw Pump—Theory and Experiment," Proceedings of the Sixth International Conference on Fluid Sealing, Munich, Germany, pp. G4:45–G4:60.
[4] Yizheng, Z., and Jin, L., 1991, "The Numerical Analysis of Labyrinth Screw Pump and Seal," ACTA Aeronaut. Astronaut. Sinica, **12**(8), pp. 323–331.
[5] Guojun, H., and Yizheng, Z., 1993, "Structures and Working Principle of Labyrinth Screw Seal and It's Head Coefficient Determination," Fluid Eng., **11**,pp. 48–50.
[6] Runmei, M., Kuisheng, W., and Jingzhong, L., 2008, " Study on Pumping Mechanism of Labyrinth Screw Pump by CFD Numerical Simulation and Pump Performance Experiments," Lubr. Eng., **2**, pp. 75–79.
[7] Runmei, M., Kuisheng, W., and Jingzhong, L., 2007, "Experimental Study of Labyrinth-Screw Pump Characteristics," Fluid Machinery, **12**, pp. 1–4,12.
[8] Zixiong, Z., and Zengnan, D., 1998, *Viscous Fluid Mechanics*, TsingHua University, Beijing, Chap. 7, pp. 10–11.
[9] Yongquan, G., 1990, *Fluid Dynamic Seal*, University of Petroleum, Beijing, pp. 430–437.